Mathematical Problems in Engineering

Theory and Applications of Fractional Order Systems

Guest Editors: Riccardo Caponetto, Josè A. Tenereiro Machado, and Juan J. Trujillo

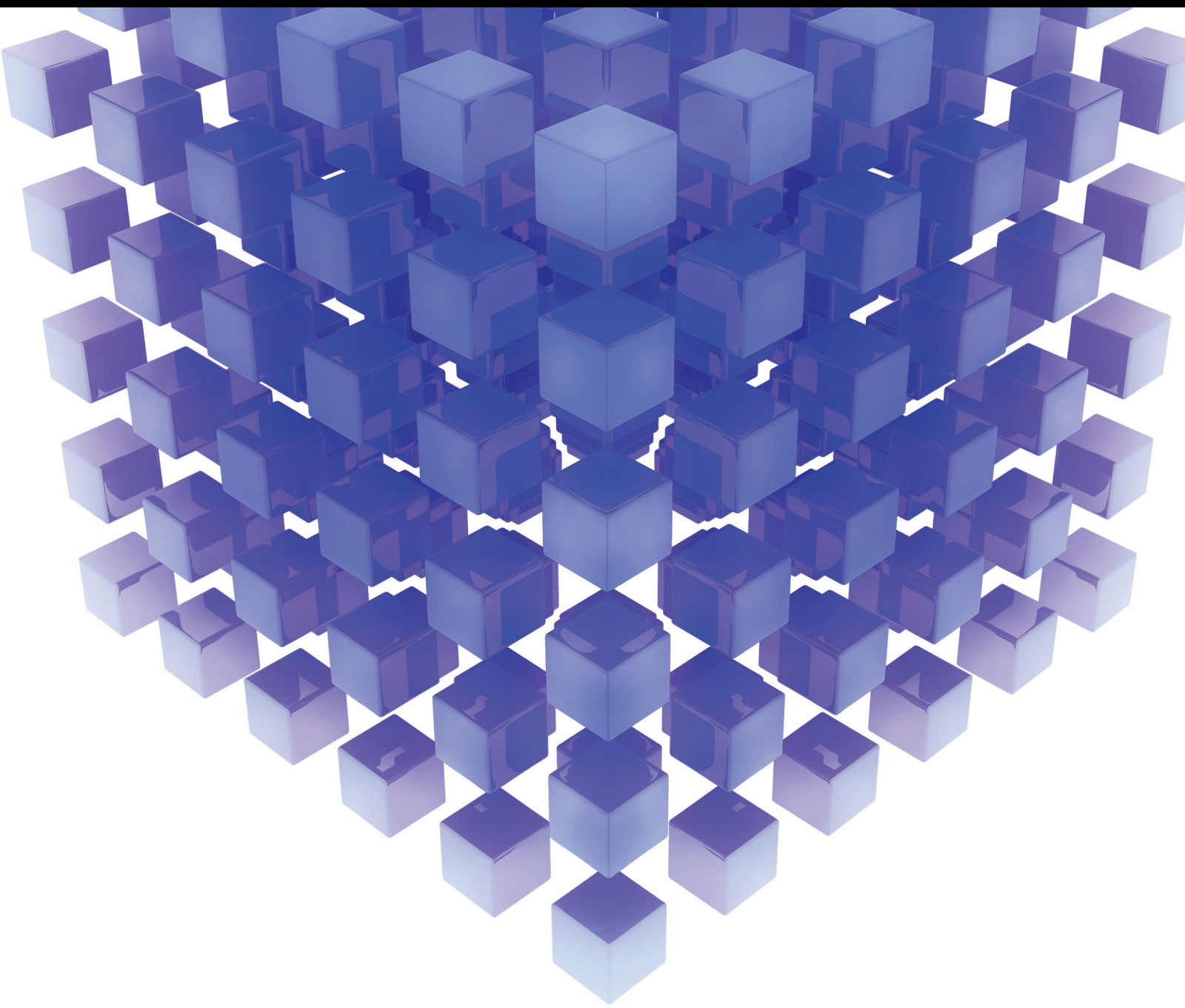

Theory and Applications of Fractional Order Systems

Mathematical Problems in Engineering

Theory and Applications of Fractional Order Systems

Guest Editors: Riccardo Caponetto, Josè A. Tenereiro Machado, and Juan J. Trujillo

Editorial Board

Contents

Hindawi Publishing Corporation
Mathematical Problems in Engineering
Volume 2014, Article ID 596195, 2 pages
http://dx.doi.org/10.1155/2014/596195

Editorial

Theory and Applications of Fractional Order Systems

Riccardo Caponetto,[1] Josè A. Tenereiro Machado,[2] and Juan J. Trujillo[3]

[1]*Department of Electrical, Electronics and Computer Engineering, University of Catania, Viale A. Doria 6, 95125 Catania, Italy*
[2]*ISEP-Institute of Engineering, Polytechnic of Porto, Department of Electrical Engineering, Rua Dr. Antonio Bernardino de Almeida 431, 4200-072 Porto, Portugal*
[3]*Department of Mathematical Analysis, University of La Laguna, C/Astr. Francisco Sanchez s/n, La Laguna, 38271 Tenerife, Spain*

Correspondence should be addressed to Riccardo Caponetto; riccardo.caponetto@dieei.unict.it

Received 16 November 2014; Accepted 16 November 2014; Published 30 December 2014

In the last decades noninteger differentiation became a popular tool for modeling the complex behaviours of physical systems from diverse domains such as mechanics, electricity, chemistry, biology, and economics. Numerous studies have validated the novel perspective demonstrating fractional order models that better characterize many real-world physical systems by means of differential operators of noninteger order. The long-range temporal or spatial dependence phenomena inherent to the fractional order systems (FOS) present unique and intriguing peculiarities, not supported by their integer-order counterpart, which raise exciting challenges and opportunities related to the development of modelling, control, and estimation methodologies involving fractional order dynamics.

The purpose of this special issue is to draw attention to the scientific community to some recent advances and possible applications of fractional order systems and to ensure the corresponding dissemination. The issue includes a collection of papers in the area of FOS and some leading and emerging specialists in the area present their latest results.

A short description of the addressed topics is as follows.

(i) Forest fires are studied in the perspective of dynamical systems, describing the global dynamics along several decades. The time is modelled as Dirac impulses with amplitude proportional to the burnt area.

(ii) A systematic form of the existing formulations of fractional derivatives and integrals is presented.

(iii) The asymptotic stability of the two-step Runge-Kutta methods for neutral delay integrodifferential-algebraic equations with many delays is developed. It has been proved that A-stable two-step Runge-Kutta methods are asymptotically stable for neutral delay integrodifferential-algebraic equations with many delays.

(iv) An efficient iteration method for Toeplitz-plus-band triangular systems is presented with $O(M\log(M))$ computational complexity and $O(M)$ memory complexity. The proposed method is compared with the regular solution with (M^2) computational complexity and $O(M^2)$ memory complexity.

(v) The fundamental solutions to time-fractional advection diffusion equation in a plane and a half-plane are obtained using the Laplace integral transform with respect to time t and the Fourier transforms with respect to the space coordinates x and y. The Cauchy, source, and Dirichlet problems are also investigated.

(vi) A novel watermarking method associated with the linear canonical transform is proposed. The linear canonical transform, which can be looked at as the generalization of the fractional Fourier transform and the Fourier transform, has received much interest and proved to be one of the most powerful tools in fractional signal processing community.

(vii) A finite series representation of the inverse Mittag-Leffler function is formulated for a range of the

parameters α and β, specifically, $0 < \alpha < 1/2$ for $\beta = 1$ and for $\beta = 2$, showing also that this finite series representation of the inverse Mittag-Leffler function greatly expedites its evaluation.

(viii) The sparse prior in fractional order gradient domain as texture-preserving strategy to restore textured images degraded by blur and/or noise is introduced. The unknown variables in proposed model using method based on half-quadratic splitting by minimizing the nonconvex energy functional are also solved.

(ix) A new general and systematic coupling scheme is developed to achieve the modified projective synchronization (MPS) of different fractional order systems under parameter mismatch via the open-plus-closed-loop (OPCL) control. Based on the stability theorem of linear fractional order systems, sufficient conditions for MPS are proposed.

(x) Several nanodiamond preparations for Raman spectroscopic studies have been studied. These nanodiamonds have been exposed to increasing temperature treatments at constant heating rates (425–575°C) aiding graphite release. Changes in the nanodiamond surface and properties with Raman signal which could be used as a detection marker are correlated.

(xi) The discrete wavelet transform via local fractional operators is structured and applied to process the signals on Cantor sets. An illustrative example of the local fractional discrete wavelet transform is also given.

Riccardo Caponetto
Josè A. Tenereiro Machado
Juan J. Trujillo

Hindawi Publishing Corporation
Mathematical Problems in Engineering
Volume 2014, Article ID 194249, 5 pages
http://dx.doi.org/10.1155/2014/194249

Research Article

An Efficient Iteration Method for Toeplitz-Plus-Band Triangular Systems Generated from Fractional Ordinary Differential Equation

Chunye Gong,[1,2,3] Weimin Bao,[1,2] Guojian Tang,[1] Changwan Min,[2] and Jie Liu[3]

[1] *College of Aerospace Science and Engineering, National University of Defense Technology, Changsha 410073, China*
[2] *Science and Technology on Space Physics Laboratory, Beijing 100076, China*
[3] *School of Computer Science, National University of Defense Technology, Changsha 410073, China*

Correspondence should be addressed to Chunye Gong; gongchunye@gmail.com

Received 2 January 2014; Accepted 27 May 2014; Published 12 June 2014

Academic Editor: Riccardo Caponetto

It is time consuming to numerically solve fractional differential equations. The fractional ordinary differential equations may produce Toeplitz-plus-band triangular systems. An efficient iteration method for Toeplitz-plus-band triangular systems is presented with $O(M\log(M))$ computational complexity and $O(M)$ memory complexity in this paper, compared with the regular solution with $O(M^2)$ computational complexity and $O(M^2)$ memory complexity. M is the discrete grid points. Some methods such as matrix splitting, FFT, compress memory storage and adjustable matrix bandwidth are used in the presented solution. The experimental results show that the presented method compares well with the exact solution and is 4.25 times faster than the regular solution.

1. Introduction

Fractional differential equation (FDE) plays an important role in dynamical systems [1] and has more than 300 years of research history [2]. Many analytical solutions and numerical solutions [3–6] have been proposed for FDE, such as finite difference method [7, 8], finite element method [9], and spectral method [10, 11]. In recent times, interest in fractional ordinary differential equations (FODE) has increased [12–15]. The derivatives in the FODE are approximated by linear combinations of function values at the discrete grid points. Compared with integer ordinary differential equations, the FODE has nonlocal effect, which means a grid point may rely on the grid points far away from its position. And a grid point of the classical integer equations may only rely on its several neighboring grid points.

For integer order equations, the coefficient matrices are often sparse. Because of the nonlocal property of fractional differential operators, the numerical methods for fractional diffusion equations often generate dense or even full coefficient matrices [16]. This nonlocal property makes the computation of FODE and FDE much heavier than that of the traditional integer equations. The short memory principle [17], parallel computing [18–21], fast Fourier transformation (FFT) [22, 23], multigrid method [24], and preconditioner technologies [25, 26] are used to overcome this heavy computation. Gong et al. presented many parallel algorithms for different FDEs on both traditional and heterogeneous parallel platforms [16, 18]. Diethelm [19] proposed a parallel second-order Adams-Bashforth-Moulton method for a FODE. Wang and Du [26] proposed a superfast-preconditioned iterative method for steady-state two-side space-fractional diffusion equations.

The fractional ordinary differential equations may produce Toeplitz-plus-band triangular systems. Toeplitz-plus-band systems were studied by professors Chan and Ng [27]. They considered the solutions of Hermitian Toeplitz-plus-band systems $(A_n + B_n)x = b$, where A_n are n-by-n Toeplitz matrices and B_n are n-by-n band matrices with bandwidth independent of n. A_n and B_n are both Hermitian matrix. The authors proved that if A_n is generated by a nonnegative piecewise continuous function and B_n is positive semidefinite, then there exists a band matrix C_n, with bandwidth

independent of n, such that the spectra of $C_n^{-1}(A_n + B_n)$ are uniformly bounded by a constant independent of n. The band preconditioner was developed for Hermitian Toeplitz systems [28]. The recursive blocked algorithms were proposed for triangular systems and the recursive algorithms lead to an automatic variable blocking that has the potential of matching the memory hierarchies of today's HPC (high performance computing) systems [29, 30].

This paper focuses on the fractional ordinary differential equation [13]:

$$u'(t) + a(t)\,{}_0D_t^{\alpha}u(t) + b(t)\,u(t) = f(t), \quad u(0) = 0, \tag{1}$$

where $0 < \alpha < 1$, $0 < t < T < +\infty$, $a(t) > 0$, and $b(t) > 0$. The fractional derivative is in the Caputo form [31].

Define $t_i = i\tau$ for $0 \le i \le M$, where M is a positive integer, and $\tau = T/M$ are step size. Assume u_i to be the numerical approximation to $u(t_i)$ and f_i the numerical approximation to $f(t_i)$. Using the Grünwald approximation, the finite difference scheme for (1) is shown as follows:

$$\frac{u_i - u_{i-1}}{\tau} + a_i\tau^{-\alpha}\sum_{k=0}^{i} w_k u_{i-k}^n + b_i u_i = f_i, \quad u_0 = 0, \tag{2}$$

where the normalized Grünwald weight w is defined by

$$w_0 = 1, \quad w_i = (-1)^i \frac{\alpha(\alpha-1)\cdots(\alpha-i+1)}{i!}, \quad i = 1, 2, 3, \ldots. \tag{3}$$

Equation (2) results in a linear system of equations

$$AU = F, \tag{4}$$

where $U = (u_1, u_2, \ldots, u_M)^T$ and $F = (f_1, f_2, \ldots, f_M)^T$. If $u_0 \neq 0$, the term should be included in F. $A = (a_{ij})_{M\times M}$ is the coefficient matrix. A is defined by

$$a_{i,j} = \begin{cases} 0 & \text{for } i < j \\ \dfrac{1}{\tau} + \dfrac{a_i w_0}{\tau^\alpha} + b_i & \text{for } i = j \\ \dfrac{-1}{\tau} + \dfrac{a_i w_1}{\tau^\alpha} & \text{for } i = j+1 \\ \dfrac{a_i w_{i-j}}{\tau^\alpha} & \text{for } i > j+1. \end{cases} \tag{5}$$

2. Method

2.1. Analysis. In a more explicit format, matrix A can be represented as

$$A = \begin{pmatrix} \frac{1}{\tau} + \frac{a_1 w_0}{\tau^\alpha} + b_1 & 0 & \cdots & 0 \\ \frac{-1}{\tau} + \frac{a_2 w_1}{\tau^\alpha} & \frac{1}{\tau} + \frac{a_2 w_0}{\tau^\alpha} + b_2 & \cdots & 0 \\ \vdots & \vdots & \ddots & \vdots \\ \frac{a_M w_{M-1}}{\tau^\alpha} & \frac{a_M w_{M-2}}{\tau^\alpha} & \cdots & \frac{1}{\tau} + \frac{a_M w_0}{\tau^\alpha} + b_n \end{pmatrix}. \tag{6}$$

```
input: M, F, A
output: F
(1) for i = 1 to M by 1 do
(2)     f_i ← f_i / a_{i,i}
(3)     for j = i + 1 to M by 1 do
(4)         f_j ← f_j − a_{i,j} f_j
```

Algorithm 1: Forward substitution for lower triangular matrix.

The linear system (4) can be solved with computational complexity $O(M^2)$, shown in Algorithm 1. The output F equals U.

From (6), we can see that A has some properties.

(1) A is a low triangular, diagonal dominant matrix.

(2) One has $|a_{i,j+1}| > |a_{i,j}|$ for $1 \le i \le M$, $j < i$. This property is determined by the normalized Grünwald weight w_i and is the mathematical background of short memory principle. This property means that for grid point p, if the distance of grid point p_1 is smaller than that of grid point p_2, p_1 has more impact on p than p_2.

(3) If A is split into two matrices B and C, $A = B - C$. B is a banded matrix and the bandwidth (number of diagonals) $\eta > 2$. Matrix C can be factorized into a product $C = DT$. D is a diagonal matrix $\mathrm{diag}\{a_1, a_2, \ldots, a_M\}$. T is a Toeplitz matrix with $M - \eta$ nonzero diagonals on its left-bottom part.

(4) The Toeplitz matrix T can be stored with $M - \eta$ memory space compared with $(M-\eta)(M-\eta+1)/2$ for a general low triangular matrix with order $M - \eta$.

2.2. Efficient Iteration Method. Equation (4) evolves as follows:

$$(B - C)U = F \tag{7}$$

$$BU^{n+1} = CU^n + F \tag{8}$$

$$BU^{n+1} = DTU^n + F \tag{9}$$

$$BU^{n+1} = D(TU^n) + F. \tag{10}$$

So the linear algebra can be solved iteratively, shown in (10). Because D is a diagonal matrix, D keeps associative law and commutative law for matrix-matrix multiplication. The rate of convergence associated with (10) depends on the eigenvalues of the iteration matrix [32]:

$$H = B^{-1}DT = B^{-1}C. \tag{11}$$

Assuming error $e^{n+1} = U^{n+1} - U$ with U satisfies $AU = F$, then

$$e^{n+1} = B^{-1}Ce^n = He^n = H^n e^1 \tag{12}$$

input: M, η, F, A
output: U
(1) $\epsilon \leftarrow 10^{-6}, \delta = 1.0$
(2) **while** $\delta > \epsilon$ **do**
(3) set $vb_{1\to M-\eta}$ with $ua_{M-\eta\to 1}$
(4) $V1 \leftarrow \mathrm{FFT}(vb)$
(5) $V2 \leftarrow \mathrm{FFT}(va)$
(6) $v \leftarrow V1 \odot V2$
(7) $u_{1\to M} \leftarrow f_{1\to M}$
(8) **for** $i = 1$ **to** $M - \eta$ *by 1* **do**
(9) $u_{\eta+i} \leftarrow u_{\eta+i} + v_{2(M-\eta)-i}$
(10) **for** $j = 1$ **to** M *by 1* **do**
(11) $u_j \leftarrow u_j d_j$
(12) **for** $i = j + 1$ **to** $\min\{j + \eta - 1, M\}$ *by 1* **do**
(13) $u_i \leftarrow u_i - b_{i-j+1} u_j$
(14) $\delta \leftarrow \max(|u_{1\to M} - ua_{1\to M}|)$
(15) $ua_{1\to M} \leftarrow ua_{1\to M}$

Algorithm 2: The efficient iteration method for FODE.

with norm $\| * \|$ [32]:

$$\left\|e^{n+1}\right\| = \left\|G^n e^1\right\| = \left\|G^n\right\| \times \left\|e^1\right\|. \tag{13}$$

So the spectral radius of H ($\rho(H)$) determines the asymptotic behavior of H^n. From Theorem 11.2.1 of [32], we can conclude that if and only if $\rho(H) < 1$, (10) will converge to $A^{-1}F$. Generally speaking, the iteration is expected to work well with small $\rho(H)$.

Assume the bandwidth of matrix B is η and $V = D(TU^n) + F$. Solving $BU^{n+1} = V$ needs about $M\eta$ arithmetical operations. If η is near $\log_2 M$, there are about $M\log_2 M$ arithmetical operations with forward substitution. So the computational complexity of $BU^{n+1} = V$ is $O(M\log_2 M)$.

Assume $E1 = TU^n$, $E2 = DE_1$, and $V = E2 + F$. The computation of $E2$ and V needs M multiplications and M additions, respectively. Because T only has nonzero $M - \eta$ diagonals on its left-bottom part, only the front $M - \eta$ elements of U^n are effective for the multiplication TU^n. The back η elements of $E1$ are zero. So $E1 = TU^n$ can be regarded as a Toeplitz matrix vector multiplication $T_1 U_1^n$ with order $M - \eta$. It is well known that Toeplitz matrix vector multiplication with order $M - \eta$ can be finished with $O(M\log_2 M) = O((M - \eta)\log_2(M - \eta))$ operations [33]. The Toeplitz matrix vector multiplication $T_1 U_1^n$ can be computed by FFTs by first embedding T_1 into a $2(M - \eta)$-by-$2(M - \eta)$ circulant matrix. The cost of circulant matrix vector multiplication is $O(2(M - \eta)\log_2(2(M - \eta)))$ by using FFTs of length $2(M - \eta)$.

So the cost of each iteration of (10) is $O(M\log_2 M)$. If A is a diagonal dominant matrix, we can expect (10) can converge with not too many iterations. The efficient iteration method is shown in Algorithm 2.

In Algorithm 2, $ua_{1\to M}$ stands for the value of previous iteration and $u_{1\to M}$ stands for the current iteration. $V1 \odot V2$ stands for $v1_i v2_i$ with $1 \le i \le 2(M - \eta) - 1$. d_i equals the reciprocal of $a_{i,i}$ with $1 \le i \le M$. b_i stands for $a_{i,1}$ with $1 \le i \le \eta$. va and vb are $2(M - \eta) - 1$ arrays. $va_{M-\eta-i+1}$ equals $-a_{\eta+i,1}$.

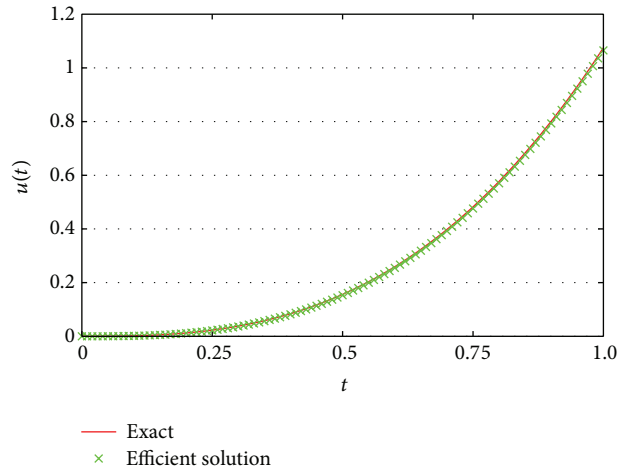

Figure 1: Comparison of exact solution to the solution of the fast solution at time $t = 1.0$.

The value of η can affect the performance of Algorithm 2 shown in Table 1.

Algorithm 2 has five features/advantages compared to Algorithm 1.

(1) Split the coefficient matrix and solve the triangular system iteratively.

(2) Use FFT to compute matrix vector multiplication.

(3) Precompute d_i.

(4) Compress storage.

(5) Adjust parameter η.

3. Numerical Example

The experiment platform is a laptop with Intel(R) Core (TM) i3-3110M CPU, 2 GB main memory, and Windows 7 operating system. The CPU clock frequency is 2.40 GHz. The code is developed with MATLAB R2012a and runs on default double precision floating point operations.

The following fractional ($\alpha = 0.8$) ordinary differential equation [13] was considered:

$$u'(t) + {}_0D_t^{\alpha} u(t) + (1 + t)\, u(t) = f(t), \quad t > 0,\ u(0) = 0, \tag{14}$$

where $f(t) = (14/\Gamma(3.8))t^{1.8} + (5/2)t^2 + (5/\Gamma(3.8))(1 + t)t^{2.8}$.

The exact solution of (14) is

$$u(t) = \frac{5}{\Gamma(3.8)} t^{2.8}. \tag{15}$$

The efficient iteration method of Algorithm 2 compares well with the exact solution to the FODE in the test case of (14), shown in Figure 1. The τ is 1.0/100. The maximum absolute error is 9.78×10^{-3}. The difference between the efficient iteration method and the forward substitution Algorithm 1 is only 2.37×10^{-10}. The efficient iteration method and

Table 1: Impact of η.

Procedure	Big η	Small η
Iterations	Less	More
$BU^{n+1} = V$	Slow	Fast
$V = D(TU^n) + F$	Fast	Slow

Table 2: Performance comparison between regular solution and the presented efficient iteration method.

M	Presented method	Regular solution	Speedup
5×10^3	0.14	0.27	1.96
1×10^4	0.41	1.10	2.67
2×10^4	1.37	4.39	3.20
4×10^4	4.51	17.74	3.93
8×10^4	14.30	60.71	4.25

Table 3: Impact of η for $M = 4 \times 10^4$.

η	Number of iterations	Runtime
$1(\lceil \log_2 M \rceil + 1)$	93	7.95
$2(\lceil \log_2 M \rceil + 1)$	57	4.62
$3(\lceil \log_2 M \rceil + 1)$	43	5.61
$4(\lceil \log_2 M \rceil + 1)$	36	4.51
$5(\lceil \log_2 M \rceil + 1)$	31	4.93
$6(\lceil \log_2 M \rceil + 1)$	28	5.01

the regular forward substitution solution have no noticeable artifacts.

The performance comparison between regular forward substitution solution of Algorithm 1 and efficient iteration method of Algorithm 2 is shown in Table 2. Columns 2 and 3 of Table 2 are the runtime and the runtime is recorded in seconds. With $M = 8 \times 10^4$, the maximum speedup is 4.25. Because the speedup increases with M, the bigger M is, the higher the speedup that can be expected is. Because of the 2 GB memory limitation, the compress memory usage is also used in Algorithm 1.

The impact of η on the performance of Algorithm 2 is shown in Table 3. The runtime of the presented method varies with η. So η is a key parameter for the performance of Algorithm 2. In real fractional ordinary applications, the proper η should be chosen.

The presented iteration method should be regarded as an iteration method to solve not only the system generated from FODE but also the more general Toeplitz-plus-band triangular systems. The technology of parallel computing is very useful, but with less mathematical background. Parallel computing is attractive for fractional differential equations [34]. As a part of future work, first, we would like to parallelize the presented solution on shared memory or distributed memory systems. Second, accelerating the presented efficient iteration method on heterogeneous architecture [35–38] should also be interesting.

Conflict of Interests

The authors declare that there is no conflict of interests regarding the publication of this paper.

Acknowledgments

This research work is supported in part by the National Natural Science Foundation of China under Grant nos. 11175253 and 61170083, in part by the Specialized Research Fund for the Doctoral Program of Higher Education under Grant no. 20114307110001, and in part by the 973 Program of China under Grant no. 61312701001. The authors would like to thank the anonymous reviewers for their helpful comments as well.

References

[1] R. Caponetto, G. Dongola, F. Pappalardo, and V. Tomasello, "Auto-tuning and fractional order controller implementation on hardware in the loop system," *Journal of Optimization Theory and Applications*, vol. 156, no. 1, pp. 141–152, 2013.

[2] J. A. Tenreiro Machado, V. Kiryakova, and F. Mainardi, "A poster about the recent history of fractional calculus," *Fractional Calculus & Applied Analysis*, vol. 13, no. 3, pp. 329–334, 2010.

[3] A. Atangana and A. Kilicman, "Analytical solutions of the space-time fractional derivative of advection dispersion equation," *Mathematical Problems in Engineering*, vol. 2013, Article ID 853127, 9 pages, 2013.

[4] S. Yu. Lukashchuk, "An approximate solution method for ordinary fractional differential equations with the Riemann-Liouville fractional derivatives," *Communications in Nonlinear Science and Numerical Simulation*, vol. 19, no. 2, pp. 390–400, 2014.

[5] D. Baleanu, K. Diethelm, E. Scalas, and J. J. Trujillo, *Fractional Calculus: Models and Numerical Methods*, vol. 3, World Scientific Publishing, 2012.

[6] E. Gao, S. Song, and X. Zhang, "A numerical algorithm for solving a four-point nonlinear fractional integro-differential equations," *Mathematical Problems in Engineering*, vol. 2012, Article ID 329575, 11 pages, 2012.

[7] S. Zhai, X. Feng, and Z. Weng, "New high-order compact ADI algorithms for 3D nonlinear time-fractional convection-diffusion equation," *Mathematical Problems in Engineering*, vol. 2013, Article ID 246025, 11 pages, 2013.

[8] J. Huang, Y. Tang, L. Vázquez, and J. Yang, "Two finite difference schemes for time fractional diffusion-wave equation," *Numerical Algorithms*, vol. 64, no. 4, pp. 707–720, 2013.

[9] N. J. Ford, J. Xiao, and Y. Yan, "A finite element method for time fractional partial differential equations," *Fractional Calculus and Applied Analysis*, vol. 14, no. 3, pp. 454–474, 2011.

[10] M. Zayernouri and G. E. Karniadakis, "Exponentially accurate spectral and spectral element methods for fractional ODEs," *Journal of Computational Physics*, vol. 257, pp. 460–480, 2014.

[11] J. Huang, N. Nie, and Y. Tang, "A second order finite difference-spectral method for space fractional diffusion equations," *Science China: Mathematics*, vol. 57, no. 6, pp. 1303–1317, 2014.

[12] J. Leszczyński and M. Ciesielski, "A numerical method for solution of ordinary differential equations of fractional order," in *Parallel Processing and Applied Mathematics*, pp. 695–702, Springer, 2006.

[13] X. Cai and J. H. Chen, "Numerical method for fractional order ordinary differential equation," *Journal of Jimei University(Natural Science)*, vol. 12, no. 4, pp. 367–370, 2007.

[14] R. Lin and F. Liu, "Fractional high order methods for the nonlinear fractional ordinary differential equation," *Nonlinear Analysis: Theory, Methods & Applications*, vol. 66, no. 4, pp. 856–869, 2007.

[15] J. Cao and C. Xu, "A high order schema for the numerical solution of the fractional ordinary differential equations," *Journal of Computational Physics*, vol. 238, pp. 154–168, 2013.

[16] C. Gong, W. Bao, and G. Tang, "A parallel algorithm for the Riesz fractional reaction-diffusion equation with explicit finite difference method," *Fractional Calculus and Applied Analysis*, vol. 16, no. 3, pp. 654–669, 2013.

[17] W. Deng, "Short memory principle and a predictor-corrector approach for fractional differential equations," *Journal of Computational and Applied Mathematics*, vol. 206, no. 1, pp. 174–188, 2007.

[18] J. Liu, C. Gong, W. Bao, G. Tang, and Y. Jiang, "Solving the caputo fractional reaction-diffusion equation on GPU," *Discrete Dynamics in Nature and Society*. In press.

[19] K. Diethelm, "An efficient parallel algorithm for the numerical solution of fractional differential equations," *Fractional Calculus and Applied Analysis*, vol. 14, no. 3, pp. 475–490, 2011.

[20] C. Gong, W. Bao, G. Tang, Y. Jiang, and J. Liu, "A parallel algorithm for the two dimensional time fractional diffusion equation with implicit difference method," *The Scientific World Journal*, vol. 2014, Article ID 219580, 8 pages, 2014.

[21] C. Gong, W. Bao, G. Tang, Y. Jiang, and J. Liu, "A domain decomposition method for time fractional reaction-diffusion equation," *The Scientific World Journal*, vol. 2014, Article ID 681707, 5 pages, 2014.

[22] H. Wang and K. Wang, "An $O(Nlog^2N)$ alternating-direction finite difference method for two-dimensional fractional diffusion equations," *Journal of Computational Physics*, vol. 230, no. 21, pp. 7830–7839, 2011.

[23] H. Wang, K. Wang, and T. Sircar, "A direct $O(Nlog^2N)$ finite difference method for fractional diffusion equations," *Journal of Computational Physics*, vol. 229, no. 21, pp. 8095–8104, 2010.

[24] H.-K. Pang and H.-W. Sun, "Multigrid method for fractional diffusion equations," *Journal of Computational Physics*, vol. 231, no. 2, pp. 693–703, 2012.

[25] S.-L. Lei and H.-W. Sun, "A circulant preconditioner for fractional diffusion equations," *Journal of Computational Physics*, vol. 242, pp. 715–725, 2013.

[26] H. Wang and N. Du, "A superfast-preconditioned iterative method for steady-state space-fractional diffusion equations," *Journal of Computational Physics*, vol. 240, pp. 49–57, 2013.

[27] R. H. Chan and K.-P. Ng, "Fast iterative solvers for Toeplitz-plus-band systems," *SIAM Journal on Scientific Computing*, vol. 14, no. 5, pp. 1013–1019, 1993.

[28] R. H. Chan and P. T. P. Tang, "Fast band-Toeplitz preconditioners for Hermitian Toeplitz systems," *SIAM Journal on Scientific Computing*, vol. 15, no. 1, pp. 164–171, 1994.

[29] I. Jonsson and B. Kågström, "Recursive blocked algorithm for solving triangular systems. I. One-sided and coupled Sylvester-type matrix equations," *ACM Transactions on Mathematical Software*, vol. 28, no. 4, pp. 392–415, 2002.

[30] I. Jonsson and B. Kågström, "Recursive blocked algorithm for solving triangular systems. II. Two-sided and generalized Sylvester and Lyapunov matrix equations," *ACM Transactions on Mathematical Software*, vol. 28, no. 4, pp. 416–435, 2002.

[31] I. Podlubny, *Fractional Differential Equations*, vol. 198, Academic Press, San Diego, Calif, USA, 1999.

[32] G. H. Golub and C. F. Van Loan, *Matrix Computations*, vol. 3, Johns Hopkins University Press, Baltimore, Md, USA, 4th edition, 2013.

[33] R. H.-F. Chan and X.-Q. Jin, *An introduction to iterative Toeplitz solvers*, vol. 5, Society for Industrial and Applied Mathematics (SIAM), Philadelphia, Pa, USA, 2007.

[34] C. Gong, W. Bao, G. Tang, B. Yang, and J. Liu, "An effcient parallel solution for Caputo fractional reaction-diffusion equation," *The Journal of Supercomputing*, 2014.

[35] X. J. Yang, X. K. Liao, K. Lu, Q. F. Hu, J. Q. Song, and J. S. Su, "The TianHe-1A supercomputer: its hardware and software," *Journal of Computer Science and Technology*, vol. 26, no. 3, pp. 344–351, 2011.

[36] Q. Wu, C. Yang, T. Tang, and L. Xiao, "Exploiting hierarchy parallelism for molecular dynamics on a petascale hetero geneous system," *Journal of Parallel and Distributed Computing*, vol. 73, no. 12, pp. 1592–1604, 2013.

[37] C. Gong, J. Liu, L. Chi, H. Huang, J. Fang, and Z. Gong, "GPU accelerated simulations of 3D deterministic particle transport using discrete ordinates method," *Journal of Computational Physics*, vol. 230, no. 15, pp. 6010–6022, 2011.

[38] C. Gong, J. Liu, H. Huang, and Z. Gong, "Particle transport with unstructured grid on GPU," *Computer Physics Communications*, vol. 183, no. 3, pp. 588–593, 2012.

Hindawi Publishing Corporation
Mathematical Problems in Engineering
Volume 2014, Article ID 238459, 6 pages
http://dx.doi.org/10.1155/2014/238459

Review Article

A Review of Definitions for Fractional Derivatives and Integral

Edmundo Capelas de Oliveira[1] and José António Tenreiro Machado[2]

[1] *Department of Applied Mathematics, IMECC-UNICAMP, 13083-859 Campinas, SP, Brazil*
[2] *Institute of Engineering, Polytechnic of Porto, Department of Electrical Engineering, Rua Dr. Antonio Bernardino de Almeida 431, 4200-072 Porto, Portugal*

Correspondence should be addressed to José António Tenreiro Machado; jtenreiromachado@gmail.com

Received 30 January 2014; Accepted 18 May 2014; Published 10 June 2014

Academic Editor: Riccardo Caponetto

This paper presents a review of definitions of fractional order derivatives and integrals that appear in mathematics, physics, and engineering.

1. Introduction

In 1695, l'Hôpital sent a letter to Leibniz. In his message, an important question about the order of the derivative emerged: What might be a derivative of order 1/2? In a prophetic answer, Leibniz foresees the beginning of the area that nowadays is named fractional calculus (FC). In fact, FC is as old as the traditional calculus proposed independently by Newton and Leibniz [1–4].

In the classical calculus, the derivative has an important geometric interpretation; namely, it is associated with the concept of tangent, in opposition to what occurs in the case of FC. This difference can be seen as a problem for the slow progress of FC up to 1900. After Leibniz, it was Euler (1738) [3] that noticed the problem for a derivative of noninteger order. Fourier (1822) [3, 5] suggested an integral representation in order to define the derivative, and his version can be considered the first definition for the derivative of arbitrary (positive) order. Abel (1826) [3, 5] solved an integral equation associated with the tautochrone problem, which is considered to be the first application of FC. Liouville (1832) [3, 5] suggested a definition based on the formula for differentiating the exponential function. This expression is known as the first Liouville definition. The second definition formulated by Liouville is presented in terms of an integral and is now called the version by Liouville for the integration of noninteger order. After a series of works by Liouville, the most important paper was published by Riemann [6], ten years after his death. We also note that both Liouville and Riemann formulations carry with them the so-called complementary function, a problem to be solved. Grünwald [7] and Letnikov [8], independently, developed an approach to noninteger order derivatives in terms of a convenient convergent series, conversely to the Riemann-Liouville approach, that is given by an integral. Letnikov showed that his definition coincides with the versions formulated by Liouville, for particular values of the order, and by Riemann, under a convenient interpretation of the so-called noninteger order difference. Hadamard (1892) [5] published a paper where the noninteger order derivative of an analytical function must be done in terms of its Taylor series.

After 1900, the FC experiences a fast development and, in an attempt to formulate particular problems, other definitions were proposed. We mention some of them. Weyl [9] introduced a derivative in order to circumvent a problem involving a particular class of functions, the periodic functions. Riesz [10, 11] proved the mean value theorem for fractional integrals and introduced another formulation that is associated with the Fourier transform. Marchaud (1927) [3, 5] introduced a new definition for noninteger order of derivatives. This definition coincides with the Liouville version for "sufficiently good" functions. Erdélyi-Kober (1940) [3, 5] presented a distinct definition for noninteger order of integration that is useful in applications involving integral and differential equations. Caputo (1967) [12] formulated a definition, more restrictive than the Riemann-Liouville

but more appropriate to discuss problems involving a fractional differential equation with initial conditions [13–21].

Due to the importance of the Caputo version, we will compare this approach with the Riemann-Liouville formulation. The definition as proposed by Caputo inverts the order of integral and derivative operators with the noninteger order derivative of the Riemann-Liouville. We summarize the difference between these two formulations. In the Caputo: first the calculate derivative of integer order and after calculate the integral of noninteger order. In the Riemann-Liouville: first calculate the integral of noninteger order and after calculate the derivative of integer order. It is important to cite that the Caputo derivative is useful to affront problems where initial conditions are done in the function and in the respective derivatives of integer order.

After the first congress at the University of New Haven, in 1974, FC has developed and several applications emerged in many areas of scientific knowledge. As a consequence, distinct approaches to solve problems involving the derivative were proposed and distinct definitions of the fractional derivative are available in the literature. This paper presents in a systematic form the existing formulations of fractional derivatives and integrals. We should mention also that we can have several alternative expressions for the same definition. Therefore, we present only those more representative and we cite particular papers [22–32] and books [33–40] that we believe are the most relevant. Furthermore, the paper does not focus on the pros and cons of each definition and does not address the support of the function that is to be differentiated or integrated.

The paper is organized as follows. Section 2 presents the adopted notation. Sections 3 and 4 list the proposed definitions of fractional derivatives and integrals, respectively. Finally, Section 5 outlines some brief remarks.

2. Notation

The following remarks clarify the notation used in the sequel in Sections 3 and 4.

(i) Let $\alpha \in \mathbb{C} : \Re(\alpha) \in (n-1, n]$, $n \in \mathbb{N}$, where $\Re(\cdot)$ denotes the real part of complex number.

(ii) Let $[a, b]$ be a finite interval in $\mathbb{R}$, $k \in \mathbb{N}$, $\nu > 0$, and $\mathtt{f}(0) \equiv f(0^+) - f(0^-)$.

(iii) The floor function, denoted by $\lfloor \cdot \rfloor$, is defined as $\lfloor x \rfloor = \max\{z \in \mathbb{Z} : z \leq x\}$.

(iv) $[\alpha]$ is the integer part of number α and $\{\alpha\}$ the fractional part, $0 \leq \{\alpha\} < 1$, so that $\alpha = [\alpha] + \{\alpha\}$.

(v) $\Delta^\alpha[f(x) - f(x_0)] \simeq \Gamma(1+\alpha)\Delta[f(x) - f(x_0)]$.

(vi) $\alpha(\cdot, \cdot)$ is the variable fractional order with $0 < \alpha(x, t) < 1$ and $(x, t) \in [a, b]$. $\alpha(x)$ is a continuous function on $(0, 1]$.

(vii) $\mathscr{C}(a, z^+)$ is a closed contour, in the complex plane, starting at $\xi = a$, encircling $\xi = z$ once in the positive sense, and returning to $\xi = a$. $\mu, \nu \in \mathbb{R}/0$, with $0 < \mu < 1$ and $0 \leq \nu \leq 1$.

(viii) Consider $z \in \mathbb{C}$ and $k \in \mathbb{R}$. The so-called k-gamma function, denoted by $\Gamma_k(z)$, is related to the classical gamma function by means of $\Gamma_k(z) = k^{z/k-1}\Gamma(z/k)$.

(ix) The so-called k-Pochhammer symbol yields $(z)_{n,k} = \Gamma_k(x + nk)/\Gamma_k(x)$.

(x) The k-fractional Hilfer derivative recovers, as particular cases, the fractional Riemann-Liouville derivative if $\nu = 0$ and $k = 1$ and the fractional Caputo derivative if $\nu = 1 = k$ [41].

3. Definitions of Fractional Derivatives

Liouville derivative:

$$\mathrm{D}^\alpha [f(x)] = \frac{1}{\Gamma(1-\alpha)} \frac{\mathrm{d}}{\mathrm{d}x} \int_{-\infty}^{x} (x-\xi)^{-\alpha} f(\xi)\, \mathrm{d}\xi, \quad -\infty < x < +\infty. \tag{1}$$

Liouville left-sided derivative:

$$\mathrm{D}_{0^+}^\alpha [f(x)] = \frac{1}{\Gamma(n-\alpha)} \frac{\mathrm{d}^n}{\mathrm{d}x^n} \int_{0}^{x} (x-\xi)^{-\alpha+n-1} f(\xi)\, \mathrm{d}\xi, \quad x > 0. \tag{2}$$

Liouville right-sided derivative:

$$\mathrm{D}_{-}^\alpha [f(x)] = \frac{(-1)^n}{\Gamma(n-\alpha)} \frac{\mathrm{d}^n}{\mathrm{d}x^n} \int_{x}^{\infty} (x-\xi)^{-\alpha+n-1} f(\xi)\, \mathrm{d}\xi, \quad x < \infty. \tag{3}$$

Riemann-Liouville left-sided derivative:

$${}^{\mathrm{RL}}\mathrm{D}_{a^+}^\alpha [f(x)] = \frac{1}{\Gamma(n-\alpha)} \frac{\mathrm{d}^n}{\mathrm{d}x^n} \int_{a}^{x} (x-\xi)^{n-\alpha-1} f(\xi)\, \mathrm{d}\xi, \quad x \geq a. \tag{4}$$

Riemann-Liouville right-sided derivative:

$${}^{\mathrm{RL}}\mathrm{D}_{b^-}^\alpha [f(x)] = \frac{(-1)^n}{\Gamma(n-\alpha)} \frac{\mathrm{d}^n}{\mathrm{d}x^n} \int_{x}^{b} (\xi-x)^{n-\alpha-1} f(\xi)\, \mathrm{d}\xi, \quad x \leq b. \tag{5}$$

Caputo left-sided derivative:

$${}_{*}\mathrm{D}_{a^+}^\alpha [f(x)] = \frac{1}{\Gamma(n-\alpha)} \int_{a}^{x} (x-\xi)^{n-\alpha-1} \frac{\mathrm{d}^n}{\mathrm{d}\xi^n} [f(\xi)]\, \mathrm{d}\xi, \quad x \geq a. \tag{6}$$

Caputo right-sided derivative:

$${}_{*}\mathrm{D}_{b^-}^\alpha [f(x)] = \frac{(-1)^n}{\Gamma(n-\alpha)} \int_{x}^{b} (\xi-x)^{n-\alpha-1} \frac{\mathrm{d}^n}{\mathrm{d}\xi^n} [f(\xi)]\, \mathrm{d}\xi, \quad x \leq b. \tag{7}$$

Grünwald-Letnikov left-sided derivative:

$$\begin{aligned} {}^{\mathrm{GL}}\mathrm{D}_{a^+}^{\alpha}\left[f(x)\right] &= \lim_{h\to 0}\frac{1}{h^{\alpha}}\sum_{k=0}^{\lfloor n\rfloor}(-1)^k\frac{\Gamma(\alpha+1)\,f(x-kh)}{\Gamma(k+1)\,\Gamma(\alpha-k+1)}, \\ & nh = x-a. \end{aligned} \tag{8}$$

Grünwald-Letnikov right-sided derivative:

$$\begin{aligned} {}^{\mathrm{GL}}\mathrm{D}_{b^-}^{\alpha}\left[f(x)\right] &= \lim_{h\to 0}\frac{1}{h^{\alpha}}\sum_{k=0}^{\lfloor n\rfloor}(-1)^k\frac{\Gamma(\alpha+1)\,f(x+kh)}{\Gamma(k+1)\,\Gamma(\alpha-k+1)}, \\ & nh = b-x. \end{aligned} \tag{9}$$

Weyl derivative:

$${}_x\mathrm{D}_{\infty}^{\alpha}\left[f(x)\right] = \mathrm{D}_{-}^{\alpha}\left[f(x)\right] = (-1)^m\left(\frac{\mathrm{d}}{\mathrm{d}\xi}\right)^n\left[{}_x\mathrm{W}_{\infty}^{\alpha}\left[f(x)\right]\right]. \tag{10}$$

Marchaud derivative:

$$\mathrm{D}_{+}^{\alpha}\left[f(x)\right] = \frac{\alpha}{\Gamma(1-\alpha)}\int_{-\infty}^{x}\frac{f(x)-f(\xi)}{(x-\xi)^{1+\alpha}}\mathrm{d}\xi. \tag{11}$$

Marchaud left-sided derivative:

$$\mathrm{D}_{+}^{\alpha}\left[f(x)\right] = \frac{\alpha}{\Gamma(1-\alpha)}\int_{0}^{\infty}\frac{f(x)-f(x-\xi)}{\xi^{1+\alpha}}\mathrm{d}\xi. \tag{12}$$

Marchaud right-sided derivative:

$$\mathrm{D}_{-}^{\alpha}\left[f(x)\right] = \frac{\alpha}{\Gamma(1-\alpha)}\int_{0}^{\infty}\frac{f(x)-f(x+\xi)}{\xi^{1+\alpha}}\mathrm{d}\xi. \tag{13}$$

Hadamard derivative [42]:

$$\mathrm{D}_{+}^{\alpha}\left[f(x)\right] = \frac{\alpha}{\Gamma(1-\alpha)}\int_{0}^{x}\frac{f(x)-f(\xi)}{\left[\ln(x/\xi)\right]^{1+\alpha}}\frac{\mathrm{d}\xi}{\xi}. \tag{14}$$

Chen left-sided derivative:

$$\begin{aligned} \mathrm{D}_{\mathrm{c}}^{\alpha}\left[f(x)\right] &= \frac{1}{\Gamma(1-\alpha)}\frac{\mathrm{d}}{\mathrm{d}x}\int_{\mathrm{c}}^{x}(x-\xi)^{-\alpha}f(\xi)\,\mathrm{d}\xi, \\ & x > \mathrm{c}. \end{aligned} \tag{15}$$

Chen right-sided derivative:

$$\begin{aligned} \mathrm{D}_{\mathrm{c}}^{\alpha}\left[f(x)\right] &= -\frac{1}{\Gamma(1-\alpha)}\frac{\mathrm{d}}{\mathrm{d}x}\int_{x}^{\mathrm{c}}(\xi-x)^{-\alpha}f(\xi)\,\mathrm{d}\xi, \\ & x < \mathrm{c}. \end{aligned} \tag{16}$$

Davidson-Essex derivative [15]:

$$\begin{aligned} \mathrm{D}_{0}^{\alpha}\left[f(x)\right] &= \frac{1}{\Gamma(1-\alpha)}\frac{\mathrm{d}^{n+1-k}}{\mathrm{d}x^{n+1-k}} \\ & \times\int_{0}^{x}(x-\xi)^{-\alpha}\frac{\mathrm{d}^k}{\mathrm{d}\xi^k}\left[f(\xi)\right]\mathrm{d}\xi. \end{aligned} \tag{17}$$

Coimbra derivative [43–45]:

$$\begin{aligned} \mathrm{D}_{0}^{\alpha(x)}\left[f(x)\right] &= \frac{1}{\Gamma(1-\alpha(x))} \\ & \times\left\{\int_{0}^{x}(x-\xi)^{-\alpha(x)}\frac{\mathrm{d}}{\mathrm{d}\xi}\left[f(\xi)\right]\mathrm{d}\xi + \mathtt{f}(0)\,x^{-\alpha(x)}\right\}. \end{aligned} \tag{18}$$

Canavati derivative:

$$\begin{aligned} {}_a\mathrm{D}_x^{\nu}\left[f(x)\right] &= \frac{1}{\Gamma(1-\mu)}\frac{\mathrm{d}}{\mathrm{d}x}\int_{0}^{x}(x-\xi)^{\mu}\frac{\mathrm{d}^n}{\mathrm{d}\xi^n}\left[f(\xi)\right]\mathrm{d}\xi, \\ & n = \lfloor\nu\rfloor, \quad \mu = n-\nu. \end{aligned} \tag{19}$$

Jumarie derivative, $n = 1$:

$$\begin{aligned} \mathrm{D}_x^{\alpha}\left[f(x)\right] &= \frac{1}{\Gamma(n-\alpha)}\frac{\mathrm{d}^n}{\mathrm{d}x^n} \\ & \times\int_{0}^{x}(x-\xi)^{n-\alpha-1}\left[f(\xi)-f(0)\right]\mathrm{d}\xi. \end{aligned} \tag{20}$$

Riesz derivative:

$$\begin{aligned} \mathrm{D}_x^{\alpha}\left[f(x)\right] = & -\frac{1}{2\cos(\alpha\pi/2)}\frac{1}{\Gamma(\alpha)}\frac{\mathrm{d}^n}{\mathrm{d}x^n} \\ & \cdot\left\{\int_{-\infty}^{x}(x-\xi)^{n-\alpha-1}f(\xi)\,\mathrm{d}\xi \right. \\ & \left. + \int_{x}^{\infty}(\xi-x)^{n-\alpha-1}f(\xi)\,\mathrm{d}\xi\right\}. \end{aligned} \tag{21}$$

Cossar derivative:

$$\mathrm{D}_{-}^{\alpha}\left[f(x)\right] = -\frac{1}{\Gamma(1-\alpha)}\lim_{N\to\infty}\frac{\mathrm{d}}{\mathrm{d}x}\int_{x}^{N}(\xi-x)^{-\alpha}f(\xi)\,\mathrm{d}\xi. \tag{22}$$

Local fractional Yang derivative [40]:

$$\mathrm{D}_{-}^{\alpha}\left[f(x)\right]\big|_{x=x_0} = \lim_{x\to x_0}\frac{\Delta^{\alpha}\left[f(x)-f(x_0)\right]}{(x-x_0)^{\alpha}}. \tag{23}$$

Left Riemann-Liouville derivative of variable fractional order:

$${}_a\mathrm{D}_x^{\alpha(\cdot,\cdot)}\left[f(x)\right] = \frac{\mathrm{d}}{\mathrm{d}x}\int_{a}^{x}(x-\xi)^{-\alpha(\xi,x)}f(\xi)\frac{\mathrm{d}\xi}{\Gamma\left[1-\alpha(\xi,x)\right]}. \tag{24}$$

Right Riemann-Liouville derivative of variable fractional order:

$${}_x\mathrm{D}_b^{\alpha(\cdot,\cdot)}\left[f(x)\right] = \frac{\mathrm{d}}{\mathrm{d}x}\int_{x}^{b}(\xi-x)^{-\alpha(\xi,x)}f(\xi)\frac{\mathrm{d}\xi}{\Gamma\left[1-\alpha(\xi,x)\right]}. \tag{25}$$

Left Caputo derivative of variable fractional order:

$${}_a\mathrm{D}_x^{\alpha(\cdot,\cdot)}\left[f(x)\right] = \int_{a}^{x}(x-\xi)^{-\alpha(\xi,x)}\frac{\mathrm{d}}{\mathrm{d}\xi}f(\xi)\frac{\mathrm{d}\xi}{\Gamma\left[1-\alpha(\xi,x)\right]}. \tag{26}$$

Right Caputo derivative of variable fractional order:

$$ {}_{x}\mathrm{D}_{b}^{\alpha(\cdot,\cdot)}\left[f(x)\right]=\int_{x}^{b}(\xi-x)^{-\alpha(\xi,x)}\frac{\mathrm{d}}{\mathrm{d}\xi}f(\xi)\frac{\mathrm{d}\xi}{\Gamma\left[1-\alpha(\xi,x)\right]}. \tag{27} $$

Caputo derivative of variable fractional order:

$$ {}_{*}\mathrm{D}_{x}^{\alpha(x)}\left[f(x)\right]=\frac{1}{\Gamma(1-\alpha(x))}\int_{0}^{x}(x-\xi)^{-\alpha(\xi,x)}\frac{\mathrm{d}}{\mathrm{d}\xi}f(\xi)\,\mathrm{d}\xi. \tag{28} $$

Modified Riemann-Liouville fractional derivative:

$$ \mathrm{D}^{\alpha}\left[f(x)\right]=\frac{1}{\Gamma(1-\alpha)}\frac{\mathrm{d}}{\mathrm{d}x}\int_{0}^{x}(x-\xi)^{-\alpha}\left[f(\xi)-f(0)\right]\mathrm{d}\xi. \tag{29} $$

Osler fractional derivative [46]:

$$ {}_{a}\mathrm{D}_{z}^{\alpha}f(z)=\frac{\Gamma(\alpha+1)}{2\pi i}\int_{\mathscr{C}(a,z^{+})}\frac{f(\xi)}{(\xi-z)^{1+\alpha}}\mathrm{d}\xi. \tag{30} $$

k-fractional Hilfer derivative [41]:

$$ {}^{k}\mathrm{D}^{\mu,\nu}f(x)=\mathrm{I}_{k}^{\nu(1-\mu)}\frac{\mathrm{d}}{\mathrm{d}x}\mathrm{I}_{k}^{(1-\mu)(1-\nu)}f(x). \tag{31} $$

4. Definitions of Fractional Integrals

Riemann-Liouville left-sided integral:

$$ {}^{\mathtt{RL}}\mathrm{I}_{a^{+}}^{\alpha}\left[f(x)\right]=\frac{1}{\Gamma(\alpha)}\int_{a}^{x}(x-\xi)^{\alpha-1}f(\xi)\,\mathrm{d}\xi,\quad x\geq a. \tag{32} $$

Riemann-Liouville right-sided integral:

$$ {}^{\mathtt{RL}}\mathrm{I}_{b^{-}}^{\alpha}\left[f(x)\right]=\frac{1}{\Gamma(\alpha)}\int_{x}^{b}(\xi-x)^{\alpha-1}f(\xi)\,\mathrm{d}\xi,\quad x\leq b. \tag{33} $$

Hadamard integral:

$$ \mathrm{I}_{+}^{\alpha}\left[f(x)\right]=\frac{1}{\Gamma(\alpha)}\int_{0}^{x}\frac{f(\xi)}{\left[\ln(\xi/x)\right]^{1-\alpha}}\cdot\frac{\mathrm{d}\xi}{\xi},\quad x>0,\ \alpha>0. \tag{34} $$

Weyl integral:

$$ {}_{x}\mathrm{W}_{\infty}^{\alpha}\left[f(x)\right]=\frac{1}{\Gamma(\alpha)}\int_{x}^{\infty}(\xi-x)^{\alpha-1}f(\xi)\,\mathrm{d}\xi. \tag{35} $$

Chen left-sided integral:

$$ \mathrm{I}_{\mathtt{c}}^{\alpha}\left[f(x)\right]=\frac{1}{\Gamma(\alpha)}\int_{\mathtt{c}}^{x}(x-\xi)^{\alpha-1}f(\xi)\,\mathrm{d}\xi,\quad x>\mathtt{c}. \tag{36} $$

Chen right-sided integral:

$$ \mathrm{I}_{\mathtt{c}}^{\alpha}\left[f(x)\right]=\frac{1}{\Gamma(\alpha)}\int_{x}^{\mathtt{c}}(\xi-x)^{\alpha-1}f(\xi)\,\mathrm{d}\xi,\quad x<\mathtt{c}. \tag{37} $$

Cossar integral [47]:

$$ \mathrm{I}_{\mathtt{c}}^{\alpha}\left[f(x)\right]=\frac{1}{\Gamma(\alpha)}\int_{\mathtt{c}}^{x}(x-\xi)^{\alpha-1}f(\xi)\,\mathrm{d}\xi,\quad x>\mathtt{c}. \tag{38} $$

Erdélyi (left-sided) integral:

$$ \mathrm{I}_{\sigma,\eta}^{\alpha}\left[f(x)\right]=\frac{\sigma x^{-\sigma(\alpha+\eta)}}{\Gamma(\alpha)}\int_{0}^{x}\left(x^{\sigma}-\xi^{\sigma}\right)^{\alpha-1}\xi^{\sigma\eta+\sigma-1}f(\xi)\,\mathrm{d}\xi. \tag{39} $$

Erdélyi (right-sided) integral:

$$ \mathrm{I}_{\sigma,\eta}^{\alpha}\left[f(x)\right]=\frac{\sigma x^{\sigma\alpha}}{\Gamma(\alpha)}\int_{x}^{\infty}\left(\xi^{\sigma}-x^{\sigma}\right)^{\alpha-1}\xi^{\sigma(1-\alpha-\eta)-1}f(\xi)\,\mathrm{d}\xi. \tag{40} $$

Kober (left-sided) integral:

$$ \mathrm{I}_{1,\eta}^{\alpha}\left[f(x)\right]=\frac{x^{-\alpha-\eta}}{\Gamma(\alpha)}\int_{0}^{x}(x-\xi)^{\alpha-1}\xi^{\eta}f(\xi)\,\mathrm{d}\xi. \tag{41} $$

Kober (right-sided) integral:

$$ \mathrm{I}_{1,\eta}^{\alpha}\left[f(x)\right]=\frac{x^{\eta}}{\Gamma(\alpha)}\int_{x}^{\infty}(\xi-x)^{\alpha-1}\xi^{-\alpha-\eta}f(\xi)\,\mathrm{d}\xi. \tag{42} $$

Local fractional Yang integral:

$$ {}_{a}\mathrm{I}_{b}^{\alpha}\left[f(x)\right]=\frac{1}{\Gamma(1+\alpha)}\int_{a}^{b}f(\xi)\,(\mathrm{d}\xi)^{\alpha}. \tag{43} $$

Left Riemann-Liouville integral of variable fractional order:

$$ {}_{a}\mathrm{I}_{x}^{\alpha(\cdot,\cdot)}\left[f(x)\right]=\int_{a}^{x}(\xi-x)^{\alpha(\xi,x)-1}f(\xi)\frac{\mathrm{d}\xi}{\Gamma\left[\alpha(\xi,x)\right]}. \tag{44} $$

Right Riemann-Liouville integral of variable fractional order:

$$ {}_{x}\mathrm{I}_{b}^{\alpha(\cdot,\cdot)}\left[f(x)\right]=\int_{x}^{b}(x-\xi)^{\alpha(\xi,x)-1}f(\xi)\frac{\mathrm{d}\xi}{\Gamma\left[\alpha(\xi,x)\right]}. \tag{45} $$

k-fractional Hilfer integral:

$$ \mathrm{I}_{k}^{\alpha}f(x)=\frac{1}{k\Gamma_{k}(\alpha)}\int_{0}^{x}(x-\xi)^{\alpha/k-1}f(\xi)\,\mathrm{d}\xi. \tag{46} $$

5. Some Remarks

Remark 1. If D^{α} is any fractional derivative, the Miller-Ross sequential derivative of order $k\alpha, k\in\mathbb{Z}$, is given by [3]

$$ \mathscr{D}^{\alpha}=D^{\alpha},\qquad \mathscr{D}^{k\alpha}=D^{\alpha}\mathscr{D}^{(k-1)\alpha}. \tag{47} $$

Remark 2. Whatever the definition employed, $\mathrm{I}^{0}f(x)=\mathrm{D}^{0}f(x)=f(x)$.

Remark 3. Some authors do not distinguish the definition employed by means of a superscript ($\mathtt{GL}$, $\mathtt{RL}$, $\mathtt{C}$, and $\mathtt{L}$) but use different fonts for the operator instead (D, D, $\mathbf{D}$, $\mathfrak{D}$, and $\mathscr{D}$). The particular correspondence between fonts and definitions varies. Very often no indication at all is given, save perhaps in the accompanying text, and the reader is presumed to understand from the context which particular definition is intended.

Remark 4. In the literature, several alternative notations for operator D may be found:

$$\begin{aligned} \mathrm{D}_{a+}^{\alpha} f(x) &= \left(\mathrm{D}_{a+}^{\alpha} f\right)(x) = {}_{a}\mathrm{D}_{x}^{\alpha} f(x) = {}_{a}\mathrm{I}_{x}^{-\alpha} f(x) \\ &= \mathrm{D}_{x-a}^{\alpha} f(x) = \frac{\mathrm{d}^{\alpha} f(x)}{\mathrm{d}(x-a)^{\alpha}}, \\ \mathrm{D}_{b-}^{\alpha} f(x) &= \left(\mathrm{D}_{b-}^{\alpha} f\right)(x) = {}_{x}\mathrm{D}_{b}^{\alpha} f(x) = {}_{x}\mathrm{I}_{b}^{-\alpha} f(x) \\ &= \mathrm{D}_{b-x}^{\alpha} f(x) = \frac{\mathrm{d}^{\alpha} f(x)}{\mathrm{d}(b-x)^{\alpha}}. \end{aligned} \tag{48}$$

Only one of the two operators I and D needs to be used, since it is all a matter of changing the sign of α. In practice, D is the one more often used.

Remark 5. In the expressions for the right and left Liouville fractional derivatives (2) and (3), respectively, some authors have a slight distinct expression, instead of 0^{+} just + and at the lower limit $-\infty$.

Remark 6. We can mention the "difference of fractional order," discussed by Bosanquet [48], and the "Ruscheweyh Derivative," presented in [42, 49–51].

Remark 7. The authors' intention is not to discuss pros and cons of the list of definitions of fractional derivatives and integrals in Sections 3 and 4. Having in mind that the reader can find benefits in applying the correct definition for his/her specific research interest, it can be said that the most used definitions are the Riemann-Liouville (e.g., in calculus), the Caputo (e.g., in physics and numerical integration), and the Grünwald-Letnikov (e.g., in signal processing, engineering, and control). The problem of initialization plays an important role in applied sciences and, consequently, various definitions are occasionally adopted within the scope of specific topics, but the overall problem remains to be clarified.

Remark 8. The paper does not focus on particular relations involving explicit parameters, intervals, or constants, associated with the distinct derivatives. For example, we can mention that, for $\Re(\alpha) = 0$, with $\alpha \neq 0$, the Liouville fractional derivatives are of purely imaginary order. Also, for $\alpha = n \in \mathbb{N}$, we recover the derivative of integer order. For example, $\mathrm{D}_{+}^{n}[f(x)] = f^{(n)}(x)$ and $\mathrm{D}_{-}^{n}[f(x)] = (-1)^{n} f^{(n)}(x)$.

Conflict of Interests

The authors declare that there is no conflict of interests regarding the publication of this paper.

References

[1] M. M. Dzherbashyan and A. B. Nersesian, "About application of some integro-differential operators," *Doklady Akademii Nauk (Proceedings of the Russian Academy of Sciences)*, vol. 121, no. 2, pp. 210–213, 1958.

[2] M. M. Dzherbashyan and A. B. Nersesian, "The criterion of the expansion of the functions to Dirichlet series," *Izvestiya Akademii Nauk Armyanskoi SSR: Seriya Fiziko-Matematicheskih Nauk*, vol. 11, no. 5, pp. 85–108, 1958.

[3] K. S. Miller and B. Ross, *An Introduction to the Fractional Calculus and Fractional Differential Equations*, John Wiley & Sons, New York, NY, USA, 1993.

[4] K. B. Oldham and J. Spanier, *The Fractional Calculus: Theory and Application of Differentiation and Integration to Arbitrary Order*, Academic Press, New York, NY, USA, 1974.

[5] J. T. Machado, V. Kiryakova, and F. Mainardi, "Recent history of fractional calculus," *Communications in Nonlinear Science and Numerical Simulation*, vol. 16, no. 3, pp. 1140–1153, 2011.

[6] B. Riemann, *Versuch Einer Allgemeinen Auffassung der Integration und Differentiation. Gesammelte Mathematische Werke und Wissenschaftlicher Nachlass*, Teubner, Leipzig, 1876, Dover, New York, NY, USA, 1953.

[7] A. K. Grünwald, "Über "begrenzte" derivationen und deren anwendung," *Zeitschrift für Mathematik und Physik*, vol. 12, pp. 441–480, 1867.

[8] A. V. Letnikov, "Theory of differentiation with an arbitrary index," *Sbornik: Mathematics*, vol. 3, pp. 1–66, 1868 (Russian).

[9] H. Weyl, "Bemerkungen zum begriff des differentialquotienten gebrochener ordung vierteljahresschr," *Naturforschende Gesellschaft in Zürich*, vol. 62, pp. 296–302, 1917.

[10] M. Riesz, "L'intégrale de Riemann-Liouville et le problème de Cauchy," *Acta Mathematica*, vol. 81, no. 1, pp. 1–222, 1949.

[11] M. Riesz, "L'intégrale de Riemann-Liouville et le problème de Cauchy pour l'équation des ondes," *Bulletin de la Société Mathématique de France*, vol. 67, pp. 153–170, 1939.

[12] M. Caputo, "Linear models of dissipation whose q is almost frequency independent-ii," *Geophysical Journal of the Royal Astronomical Society*, vol. 13, no. 5, pp. 529–539, 1967.

[13] R. Figueiredo Camargo, A. O. Chiacchio, and E. Capelas de Oliveira, "Differentiation to fractional orders and the fractional telegraph equation," *Journal of Mathematical Physics*, vol. 49, no. 3, Article ID 033505, 2008.

[14] R. Caponetto, G. Dongola, L. Fortuna, and I. Petras, *Fractional Order Systems: Modeling and Control Applications*, World Scientific, Singapore, 2010.

[15] M. Davison and C. Essex, "Fractional differential equations and initial value problems," *The Mathematical Scientist*, vol. 23, no. 2, pp. 108–116, 1998.

[16] G. Jumarie, "On the solution of the stochastic differential equation of exponential growth driven by fractional Brownian motion," *Applied Mathematics Letters*, vol. 18, no. 7, pp. 817–826, 2005.

[17] G. Jumarie, "An approach to differential geometry of fractional order via modified Riemann-Liouville derivative," *Acta Mathematica Sinica*, vol. 28, no. 9, pp. 1741–1768, 2012.

[18] G. Jumarie, "On the derivative chain-rules in fractional calculus via fractional difference and their application to systems modelling," *Central European Journal of Physics*, vol. 11, no. 6, pp. 617–633, 2013.

[19] A. A. Kilbas, H. M. Srivastava, and J. J. Trujillo, *Theory and Applications of Fractional Differential Equations*, vol. 204 of *North-Holland Mathematics Studies*, Elsevier, Amsterdam, The Netherlands, 2006.

[20] C. A. Monje, Y. Chen, B. M. Vinagre, D. Xue, and V. Feliu, *Fractional-Order Systems and Controls: Fundamentals and applications*, Springer, London, UK, 2010.

[21] I. Podlubny, *Fractional Differential Equations: An Introduction to Fractional Derivatives, Fractional Differential Equations, to*

Methods of Their Solution, vol. 198 of *Mathematics in Science and Engineering*, Academic Press, San Diego, Calif, USA, 1999.

[22] E. C. Grigoletto and E. C. de Oliveira, "Fractional versions of the fundamental theorem of calculus," *Applied Mathematics*, vol. 4, pp. 23–33, 2013.

[23] G. H. Hardy, "Fractional versions of the fundamental theorem of calculus," *The Journal of the London Mathematical Society I*, vol. 20, no. 1, pp. 48–57, 2013.

[24] Q. A. Naqvi and M. Abbas, "Complex and higher order fractional curl operator in electromagnetics," *Optics Communications*, vol. 241, no. 4–6, pp. 349–355, 2004.

[25] Z. M. Odibat and N. T. Shawagfeh, "Generalized Taylor's formula," *Applied Mathematics and Computation*, vol. 186, no. 1, pp. 286–293, 2007.

[26] E. Capelas de Oliveira and J. Vaz Jr., "Tunneling in fractional quantum mechanics," *Journal of Physics A: Mathematical and Theoretical*, vol. 44, no. 18, Article ID 185303, 2011.

[27] H. T. C. Pedro, M. H. Kobayashi, J. M. C. Pereira, and C. F. M. Coimbra, "Variable order modeling of diffusive-convective effects on the oscillatory flow past a sphere," *Journal of Vibration and Control*, vol. 14, no. 9-10, pp. 1659–1672, 2008.

[28] B. Ross, S. G. Samko, and E. R. Love, "Functions that have no first order derivative might have fractional derivatives of all orders less than one," *Real Analysis Exchange*, vol. 20, no. 2, pp. 140–157, 1994-1995.

[29] V. E. Tarasov, "Fractional vector calculus and fractional Maxwell's equations," *Annals of Physics*, vol. 323, no. 3, pp. 2756–2778, 2008.

[30] V. E. Tarasov, *Fractional Dynamics: Applications of Fractional Calculus to Dynamics of Particles, Fields and Media*, Nonlinear Physical Science, Springer, Heidelberg, Germany, 2011.

[31] J. J. Trujillo, M. Rivero, and B. Bonilla, "On a Riemann-Liouville generalized Taylor's formula," *Journal of Mathematical Analysis and Applications*, vol. 231, no. 1, pp. 255–265, 1999.

[32] D. Valerio, J. J. Trujillo, M. Rivero, J. T. Machado, and D. Baleanu, "Fractional calculus: a survey of useful formulas," *The European Physical Journal Special Topics*, vol. 222, no. 8, pp. 1827–1846, 2013.

[33] G. A. Anastassiou, *Fractional Differentiation Inequalities*, Springer, Dordrecht, The Netherlands, 2009.

[34] D. Baleanu, K. Diethelm, E. Scalas, and J. J. Trujillo, *Fractional Calculus: Models and Numerical Methods*, vol. 3 of *Series on Complexity, Nonlinearity and Chaos*, World Scientific, Singapore, 2012.

[35] V. Kiryakova, *Generalized Fractional Calculus and Applications*, vol. 301, Longman Scientific & Technical, Harlow, NY, USA, 1994.

[36] F. Mainardi, *Fractional Calculus and Waves in Linear Viscoelasticity*, Imperial College Press, London, UK, 2010.

[37] A. M. Mathai and H. J. Haubold, *Special Functions for Applied Scientists*, Springer, New York, NY, USA, 2008.

[38] D. Valerio and J. S. da Costa, *An Introduction to Fractional Control*, IET, Stevenage, UK, 2012.

[39] X. J. Yang, *Local Fractional Functional Analysis and Its Applications*, Asian Academic Publisher Limited, Hong Kong, 2011.

[40] X. J. Yang, *Advanced Local Fractional Calculus and Its Applications*, World Science, New York, NY, USA, 2012.

[41] G. A. Dorrego and R. A. Cerutti, "The k-fractional Hilfer derivative," *International Journal of Mathematical Analysis*, vol. 7, no. 11, pp. 543–550, 2013.

[42] S. G. Samko, A. A. Kilbas, and O. I. Marichev, *Fractional Integrals and Derivatives: Theory and Applications*, Gordon and Breach Science Publishers, Amsterdam, The Netherlands, 1993.

[43] C. F. M. Coimbra, "Mechanics with variable-order differential operators," *Annalen der Physik*, vol. 12, no. 11-12, pp. 692–703, 2003.

[44] L. E. S. Ramirez and C. F. M. Coimbra, "On the selection and meaning of variable order operators for dynamic modeling," *International Journal of Differential Equations*, vol. 2010, Article ID 846107, 16 pages, 2010.

[45] L. E. S. Ramirez and C. F. M. Coimbra, "On the variable order dynamics of the nonlinear wake caused by a sedimenting particle," *Physica D: Nonlinear Phenomena*, vol. 240, no. 13, pp. 1111–1118, 2011.

[46] T. J. Osler, "Leibniz rule for fractional derivatives generalized and an application to infinite series," *SIAM Journal on Applied Mathematics*, vol. 18, pp. 658–674, 1970.

[47] J. Cossar, "A theorem on Cesàro summability," *Journal of the London Mathematical Society I*, vol. 16, pp. 56–68, 1941.

[48] L. S. Bosanquet, "Note on convexity theorems," *Journal of the London Mathematical Society I*, vol. 18, no. 4, pp. 146–148, 1943.

[49] A. A. Lupas, "Some differential subordinations using Ruscheweyh derivative and Salagean operator," *Advances in Difference Equations*, vol. 2013, article 150, 2013.

[50] M. M. Meerschaert, J. Mortensen, and S. W. Wheatcraft, "Fractional vector calculus for fractional advection-dispersion," *Physica A: Statistical Mechanics and Its Applications*, vol. 367, no. 8, pp. 181–190, 2006.

[51] S. Ruscheweyh, "New criteria for univalent functions," *Proceedings of the American Mathematical Society*, vol. 49, no. 1, pp. 109–115, 1975.

Hindawi Publishing Corporation
Mathematical Problems in Engineering
Volume 2014, Article ID 918371, 7 pages
http://dx.doi.org/10.1155/2014/918371

Research Article

The Stability of Two-Step Runge-Kutta Methods for Neutral Delay Integro Differential-Algebraic Equations with Many Delays

Haiyan Yuan[1,2] and Jihong Shen[1]

[1] *College of Automation, Harbin Engineering University, Harbin 150001, China*
[2] *Department of Mathematics, Heilongjiang Institute of Technology, Harbin 150050, China*

Correspondence should be addressed to Jihong Shen; shenjihong@hrbeu.edu.cn

Received 3 January 2014; Revised 22 April 2014; Accepted 22 April 2014; Published 9 June 2014

Academic Editor: J. A. Tenreiro Machado

This paper studies the asymptotic stability of the two-step Runge-Kutta methods for neutral delay integro differential-algebraic equations with many delays. It proves that A-stable two-step Runge-Kutta methods are asymptotically stable for neutral delay integro differential-algebraic equations with many delays.

1. Introduction

The stability of numerical methods for delay differential equations has been intensively studied in [1–3] for many years. These equations appeared in a wide variety of scientific and engineering fields, such as circuit analysis, computer-aided design power systems, and optimal control. The structure for these, the order of convergence, and the asymptotic stability of numerical methods have been studied in [4–6]. Zhu and Petzold investigated the asymptotic stability of neutral delay differential equations with θ-methods, Runge-Kutta methods, BDF methods, and linear multistep methods [7]. Zhao et al. studied the stability of neutral delay differential equations with Rosenbrock methods [8]. Yu et al. studied the general neutral delay differential equations with multistep methods [9]. More recently, there is a growing interest in the analysis of delay integro differential equations. Baker and Ford [10] studied the asymptotic stability of a class of linear multistep (LM) methods for scalar linear delay integro differential equations; Koto [11] dealt with the linear stability of Runge-Kutta (R-K) methods for systems of delay integro differential equations; Huang and Vandewalle [12] gave sufficient and necessary stability conditions for exact and discrete solutions of linear scalar delay integro differential equations, and Luzyanina et al. [13] developed computational procedures for determining the stability of delay integro differential equations. Zhang and Vandewalle [14] gave the stability criteria for exact and discrete solution of neutral multidelay integro differential equations. Although the stability of numerical methods for delay integro differential equations has been very intensively studied, the stability of delay integro differential equations with many delays has not been studied so far.

In this paper, we focus on the asymptotic stability of numerical methods for neutral delay integro differential-algebraic equations with many delays. This paper is structured as follows. In Section 2 we give asymptotic stability of the analytical solution and introduce two-step Runge-Kutta methods and the stability region. In Section 3, we deal with the asymptotic stability of two-step Runge-Kutta method for neutral delay integro differential-algebraic equations with many delays; the theoretical results are proved. In Section 4, an example is given to illustrate the theoretical results.

2. Asymptotic Stability of the Analytical Solution

2.1. Asymptotic Stability of the Analytical Solution of Neutral Delay Integro Differential-Algebraic Equation with Many Delays. In this section, we consider the following linear

system:

$$Au'(t) + Bu(t) + \sum_{q=1}^{m} C_q u'(t-\tau_q) + \sum_{q=1}^{m} D_q u(t-\tau_q) + \sum_{q=1}^{m} G_q \int_{t-\tau_q}^{t} u(\delta)\, d\delta = 0, \quad t \geq 0, \qquad (1)$$
$$u(t) = \varphi(t), \quad t \in [-\tau, 0),$$

where A, B, C_q, D_q, $G_q \in R^{d\times d}$, A is a singular matrix, τ_q is a given positive delay constant ($q = 1, 2, \ldots, m$), and $0 < \tau_1 \leq \tau_2 \leq \cdots \leq \tau_m = \tau$. $\varphi(t)$ denotes a given vector-valued function and $u(t)$ is a vector-valued unknown function to be solved for $t \geq 0$.

In order to obtain the characteristic equation of system (1), we focus on the exponential solutions $u(t) = e^{st}x$ of (1); here $x = (x_1, x_2, \ldots, x_d)^{\mathrm{T}} \in C^d$ denotes the unknown vector. Then we have

$$u(t) = \left(e^{st}x_1, e^{st}x_2, \ldots, e^{st}x_d\right)^{\mathrm{T}}, \qquad (2a)$$

$$u'(t) = se^{st}x, \qquad (2b)$$

$$u(t-\tau_q) = \left(e^{s(t-\tau_q)}x_1, e^{s(t-\tau_q)}x_2, \ldots, e^{s(t-\tau_q)}x_d\right)^{\mathrm{T}}, \quad q = 1, 2, \ldots, m, \qquad (2c)$$

$$u'(t-\tau_q) = se^{s(t-\tau_q)}x, \quad q = 1, 2, \ldots, m. \qquad (2d)$$

Substituting the above results into (1), we have the following equation:

$$\left[sA + B + s\sum_{q=1}^{m} C_q e^{-s\tau_q} + \sum_{q=1}^{m} D_q e^{-s\tau_q} + s^{-1}\sum_{q=1}^{m} G_q\left(1 - e^{-s\tau_q}\right)\right] x = 0. \qquad (2e)$$

The existence of a nonzero x in (2e) implies the characteristic equation of system (1) holds; that is, the following equation holds:

$$\det\left[sA + B + s\sum_{q=1}^{m} C_q e^{-s\tau_q} + \sum_{q=1}^{m} D_q e^{-s\tau_q} + s^{-1}\sum_{q=1}^{m} G_q\left(1 - e^{-s\tau_q}\right)\right] = 0. \qquad (3)$$

Definition 1 (see [13]). Equation (1) is said to be asymptotically stable, if for any continuous differential initial function and for any delay $\tau_q > 0$, $q = 1, 2, \ldots, m$ the analytical solution to (1) satisfies $\lim_{t\to\infty} u(t) = 0$.

We know that the stability of analytical solution can be studied via the characteristic equation, so we give a criterion for the asymptotic stability of (1), which is based on the following lemmas.

Lemma 2 (see [14]). *Assume*

$$\operatorname{Sup}\{\operatorname{Re}(\lambda) : p(\lambda) = 0\} < 0, \qquad (4)$$

where $p(\lambda) = \det\{\lambda A + B + \lambda\sum_{q=1}^{m} C_q e^{-\lambda\tau_q} + \sum_{q=1}^{m} D_q e^{-\lambda\tau_q} + \sum_{q=1}^{m} G_q\tau_q\eta(e^{-\lambda\tau_q})\}$ *is the characteristic polynomial of* (1). *Then, system* (1) *is asymptotically stable.*

Where $\eta(z)$ is a complex function defined by

$$\eta(z) = \begin{cases} \dfrac{1-z}{\ln z}, & z \in C \setminus \{0, 1\} \\ 0, & z = 0 \\ -1, & z = 1. \end{cases} \qquad (5)$$

And $\ln z = \ln|z| + i\arg z$ ($z = 0, 1$; $-\pi < \arg z \leq \pi$) is the principal branch of the multivalued complex natural logarithm.

Lemma 3 (see [14]). *Function $\eta(z)$ is analytic in $C \setminus R_0^-$ and satisfies $|\eta(z)| \leq 1$ for $|z| \leq 1$, where $R_0^- = \{x \in R : x \leq 0\}$.*

Lemma 4. *If the matrix $(A + \sum_{q=1}^{m} C_q e^{-\lambda\tau_q})$ is invertible for $\operatorname{Re}(\lambda) \geq r$, where $r \in R$, then the function*

$$\tilde{p}(\lambda) = \det\left\{\lambda^2 I_d + \left(A + \sum_{q=1}^{m} C_q e^{-\lambda\tau_q}\right)^{-1} \times \left(\lambda B + \lambda\sum_{q=1}^{m} D_q e^{-\lambda\tau_q} + \sum_{q=1}^{m} G_q\left(1 - e^{-\lambda\tau_q}\right)\right)\right\} \qquad (6)$$

has at most a finite number of zeros for $\operatorname{Re}(\lambda) \geq r$.

Proof. When $\operatorname{Re}(\lambda) \geq r$, the function $\tilde{p}(\lambda)$ can be expanded into the following form:

$$\tilde{p}(\lambda) = \lambda^{2d} + \psi_{2d-1}\left(e^{-\lambda\tau_1}, e^{-\lambda\tau_2}, \ldots, e^{-\lambda\tau_{m1}}\right)\lambda^{2d-1} + \cdots + \psi_0\left(e^{-\lambda\tau_1}, e^{-\lambda\tau_2}, \ldots, e^{-\lambda\tau_{m1}}\right), \qquad (7)$$

where $\psi_i(e^{-\lambda\tau_1}, e^{-\lambda\tau_2}, \ldots, e^{-\lambda\tau_{m1}})$, $i = 0, 1, \ldots, 2d-1$, are rational functions for the expressions $e^{-\lambda\tau_1}, e^{-\lambda\tau_2}, \ldots, e^{-\lambda\tau_{m1}}$, and they have no poles for $\operatorname{Re}(\lambda) \geq r$.

Since $\tau_i > 0$, we have that

$$\left|e^{-\lambda\tau_i}\right| = e^{-\tau_i \operatorname{Re}(\lambda)} \leq e^{-\tau_i r}, \quad \text{for } \operatorname{Re}(\lambda) \geq r. \qquad (8)$$

Hence, there exist constants $K_i > 0$ such that

$$\left|\psi_i\left(e^{-\lambda\tau_1}, e^{-\lambda\tau_2}, \ldots, e^{-\lambda\tau_{m1}}\right)\right| \leq K_i, \quad i = 0, 1, \ldots, 2d-1. \qquad (9)$$

Let M be a positive number large enough such that

$$\frac{K_{2d-1}}{M} + \frac{K_{2d-2}}{M^2} + \cdots + \frac{K_0}{M^{2d}} < 1, \tag{10}$$

which implies that, for $\mathrm{Re}(\lambda) \geq r$ and $|\lambda| \geq M$,

$$\left|\widetilde{p}(\lambda)\right| \geq |\lambda|^{2d}\left[1 - \frac{K_{2d-1}}{M} - \frac{K_{2d-2}}{M^2} - \cdots - \frac{K_0}{M^{2d}}\right] > 0. \tag{11}$$

That is, $\widetilde{p}(\lambda) \neq 0$ in the set $\{\lambda : \mathrm{Re}\,\lambda \geq r, |\lambda| \geq M\}$.

By the isolation property of the zeros for analytic functions, $\widetilde{p}(\lambda)$ has at most a finite number of zeros in the set $\{\lambda : \mathrm{Re}\,\lambda \geq r, |\lambda| < M\}$; this proves the lemma. □

In the following, we denote the spectrum of a square matrix A by $\sigma(A)$ and introduce the set

$$C^- = \{z \in C : \mathrm{Re}(z) < 0\}. \tag{12}$$

Theorem 5. *System* (1) *is asymptotically stable if the following conditions are satisfied:*

(a) $\det(A + \sum_{q=1}^{m} \xi_q C_q) \neq 0$ *for* $|\xi_q| \leq 1$,

(b) $\sigma(G(\xi)) \subseteq C^-$ *for* $\xi = (\xi_1, \xi_2, \ldots, \xi_m)^{\mathrm{T}}$ *with* $|\xi_q| \leq 1$, *where*

$$G(\xi) = \left(A + \sum_{q=1}^{m} \xi_q C_q\right)^{-1} \times \left(-B - \sum_{q=1}^{m} \xi_q D_q - \sum_{q=1}^{m} \eta(\xi_q) G_q \tau_q\right). \tag{13}$$

Proof. When $|\xi_q| \leq 1$, $q = 1, 2, \ldots, m$, condition (a) leads to

$$\begin{aligned}\widehat{P}(\lambda, \xi_1, \xi_2, \ldots, \xi_m) &= \det\left(\lambda A + \lambda \sum_{q=1}^{m} \xi_q C_q + B + \sum_{q=1}^{m} \xi_q D_q + \sum_{q=1}^{m} \eta(\xi_q) G_q \tau_q\right) \\ &= \det\left(A + \sum_{q=1}^{m} \xi_q C_q\right) \det\left(\lambda I_d - G(\xi)\right).\end{aligned} \tag{14}$$

Condition (b) leads to

$$P(\lambda) = \widehat{P}\left(\lambda, e^{-\lambda\tau_1}, e^{-\lambda\tau_2}, \ldots, e^{-\lambda\tau_m}\right) \neq 0 \quad \text{for } \mathrm{Re}(\lambda) \geq 0. \tag{15}$$

Hence

$$\mathrm{Sup}\{\mathrm{Re}(\lambda) : P(\lambda) = 0\} \leq 0. \tag{16}$$

Now we will show that the strict inequality in (16) holds. Define

$$F(\xi_1, \xi_2, \ldots, \xi_m) = \det\left(A + \sum_{q=1}^{m} \xi_q C_q\right), \tag{17}$$

and then $F(\xi_1, \xi_2, \ldots, \xi_m)$ is a multivariate polynomial and is nonzero on the compact domain defined by $|\xi_q| \leq 1$, $q = 1, 2, \ldots, m$, and equal to 1 at the origin. Hence, its modulus is bounded; that is,

$$\begin{aligned}&\left|F(\xi_1, \xi_2, \ldots, \xi_m)\right| \geq \varepsilon > 0, \\ &\text{when } \left|\xi_q\right| \leq 1, \quad \text{for } q = 1, 2, \ldots, m.\end{aligned} \tag{18}$$

By the continuity of F, there exists a $\delta > 0$ such that

$$\begin{aligned}&\left|F(\xi_1, \xi_2, \ldots, \xi_m)\right| > 0, \\ &\text{when } \left|\xi_q\right| \leq 1 + \delta, \quad \text{for } q = 1, 2, \ldots, m.\end{aligned} \tag{19}$$

It follows from this that

$$\begin{aligned}&\det\left(A + \sum_{q=1}^{m} \xi_q C_q\right) \neq 0, \\ &\text{when } \left|e^{-\lambda\tau_q}\right| \leq 1 + \delta, \quad \text{for } q = 1, 2, \ldots, m.\end{aligned} \tag{20}$$

Let r be the strictly positive number $r = \ln(1 + \delta)/\tau$; then

$$\det\left(A + \sum_{q=1}^{m} e^{-\lambda\tau_q} C_q\right) \neq 0 \quad \text{for } \mathrm{Re}(\lambda) \geq -r. \tag{21}$$

Thus, the equation $\widetilde{P}(\lambda) = 0$ has only a finite number of roots when $\mathrm{Re}(\lambda) \geq -r$, and it holds true for the equation $p(\lambda) = 0$ by condition (a). Combined with (16) we get that the characteristic equation has at most a finite number of roots in the region $\{\lambda : -r \leq \mathrm{Re}(\lambda) < 0\}$.

Let

$$-\gamma = \max_{-r \leq \mathrm{Re}(\lambda) < 0} \{\mathrm{Re}(\lambda)\}; \tag{22}$$

then $\gamma > 0$.

When $\mathrm{Re}(\lambda) > -\gamma$, the characteristic equation $p(\lambda) = 0$ has no root. Hence, a strict inequality holds in (16). By Lemma 2, the proof is completed. □

2.2. The Two-Step Runge-Kutta Methods and the Stability Region. Consider the two-step Runge-Kutta method:

$$\begin{aligned}Y^{(n)} &= hC_{11}F\left(t_n, Y^{(n)}\right) + C_{12}y^{(n-1)} \\ y^{(n)} &= hC_{21}F\left(t_n, Y^{(n)}\right) + C_{22}y^{(n-1)}\end{aligned} \tag{23}$$

for solving the initial value problem (1).

In order to simplify the analysis, we consider two-step Runge-Kutta method (TSRK) of the form

$$\begin{aligned} u_{n+1} &= (1-\theta)\, u_n + \theta u_{n-1} \\ &\quad + h \sum_{j=1}^{s} \widehat{b}_j f\left(t_j, U_n^j\right) \\ &\quad + h \sum_{j=1}^{s} \widetilde{b}_j f\left(\widetilde{t}_j, U_{n-1}^j\right), \end{aligned} \tag{24a}$$

$$U_n^i = u_n + h \sum_{j=1}^{s} \widetilde{a}_{i,j} f\left(t_j, U_n^j\right) \quad i = 1, 2, \ldots, s, \tag{24b}$$

where $t_j = t_n + c_j h$, $\widetilde{t}_j = t_{n-1} + c_j h$, u_i is an approximation to $u(t_i)$, h is a fixed step-size, θ, $\widehat{b}_j$, $\widetilde{b}_j$, $\widetilde{a}_{i,j}$, and c_j are coefficients of the method, $0 \le \theta \le 1$.

These methods are a subclass of general linear methods introduced by Butcher [15] and could be possibly also referred to as two-step hybrid methods. They generalize k-step collocation methods (with $k = 2$) for ordinary differential equations (ODEs) studied by Lie and Nørsett [16] and Lie [17] and two-step Runge-Kutta methods for ODEs investigated by Byrne and Lambert [18]. The variable stepsize continuous two-step Runge-Kutta methods for ODEs were investigated by Jackiewicz and Tracogna [19]. Here we will represent (24a) and (24b) by the following table of the coefficients:

$$\begin{array}{c|c} C & A \\ \hline \theta & \begin{array}{c} \widehat{b}^{\mathrm{T}} \\ \\ \widetilde{b}^{\mathrm{T}} \end{array} \end{array} = \begin{array}{c|cccc} c_1 & \widetilde{a}_{11} & \widetilde{a}_{12} & \cdots & \widetilde{a}_{1s} \\ c_2 & \widetilde{a}_{21} & \widetilde{a}_{22} & \cdots & \widetilde{a}_{2s} \\ \vdots & \vdots & \vdots & \ddots & \vdots \\ c_s & \widetilde{a}_{s1} & \widetilde{a}_{s2} & \cdots & \widetilde{a}_{ss} \\ \hline & \widehat{b}_1 & \widehat{b}_2 & \cdots & \widehat{b}_s \\ \theta & & & & \\ & \widetilde{b}_1 & \widetilde{b}_2 & \cdots & \widetilde{b}_s \end{array}, \tag{25}$$

where $c_i = \sum_{j=1}^{s} \widetilde{a}_{ij}$ and $\sum_{j=1}^{s} (\widehat{b}_j + \widetilde{b}_j) = 1 + \theta$.

Apply (24a) and (24b) to the basic test equation

$$u'(t) = a u(t) \quad t \ge 0, \ \operatorname{Re} a < 0, \tag{26}$$

which gives the following equations:

$$\begin{aligned} u_{n+1} &= (1-\theta)\, u_n + \theta u_{n-1} + \alpha \left(\sum_{j=1}^{s} \widehat{b}_j U_n^j + \widetilde{b}_j U_{n-1}^j \right) \\ U_n^i &= u_n + \alpha \sum_{j=1}^{s} \widetilde{a}_{i,j} U_n^j. \end{aligned} \tag{27}$$

Rewriting (27) we obtain

$$u_{i+1} = R(\alpha, \theta)\, u_i + S(\alpha, \theta)\, u_{i-1}, \tag{28}$$

where

$$\begin{aligned} R(\alpha, \theta) &= 1 - \theta + \alpha \widehat{b}^{\mathrm{T}} \left(I - \alpha \widetilde{A}\right)^{-1} e, \\ S(\alpha, \theta) &= \theta + \alpha \widetilde{b}^{\mathrm{T}} \left(I - \alpha \widetilde{A}\right)^{-1} e, \\ \alpha &= ah, \quad e = [1, 1, \ldots, 1]_s^{\mathrm{T}}. \end{aligned} \tag{29}$$

To investigate the stability properties of (24a) and (24b) with (26), we must investigate the asymptotic behaviors of the solution to (28). This is determined by the location of roots of the characteristic polynomial

$$\varphi(z) = z^2 - R(a, \theta)\, z - S(a, \theta). \tag{30}$$

The stability region of the two-step Runge-Kutta methods (24a) and (24b) is the set of all points α for which the roots of $\varphi(z)$ are inside or on the unit circle with those on the unit circle being simple. If $\varphi(z)$ is a Schur polynomial for any α with $\operatorname{Re} \alpha < 0$, the stability of the two-step Runge-Kutta method contains the negative half plane; the method is said to be A-stable for ODEs.

3. Asymptotic Stability of TSRK Methods for Neutral Delay Integro Differential-Algebraic Equation with Many Delays

In this section, we will confine our discussion to neutral delay integro differential-algebraic equation with commensurate delays, that is, systems of the form (1) with $\tau_q = q\tau$, $\tau = Mh$, M is a positive integer, $q = 1, 2, \ldots, m$.

Definition 6 (see [20]). A numerical method for asymptotically stable system (1) is called asymptotically stable if the numerical solution satisfies

$$\lim_{n \to \infty} u_n = 0. \tag{31}$$

Applying the two-step method (24a) and (24b) to (1), we have

$$u_{n+1} = (1-\theta)\, u_n + \theta u_{n-1} + \sum_{j=1}^{s} \widehat{b}_j K_{n,j} + \sum_{j=1}^{s} \widetilde{b}_j K_{n-1,j}, \tag{32}$$

$$\begin{aligned} &AK_{n,i} + hB\left(u_n + \sum_{j=1}^{s} \widetilde{a}_{ij} k_{n,j} \right) + \sum_{q=1}^{m} C_q K_{n-qM,i} \\ &\quad + h \sum_{q=1}^{m} D_q \left(u_{n-qM} + \sum_{j=1}^{s} \widetilde{a}_{ij} K_{n-qM,j} \right) \\ &\quad + h \sum_{q=1}^{m} \sum_{\gamma=0}^{qM} \gamma_r G_q \cdot \left(u_{n-r} + \sum_{j=1}^{s} \widetilde{a}_{ij} k_{n-r,j} \right) = 0 \\ &\qquad \text{for } i = 1, 2, \ldots, s, \end{aligned} \tag{33}$$

where $K_{n,i} = [K_{n,i}^1, K_{n,i}^2, \ldots, K_{n,i}^d]^{\mathrm{T}}$, $i = 1, 2, \ldots, s$, are stage derivatives multiplied by h.

Let

$$\begin{aligned} \widehat{b}^{\mathrm{T}} &= \left[\widehat{b}_1, \widehat{b}_2, \ldots, \widehat{b}_s\right], \qquad \widetilde{b}^{\mathrm{T}} = \left[\widetilde{b}_1, \widetilde{b}_2, \ldots, \widetilde{b}_s\right], \\ \widetilde{A} &= \left(\widetilde{a}_{ij}\right). \end{aligned} \tag{34}$$

We assume that all the eigenvalues of $\widetilde{A}$ have positive real part. Rearrange the variables of the stage derivatives as

$$K_n = \left[K_{n,1}^1, K_{n,2}^1, \ldots, K_{n,s}^1, K_{n,1}^2, K_{n,2}^2, \ldots, K_{n,s}^2, \ldots, K_{n,1}^d, K_{n,2}^d, \ldots, K_{n,s}^d\right]^{\mathrm{T}}. \tag{35}$$

Define

$$Y_n = \left(K_n^{\mathrm{T}}, u_{n+1}^{\mathrm{T}}\right)^{\mathrm{T}}, \qquad \overline{B} = hB, \qquad \overline{D}_q = hD_q, \qquad \overline{\overline{G}}_q = h^2 G_q. \tag{36}$$

Rewrite (32) and (33) in the form

$$\begin{aligned}
&\begin{bmatrix} A\otimes I_s + \overline{B}\otimes\widetilde{A} & 0 \\ -I_d\otimes\widehat{b}^{\mathrm{T}} & I_d \end{bmatrix} Y_n \\
&\quad + \begin{bmatrix} 0 & \overline{B}\otimes e \\ -I_d\otimes\widetilde{b}^{\mathrm{T}} & -(1-\theta)I_d \end{bmatrix} Y_{n-1} \\
&\quad + \begin{bmatrix} 0 & 0 \\ 0 & -\theta I_d \end{bmatrix} Y_{n-2} \\
&\quad + \sum_{q=1}^{m} \begin{bmatrix} C_q\otimes I_s + \overline{D}_q\otimes\widetilde{A} & 0 \\ 0 & 0 \end{bmatrix} Y_{n-qM} \\
&\quad + \sum_{q=1}^{m} \begin{bmatrix} 0 & \overline{D}_q\otimes e \\ 0 & 0 \end{bmatrix} Y_{n-qM-1} \\
&\quad + \sum_{q=1}^{m}\sum_{r=0}^{Mq} \begin{bmatrix} C_q\otimes I_s + \overline{D}_q\otimes\widetilde{A} & 0 \\ 0 & 0 \end{bmatrix} Y_{n-r} \\
&\quad + \sum_{q=1}^{m}\sum_{r=0}^{Mq} \begin{bmatrix} 0 & \gamma_r\overline{\overline{G}}_q\otimes e \\ 0 & 0 \end{bmatrix} Y_{n-r-1} = 0.
\end{aligned} \tag{37}$$

The characteristic polynomial of (37) is given by

$$p(z) = \det\begin{bmatrix} T_1(z) & T_2(z) \\ T_3(z) & T_4(z) \end{bmatrix}, \quad z\in C, \tag{38}$$

where

$$\begin{aligned}
T_1(z) &= z^2\left[\left(A\otimes I_s + \overline{B}\otimes\widetilde{A}\right) + \sum_{q=1}^{m}\left(C_q\otimes I_s + \overline{D}_q\otimes\widetilde{A}\right)z^{-qM} + \sum_{q=1}^{m}\sum_{r=0}^{Mq}\gamma_r\overline{\overline{G}}_q\otimes\widetilde{A}z^{-r}\right], \\
T_2(z) &= z\left[\overline{B}\otimes e + \sum_{q=1}^{m}\overline{D}_q\otimes e z^{-qM} + \sum_{q=1}^{m}\sum_{r=0}^{Mq}\gamma_r\overline{\overline{G}}_q\otimes e r^{-r}\right], \\
T_3(z) &= -z^2 I_d\otimes\widehat{b}^{\mathrm{T}} - zI_d\otimes\widetilde{b}^{\mathrm{T}}, \\
T_4(z) &= z^2 I_d - z(1-\theta)I_d - \theta I_d.
\end{aligned} \tag{39}$$

Following from the theorem on difference equations, we get that if all the zeros z of (38) satisfy $|z| < 1$, then

$$\lim_{n\to\infty} Y_n = 0. \tag{40}$$

Hence, we formulate the following lemmas.

Lemma 7 (see [21]). *If all the zeros z of* (38) *satisfy $|z| < 1$, then numerical method ((32) and (33)) satisfies*

$$\lim_{n\to\infty} u_n = 0. \tag{41}$$

Lemma 8. *Assume that condition (a) of Theorem 5 holds and assume that $[I_s - \lambda_l(r(z))\widetilde{A}]$ are invertible for $|z| \geq 1$, where*

$$r(z) = \left(A + \sum_{q=1}^{m} z^{-qM}C_q\right)^{-1} \times \left(-\overline{B} - \sum_{q=1}^{m} z^{-qM}\overline{D}_q - \sum_{q=1}^{m}\sum_{r=0}^{qM}\gamma_r z^{-r}\overline{\overline{G}}_q\right); \tag{42}$$

then, $\det[T_1(z)] \neq 0$, *for* $|z| \geq 1$.

Proof. Condition (a) in Theorem 5 implies that the matrix $(A + \sum_{q=1}^{m} z^{-qM}C_q)$ is invertible for $|z| \geq 1$; then $T_1(z) = z^2[(A + \sum_{q=1}^{m} z^{-qM}C_q)\otimes I_s][I_d\otimes I_s - r(z)\otimes\widetilde{A}]$.

We have that

$$\begin{aligned}
\det\left[T_1(z)\right] &= z^{2sd}\left[\det\left(A + \sum_{q=1}^{m} z^{-qM}C_q\right)\right]^s \times \det\left[I_d\otimes I_s - r(z)\otimes\widetilde{A}\right] \\
&= z^{2sd}\left[\det\left(A + \sum_{q=1}^{m} z^{-qM}C_q\right)\right]^s \times \prod_{l=1}^{d}\prod_{j=1}^{s}\left[1 - \lambda_l(r(z))\lambda_j\left(\widetilde{A}\right)\right].
\end{aligned} \tag{43}$$

The matrix $I_s - \lambda_l(r(z))\widetilde{A}$ is invertible meaning that $\lambda_l(r(z))\lambda_j(\widetilde{A}) \neq 1$ for all l, j.

Hence, $\det[T_1(z)] \neq 0$, for $|z| \geq 1$. □

Theorem 9. *If the system ((32) and (33)) satisfies Lemma 8 and the following conditions,*

($\widetilde{a}$) $\det(A + \sum_{q=1}^{m} \xi_q C_q) \neq 0$, *for* $|\xi_q| \leq 1$;

($\widetilde{b}$) $|1 - \theta - z^{-1}\theta - (\widehat{b}^{\mathrm{T}} + z^{-1}\widetilde{b}^{\mathrm{T}})[I_d \otimes I_s - r(z) \otimes \widetilde{A}]^{-1}[e_s \otimes r(z)]| < 1$, *for* $|z| \geq 1$,

then the solution of the TSRK methods for (1) *is asymptotically stable.*

Proof. By Lemma 7, we need to prove that all the zeros of (38) satisfy $|z| < 1$.

If these were not true, there would exist a $z_0 \in C$ with $|z_0| \geq 1$, such that

$$\det \begin{bmatrix} T_1(z_0) & T_2(z_0) \\ T_3(z_0) & T_4(z_0) \end{bmatrix} = 0. \tag{44}$$

By Lemma 8, we have that $\det[T_1(z_0)] \neq 0$.

Hence, (44) is equivalent to

$$\det \left\lfloor T_4(z_0) - T_3(z_0) T_1^{-1}(z_0) T_2(z_0) \right\rfloor = 0. \tag{45}$$

Using the Kronecker product [5, chapter 4], we have that

$$\begin{aligned} &\det \left\lfloor T_4(z_0) - T_3(z_0) T_1^{-1}(z_0) T_2(z_0) \right\rfloor \\ &\quad = \det \Bigg\{ z_0^2 I_d - z_0(1-\theta) I_d - \theta I_d \\ &\qquad - \left(z_0^2 I_d \otimes \widehat{b}^{\mathrm{T}} + z_0 I_d \otimes \widetilde{b}^{\mathrm{T}} \right) \\ &\qquad \times z_0^{-2} \left[\left(A + \sum_{q=1}^{m} z_0^{-qM} C_q \right) \otimes I_s \right]^{-1} \\ &\qquad \cdot \left[I_d \otimes I_s - r(z_0) \otimes \widetilde{A} \right]^{-1} \\ &\qquad \cdot z_0 \Bigg[\overline{B} \otimes e + \sum_{q=1}^{m} \overline{D}_q \otimes e z_0^{-qM} \\ &\qquad + \sum_{q=1}^{m} \sum_{r=0}^{Mq} \gamma_r \overline{\overline{G}}_q \otimes e z_0^{-r} \Bigg] \Bigg\} \\ &\quad = z_0^d \det \Big\{ z_0 I_d - \Big[(1-\theta) I_d - z_0^{-1} \theta I_d \\ &\qquad - \left(I_d \otimes \widehat{b}^{\mathrm{T}} + z_0^{-1} I_d \otimes \widetilde{b}^{\mathrm{T}} \right) \\ &\qquad \times \left[I_d \otimes I_s - r(z_0) \otimes \widetilde{A} \right]^{-1} \\ &\qquad \times \left[e \otimes r(z_0) \right] \Big] \Big\}. \end{aligned} \tag{46}$$

Combining (45) and (46) gives that

$$\begin{aligned} &\det \Big\{ z_0 I_d - \Big[(1-\theta) I_d - z_0^{-1} \theta I_d \\ &\qquad - \left(I_d \otimes \widehat{b}^{\mathrm{T}} + z_0^{-1} I_d \otimes \widetilde{b}^{\mathrm{T}} \right) \\ &\qquad \cdot \left[I_d \otimes I_s - r(z_0) \otimes \widetilde{A} \right]^{-1} \left[e \otimes r(z_0) \right] \Big] \Big\} = 0, \end{aligned} \tag{47}$$

which implies $|1-\theta-z_0^{-1}\theta-(\widehat{b}^{\mathrm{T}}+z_0^{-1}\widetilde{b}^{\mathrm{T}})[I_d \otimes I_s - r(z_0) \otimes \widetilde{A}]^{-1}[e \otimes r(z_0)]| \geq 1$.

This contradicts the assumption that ($\widetilde{b}$) for $|z_0| \geq 1$. Hence, the theorem is proved. □

4. Numerical Experiments

Example 1. Consider the following linear system:

$$\begin{aligned} &Au'(t) + Bu(t) + \sum_{q=1}^{m} C_q u'(t - \tau_q) \\ &\quad + \sum_{q=1}^{m} D_q u(t - \tau_q) \\ &\quad + \sum_{q=1}^{m} G_q \int_{t-\tau_q}^{t} u(\delta)\, d\delta = 0, \quad t \geq 0, \\ &u(t) = \varphi(t), \quad t \in [-\tau, 0), \end{aligned} \tag{48}$$

with $m = 2$, $\tau_1 = 1$, $\tau_2 = 2$, and $\varphi(t) = (\cos(t), \sin(t), \cos(t))^{\mathrm{T}}$ for $t \in [-2, 0]$, where

$$\begin{gathered} A = \begin{bmatrix} 1 & 0 & 0 \\ 0 & 0 & 0 \\ 0 & 1 & 0 \end{bmatrix}, \qquad B = \begin{bmatrix} 1.5 & 0 & 0 \\ 0 & 0 & -0.4 \\ 0 & 0.8 & 0.5 \end{bmatrix}, \\ D_1 = \begin{bmatrix} 0.2 & 0.4 & 0 \\ 0 & 0 & 0.1 \\ 0 & 0.2 & -0.2 \end{bmatrix}, \qquad D_2 = \begin{bmatrix} 0.1 & 0 & 0 \\ 0 & 0 & 0.1 \\ 0 & 0.15 & 0.8 \end{bmatrix}, \\ G_1 = \begin{bmatrix} 0.2 & 0 & 0 \\ 0 & 0 & -0.2 \\ 0 & 0.1 & 0.25 \end{bmatrix}, \qquad G_2 = \begin{bmatrix} 0.1 & 0 & 0 \\ 0 & 0 & -0.2 \\ 0 & 0.05 & 0.25 \end{bmatrix}, \end{gathered} \tag{49}$$

and $C_1 = -0.3A$ and $C_2 = -0.5A$.

Here the matrix coefficients satisfy Theorem 9. Hence, the system is asymptotically stable.

We choose the A-stable TSRK methods as follows [22]:

$$\begin{array}{c|c} C & A \\ \hline \theta & \begin{matrix} \widehat{b}^{\mathrm{T}} \\ \widetilde{b}^{\mathrm{T}} \end{matrix} \end{array} = \begin{array}{c|cc} \frac{51}{32} & \frac{5151}{9760} & \frac{2601}{2440} \\ \frac{103}{256} & -\frac{10609}{156160} & \frac{73439}{156160} \\ \hline & \frac{636886846889}{1074516737280} & \frac{61448158637}{134314592160} \\ \frac{16977449}{36697976} & & \\ & \frac{21872982199}{1074516737280} & \frac{52658918227}{134314592160} \end{array}, \tag{50}$$

where

$$c_i = \sum_{j=1}^{s} \widetilde{a}_{ij}, \qquad \sum_{j=1}^{s} \left(\widehat{b}_j + \widetilde{b}_j \right) = 1 + \theta. \tag{51}$$

It can be easily seen that the A-stable TSRK method is asymptotically stable, which illuminates the conclusion of Theorem 9.

5. Conclusions

This paper develops the asymptotic stability of the two-step Runge-Kutta methods for neutral delay integro differential-algebraic equations with many delays. It studies the asymptotic stability of the analytical solution and introduces two step Runge-Kutta methods and the stability region. It also deals with the asymptotic stability of two-step Runge-Kutta method for neutral delay integro differential-algebraic equations with many delays and proves that the A-stable two-step Runge-Kutta methods are asymptotically stable for neutral delay integro differential-algebraic equations with many delays.

Conflict of Interests

The authors declare that there is no conflict of interests regarding the publication of this paper.

Acknowledgment

This work was supported by the Doctor Foundation of Heilongjiang Institute of Technology (2012BJ27).

References

[1] K. E. Brenan, S. L. Campbell, and L. R. Petzold, *Numerical Solution of Initial-Value Problem in Differential-Algebraic Equations*, SIAM, Philadephia, Pa, USA, 2nd edition, 1995.

[2] E. Hairer, S. P. Norsett, and G. Wanner, *Solving Ordinary Differential-Algebraic Equations q Stiff and Differential-Algebraic Problems*, Springer, New York, NY, USA, 1992.

[3] L. R. Petzold, *Numerical Solutions of Differential-Algebraic Equations*, Clarendon Press, Oxford, UK, 1995.

[4] U. M. Ascher and L. R. Petzold, "The numerical solution of delay-differential-algebraic equations of retarded and neutral type," *SIAM Journal on Numerical Analysis*, vol. 32, no. 5, pp. 1635–1657, 1995.

[5] S. L. Campbell, "Singular linear systems of differential equations with delays," *Applicable Analysis*, vol. 11, no. 2, pp. 129–136, 1980.

[6] R. K. Brayton and R. A. Willoughby, "On the numerical integration of a symmetric system of difference-differential equations of neutral type," *Journal of Mathematical Analysis and Applications*, vol. 18, pp. 182–189, 1967.

[7] W. Zhu and L. R. Petzold, "Asymptotic stability of linear delay differential-algebraic equations and numerical methods," *Applied Numerical Mathematics*, vol. 24, no. 2-3, pp. 247–264, 1997.

[8] J. J. Zhao, Y. Xu, S. Y. Dong, and M. Z. Liu, "Stability of the Rosenbrock methods for the neutral delay differential-algebraic equations," *Applied Mathematics and Computation*, vol. 168, no. 2, pp. 1128–1144, 2005.

[9] Q. H. Yu, L. P. Sun, and Y. Li, "Asymptotic stability of linear multistep methods for generalized neutral delay differential-algebraic equations," *Journal of System Simulation*, vol. 21, no. 20, pp. 6432–6435, 2009.

[10] C. T. H. Baker and N. J. Ford, "Stability properties of a scheme for the approximate solution of a delay-integro-differential equation," *Applied Numerical Mathematics*, vol. 9, no. 3–5, pp. 357–370, 1992.

[11] T. Koto, "Stability of Runge-Kutta methods for delay integro-differential equations," *Journal of Computational and Applied Mathematics*, vol. 145, no. 2, pp. 483–492, 2002.

[12] C. Huang and S. Vandewalle, "An analysis of delay-dependent stability for ordinary and partial differential equations with fixed and distributed delays," *SIAM Journal on Scientific Computing*, vol. 25, no. 5, pp. 1608–1632, 2004.

[13] T. Luzyanina, K. Engelborghs, and D. Roose, "Computing stability of differential equations with bounded distributed delays," *Numerical Algorithms*, vol. 34, no. 1, pp. 41–66, 2003.

[14] C. J. Zhang and S. F. Vandewalle, "Stability criteria for exact and discrete solutions of neutral multidelay-integro-differential equations," *Advances in Computational Mathematics*, vol. 28, no. 4, pp. 383–399, 2008.

[15] J. C. Butcher, *The Numerical Analysis of Ordinary Differential Equations*, John Wiley & Sons, Chichester, UK, 1987.

[16] I. Lie and S. P. Nørsett, "Superconvergence for multistep collocation," *Mathematics of Computation*, vol. 52, no. 185, pp. 65–79, 1989.

[17] I. Lie, "Local error estimation for multistep collocation methods," *Numerical Mathematics*, vol. 30, no. 1, pp. 126–144, 1990.

[18] G. D. Byrne and R. J. Lambert, "Pseudo-Runge-Kutta methods involving two points," *Journal of the Association for Computing Machinery*, vol. 13, pp. 114–123, 1966.

[19] Z. Jackiewicz and S. Tracogna, "Variable stepsize continuous two-step Runge-Kutta methods for ordinary differential equations," *Numerical Algorithms*, vol. 12, no. 3-4, pp. 347–368, 1996.

[20] Q. Wang, Y. H. Cong, and J. J. Li, "Stability of two-step Runge-Kutta methods for neutral delay-integro-differential-algebraic equations," *Journal of Shanghai Normal University: Natural Sciences*, vol. 39, no. 6, pp. 551–557, 2010.

[21] P. Hu and C. Huang, "Analytical and numerical stability of nonlinear neutral delay integro-differential equations," *Journal of the Franklin Institute: Engineering and Applied Mathematics*, vol. 348, no. 6, pp. 1082–1100, 2011.

[22] Z. Jackiewicz, R. Renaut, and A. Feldstein, "Two-step Runge-Kutta methods," *SIAM Journal on Numerical Analysis*, vol. 28, no. 4, pp. 1165–1182, 1991.

Hindawi Publishing Corporation
Mathematical Problems in Engineering
Volume 2014, Article ID 575872, 8 pages
http://dx.doi.org/10.1155/2014/575872

Research Article

Analysis of Forest Fires by means of Pseudo Phase Plane and Multidimensional Scaling Methods

J. A. Tenreiro Machado[1] and António M. Lopes[2]

[1] *Institute of Engineering, Polytechnic of Porto, Rua Dr. António Bernardino de Almeida 431, 4200-072 Porto, Portugal*
[2] *Institute of Mechanical Engineering, Faculty of Engineering, University of Porto, Rua Dr. Roberto Frias, 4200-465 Porto, Portugal*

Correspondence should be addressed to J. A. Tenreiro Machado; jtenreiromachado@gmail.com

Received 2 February 2014; Accepted 20 May 2014; Published 5 June 2014

Academic Editor: Riccardo Caponetto

Forest fires dynamics is often characterized by the absence of a characteristic length-scale, long range correlations in space and time, and long memory, which are features also associated with fractional order systems. In this paper a public domain forest fires catalogue, containing information of events for Portugal, covering the period from 1980 up to 2012, is tackled. The events are modelled as time series of Dirac impulses with amplitude proportional to the burnt area. The time series are viewed as the system output and are interpreted as a manifestation of the system dynamics. In the first phase we use the pseudo phase plane (PPP) technique to describe forest fires dynamics. In the second phase we use multidimensional scaling (MDS) visualization tools. The PPP allows the representation of forest fires dynamics in two-dimensional space, by taking time series representative of the phenomena. The MDS approach generates maps where objects that are perceived to be similar to each other are placed on the map forming clusters. The results are analysed in order to extract relationships among the data and to better understand forest fires behaviour.

1. Introduction

Forest fires, being caused by natural factors, human negligence, or human intent, consume every year vast areas of vegetation. Fire compromises ecosystems, has direct impact upon economy due to the destruction of property and infrastructures, raises the carbon dioxide emissions to the atmosphere, affects the water cycle, contributes to soil erosion, and has long-term economic implications associated with the climate change. In many regions and countries, like the United States, Australia, Russia, Brazil, China, and the Mediterranean Basin, fire is a major concern nowadays, demanding efficient policies for fire prevention and suppression and recovery of the affected areas.

Climate conditions, terrain orography, and type of vegetation are important factors that condition fire propagation and the total burnt area. The efficacy of detection and suppression strategies is fundamental in order to mitigate fire impact. However, fires caused by incendiaries contribute to increasing the complexity of the phenomena. Understanding forest fires behaviour and the underlying patterns in terms of fire size and spatiotemporal distributions may help the decision makers to take preventive measures beforehand, identifying possible hazards and deciding strategies for fire prevention, detection, and suppression.

Classical statistical tools have been used to investigate forest fires. However, those methods do not capture neither all characteristics underneath forest fires dynamics nor the fire dynamics along the years [1]. Forest fires are complex phenomena that exhibit intricate correlations in terms of fire size, location, and time. Forest fires dynamics unveil long range memory, self-similarity, and absence of a characteristic length-scale [2–10], which are features also found in fractional order systems [11–18].

In this paper we look at forest fires from the perspective of dynamical systems. A public domain forest fires catalogue containing data of events that occurred in Portugal, in the period from 1980 up to 2012, is tackled. The data is analysed in an annual basis, modelling the occurrences as sequences of Dirac impulses with amplitude proportional to

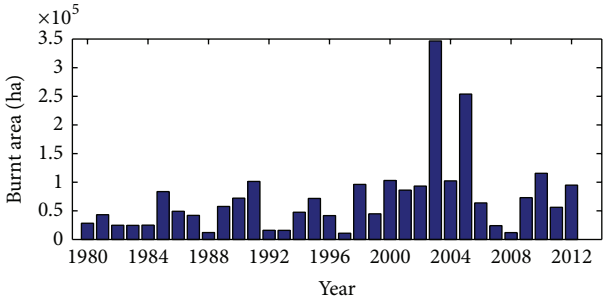

Figure 1: Yearly evolution of the burnt area, corresponding to forest fires registered in Portugal in the time period 1980–2012 (they are considered events with burnt area equal to or greater than 10 ha).

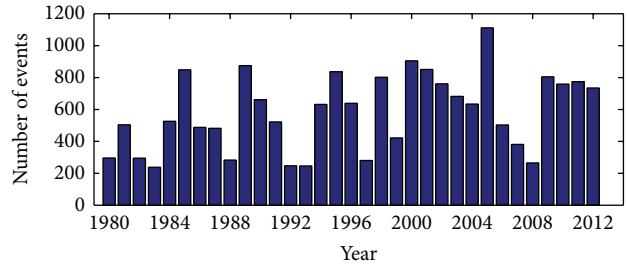

Figure 2: Yearly evolution of the number of forest fires, registered in Portugal in the time period 1980–2012 (they are considered events with burnt area equal to or greater than 10 ha).

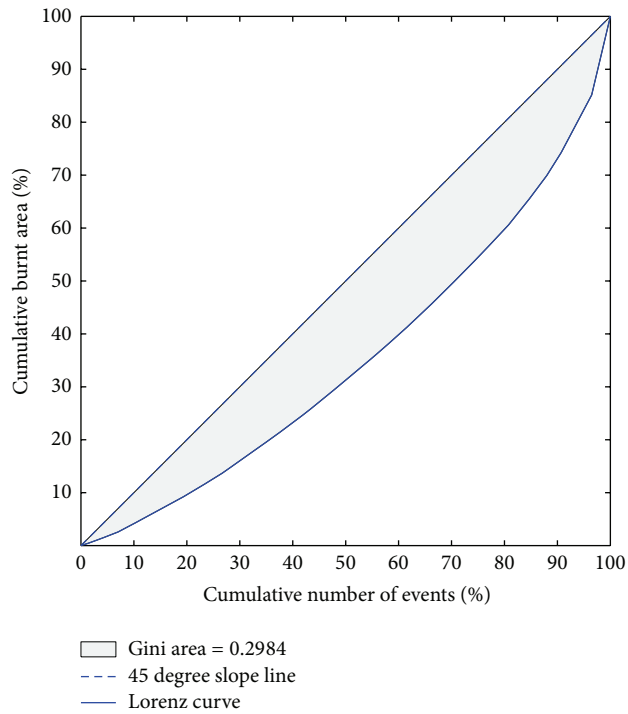

Figure 3: Lorenz curve corresponding to forest fires registered in Portugal in the time period 1980–2012 (they are considered events with burnt area equal to or greater than 10 ha).

the events. Therefore, we are not modelling the dynamics of each particular forest fire. Otherwise, we are describing the global fire dynamics along several decades. The time series are viewed as the output of a dynamical system and are interpreted as a manifestation of the system dynamics. In the first phase, we use the pseudo phase plane (PPP) technique. The optimal time delay for the PPP is determined by means of the autocorrelation function. The PPP portraits are compared using an appropriate metric and the results are visualized through phylogenetic trees, generated by hierarchical clustering algorithms. In the second phase, the multidimensional scaling (MDS) tools are adopted to compare and extract relationships among the data.

Having these ideas in mind, the paper is organized as follows. In Section 2 we briefly describe the forest fire catalogue used in this work. In Section 3 we address the problem by means of the PPP and visualization of trees generated by hierarchical clustering algorithms. In Section 4 we use the MDS method. The approach is applied to the data and the main results are interpreted and analysed. Finally, in Section 5, we outline the main conclusions.

2. Forest Fires Dataset

Data of forest fires collected at the Portuguese Institute of Nature and Forest Conservation (INCF), available online at http://www.icnf.pt/portal/florestas/dfci/inc/estatisticas, is used [19]. The INCF dataset contains events since 1980 and up to 2012. Ignitions might have different sources, as natural causes, human negligence, or human intentionality, among others. The data was retrieved in December, 2013. Each data record contains information about the events date, time (with one minute resolution), geographic location, and size (in terms of burnt area). We discard small size events, as those are prone to measurement errors. Moreover, some small events may be missing because probably they were not reported. For that purpose we adopt a cutoff threshold value of 10 hectares for the burnt area. Experiments showed this value as a good trade-off between catalogue completeness and results accuracy.

The evolution of the burnt area and the number of occurrences are depicted in Figures 1 and 2, respectively. In Figure 3 we depict the Lorenz curve relating to the cumulative burnt area and the cumulative number of events. The Gini coefficient, given by the double of the Gini area, measures the inequality among values of burnt area, being equal to 0.5968.

The time series representative of the occurrences is shown in Figure 4, where we can note the yearly periodicity of the events, with the peaks of burnt area occurring in summer. During the period covered by the catalogue, stronger fire activity has been verified around the middle of the decade 2000–2009.

Using the Fourier transform (FT), the forest fires data is analyzed in the frequency-domain. For each annual time series (33 in total) the amplitude spectra are computed and approximated by a power law (PL) function. The PL parameters are interpreted as the signature of the system dynamics. For example, Figure 5 depicts the amplitude spectra for year

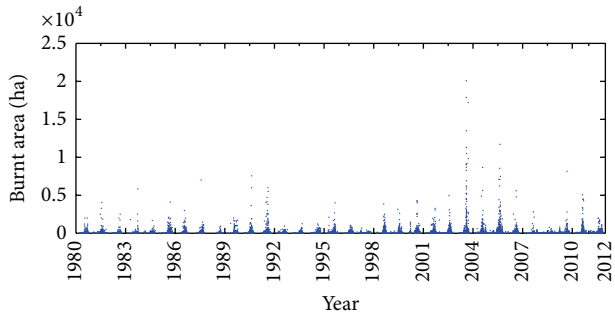

Figure 4: Burnt area versus time of the occurrences registered in Portugal in the time period 1980–2012, with burnt area equal to or greater than 10 ha.

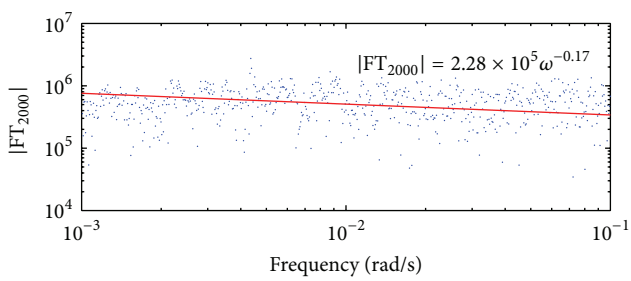

Figure 5: Amplitude spectra, $|\mathrm{FT}_{2000}|$, of the time series corresponding to year 2000 and PL approximation.

2000, $|\mathrm{FT}_{2000}|$. In this case, the PL approximation is $|\mathrm{FT}_{2000}| = 2.28 \times 10^5 \omega^{-0.17}$, unveiling fractional order characteristics. However, the FT characterizes the global dynamics and may not constitute the best tool to depict the time-varying artifacts present in response of complex system. This means that different approaches are needed to better understand forest fires.

3. Analysis of Forest Fires by means of PPP

The PPP is a particular case of the pseudo phase space (PPS), which is justified by Takens' embedding theorem [20]. The PPS allows the representation of system dynamics in a higher dimensional space, by taking a smaller sample of signals representing measurements of the system time history [21–23]. The PPS is useful in analysing signals with nonlinear behaviour and systems where complete information about all system states is unavailable. When compared to the classical phase space technique, the PPS reconstruction has the advantage of being more robust to signal noise.

In practical terms, we construct a n-dimensional phase space, $U(t)$:

$$U(t) = [s(t), s(t+\tau), s(t+2\tau), \ldots, s(t+(n-1)\tau)], \tag{1}$$

where $n \in \mathbf{N}$ and $\tau \in \mathbf{R}^+$ represent the time delay and embedding dimension, respectively. The matrix $U(t)$ is usually plotted in a n-dimensional diagram. For $n = 2$ a two-dimensional time delay space is obtained and the PPS reduces to the PPP. In this case we have $U(t) = [s(t), s(t+\tau)]$ related to the model given by the state vectors $[s(t), \dot{s}(t)]$. The choice of the time delay τ is critical and must be accomplished adopting some criterion.

In this section we analyse forest fires in an annual basis, representing the events of the ith year ($i = 1980, \ldots, 2012$) by

$$x_i(t) = \sum_{k=1}^{T} S_k \delta(t - t_k) \tag{2}$$

leading to 33 one-year length time series.

This means that the events are modelled as Dirac impulses, where S_k represents fire size, t_k is the instant of occurrence, parameter t represents time, and T is the total time length, in minutes, corresponding to year i.

The signals $x_i(t)$ are then normalized according to the following equation:

$$\tilde{x}_i(t) = \frac{x_i(t) - \mu}{\sigma}, \tag{3}$$

where μ and σ represent the global mean and standard deviation values, that is, the values calculated for the whole set of events registered during the time period 1980–2012, with minimum magnitude equal to 10 ha.

To implement the PPP, we firstly integrate the signals $\tilde{x}_i(t)$, (to be denoted $\widetilde{X}_i(t) = \int_0^t \tilde{x}_i(u)du$, $0 \le t \le T$, where $t = 0$ corresponds to the first minute of each year, i) that represent the normalized time series of the occurrences in every year ($i = 1980, \ldots, 2012$). The correlation function, $r_{ii}[\widetilde{X}_i(t), \widetilde{X}_i(t-\tau)]$, is then used to correlate $\widetilde{X}_i(t)$ with its time delayed version $\widetilde{X}_i(t-\tau)$:

$$r_{ii}(\tau) = \frac{\sum_{t=1}^{T} \widetilde{X}_i(t) \cdot \widetilde{X}_i(t-\tau)}{\sqrt{\sum_{t=1}^{T} \widetilde{X}_i(t)^2 \cdot \sum_{t=1}^{T} \widetilde{X}_i(t-\tau)^2}}, \quad i = 1980, \ldots, 2012. \tag{4}$$

For each case, values within the interval $\tau \in [1440, 288000]$ minute (i.e., $\tau \in [1, 200]$ days) are tested and the optimal time delay, τ_{m_i}, is computed, corresponding to the time at which the correlation function has its first point of inflection.

Figure 6 depicts, for example, the signals $\tilde{x}_{2000}(t)$ and $\widetilde{X}_{2000}(t)$, representative of the events that occurred in year 2000. The normalized time series, $\tilde{x}_{2000}(t)$, reveals a "noisy" nature, while the corresponding integral, $\widetilde{X}_{2000}(t)$, is much smoother, showing more clearly possible correlations between multiple points. The larger discontinuities observed in the amplitude correspond to instants of sudden increase in fire activity.

In Figure 7, the correlation function for year $i = 2000$, $r_{ii}[\widetilde{X}_{2000}(t), \widetilde{X}_{2000}(t-\tau)]$ versus the time delay, τ is presented. In this case, the optimal time delay yields $\tau_{m_{2000}} = 106$ days. The optimal time delays calculated for the 33 one-year length time series are summarized in Table 1.

Figure 8 gives a global perspective of the PPP portraits, $\widetilde{X}_i(t-\tau_{m_i})$ versus $\widetilde{X}_i(t)$, for the 33 time series. Figure 9, serving

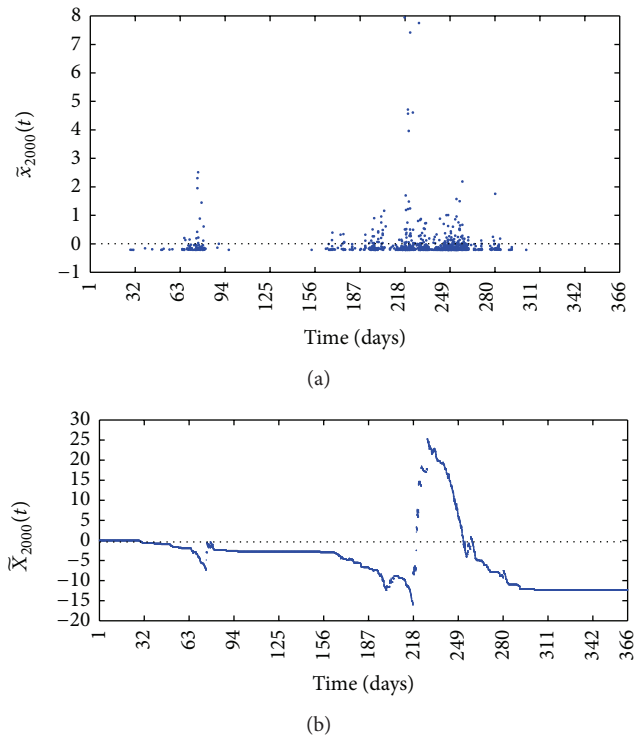

Figure 6: Graphical representation of the events that occurred in year 2000: (a) normalized time series, $\tilde{x}_{2000}(t)$, and (b) normalized time series integral, $\widetilde{X}_{2000}(t)$. The cutoff threshold value $S_k = 10$ ha was adopted.

as an example, details the results obtained for the initial and final time series, that is, years 1980 and 2012, respectively. Both figures reveal complex patterns that resemble those found in chaotic systems, demonstrating the rich dynamics of forest fires.

To compare the 33 PPP patterns we calculate a 33×33 similarity matrix $\mathbf{E} = [e_{ij}]$, based on the 2-dimensional correlation, d_{ij} $(i, j = 1980, \ldots, 2012)$, between the PPP curves, defined by

$$d_{ij} = \left| \left(\sum_{t=1}^{T} \left[\widetilde{X}_i(t) \cdot \widetilde{X}_j(t) + \widetilde{X}_i\left(t - \tau_{m_i}\right) \cdot \widetilde{X}_j\left(t - \tau_{m_j}\right) \right] \right) \times \left(\sum_{t=1}^{T} \left[\widetilde{X}_i^2(t) + \widetilde{X}_i^2\left(t - \tau_{m_i}\right) \right]^2 \cdot \sum_{t=1}^{T} \left[\widetilde{X}_j^2(t) + \widetilde{X}_j^2\left(t - \tau_{m_j}\right) \right]^2 \right)^{-1/2} \right|, \quad (5)$$

$$e_{ij} = \frac{d_{ij}}{\max\left\{d_{ij}\right\}}.$$

Table 1: Optimal time delays for the 33 time series during the period 1980–2012.

Year	τ_{m_i} (days)	r_{ii} (τ_{m_i})
1980	99	0.7926
1981	99	0.8577
1982	97	0.8503
1983	146	−0.1871
1984	129	0.6520
1985	112	0.7487
1986	48	0.8941
1987	155	0.5918
1988	106	0.5567
1989	163	0.3985
1990	34	0.6606
1991	163	0.3458
1992	122	0.7998
1993	114	0.7617
1994	101	0.7726
1995	116	0.9506
1996	117	0.7622
1997	98	0.9423
1998	172	0.0907
1999	100	0.6130
2000	106	−0.0433
2001	173	0.7722
2002	158	−0.2180
2003	165	−0.8656
2004	168	−0.7299
2005	165	−0.9852
2006	62	0.1518
2007	40	0.9445
2008	111	0.9682
2009	111	0.8566
2010	144	−0.8174
2011	55	0.9683
2012	200	−0.8595

Figure 10 depicts $\mathbf{E}$ as a contour map. To facilitate the comparison, the cases $i = j$ (i.e., those with maximum correlation value) are removed from the graph, due to their higher values.

The map reveals strong correlations between certain years, corresponding to extreme values of e_{ij}. This is well noted, for example, for the groups of years {1998, 1999}, {1998, 2000}, {1998, 2001}, {1999, 2001}, {1999, 2006}, {1999, 2007}, {1999, 2012}, {2001, 2008}, {2002, 2006}, {1993, 2008}, {2002, 2012}, and {2006, 2012}. Nevertheless, the comparison requires a considerable amount of work and is based on pairwise comparisons.

As an alternative method to visualize and to compare results, a hierarchical clustering algorithm is adopted [24–26]. A phylogenetic tree and circular phylogram are generated, using the successive (agglomerative) clustering and

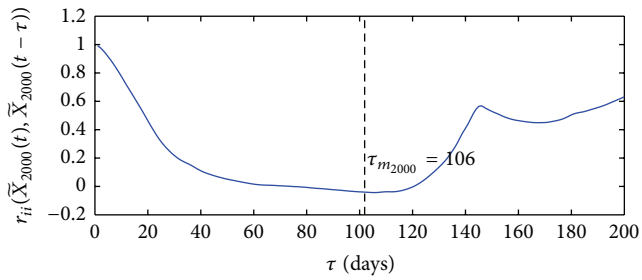

FIGURE 7: Correlation, r_{ii}, as a function of the time delay, τ, corresponding to year 2000.

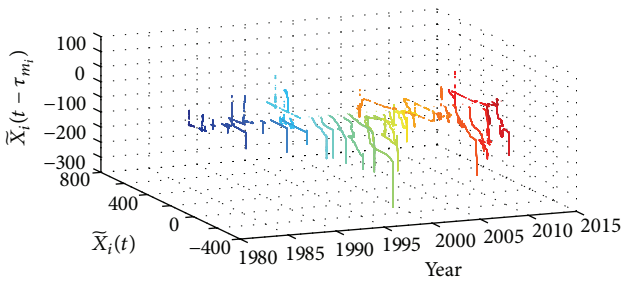

FIGURE 8: The PPP portraits for the 33 time series.

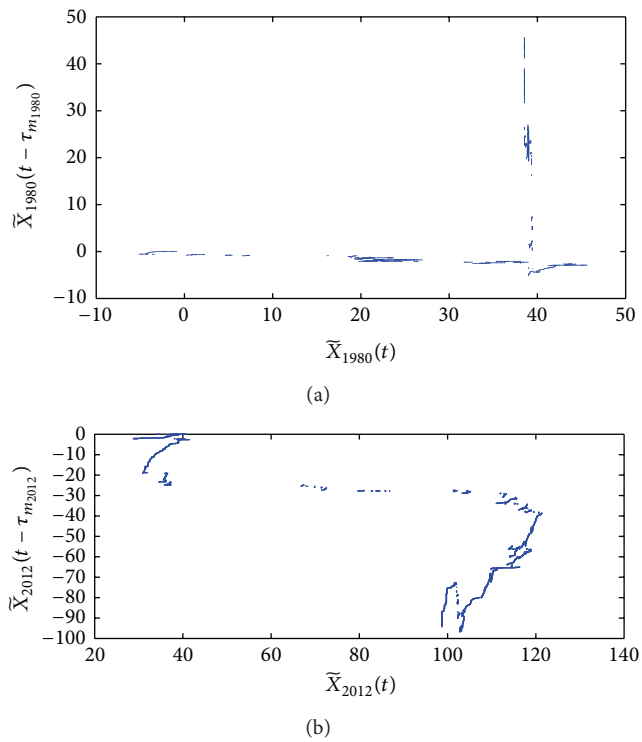

FIGURE 9: The PPP portraits for the initial and final time series, years (a) 1980 and (b) 2012.

average-linkage method (Figure 11). The software PHYLIP was used for generating both graphs (http://evolution.genetics.washington.edu/phylip.html).

Figure 11 unveils groups of objects (years) in such a way that objects in the same group (cluster) are more similar to each other than to those in other groups. For example, we can easily identify clusters composed by years $\mathscr{A} = \{1998, 2002, 2006, 2012\}$, $\mathscr{B} = \{1999, 2000, 2007\}$, $\mathscr{C} = \{2004, 2010\}$, and $\mathscr{D} = \{1991, 2003, 2005\}$. Years in the same cluster have identical time-amplitude fire pattern. Both representations of Figures 10 and 11 can be used to visualise the clusters of forest fires, on an annual basis. Figure 11 leads to a result that is easier to interpret, as it identifies groups of objects that are similar, while Figure 10 just maps similarities between pairs of objects.

4. MDS Analysis and Visualization

In this section we adopt the MDS tool to visualize the relationships between forest fires events. An appropriate metric is proposed and the generated MDS graphs are analysed.

The MDS is a statistical technique for visualizing data. The MDS approach generates maps where objects that are perceived to be similar to each other are placed on the map forming clusters. The maps are indeterminate with respect to translation, rotation, and reflection and the axes have no special meaning. The algorithm requires the definition of a similarity measure (or, inversely, of a distance) and the construction of a $s \times s$ symmetric matrix of similarities (or distances) between each pair of s objects. MDS reproduces the observed similarities by assigning a point to each object

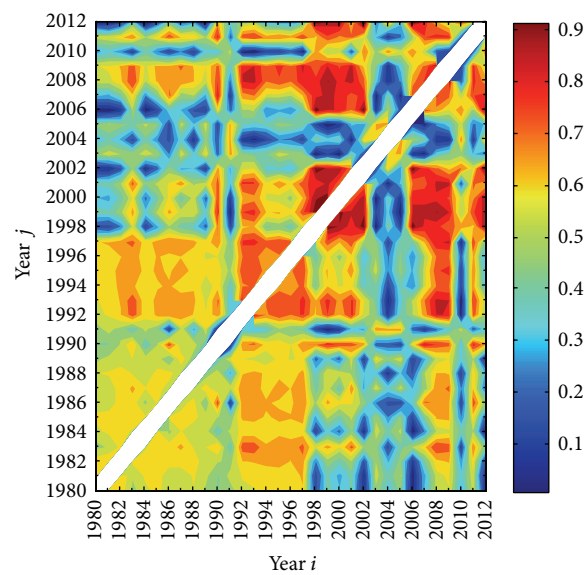

FIGURE 10: Similarity matrix, $\mathbf{E}$, between yearly time series in the period 1980–2012. The cutoff threshold value $S_k = 10$ ha was adopted.

in a m-dimensional space. For $m = 2$ or $m = 3$ dimensions the points may be displayed on a "map" [27–33].

We adopt the 33×33 similarity matrix $\mathbf{E} = [e_{ij}]$, defined by (5). The MDS map for $m = 3$ is depicted in Figure 12. A shorter (larger) distance between two points on the map means that the corresponding objects are more

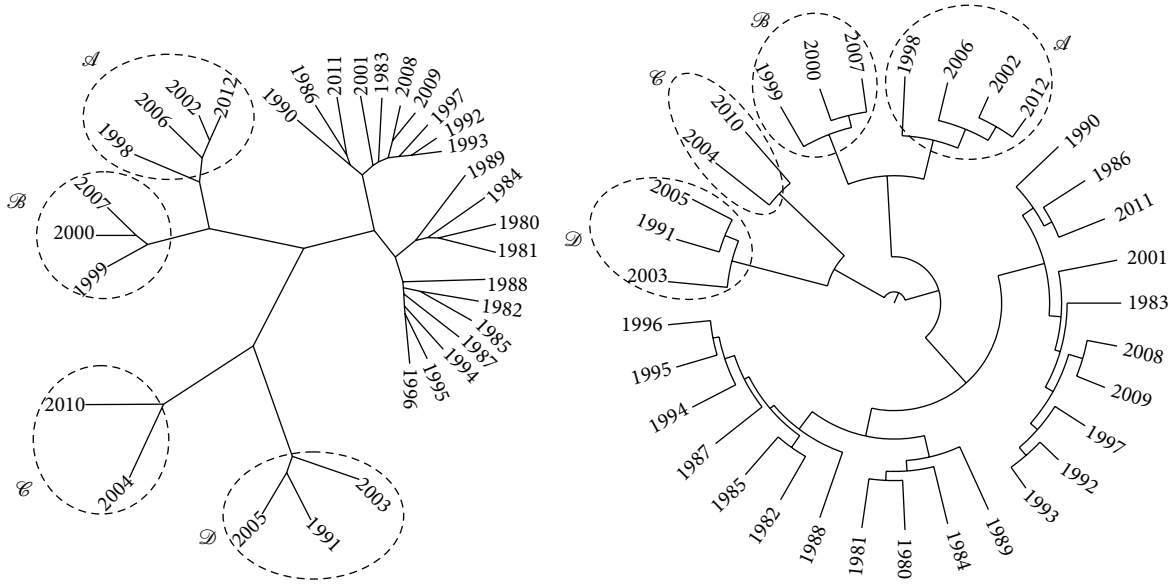

Figure 11: Similarity matrix, **E**, between yearly time series in the period 1980–2012. The cutoff threshold value $S_k = 10$ ha was adopted: (a) phylogenetic tree and (b) circular phylogram.

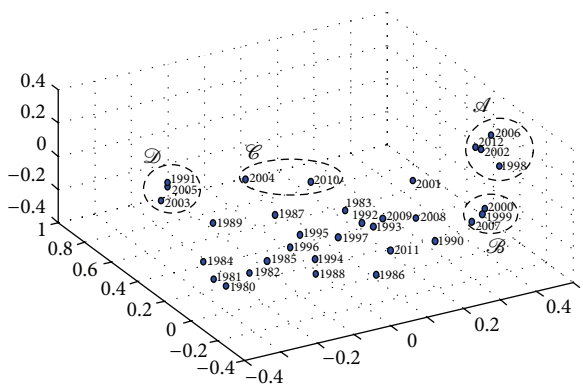

Figure 12: MDS map for the 33 time series, similarity index e_{ij} and $m = 3$.

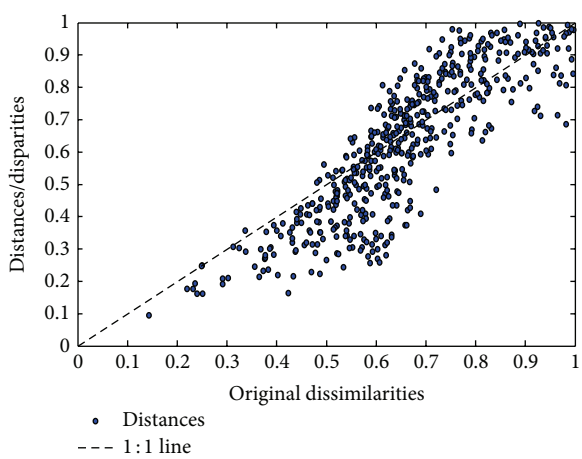

Figure 13: Shepard plot for the 33 time series, similarity index e_{ij} and $m = 3$.

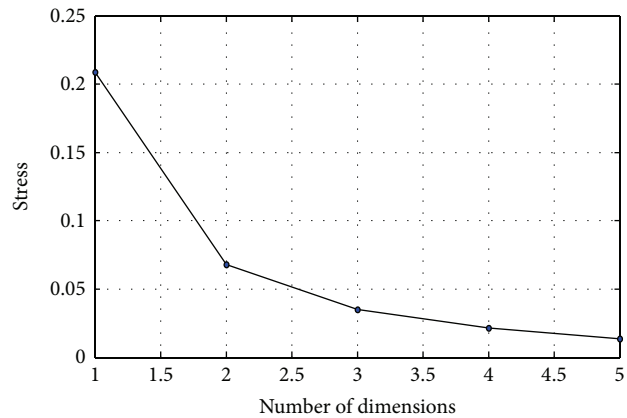

Figure 14: Stress plot for the 33 time series and similarity index e_{ij}.

similar (distinct). Figures 13 and 14 depict the Shepard and stress plots, respectively, that assess the quality of the MDS maps. The Shepard diagram shows an acceptable distribution of points around the 45 degree line, which means a good fit of the distances to the dissimilarities. On the other hand, the stress plot reveals that a three dimensional space well describes the locus of the points. Often, the maximum curvature point of the stress line is adopted as the criterion for deciding the dimensionality of the MDS map.

The MDS map of Figure 12 exposes the clusters that were previously identified by the hierarchical clustering (Figure 11). Comparing the MDS maps and the visualization trees, we conclude that both allow easy interpretation of the results and that there is no multiannual pattern. The MDS maps have the advantage of being more intuitive, mainly when dealing with a large number of objects.

5. Conclusion

This paper analysed forest fires data, adopting tools normally used in dynamical systems analysis. The data consisted in a public domain forest fires catalogue, containing information for Portugal and covering 33 years during the period 1980–2012. The events were modelled as time series of Dirac impulses with amplitude proportional to the burnt area. The data was analysed in an annual basis using the PPP and MDS tools. The PPP was used to model forest fires dynamics. Based on an appropriate correlation index, the MDS was adopted to compare annual patterns. Those tools allow different perspectives over forest fires that may be used to better understand such a complexity phenomenon.

Conflict of Interests

The authors declare that there is no conflict of interests regarding the publication of this paper.

References

[1] E. Alvarado, D. V. Sandberg, and S. G. Pickford, "Modeling large forest fires as extreme events," *Northwest Science*, vol. 72, pp. 66–75, 1998.

[2] C. M. A. Pinto, A. M. Lopes, and J. A. Tenreiro Machado, "A review of power laws in real life phenomena," *Communications in Nonlinear Science and Numerical Simulation*, vol. 17, no. 9, pp. 3558–3578, 2012.

[3] P. Bak, K. Chen, and C. Tang, "A forest-fire model and some thoughts on turbulence," *Physics Letters A*, vol. 147, no. 5-6, pp. 297–300, 1990.

[4] I. C. Prentice, D. I. Kelley, P. N. Foster, P. Friedlingstein, S. P. Harrison, and P. J. Bartlein, "Modeling fire and the terrestrial carbon balance," *Global Biogeochemical Cycles*, vol. 25, no. 3, 2011.

[5] W. J. Reed and K. S. McKelvey, "Power-law behaviour and parametric models for the size-distribution of forest fires," *Ecological Modelling*, vol. 150, no. 3, pp. 239–254, 2002.

[6] I. N. Fletcher, L. E. O. C. Arago, A. Lima, Y. Shimabukuro, and P. Friedlingstein, "Fractal properties of forest fires in Amazonia as a basis for modelling pan-tropical burned area," *Biogeosciences Discussions*, vol. 10, pp. 14141–14167, 2013.

[7] B. D. Malamud, G. Morein, and D. L. Turcotte, "Forest fires: an example of self-organized critical behavior," *Science*, vol. 281, no. 5384, pp. 1840–1842, 1998.

[8] W. J. Reed and B. D. Hughes, "From gene families and genera to incomes and internet file sizes: why power-laws are so common in nature," *Physical Review E*, vol. 66, no. 6, Article ID 067103, 2002.

[9] L. Telesca, G. Amatulli, R. Lasaponara, M. Lovallo, and A. Santulli, "Time-scaling properties in forest-fire sequences observed in Gargano area (southern Italy)," *Ecological Modelling*, vol. 185, no. 2-4, pp. 531–544, 2005.

[10] L. Telesca, G. Amatucci, R. Lasaponara, M. Lovallo, and M. J. Rodrigues, "Space-time fractal properties of the forest-fire series in central Italy," *Communications in Nonlinear Science and Numerical Simulation*, vol. 12, no. 7, pp. 1326–1333, 2007.

[11] F. Mainardi, *Fractional Calculus and Waves in Linear Viscoelasticity*, Imperial College Press, London, UK, 2010.

[12] S. G. Samko, A. A. Kilbas, and O. I. Marichev, *Fractional Integrals and Derivatives: Theory and Applications*, Gordon and Breach Science Publishers, London, UK, 1993.

[13] K. S. Miller and B. Ross, *An Introduction to the Fractional Calculus and Fractional Differential Equations*, A Wiley-Interscience Publication, John Wiley & Sons, New York, NY, USA, 1993.

[14] I. Podlubny, *Fractional Differential Equations*, vol. 198 of *Mathematics in Science and Engineering*, Academic Press, San Diego, Calif, USA, 1999.

[15] A. A. Kilbas, H. M. Srivastava, and J. J. Trujillo, *Theory and Applications of Fractional Differential Equations*, vol. 204 of *North-Holland Mathematics Studies*, Elsevier, Amsterdam, The Netherlands, 2006.

[16] D. Baleanu, K. Diethelm, E. Scalas, and J. J. Trujillo, *Fractional Calculus: Models and Numerical Methods*, vol. 3 of *Series on Complexity, Nonlinearity and Chaos*, World Scientific, Singapore, 2012.

[17] M. D. Ortigueira, *Fractional Calculus for Scientists and Engineers*, vol. 84 of *Lecture Notes in Electrical Engineering*, Springer, Dordrecht, The Netherlands, 2011.

[18] D. Baleanu, A. K. Golmankhaneh, A. K. Golmankhaneh, and R. R. Nigmatullin, "Newtonian law with memory," *Nonlinear Dynamics*, vol. 60, no. 1-2, pp. 81–86, 2010.

[19] Portuguese Institute of Nature and Forest Conservation (INCF), http://www.icnf.pt/portal/florestas/dfci/inc/estatisticas .

[20] F. Takens, "Detecting strange attractors in turbulence," in *Dynamical Systems and Turbulence, Warwick 1980*, vol. 898 of *Lecture Notes in Mathematics*, pp. 366–381, Springer, Berlin, Germany, 1981.

[21] M. F. M. Lima and J. A. Tenreiro Machado, "Representation of robotic fractional dynamics in the pseudo phase plane," *Acta Mechanica Sinica*, vol. 27, no. 1, pp. 28–35, 2011.

[22] J. Gao, J. Hu, and W.-W. Tung, "Entropy measures for biological signal analyses," *Nonlinear Dynamics*, vol. 68, no. 3, pp. 431–444, 2012.

[23] A. M. Lopes and J. A. Tenreiro Machado, "Dynamic analysis of earthquake phenomena by means of pseudo phase plane," *Nonlinear Dynamics*, vol. 74, no. 4, pp. 1191–1202, 2013.

[24] A. K. Jain and R. C. Dubes, *Algorithms for Clustering Data*, Prentice Hall Advanced Reference Series, Prentice Hall, Englewood Cliffs, NJ, USA, 1988.

[25] S. C. Johnson, "Hierarchical clustering schemes," *Psychometrika*, vol. 32, no. 3, pp. 241–254, 1967.

[26] J. A. Tenreiro Machado and A. M. Lopes, "Analysis and visualization of seismic data using mutual information," *Entropy*, vol. 15, no. 9, pp. 3892–3909, 2013.

[27] A. M. Costa, J. T. Machado, and M. D. Quelhas, "Histogram-based DNA analysis for the visualization of chromosome, genome and species information," *Bioinformatics*, vol. 27, no. 9, pp. 1207–1214, 2011.

[28] T. Cox and M. Cox, *Multidimensional Scaling*, Chapman & Hall/CRC, New York, NY, USA, 2001.

[29] R. N. Shepard, "The analysis of proximities: multidimensional scaling with an unknown distance function. II," *Psychometrika*, vol. 27, pp. 219–246, 1962.

[30] J. Kruskal and M. Wish, *Multidimensional Scaling*, Sage, Newbury Park, Calif, USA, 1978.

[31] W. L. Martinez and A. R. Martinez, *Exploratory Data Analysis with MATLAB*, Chapman & Hall/CRC, London, UK, 2005.

[32] I. Borg and P. J. F. Groenen, *Modern Multidimensional Scaling—Theory and Applications*, Springer Series in Statistics, Springer, New York, NY, USA, 2005.

[33] C. Tzagarakis, T. A. Jerde, S. M. Lewis, K. Uğurbil, and A. P. Georgopoulos, "Cerebral cortical mechanisms of copying geometrical shapes: a multidimensional scaling analysis of fMRI patterns of activation," *Experimental Brain Research*, vol. 194, no. 3, pp. 369–380, 2009.

Hindawi Publishing Corporation
Mathematical Problems in Engineering
Volume 2014, Article ID 356906, 10 pages
http://dx.doi.org/10.1155/2014/356906

Research Article

The Restoration of Textured Images Using Fractional-Order Regularization

Ying Fu,[1] Xiaohua Li,[1] Lei Liang,[2] Yi Zhang,[1] and Jiliu Zhou[3]

[1] *College of Computer Science, Sichuan University, Chengdu 610064, China*
[2] *Autonavi Company, Beijing 100102, China*
[3] *Chengdu University, Chengdu 610106, China*

Correspondence should be addressed to Ying Fu; fuying0719@gmail.com

Received 9 December 2013; Revised 26 February 2014; Accepted 27 February 2014; Published 14 April 2014

Academic Editor: Juan J. Trujillo

Image restoration problem is ill-posed, so most image restoration algorithms exploit sparse prior in gradient domain to regularize it to yield high-quality results, reconstructing an image with piecewise smooth characteristics. While sparse gradient prior has good performance in noise removal and edge preservation, it also tends to remove midfrequency component such as texture. In this paper, we introduce the sparse prior in fractional-order gradient domain as texture-preserving strategy to restore textured images degraded by blur and/or noise. And we solve the unknown variables in the proposed model using method based on half-quadratic splitting by minimizing the nonconvex energy functional. Numerical experiments show our algorithm's robust outperformance.

1. Introduction

Mathematically, the image degradation is modeled as

$$\mathbf{y} = \mathbf{x} \otimes \mathbf{h} + \mathbf{n}, \tag{1}$$

where $\mathbf{x}$ is the original latent image and $\mathbf{y}$ is an observed image degraded by blur and/or noise, which is produced by convolving $\mathbf{x}$ with a blur point-spread-function (a.k.a. kernel) $\mathbf{h}$ and adding zero mean Gaussian noise $\mathbf{n}$. Image restoration is recovering latent image from observed image.

Image restoration is ill-posed problem, so many methods introducing priors based on natural image statistics can regularize it. Total variation regularization is originally used for noise reduction [1, 2] and has also been used for image deblurring [3]. Chan and Wong [4] introduced total variational blind deconvolution method for motion blur kernel and out-of-focus kernel. Heavy-tailed natural image priors [5, 6] and hyper-Laplacian priors [7–10] were also extensively introduced. Numerous regularization approaches have been proposed too. Wang et al. [7] presented a fast total variation deconvolution algorithm to compute TV image deconvolution. Krishnan and Fergus [8] take a novel approach to the image restoration problem arising from the use of a hyper-Laplacian prior. Xu and Jia [11] developed a fast TV-l_1 deconvolution method based on half-quadratic splitting.

While image reconstructed by algorithms above suppresses noise and preserve edges, it has piecewise smooth characteristic that the mid-frequency components such as textures are removed too.

In digital images, the gray values between neighboring pixels have high correlation. This highly self-similar fractal information of image fractal information is usually represented by complex textural features, and the works in [12–18] showed that fractional-order gradient is more suitable to deal with fractal-like textures. It has been proved in [12] that the fractional-order derivative satisfies the lateral inhibition principle of biologic visual system better than the integer-order derivative. The fractional-order derivative operators have been used in texture enhancement [13], image denoising [14, 15], and image inpainting [16, 17]. Jun and Zhihui [14] replaced the first-order derivative in the regularized term of ROF model with the fractional-order derivative. Bai and Feng [15] designed fractional-order anisotropic diffusion equation to remove noise. Zhang et al. [16] exploited fractional-order TV sinogram inpainting model to reduce metal artifacts for X-ray computed tomography. In [18], fractional total

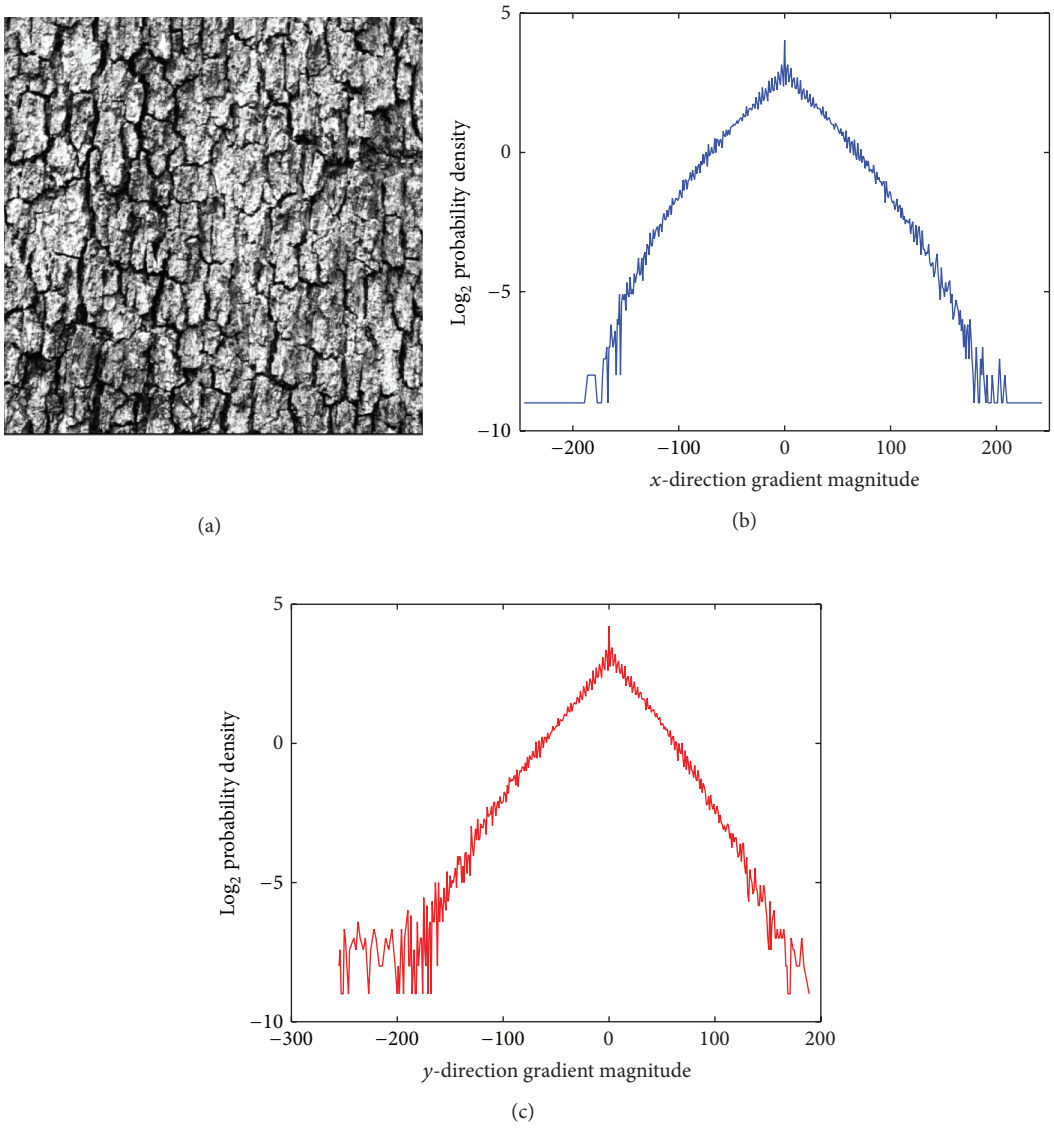

Figure 1: (a) A textured image. (b) The x-direction log distribution of gradient magnitudes. (c) The y-direction log distribution of gradient magnitudes.

variation method was introduced to restore textured image. This work shows that the fractional-order derivative not only nonlinearly preserves the textural details but also eliminates the staircase effect caused by low integral-order derivative in image processing. Different from work in [18], the sparse prior in fractional-order gradient domain is considered in our work, which is more suitable for the texture of image. It is explained clearly in Figures 2 and 3.

This paper presents fractional-order regularization for the restoration of textured image degraded by blur and/or additive noise. R. Tony uses the Laplacian prior in fractional-order gradient domain for $\alpha = 1$ to preserve the texture. According to our analysis in the next section, hyper-Laplacian image prior in fractional-order gradient domain for $0 < \alpha \leq 1$ is more suitable to keep different texture for different texture image.

The outline of this paper is as follows. In Section 2, we analyze the reason why integral-order regularization fails to restore image texture. In Section 3, our fractional-order regularization model is proposed and based on half-quadratic splitting, we solve model using efficient alternating minimization method. Numerical experiments and comments are provided in Section 4 and the paper is concluded in Section 5.

2. Motivation

The prior $p(\mathbf{x})$ favors natural image, usually based on the observation that their heavy-tailed gradient distribution is sparse. For example, Figure 1 shows textured image and a histogram of its gradient magnitudes in x-direction and y-direction, respectively. The distribution shows that the image

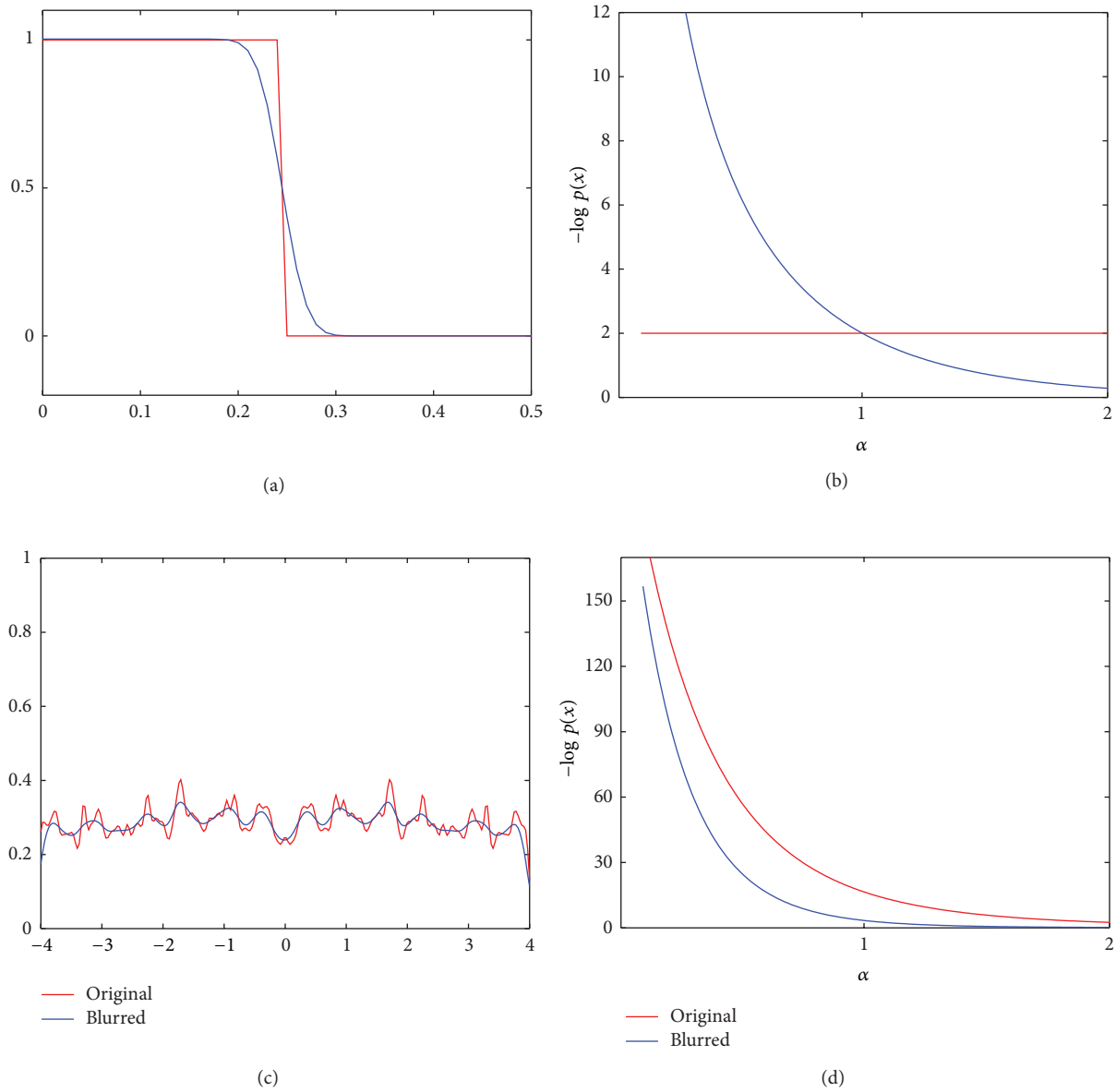

FIGURE 2: Analysis of restoration on 1D signal using gradient prior. ((a) and (c)) Sharp and blurred signal; ((b) and (d)) sum of gradients $-\log\ p(\mathbf{x}) = \sum_i |G_i(\mathbf{x})|^\alpha$ as a function of α.

contains primarily small or zero gradients, but a few gradients have large magnitudes. A common measure [19] is

$$\log\ p(\mathbf{x}) = -\sum_i \left|G_{x,i}(\mathbf{x})\right|^\alpha + \left|G_{y,i}(\mathbf{x})\right|^\alpha + \text{constant}, \tag{2}$$

where $G_{x,i}(\mathbf{x})$ and $G_{y,i}(\mathbf{x})$ denote the horizontal and vertical derivatives at pixel i (here, the simple $[-1\ \ 1]$ and $[-1\ \ 1]^T$ filters are used) and exponent value $\alpha \in (0, 2]$. $\alpha < 1$ leads to sparse prior and natural images usually correspond to α in the range of $[0.5, 0.8]$ [19]. $\alpha = 1$ and $\alpha = 2$ are Laplacian prior and Gaussian prior, respectively.

The image restoration methods use the sparse prior term as a regularized term of variational energy functional [19], which is

$$\min_{\mathbf{x}} \lambda\left(\mathbf{x} \otimes \mathbf{h} - \mathbf{y}\right) + \sum_{i=1}^{I}\left(\left|G_{x,i}\mathbf{x}\right|^\alpha + \left|G_{y,i}\mathbf{x}\right|^\alpha\right). \tag{3}$$

The failure of restoring texture with the sparse gradient prior depends on the fact that the value of energy does not always decrease during restoration process, so the no-blur explanation is usually favored. To understand this, consider the 1D signals in Figure 2.

For sharp edge in Figure 2(a), while Gaussian prior favors the blurry explanation, the sparse prior ($\alpha < 1$) favors the correct sharp explanation in Figure 2(b). The signal considered

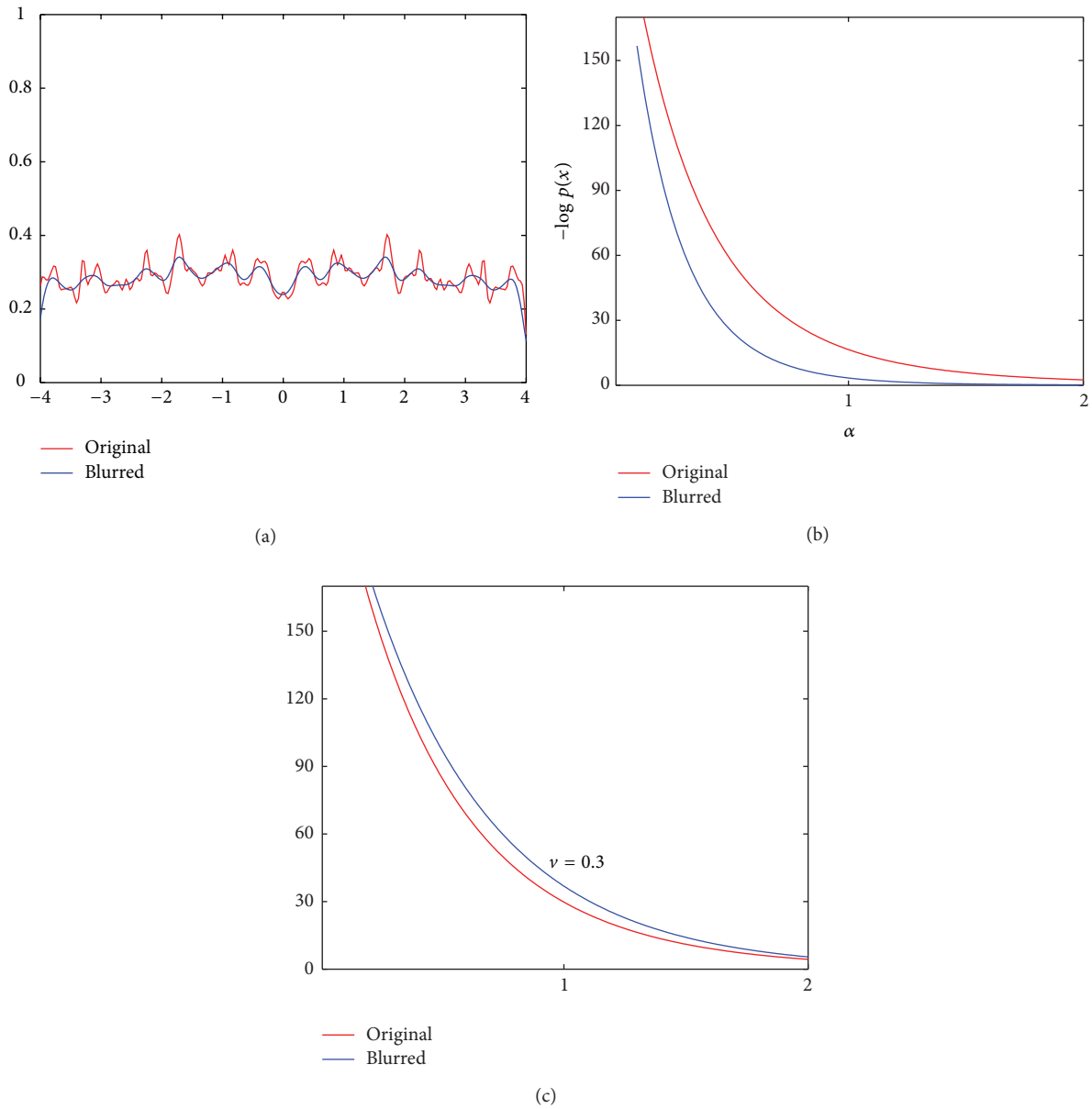

FIGURE 3: Analysis of restoration on 1D signal: (a) sharp versus blurred signal; (b) sum of gradients $-\log\ p(\mathbf{x}) = \sum_i |G_i(\mathbf{x})|^\alpha$ as a function of α; (c) sum of gradients $-\log\ p(\mathbf{x}) = \sum_i |G_i^\nu(\mathbf{x})|^\alpha$ as a function of α (the value of ν is 0.3).

in Figure 2(c) illustrates that natural image contains a lot of medium contrast textures, which dominate the statistics more than step edges. As a result, blurring natural image reduces the overall contrast which cannot be restored by Gaussian prior or even sparse priors as in Figure 2(d).

The reason is that the gradient profile in fractal-like textures is close to Gaussian distribution and these small values are severely penalized by the sparse gradient prior.

A fractional-order gradient log distribution can be expressed as follows [18]:

$$\log\ p(\mathbf{x}) = -\sum_i \left|G_{x,i}^\nu \mathbf{x}\right|^\alpha + \left|G_{y,i}^\nu \mathbf{x}\right|^\alpha + \text{constant}, \tag{4}$$

where $G_{x,i}^\nu \mathbf{x}$ and $G_{y,i}^\nu \mathbf{x}$ denote the horizontal and vertical fractional-order derivatives at pixel i and ν is the fractional order $\nu \in (0, 4]$. The exponent value is the same as α value in (2).

Compared with result in Figure 3(b), the sharp explanation in Figure 3(c) is favored by sparse prior even by Gaussian prior in fractional-order gradient domain.

3. The Proposed Model and Algorithm

The corresponding energy functional is as follows [18]:

$$\min_{\mathbf{x}} \lambda\left(\mathbf{x} \otimes \mathbf{h} - \mathbf{y}\right) + \sum_{i=1} \left(\left|G_{x,i}^\nu \mathbf{x}\right|^\alpha + \left|G_{y,i}^\nu \mathbf{x}\right|^\alpha\right), \tag{5}$$

Figure 4: Deblurring: (a) clear image; (b) synthesized blurred image with PSF (fspecial("motion",10,20)); (c) image restoration by Lucy-Richardson algorithm; (d) image restoration by IOR; (e) image restoration by [18]; (f) image restoration by FOR (g) closeups of (d), (e), and (f).

where i is the pixel index and $\otimes$ is the 2-dimensional convolution operator, and a weighting term $\lambda = 3e^3$ controls the strength of the regularization. $G^{v}_{x,i}\mathbf{x}$ and $G^{v}_{y,i}\mathbf{x}$ denote the horizontal and vertical fractional-order derivatives at pixel i defined by our coauthor as Tables 1 and 2 [16].

The coefficients of the operator in Tables 1 and 2 are

$$Cs_{-1} = \frac{v}{4} + \frac{v^2}{8}$$

$$Cs_0 = 1 - \frac{v^2}{2} - \frac{v^3}{8}$$

$$Cs_1 = -\frac{5v}{4} - \frac{5v^3}{16} + \frac{v^4}{16}$$

$$\vdots$$

$$Cs_k = \frac{1}{\Gamma(-v)}\left[\frac{\Gamma(k-v-1)}{(k+1)!}\cdot\left(\frac{v}{4}+\frac{v^2}{8}\right) + \frac{\Gamma(k-v)}{k!}\cdot\left(1-\frac{v^2}{4}\right) + \frac{\Gamma(k-v-1)}{(k-1)!}\cdot\left(-\frac{v}{4}+\frac{v^2}{8}\right)\right],$$

$$\vdots$$

$$Cs_{n-2} = \frac{1}{\Gamma(-v)}\left[\frac{\Gamma(n-v-1)}{(n-1)!}\cdot\left(\frac{v}{4}+\frac{v^2}{8}\right)\right.$$

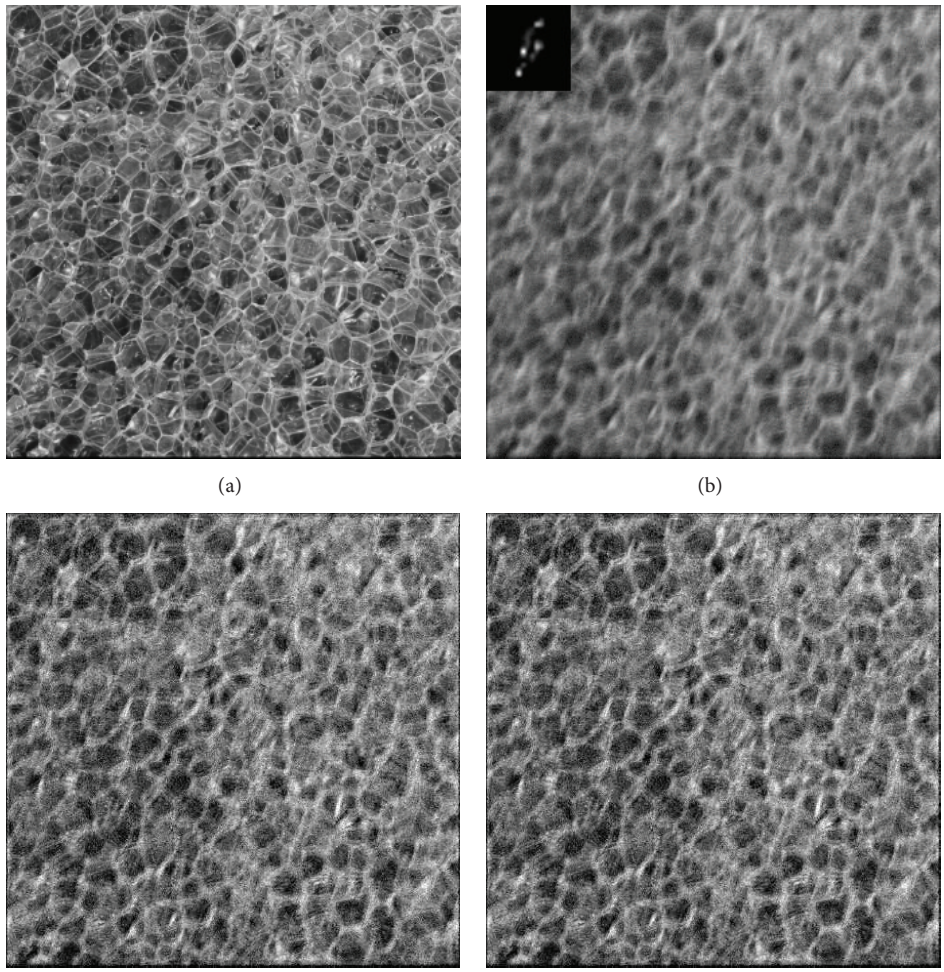

Figure 5: Deblurring and denoising: (a) clear image; (b) synthesized blurred image and adding white Gaussian noise (its standard variance is 0.003); (c) image restoration by IOR; (d) image restoration by FOR.

$$
\begin{aligned}
&+\frac{\Gamma(n-\nu-2)}{(n-2)!}\cdot\left(1-\frac{\nu^2}{4}\right)\\
&+\frac{\Gamma(n-\nu-3)}{(n-3)!}\cdot\left(-\frac{\nu}{4}+\frac{\nu^2}{8}\right)\Bigg],\\
&\vdots\\
Cs_{n-2}=&\frac{\Gamma(n-\nu-1)}{(n+1)!\Gamma(-\nu)}\cdot\left(1-\frac{\nu^2}{8}\right)\\
&+\frac{\Gamma(n-\nu-2)}{(n-2)!\Gamma(-\nu)}\cdot\left(-\frac{\nu}{4}+\frac{\nu^2}{8}\right)\\
Cs_n=&\frac{\Gamma(n-\nu-1)}{(n-1)!\Gamma-\nu}\cdot\left(-\frac{\nu}{4}+\frac{\nu^2}{8}\right).
\end{aligned}
\tag{6}
$$

Equation (5) contains nonlinear penalties for regularization term, so we propose alternating minimization (AM) method, based on a half-quadratic splitting to solve it [18, 20]. We introduce auxiliary variables u and $\mathbf{w}=(w_x,w_y)$ at each pixel, so the energy functional in (5) can be modified as

$$
\begin{aligned}
\min_{\mathbf{x},\mathbf{w}}&\frac{\theta}{2}(\mathbf{x}\otimes\mathbf{h}-\mathbf{y})^2+\lambda|u|\\
&+\sum_{i=1}\left(\frac{\beta}{2}\left(\left\|G_{x,i}^{\nu}\mathbf{x}-w_{x,i}\right\|_2^2+\left\|G_{y,i}^{\nu}\mathbf{x}-w_{y,i}\right\|_2^2\right)\right.\\
&\left.+\left|w_{x,i}\right|^{\alpha}+\left|w_{y,i}\right|^{\alpha}\right),
\end{aligned}
\tag{7}
$$

where the first two terms are used to ensure the similarity between the measures and the corresponding auxiliary variables. As $\beta\rightarrow\infty$ and $\theta\rightarrow\infty$ the solution of (6) converges to that of (5). Equation (7) can be solved by AM method through fixing other variables to solve $\mathbf{x},\mathbf{w},$ and u independently.

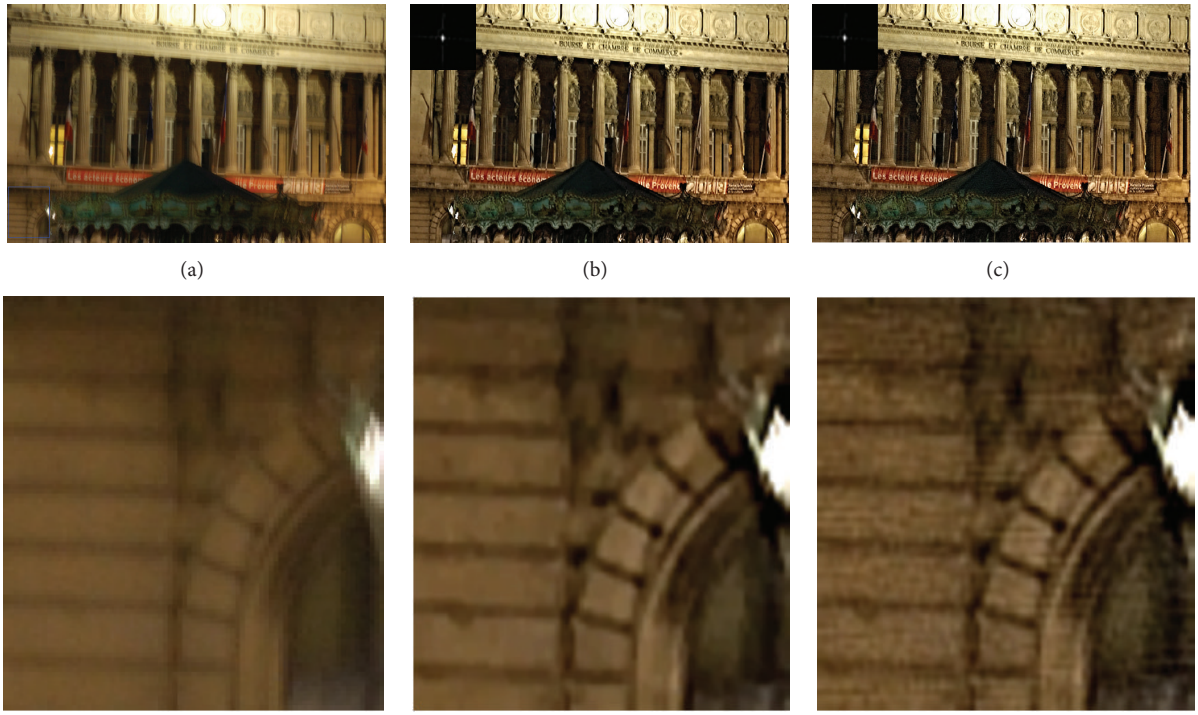

(a) (b) (c)

(d)

Figure 6: Testing our algorithm with real-life blurry images. (a) Blurry image. (b) Restored image by using the algorithm in [9]. (c) Restored image by our algorithm. (d) Comparison of details of image window. Left: details in (a), middle: details in (b), and right: details in (c).

3.1. $\mathbf{x}$ *Subsolution.* Given fixed values of u and $\mathbf{w}$ from the previous iteration, (7) is quadratic in $\mathbf{x}$. So we compute $\mathbf{x}$ by minimizing

$$E(\mathbf{x}; u, \mathbf{w}) = \left\|\mathbf{x} \otimes \mathbf{h} - \mathbf{y} - u\right\|^2 + \sum_{i=1} \left(\frac{\beta}{\theta} \left(\left\|G_{x,i}^{v}\mathbf{x} - w_{x,i}\right\|_2^2 + \left\|G_{y,i}^{v}\mathbf{x} - w_{y,i}\right\|_2^2 \right) \right). \tag{8}$$

The optimal $\mathbf{x}$ is

$$\left(\frac{\theta}{\beta}\mathbf{H}^T\mathbf{H} + G_x^{v\,T}G_x^{v} + G_y^{v\,T}G_y^{v} \right)\mathbf{x} = G_x^{v\,T}w_x + G_y^{v\,T}w_y + \frac{\theta}{\beta}\mathbf{H}^T(\mathbf{y} + u), \tag{9}$$

where $\mathbf{Hx} = \mathbf{h} \otimes \mathbf{x}$. According to Parseval's theorem after the Fourier transform, (8) has the closed form solution in minimization, which enables us to find the optimal $\mathbf{x}$ directly:

$$\mathbf{x} = F^{-1}\left(\left(F(G_x^{v})^* F(w_x) + F(G_y^{v})^* F(w_y) + \frac{\theta}{\beta}F(\mathbf{H})^* F(\mathbf{y} + u) \right) \times \left(F(G_x^{v})^* F(G_x^{v}) + F(G_y^{v})^* F(G_y^{v}) + \frac{\theta}{\beta}F(\mathbf{H})^* F(\mathbf{H}) \right)^{-1} \right), \tag{10}$$

where $F(\cdot)$ and $F(\cdot)^{-1}$ denote the fast Fourier transform and inverse fast Fourier transform, respectively. $*$ is the complex conjugate operator.

3.2. u *Subsolution.* Here, u and $\mathbf{w}$ belong to different terms. They are not coupled with each other in the functional, so their optimization is independent. Given fixed value of $\mathbf{x}$, we compute u by minimizing

$$E(u; \mathbf{x}) = \frac{1}{2}\left\|u - (\mathbf{x} \otimes \mathbf{h} - \mathbf{y})\right\| + \frac{\lambda}{\theta}|u|. \tag{11}$$

According to shrinkage formula [21], the optimal u is

$$u = \operatorname{sign}(\mathbf{x} \otimes \mathbf{h} - \mathbf{y}) \max\left(\left\|\mathbf{x} \otimes \mathbf{h} - \mathbf{y}\right\| - \frac{\lambda}{\theta}, 0 \right). \tag{12}$$

3.3. $\mathbf{w}$ *Subsolution.* We have the following:

$$\begin{aligned} \dot{E}(w_x; \mathbf{x}) &= |w_x|^{\alpha} + \frac{\beta}{2}\left(\left\|G_x^{v}\mathbf{x} - w_x\right\|_2^2 \right), \\ E(w_y; \mathbf{x}) &= |w_y|^{\alpha} + \frac{\beta}{2}\left(\left\|G_y^{v}\mathbf{x} - w_y\right\|_2^2 \right). \end{aligned} \tag{13}$$

Input: observed image $\mathbf{y}$, PSF $\mathbf{h}$, penalty parameters λ, exponent α and fractional-order ν
Input: β_0, β_{Max}, θ_0, θ_{Max}
Initialize $\mathbf{x} = \mathbf{y}$, $\theta = \theta_0$, $\beta = \beta_0$
while $\theta < \theta_{\text{Max}}$, do
  solve for u using (12)
while $\beta < \beta_{\text{Max}}$ do
  Given $\mathbf{x}$, solve for $\mathbf{w}$ according to our discussion
  Given $\mathbf{w}$, solve for $\mathbf{x}$ using (10)
  $\beta = 2\beta$
end while
  $\theta = 2\theta$
end while
Output: Estimated image $\mathbf{x}$

Algorithm 1: Fractional-order regularization.

Table 1: Operator of x-direction: $G_x^\nu \mathbf{x}$.

(a)

$\vdots$	$\vdots$	$\vdots$		$\vdots$		$\vdots$	$\vdots$	$\vdots$
0	0	0	$\cdots$	0	$\vdots$	0	0	0
Cs_{-1}	Cs_0	Cs_1	$\cdots$	Cs_k	$\cdots$	Cs_{n-2}	Cs_{n-1}	Cs_n
0	0	0	$\cdots$	0	$\vdots$	0	0	0
$\vdots$	$\vdots$	$\vdots$		$\vdots$		$\vdots$	$\vdots$	$\vdots$

(b)

$\vdots$	$\vdots$	$\vdots$		$\vdots$		$\vdots$	$\vdots$	$\vdots$
0	0	0	$\cdots$	0	$\vdots$	0	0	0
Cs_n	Cs_{n-1}	Cs_{n-2}	$\cdots$	Cs_k	$\cdots$	Cs_1	Cs_0	Cs_{-1}
0	0	0	$\cdots$	0	$\vdots$	0	0	0
$\vdots$	$\vdots$	$\vdots$		$\vdots$		$\vdots$	$\vdots$	$\vdots$
				7				

Table 2: Operator of y-direction: $G_y^\nu \mathbf{x}$.

(a)

$\cdots$	0	Cs_n	0	$\cdots$
$\cdots$	0	Cs_{n-1}	0	$\cdots$
$\cdots$	0	Cs_{n-2}	0	$\cdots$
	$\vdots$	$\vdots$	$\vdots$	
$\cdots$	0	Cs_n	0	$\cdots$
	$\vdots$	$\vdots$	$\vdots$	
$\cdots$	0	Cs_1	0	$\cdots$
$\cdots$	0	Cs_0	0	$\cdots$
$\cdots$	0	Cs_{-1}	0	$\cdots$

(b)

$\cdots$	0	Cs_{-1}	0	$\cdots$
$\cdots$	0	Cs_0	0	$\cdots$
$\cdots$	0	Cs_1	0	$\cdots$
	$\vdots$	$\vdots$	$\vdots$	
$\cdots$	0	Cs_k	0	$\cdots$
	$\vdots$	$\vdots$	$\vdots$	
$\cdots$	0	Cs_{n-2}	0	$\cdots$
$\cdots$	0	Cs_{n-1}	0	$\cdots$
$\cdots$	0	Cs_n	0	$\cdots$

For $\alpha = 2$ case, the subproblem about w_x and w_y is quadratic.

For $\alpha = 1$ case, the optimal solution for w_x and w_y can be derived by shrinkage formula too:

$$\begin{aligned} \dot{w}_x &= \operatorname{sign}\left(G_x^\nu \mathbf{x}\right) * \max\left(\operatorname{abs}\left(G_x^\nu \mathbf{x}\right) - \frac{1}{\beta}, 0\right), \\ w_y &= \operatorname{sign}\left(G_y^\nu \mathbf{x}\right) * \max\left(\operatorname{abs}\left(G_y^\nu \mathbf{x}\right) - \frac{1}{\beta}, 0\right). \end{aligned} \tag{14}$$

For the other α case, setting the derivative of (13) with regard to w_x and w_y to zero gives

$$\begin{aligned} \dot{\alpha}\left|w_x\right|^{\alpha-1} \operatorname{sign}\left(w_x\right) + \beta\left(w_x - G_x^\nu \mathbf{x}\right) &= 0, \\ \alpha\left|w_y\right|^{\alpha-1} \operatorname{sign}\left(w_y\right) + \beta\left(w_y - G_y^\nu \mathbf{x}\right) &= 0. \end{aligned} \tag{15}$$

Two special α cases are discussed here.

For $\alpha = 1/2$ case, about w_x, (15) becomes

$$\frac{1}{2}\left|w_x\right|^{-1/2} \operatorname{sign}\left(w_x\right) + \beta\left(w_x - G_x^\nu \mathbf{x}\right) = 0, \tag{16}$$

$$w_x^3 - 2\left(G_x^\nu \mathbf{x}\right) w_x^2 + \left(G_x^\nu \mathbf{x}\right)^2 w_x - \frac{\operatorname{sign}\left(w_x\right)}{4\beta^2} = 0. \tag{17}$$

Because $G_x^\nu \mathbf{x}$ is fixed and w_x lies between 0 and $G_x^\nu \mathbf{x}$, we can replace $\operatorname{sign}(w_x)$ with $\operatorname{sign}(G_x^\nu \mathbf{x})$. Equation (17) can be rewritten as

$$w_x^3 - 2\left(G_x^\nu \mathbf{x}\right) w_x^2 + \left(G_x^\nu \mathbf{x}\right)^2 w_x - \frac{\operatorname{sign}\left(G_x^\nu \mathbf{x}\right)}{4\beta^2} = 0. \tag{18}$$

Table 3: PSNR and SSIM of image restoration by IOR and FOR.

Image	α	$\mathrm{PSNR}_{\mathrm{IOR}}$	$\mathrm{SSIM}_{\mathrm{IOR}}$	ν	α	$\mathrm{PSNR}_{\mathrm{FOR}}$	$\mathrm{SSIM}_{\mathrm{FOR}}$
Barbara (256 ∗ 256)	0.8	—	0.8411	0.4	0.3	—	0.8580
Bubble (512 ∗ 512)	0.4	2.5249	0.6949	1.8	0.4	2.7343	0.6987

So we can get the cubic polynomials about w_x and w_y:

$$\begin{aligned} &\dot{w}_x^3 - 2\left(G_x^\nu \mathbf{x}\right) w_x^2 + \left(G_x^\nu \mathbf{x}\right)^2 w_x - \frac{\operatorname{sign}\left(G_x^\nu \mathbf{x}\right)}{4\beta^2} = 0, \\ &w_y^3 - 2\left(G_y^\nu \mathbf{x}\right) w_y^2 + \left(G_y^\nu \mathbf{x}\right)^2 w_y - \frac{\operatorname{sign}\left(G_y^\nu \mathbf{x}\right)}{4\beta^2} = 0. \end{aligned} \tag{19}$$

The value of w_x and w_y is either 0 or the root of cubic polynomial in (19).

For $\alpha = 2/3$ case, we can get the quartic polynomials about w_x and w_y:

$$\begin{aligned} &\dot{w}_x^4 - 3\left(G_x^\nu \mathbf{x}\right) w_x^3 + 3\left(G_x^\nu \mathbf{x}\right)^2 w_x^2 - \left(G_x^\nu \mathbf{x}\right)^3 w_x + \frac{8}{27\beta^3} = 0, \\ &w_y^4 - 3\left(G_y^\nu \mathbf{x}\right) w_y^3 + 3\left(G_y^\nu \mathbf{x}\right)^2 w_y^2 - \left(G_y^\nu \mathbf{x}\right)^3 w_y + \frac{8}{27\beta^3} = 0. \end{aligned} \tag{20}$$

The value of w_x and w_y is either 0 or the root of cubic polynomial in (20).

Given the roots of cubic and quartic polynomials and zero solution, we need to determine which one corresponds to the global minima of (12), which can be confirmed by the following scheme.

Let r be the nonzero real root. If 0 value is the optimum solution of (13), for $G_x^\nu \mathbf{x}$, this implies

$$|r|^\alpha + \frac{\beta}{2}\left(r - G_x^\nu \mathbf{x}\right)^2 > \frac{\beta\left(G_x^\nu \mathbf{x}\right)^2}{2}, \tag{21}$$

$$\operatorname{sign}(r)\,|r|^{(\alpha-1)} + \frac{\beta}{2}\left(r - G_x^\nu \mathbf{x}\right) \lessgtr 0, \quad r \lessgtr 0. \tag{22}$$

We can use (15) to eliminate $\operatorname{sign}(r)|r|^{(\alpha-1)}$ from (15) and (22), yielding the condition

$$r \lessgtr 2G_x^\nu \mathbf{x}\frac{\alpha - 1}{\alpha - 2}, \tag{23}$$

since $\operatorname{sign}(r) = \operatorname{sign}(G_x^\nu \mathbf{x})$. So $w_x = r$ if r is between $2G_x^\nu \mathbf{x}/3$ and $G_x^\nu \mathbf{x}$ in the $\alpha = 1/2$ case or between $G_x^\nu \mathbf{x}/2$ and $G_x^\nu \mathbf{x}$ in the $\alpha = 2/3$ case. Otherwise, $w_x = 0$. The same scheme applies to $G_y^\nu \mathbf{x}$.

For other α cases, w_x and w_y can be computed by Newton method.

3.4. Algorithm. β and θ are positive values to enforce the similarity between the auxiliary variables and the respective terms. We empirically set $\beta_0 = 1$, $\beta_{\mathrm{Max}} = 256$ and $\theta_0 = 1$, $\theta_{\mathrm{Max}} = \lambda$.

The algorithm of this fractional-order regularization model is shown in Algorithm 1.

4. Numerical Experiments

We consider the restoration of a blur- and noise-contaminated test image represented by 255 × 255 pixels. In order to compare the accuracy of FOR (fractional order regularization) and IOR (integer order regularization) more precisely, we list in Table 3 the peak signal-to-noise ratio (PSNR) and gray-scale structural similarity (SSIM) as quality metric. PSNR is most easily defined via the mean squared error (MSE). Given a noise-free M by N image I and its noisy approximation $\widehat{I}$, MSE is defined as

$$\mathrm{MSE} = \frac{1}{MN}\sum_{m=1,n=1}^{M,N}\left[I(m,n) - \widehat{I}(m,n)\right]. \tag{24}$$

PSNR is defined as

$$\mathrm{PSNR} = \frac{1}{10}\log\left(\frac{255^2}{\mathrm{MSE}}\right)(\mathrm{dB}), \tag{25}$$

and SSIM is defined as

$$\mathrm{SSIM} = \frac{\left(2\mu_I\mu_K + c_1\right)\left(2\sigma_{IK} + c_2\right)}{\left(\mu_I^2 + \mu_K^2 + c_1\right)\left(\sigma_I^2 + \sigma_K^2 + c_2\right)}, \tag{26}$$

where I and K are different images, μ_I and μ_K are the average of I and K, respectively, σ_I^2 and σ_K^2 are the variance of I and K, respectively, and σ_{IK} is the covariance of I and K. c_1 and c_2 are constant.

The desired blur- and noise-free image is depicted in Figure 4. The image is contaminated by motion blur generated by Matlab function (fspecial("motion",10,20)). The resulting image is displayed in Figure 4(f). In Table 3 the second column, with header PSNR and SSIM values for images that have been corrupted by motion blur, is characterized by $\nu = 0.4$ and $\alpha = 0.3$.

The desired blur- and noise-contaminated image is depicted in Figure 5. The image is contaminated by motion blur, adding white Gaussian noise (its standard variance is 0.003). The resulting image is displayed in Figure 5(d). In Table 3 the third column, with header PSNR and SSIM values for images that have been corrupted by motion blur, is characterized by $\nu = 1.8$ and $\alpha = 0.4$.

Figure 6 shows the result of deconvolving a real blurry image. We estimate the blur kernel using the algorithm in [9]. Again, textured regions are better reconstructed using our method in visual quality. Figure 6(b) is restored by total variation. Figure 6(c) is restored by fractional-order total variation. Figure 6(d) shows the details in Figure 6(b) and Figure 6(c).

5. Conclusion

By introducing sparse prior in fractional-order gradient domain, we propose a fractional-order regularization method for the restoration of textured image degraded by blur and/or noise. The regularizer is constructed by using fractional-order derivatives, where the choice of the fractional-order is driven by different textured image. This makes the proposed model an efficient tool to preserve texture well. Numerical results show that the proposed model yields better SSIM and PSNR value and visual effects than using integral-order regularization method.

Our following work is to use an automatic texture detection procedure for textured image restoration. Different parameters are applied for different textures.

Conflict of Interests

The authors declare that there is no conflict of interests regarding the publication of this paper.

Acknowledgment

This work was supported by the National Natural Science Foundation of China (NSFC) (no. 61302028). This document is a collaborative effort.

References

[1] L. I. Rudin, S. Osher, and E. Fatemi, "Nonlinear total variation based noise removal algorithms," *Physica D: Nonlinear Phenomena*, vol. 60, no. 1–4, pp. 259–268, 1992.

[2] T. F. Chan, S. Osher, and J. Shen, "The digital TV filter and nonlinear denoising," *IEEE Transactions on Image Processing*, vol. 10, no. 2, pp. 231–241, 2001.

[3] Y. Li and F. Santosa, "A computational algorithm for minimizing total variation in image restoration," *IEEE Transactions on Image Processing*, vol. 5, no. 6, pp. 987–995, 1996.

[4] T. F. Chan and C.-K. Wong, "Total variation blind deconvolution," *IEEE Transactions on Image Processing*, vol. 7, no. 3, pp. 370–375, 1998.

[5] R. Fergus, B. Singh, A. Hertzmann, S. T. Roweis, and W. T. Freeman, "Removingcamera shake from a single photograph," *ACM Transactionson Graphics*, vol. 25, pp. 787–794.

[6] Q. Shan, J. Jia, and A. Agarwala, "High-quality motion deblurring from a single image," *ACM Transactions on Graphics*, vol. 27, no. 3, article 73, 2008.

[7] Y. Wang, J. Yang, W. Yin, and Y. Zhang, "A new alternating minimization algorithm for total variation image reconstruction," *SIAM Journal on Imaging Sciences*, vol. 1, no. 3, pp. 248–272, 2008.

[8] D. Krishnan and R. Fergus, "Fast image deconvolution using hyper-laplacianpriors," in *Advances in Neural Information Processing Systems*, pp. 1033–1041.

[9] D. Krishnan, T. Tay, and R. Fergus, "Blind deconvolution using a normalized sparsity measure," in *Proceedings of the IEEE Conference on Computer Vision and Pattern Recognition (CVPR '11)*, pp. 233–240, Providence, RI, USA, June 2011.

[10] J. Yang, Y. Zhang, and W. Yin, "An efficient tv-l1 algorithm for deblurring multichannel images corrupted by impulsive noise," *SIAM Journal on Scientific Computing*, vol. 31, no. 4, pp. 2842–2865, 2009.

[11] L. Xu and J. Jia, "Two-phase kernel estimation for robust motion deblurring," in *Proceedings of the 11th European Conference on Computer Vision (ECCV '10)*, pp. 157–170, 2010.

[12] Y. Pu, W. Wang, J. Zhou, Y. Wang, and H. Jia, "Fractional differential approach to detecting textural features of digital image and its fractional differential filter implementation," *Science in China F: Information Sciences*, vol. 51, no. 9, pp. 1319–1339, 2008.

[13] P. Yi-Fei, "Fractional differential analysis for texture of digital image," *Journal of Algorithms and Computational Technology*, vol. 1, pp. 357–380, 2007.

[14] Z. Jun and W. Zhihui, "A class of fractional-order multi-scale variational models and alternating projection algorithm for image denoising," *Applied Mathematical Modelling*, vol. 35, no. 5, pp. 2516–2528, 2011.

[15] J. Bai and X.-C. Feng, "Fractional-order anisotropic diffusion for image denoising," *IEEE Transactions on Image Processing*, vol. 16, no. 10, pp. 2492–2502, 2007.

[16] Y. Zhang, Y.-F. Pu, J.-R. Hu, Y. Liu, and J.-L. Zhou, "A new CT metal artifacts reduction algorithm based on fractional-order sinogram inpainting," *Journal of X-Ray Science and Technology*, vol. 19, no. 3, pp. 373–384, 2011.

[17] Y. Zhang, Y.-F. Pu, J.-R. Hu, and J.-L. Zhou, "A class of fractional-order variational image inpainting models," *Applied Mathematics and Information Sciences*, vol. 6, no. 2, pp. 299–306, 2012.

[18] R. H. Chan, A. Lanza, S. Morigi, and F. Sgallari, "An adaptive strategy for the restoration of textured images using fractional order regularization," *Numerical Mathematics: Theory, Methods and Applications*, vol. 6, no. 1, pp. 276–296, 2013.

[19] A. Levin, Y. Weiss, F. Durand, and W. T. Freeman, "Understanding and evaluating blind deconvolution algorithms," in *Proceedings of the IEEE Computer Society Conference on Computer Vision and Pattern Recognition Workshops (CVPR Workshops '09)*, pp. 1964–1971, Miami, Fla, USA, June 2009.

[20] R. H. Chan and H. X. Liang, *A Fast and Efficient Half-Quadratic Algorithmfor tv-l1 Image Restoration*, The Chinese University of Hong Kong, 2011.

[21] A. Chambolle, R. A. DeVore, N.-Y. Lee, and B. J. Lucier, "Nonlinear wavelet image processing: variational problems, compression, and noise removal through wavelet shrinkage," *IEEE Transactions on Image Processing*, vol. 7, no. 3, pp. 319–335, 1998.

Hindawi Publishing Corporation
Mathematical Problems in Engineering
Volume 2014, Article ID 567898, 10 pages
http://dx.doi.org/10.1155/2014/567898

Research Article

Modified Projective Synchronization between Different Fractional-Order Systems Based on Open-Plus-Closed-Loop Control and Its Application in Image Encryption

Hongjuan Liu,[1,2] Zhiliang Zhu,[1] Hai Yu,[1] and Qian Zhu[1,2]

[1] *Software College, Northeastern University, Shenyang 110819, China*
[2] *School of Information Science & Engineering, Northeastern University, Shenyang 110819, China*

Correspondence should be addressed to Hongjuan Liu; liuhongjuan0125@163.com

Received 27 November 2013; Accepted 13 February 2014; Published 27 March 2014

Academic Editor: Riccardo Caponetto

A new general and systematic coupling scheme is developed to achieve the modified projective synchronization (MPS) of different fractional-order systems under parameter mismatch via the Open-Plus-Closed-Loop (OPCL) control. Based on the stability theorem of linear fractional-order systems, some sufficient conditions for MPS are proposed. Two groups of numerical simulations on the incommensurate fraction-order system and commensurate fraction-order system are presented to justify the theoretical analysis. Due to the unpredictability of the scale factors and the use of fractional-order systems, the chaotic data from the MPS is selected to encrypt a plain image to obtain higher security. Simulation results show that our method is efficient with a large key space, high sensitivity to encryption keys, resistance to attack of differential attacks, and statistical analysis.

1. Introduction

Fractional calculus, which is a mathematical topic with more than 300-year history, was not applied to physics and engineering until recent decades. A fractional-order system is characterized as a dynamical system described by fractional derivatives and integrals. It is demonstrated that some fractional-order differential systems behave chaotically or hyperchaotically, such as the fractional-order Lorenz system [1], fractional-order Lü system [2], fractional-order Rössler system [3], and fractional-order Arneodo system [4]. Recently, the control and synchronization of the fractional-order chaotic systems start to attract a great deal of attention due to their potential applications in secure communication and control processing. Some approaches have been proposed to achieve chaos synchronization between fractional-order chaotic systems, such as adaptive control [5], a scalar transmitted signal method [6], sliding mode control [7], and fuzzy logic constant control [8].

Other than the above studies, the Open-Plus-Closed-Loop (OPCL) control method is a more general and physically realizable coupling scheme that can provide stable synchronization in identical and mismatched oscillators [9, 10]. The advantage of the OPCL coupling includes the following two aspects. First of all, OPCL coupling provides synchronization in all systems without restrictions on the symmetry class of a dynamical system. Secondly, in the synchronization regimes, the OPCL coupling can realize stable amplification or attenuation in identical and mismatched systems. Until now, many researchers have achieved their synchronization scenarios for integer-order or fractional-order systems through OPCL control [11–13]. It should be noted that most of the existing works focus on synchronization between identical chaotic systems. However, in practice applications, most systems are nonidentical and parameter mismatches are inevitable because of noise or other uncertain factors. Our coupling strategies need to be formulated to ensure stable synchronization in the presence of mismatch. As a matter of fact, OPCL control can be utilized to achieve synchronization of fractional-order chaotic systems with different structure.

Specially, we will realize modified projective synchronization (MPS) of two different fractional-order systems with parameter mismatches. In MPS, the states of the drive and response systems synchronize up to a constant scaling matrix

with the complete synchronization, antisynchronization, and projective synchronization as the special cases. Based on the OPCL control, a general coupling method is proposed for MPS of two nonidentical fractional-order systems. The proposed coupling scheme is theoretically proved based on stability theory of linear fractional differential equations and its effectiveness is verified by two groups of numerical simulations. Finally, based on the realized MPS, an image encryption scheme with diffusion and confusion is designed. Both the unpredictability of scaling matrix and the use of fractional-order systems will raise the security level of the encryption scheme. According to the analysis of simulations, really satisfactory results are obtained, with large key space, high sensitivity to initial conditions, and high security.

2. The MPS through OPCL Coupling

2.1. Theory Analysis. There are several definitions of fractional derivatives. The Caputo derivative is more popular in the real applications, because the inhomogeneous initial conditions are allowed, if such conditions are necessary. The Caputo definition of the fractional derivative [15], which sometimes is called smooth fractional derivative, is defined as

$$\begin{aligned}\frac{d^q f(t)}{dt^q} &\equiv D^q f(t)\\ &= \frac{1}{\Gamma(m-q)}\int_0^t (t-\tau)^{m-q-1} f^{(m)}(\tau)\,d\tau,\end{aligned} \tag{1}$$

where m is the smallest integer larger than q, D^q denotes the Caputo definition of the fractional derivative, $f^{(m)}(t)$ is the m-order derivative in the usual sense, and Γ stands for gamma function.

As to the fractional-order chaotic systems, we will briefly describe how to synchronize two different systems via the OPCL coupling method. Assume the fractional-order chaotic system in the drive part is as follows:

$$D^q x = f(x) + \Delta f(x), \tag{2}$$

where $x \in R^n$, $f : R^n \to R^n$ is a continuous vector function, and $\Delta f(x)$ contains mismatch parameters. If the system parameters are not disturbed in the theory, we set zero to the value of $\Delta f(x)$. $q = (q_1, q_2, \ldots, q_n)^T$ for $0 < q_i < 1$ $(i = 1, 2, \ldots, n)$ is the order of fractional-order system. If $q_1 = q_2 = \cdots = q_n$, we call the system (2) a commensurate fractional-order system, otherwise an incommensurate fractional-order system [16].

Then, the controlled response system is constructed as

$$D^q y = g(y) + u(t), \tag{3}$$

where $y \in R^n$, $g : R^n \to R^n$ is a continuous vector function, and $u(t)$ is the controller to be designed.

Definition 1 (MPS). For the drive system (2) and controlled response system (3), it is said to be modified projective synchronization (MPS), if there exists a constant matrix $k = \mathrm{diag}(k_1, k_2, \ldots, k_n)$, such that $\lim_{t\to+\infty}\|e\| = \lim_{t\to+\infty}\|y - kx\| = 0$.

Remark 2. Due to the vector function $f \neq g$, the systems (2) and (3) are nonidentical chaotic systems.

Remark 3. Complete synchronization, antisynchronization, and projective synchronization are the special cases of MPS, where $k_1 = k_2 = \cdots = k_n = 1$, $k_1 = k_2 = \cdots = k_n = -1$, and $k_1 = k_2 = \cdots = k_n$, respectively.

According to the OPCL control [9, 10], we design the controller $u(t)$ as in the form of

$$u(t) = D^q kx - g(kx) + (H - Jg(kx))(y - kx), \tag{4}$$

where $J = \partial/\partial(kx)$ is the Jacobian matrix of the dynamic system and $H \in (n \times n)$ is an arbitrary constant matrix. Then, $g(y)$ can be written, using the Taylor series expansion, by

$$g(y) = g(kx) + Jg(kx)(y - kx) + \cdots. \tag{5}$$

Keeping the first order terms in (5) and putting (5) and (4) into (3), the error dynamics between systems (2) and (3) is then obtained to be

$$D^q e = D^q y - D^q kx = H(y - kx) = He. \tag{6}$$

In order to research the synchronization stability of the two incommensurate or two commensurate fractional-order systems by OPCL coupling, we provide the following two theorems.

Theorem 4 (see [17]). *Consider incommensurate fractional-order dynamical system $D^q x(t) = Ax(t)$ with $q = (q_1, q_2, \ldots, q_n)^T$, $0 < q_i < 1$, $(i = 1, 2, \ldots, n)$, $x \in R^n$, and $A \in R^{n\times n}$. Set M to be the lowest common multiple of the denominators u_i of q_i, where $q_i = v_i/u_i$ and $\gcd(u_i, v_i) = 1$. The zero solution of the system is asymptotically stable if all roots λ of the equation $\Delta(\lambda) = \det(\mathrm{diag}(\lambda^{Mq_1}, \lambda^{Mq_2}, \ldots, \lambda^{Mq_n}) - A) = 0$ satisfy the condition $|\arg(\lambda)| > \pi/2M$.*

Theorem 5 (see [18]). *For commensurate fractional-order dynamical system $D^q x(t) = Ax(t)$ with $0 < q < 1$, $x \in R^n$, and $A \in R^{n\times n}$, the system is asymptotically stable if and only if $|\arg(\lambda)| > q\pi/2$ is satisfied for all eigenvalues λ of A. Also, this system is stable if and only if $|\arg(\lambda)| \geq q\pi/2$ is satisfied for all eigenvalues λ of A with those critical eigenvalues satisfying $|\arg(\lambda)| = q\pi/2$ having geometric multiplicity of one.*

From the two theorems, we can easily obtain the following two corollaries.

Corollary 6. *When system (2) and system (3) are incommensurate fractional-order systems, set M as the lowest common multiple of the denominators u_i of q_i, where $q_i = v_i/u_i$, $\gcd(u_i, v_i) = 1$. The zero solution of the error system (6) is asymptotically stable if all roots λ of the equation $\Delta(\lambda) = \det(\mathrm{diag}(\lambda^{Mq_1}, \lambda^{Mq_2}, \ldots, \lambda^{Mq_n}) - H) = 0$ satisfy the condition $|\arg(\lambda)| > \pi/2M$.*

Corollary 7. *When system (2) and system (3) are commensurate fractional-order systems, the error system (6) is asymptotically stable if and only if $|\arg(\lambda)| > q\pi/2$ is satisfied for all eigenvalues λ of H.*

Remark 8. According to the original OPCL control method [9, 10], the control matrix H can be designed as simple as possible as long as the condition $|\arg(\lambda)| > q\pi/2$ or $|\arg(\lambda)| > \pi/2M$ holds. For example, when $[Jg(kx)]_{ij}$ is a constant, we then set $H_{ij} = [Jg(kx)]_{ij}$ such that $[H - Jg(kx)]_{ij} = 0$. When $[Jg(kx)]_{ij}$ is a variable, we choose $H_{ij} = p_{ij}$, where p_{ij} are control parameters.

2.2. Numerical Method for Solving Fractional-Order Systems. An efficient method for solving fractional-order differential equations is the improved predictor-corrector algorithm [19], which will be used in numerical simulation section. The algorithm can be interpreted as a fractional variant of the classical second-order Adams-Bashforth-Moulton method.

Consider the following differential equation:

$$D_t^q x(t) = f(t, x(t)), \quad 0 \le t \le T. \tag{7}$$

The initial values are $x^{(k)}(0) = x_0^{(k)}$, $k = 0, 1, \ldots, m-1$, and $m = [q]$. It is equivalent to the Volterra integral equation. Consider

$$x(t) = \sum_{k=0}^{m-1} x_0^{(k)} \frac{t^k}{k!} + \frac{1}{\Gamma(q)} \int_0^t (t-\tau)^{q-1} f(\tau, x(\tau))\, d\tau. \tag{8}$$

Set $h = T/N, t_n = nh, n = 0, 1, \ldots, N \in Z^+$. Then, (8) can be discretized as follows:

$$\begin{aligned} x_h(t_{n+1}) &= \sum_{k=0}^{m-1} x_0^{(k)} \frac{t_{n+1}^k}{k!} + \frac{h^q}{\Gamma(q+2)} f\left(t_{n+1}, x_h^q(t_{n+1})\right) \\ &\quad + \frac{h^q}{\Gamma(q+2)} \sum_{j=0}^{n} a_{j,n+1} f\left(t_j, x_h(t_j)\right), \end{aligned} \tag{9}$$

where,

$$a_{j,n+1} = \begin{cases} n^{q+1} - (n-\alpha)(n+1)^q, & j = 0 \\ (n-j+2)^{q+1} + (n-j)^{q+1} - 2(n-j+1)^{q+1}, & 1 \le j \le n \\ 1, & j = n+1. \end{cases} \tag{10}$$

The preliminary approximation $x_h^p(t_{n+1})$ is called predictor and is given by

$$x_h^p(t_{n+1}) = \sum_{k=0}^{m-1} x_0^{(k)} \frac{t_{n+1}^k}{k!} + \frac{1}{\Gamma(q)} \sum_{j=0}^{n} b_{j,n+1} f\left(t_j, x_h(t_j)\right), \tag{11}$$

where $b_{j,n+1} = (h^q/q)((n-j+1)^q - (n-j)^q)$.

The error estimate is $\max|x(t_j) - x_h(t_j)| = O(h^p)$ $(j = 0, 1, \ldots, N)$, where $p = \min(2, 1+q)$.

2.3. Numerical Examples. In this section, to demonstrate the effectiveness of the proposed OPCL based MPS scheme for different fractional-order systems, we provide two groups of numerical examples. Firstly, fractional-order Arneodo system and fractional-order Lü system are used to verify the incommensurate synchronization. Secondly, fractional-order Lorenz system and fractional-order financial system are introduced to validate the commensurate case.

2.3.1. MPS between Fractional-Order Arneodo System and Fractional-Order Lü System. The fractional-order incommensurate Arneodo system with parameter perturbation is defined as

$$\begin{aligned} D^{q_1} x_1 &= x_2, \\ D^{q_2} x_2 &= x_3, \\ D^{q_3} x_3 &= (\alpha + \Delta\alpha) x_1 + (\beta + \Delta\beta) x_2 + (\gamma + \Delta\gamma) x_3 + x_1^3, \end{aligned} \tag{12}$$

where $\Delta\alpha$, $\Delta\beta$, and $\Delta\gamma$ are the mismatches in parameters. When $(\alpha, \beta, \gamma) = (5.5, -3.5, -1)$ and $(q_1, q_2, q_3) = (0.9, 0.92, 0.96)$, the Arneodo system exhibits chaotic behavior.

The fractionalized version of Lü system reads

$$\begin{aligned} D^{q_1} y_1 &= a(y_2 - y_1), \\ D^{q_2} y_2 &= c y_2 - y_1 y_3, \\ D^{q_3} y_3 &= y_1 y_2 - b y_3. \end{aligned} \tag{13}$$

It has been shown that system (13) will exhibit chaotic behavior when $a = 36$, $b = 3$, $c = 20$, and $(q_1, q_2, q_3) = (0.9, 0.92, 0.96)$.

From system (13), we can obtain the Jacobian matrix:

$$Jg(kx) = \frac{\partial g(kx)}{\partial(kx)} = \begin{pmatrix} -a & a & 0 \\ -k_3 x_3 & c & -k_1 x_1 \\ k_2 x_2 & k_1 x_1 & -b \end{pmatrix}. \tag{14}$$

The constant matrix H for response Lü system is selected as

$$H = \begin{pmatrix} -a & a & 0 \\ p_1 & c & p_2 \\ p_3 & p_4 & -b \end{pmatrix}. \tag{15}$$

On the basis of Definition 1, the error vector of MPS can be expressed by

$$e = He = (e_1, e_2, e_3)^T = (y_1 - k_1 x_1, y_2 - k_2 x_2, y_3 - k_3 x_3)^T. \tag{16}$$

Consequently, define (12) as the drive system and the response system controlled by OPCL coupling is obtained as

$$\begin{aligned} D^{q_1} y_1 &= a(y_2 - y_1) + k_1 x_2 - a(k_2 x_2 - k_1 x_1), \\ D^{q_2} y_2 &= c y_2 - y_1 y_3 + k_2 x_3 - (c k_2 x_2 - k_1 x_1 k_3 x_3) \\ &\quad + (p_1 + k_3 x_3) e_1 + (p_2 + k_1 x_1) e_3, \end{aligned}$$

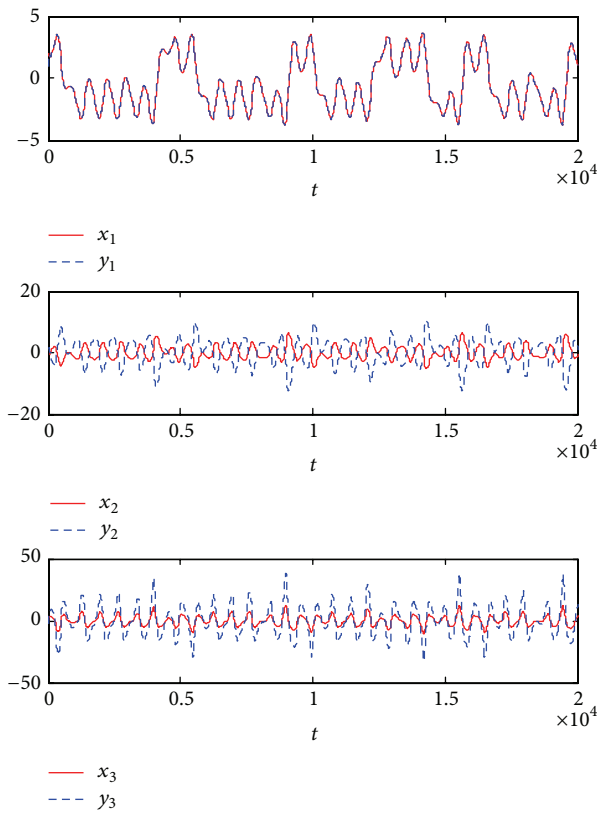

Figure 1: The time evolutions of states for coupled system (12) and system (17).

$$D^{q_3} y_3 = y_1 y_2 - b y_3 + k_3 \left((\alpha + \Delta\alpha) x_1 + (\beta + \Delta\beta) x_2 + (\gamma + \Delta\gamma) x_3 + x_1^3 \right) - (k_1 x_1 k_2 x_2 - b k_3 x_3) + (p_3 - k_2 x_2) e_1 + (p_4 - k_1 x_1) e_2. \tag{17}$$

Thus, by choosing appropriate p_1, p_2, p_3, and p_4, we can stabilize the error vector (16). Now we choose $p_1 = -30$, $p_2 = 0$, $p_3 = 0$, and $p_4 = 0$, where p_1 decides the rate of achieving synchronization. Let us determine the stability of (16) for these p_i's. According to Corollary 6, we constitute $\Delta(\lambda)$ for (15) as follows:

$$\Delta(\lambda) = \det\left(\operatorname{diag}\left(\lambda^{45}, \lambda^{46}, \lambda^{48}\right) - \begin{pmatrix} -36 & 36 & 0 \\ -30 & 20 & 0 \\ 0 & 0 & -3 \end{pmatrix} \right) = 0. \tag{18}$$

Solving this equation for λ, we can see that $\min(|\arg(\lambda_i)|) = 0.0452$ which is greater than $\pi/2M = 0.0314$. Therefore, based on Corollary 6, we conclude the stability of (16), implying that the MPS between fractional-order system (12) and system (17) can be achieved theoretically.

In numerical simulation, for further reduction in coupling complexity, we set the parameter mismatches in drive system (12) as $\Delta\alpha = 1$, $\Delta\beta = 0$, and $\Delta\gamma = 0$. Then, choose scale constant vector as $k = (1, -2, 3)$, the initial conditions as $(x_1(0), x_2(0), x_3(0)) = (2, -1, 1,)$, $(y_1(0), y_2(0)$, and $y_3(0)) = (1, -2, 3)$. The corresponding numerical results are shown in Figures 1 and 2. Figure 1 depicts the time evolutions of state variables in the drive system (12) and the response system (17) with the scaling matrix k.

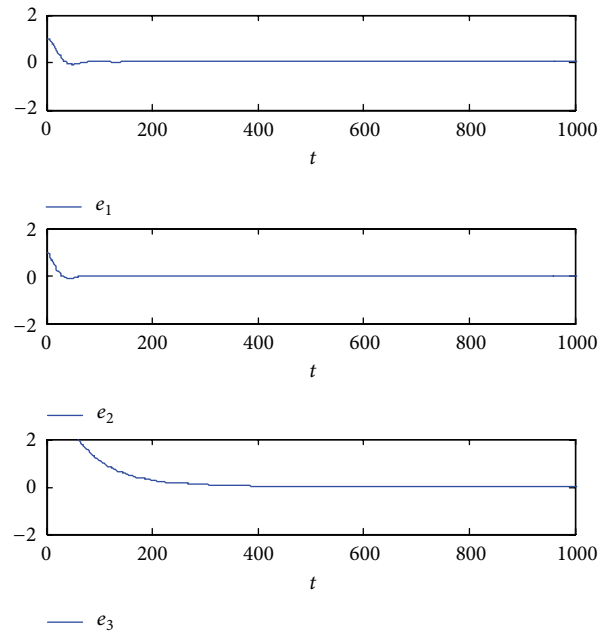

Figure 2: The time evolutions of MFPS errors between system (12) and system (17).

Figure 2 displays the error state trajectories of the two systems. And the error state trajectories asymptotically converge to zero, which implies that the MPS between the incommensurate system (12) and system (17) is realized.

2.3.2. MPS between Fractional-Order Lorenz System and Fractional-Order Financial System. The fractional-order Lorenz system with parameter perturbation is expressed as

$$\begin{aligned} D^q x_1 &= (\alpha + \Delta\alpha)(x_2 - x_1), \\ D^q x_2 &= (\beta + \Delta\beta) x_1 - x_1 x_3 - x_2, \\ D^q x_3 &= x_1 x_2 - (\gamma + \Delta\gamma) x_3, \end{aligned} \tag{19}$$

where $\Delta\alpha$, $\Delta\beta$, and $\Delta\gamma$ are the mismatches in parameters. When $(\alpha, \beta, \gamma) = (10, 28, 8/3)$ and $q \geq 0.993$, the Lorenz system exhibits chaotic behavior.

The fractional-order financial system reads

$$\begin{aligned} D^q y_1 &= y_3 + (y_2 - a) y_1, \\ D^q y_2 &= 1 - b y_2 - y_1^2, \\ D^q y_3 &= -y_1 - c y_3. \end{aligned} \tag{20}$$

It has been shown that system (20) will exhibit chaotic behavior when $a = 3, b = 0.1, c = 1$, and $q \geq 0.85$.

Therefore, we can obtain the Jacobian matrix of system (20):

$$Jg(kx) = \frac{\partial g(kx)}{\partial (kx)} = \begin{pmatrix} k_2x_2 - a & k_1x_1 & 1 \\ -k_1x_1 & -b & 0 \\ -1 & 0 & -c \end{pmatrix}. \quad (21)$$

The constant matrix H for response system is selected as

$$H = \begin{pmatrix} p_1 & p_2 & 1 \\ p_3 & -b & 0 \\ -1 & 0 & -c \end{pmatrix}. \quad (22)$$

According to the error vector defined by (16), if system (19) is considered as drive system, the response system controlled by OPCL coupling is obtained as

$$\begin{aligned} D^q y_1 &= y_3 + (y_2 - a) y_1 + k_1 (\alpha + \Delta\alpha)(x_2 - x_1) \\ &\quad - k_3x_3 - (k_2x_2 - a) k_1x_1 \\ &\quad + (p_1 - k_2x_2 + a) e_1 + (p_2 - k_1x_1) e_2, \\ D^q y_2 &= 1 - by_2 - y_1^2 \\ &\quad + k_2((\beta + \Delta\beta) x_1 - x_1x_3 - x_2) - 1 \\ &\quad + bk_2x_2 + (k_1x_1)^2 + (p_3 + k_1x_1) e_1, \\ D^q y_3 &= -y_1 - cy_3 \\ &\quad + k_3(x_1x_2 - (\gamma + \Delta\gamma) x_3) + k_1x_1 + ck_3x_3. \end{aligned} \quad (23)$$

Thus by choosing appropriate p_1, p_2, and p_3, we can stabilize the error vector (16). Here, we choose $p_1 = -30$, $p_2 = -10$, and $p_3 = 10$, where p_1 decides the rate of achieving synchronization. In numerical simulation, for further reduction in coupling complexity, we set the parameter mismatches in drive system (19) as $\Delta\alpha = 0.01$, $\Delta\beta = 0$, and $\Delta\gamma = 0$. Then, set the fractional-order of two systems as $q = 0.998$ and choose scale constant vector as $k = (2, -1, -3)$ and the initial conditions as $(x_1(0), x_2(0), x_3(0)) = (2, -1, 1)$ and $(y_1(0), y_2(0), y_3(0)) = (1, 1, -2)$. The corresponding simulation results for the time evolutions of state errors are shown in Figure 3, from which we can see that the MPS between two commensurate fractional-order chaotic systems can also be achieved.

The simulation results of the two examples demonstrate that the nonidentical fractional-order chaotic systems with mismatches can achieve the MPS under the OPCL coupling.

3. A Novel Image Encryption Scheme Based on MPS

3.1. Scheme Description. Based on the MPS between fractional-order Arneodo system and fractional-order Lü system, an image encryption scheme is designed for the sake of higher security.

Sender A has the drive system (12) and the response system (17). Receiver B only holds the drive system (12) and

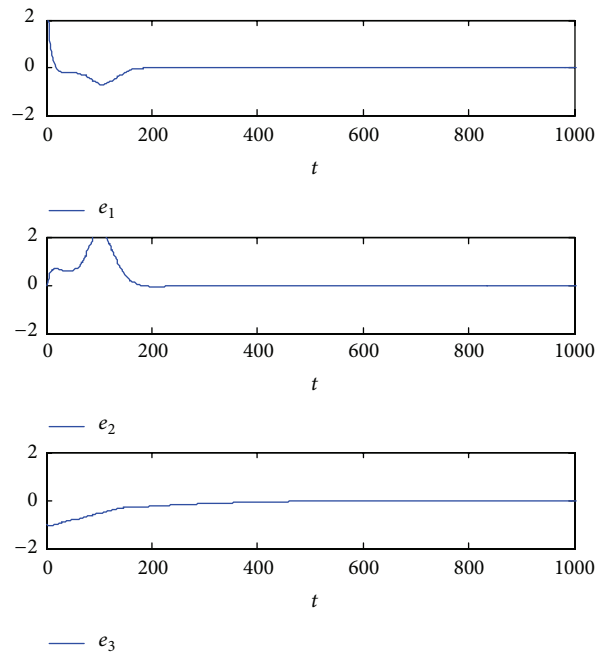

Figure 3: The time evolutions of MFPS errors between system (19) and system (23).

scaling matrix k. A and B share the initial conditions of system (12) and a symmetric key set. Consider

$$H_s = \{h_1, h_2, \ldots, h_{12}\}. \quad (24)$$

Here, $h_1 = \alpha$, $h_2 = \beta$, and $h_3 = \gamma$ are parameters of drive system (12), $h_4 = q_1$, $h_5 = q_2$, and $h_6 = q_3$ are fractional derivatives of drive system (12), $h_7 \sim h_9$ are initial conditions of system (12), and $h_{10} \sim h_{12}$ are the main diagonal elements of scaling matrix k.

The typical image encryption framework is used to encrypt plain image, which is illustrated in Figure 4.

The image cryptosystem in Figure 4 includes two stages, chaotic confusion and pixel diffusion, where the former process permutes a plain image and the latter process changes the value of each pixel one by one. As shown in Figure 4, the confusion and diffusion processes are both repeated several times to enhance the security of this cryptosystem. Suppose that the size of image is $M \times N$ and the detailed encryption algorithm is described as follows.

(1) A first selects the initial conditions and scaling matrix k and then uses them and systems (12) and (17) to generate chaotic data; set the chaotic stream after synchronous time t_0 as $S = (x_1(t), x_2(t), x_3(t), y_1(t), y_2(t), y_3(t))$, $t > t_0$.

(2) In the confusion process, A utilizes the discrete data of system (17) to permute the position of pixel; set $r_x = \text{abs}(\text{fix}(y_3(t_1)))$ and $r_y = \text{abs}(\text{fix}(y_3(t_1 + t_2)))$, where $\text{fix}(\cdot)$ is the function to obtain the integer part, $t_1 > t_0$, and t_2 is the

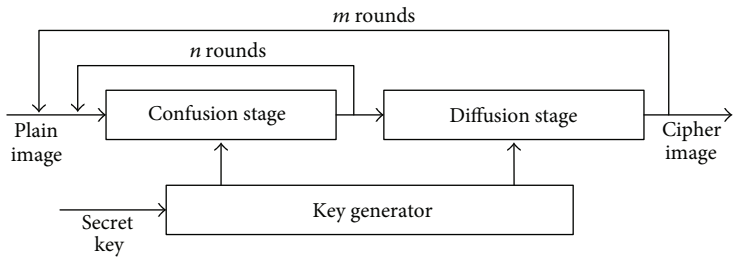

Figure 4: Block diagram of the image cryptosystem.

time interval of the two parameters; the position of pixel is permuted as follows:

$$x_{i+1} = \left(x_i + y_i + r_x + r_y\right) \bmod M,$$
$$y_{i+1} = \left(y_i + r_y + C\sin\frac{2\pi x_{i+1}}{N}\right) \bmod N, \tag{25}$$

where (x_i, y_i) and (x_{i+1}, y_{i+1}) are considered as the positions of image pixel before and after permutation.

(3) In the diffusion stage, the pixel value of image is substituted with its position information by A; according to the chaotic stream S, we can obtain two substitution parameters:

$$c = \operatorname{abs}\left(10^l y_1 - \operatorname{round}\left(10^l y_1\right)\right) \times 10^3,$$
$$d = \operatorname{abs}\left(10^l y_2 - \operatorname{round}\left(10^l y_2\right)\right) \times 10^3, \tag{26}$$

where round( ) is rounding function and l is a positive integer; the biggest value of the parameter l relates to the precision of the computer; therefore, the range of parameter l is from 1 to 14 in current experiment, which can be used as secret key; the substitution of pixel value is in the form of

$$v = p \oplus \left(c \times x_i + d \times y_i\right) \bmod L, \tag{27}$$

where p and v are the pixel values of image before and after substitution and L is the grey level of pixel.

The decryption procedure is similar to that of encryption process with reverse operational sequences to those described above. When B receives the cipher image, it uses the chaotic stream $S_1 = (x_1(t), x_2(t), x_3(t))$, $t > t_0$, generated by the system (12) and the initial condition of system (12) and scaling matrix k to generate $S_2 = (y_1(t), y_2(t), y_3(t))$, $t > t_0$, by $y_1(t) = k_1 x_1(t)$, $y_2(t) = k_2 x_2(t)$, and $y_3(t) = k_3 x_3(t)$. Firstly, substitute the grey values in cipher image back to original ones, namely, for every position (x_i, y_i) and corresponding grey value v of cipher image; compute original grey value as follows:

$$p = v \oplus \left(c \times x_i + d \times y_i\right) \bmod L, \tag{28}$$

where substitution parameters c and d can be computed by (26). After all pixels return to original grey values, then, the pixel in position (x_{i+1}, y_{i+1}) should be moved back to the original position (x_i, y_i) by following inverse operation:

$$y_i = \left(y_{i+1} - 1 - r_y - C\sin\frac{2\pi x_{i+1}}{N} + 2N\right) \bmod N,$$
$$x_i = \left(x_{i+1} - 1 - y_i - r_x - r_y + 2M\right) \bmod M, \tag{29}$$

where the values of r_x and r_y are the same as they are in (25). After the two steps are followed, the plain image can be resumed and the process of decipher is over.

3.2. Experimental Results and Security Analysis. To demonstrate the validity and efficiency of our scheme, a group of experiments for gray Lena image (256 × 256) is carried out with results shown in Figure 5. Here, the key set is selected the same as Section 2.2. Figure 5(b) is the cipher image for original image in Figure 5(a). The histograms of plain image and cipher image illustrated in Figures 5(c) and 5(d) demonstrate that although the grey distribution of original images is not uniform, the grey values of cipher images become uniformly distributed and their statistical property is absolutely changed. A good encryption should be able to resist all kinds of known attacks and some security analyses have been performed on the proposed image encryption scheme.

3.2.1. Key Space. The key space of a good image encryption algorithm should be sufficiently large to make brute-force attack infeasible. The key space of the proposed method is much larger than those of previous methods because system parameters, fractional derivative, and initial conditions of drive system (12) and diagonal elements of scaling matrix k are all cipher key ones; moreover, the mismatch parameters $\Delta\alpha$, $\Delta\beta$, and $\Delta\gamma$ of drive system (12), time point t_1, time interval t_2, and positive integer l are all also secret keys. So this is enough to resist all kinds of brute-force attacks.

3.2.2. Key Sensitivity. A good encryption scheme should be sensitive to cipher keys in process of both enciphering and deciphering. Namely, when an image is encrypted, tiny change of keys should receive two completely different cipher images and, when an image is decrypted, tiny change of keys can cause the failure of deciphering.

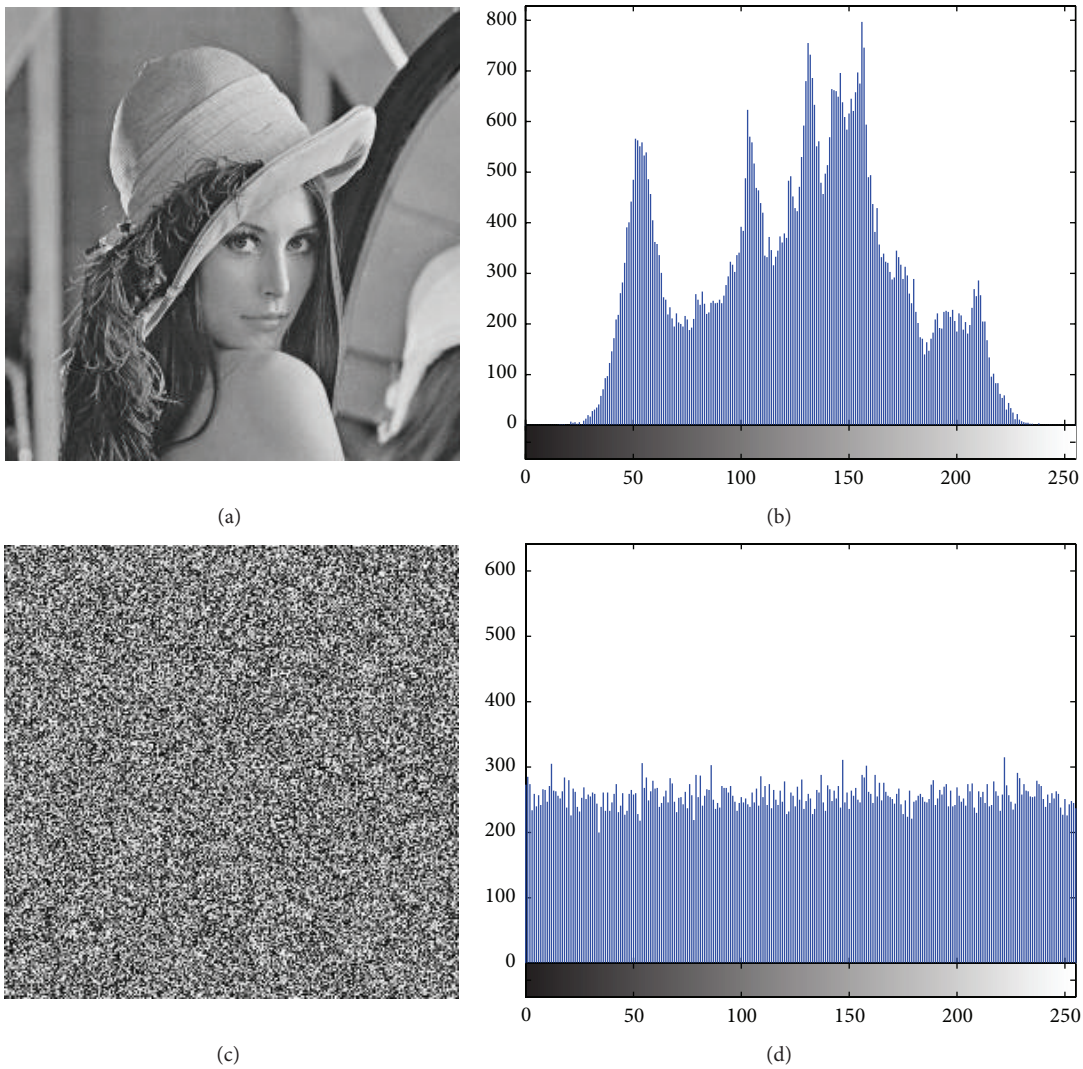

Figure 5: The encrypted results for Lena image: (a) plain Lena image; (b) histogram of Lena image; (c) cipher image; (d) histogram of cipher image.

(1) *Key Sensitivity in Encryption*. The following key sensitivity tests in encryption have been performed based on the 256 × 256 gray Lena image.

Test 1. One of the initial conditions of the drive system (12) is changed a bit; here, we let the first initial condition of system (12) be changed, using $x_1(0) = x_1(0) + 10^{-4}$.

Test 2. One of the system parameters of the drive system (12) is changed slightly; here, we alter the second parameter, using $\beta = \beta + 10^{-4}$.

Test 3. One of the fractional derivatives of the drive system (12) is changed, using $q_1 = q_1 + 0.01$.

Test 4. One element of the scaling matrix is altered, using $k_1 = k_1 + 1$.

Table 1: Percentage difference between cipher images.

	Test 1	Test 2	Test 3	Test 4
Two cipher images	99.56%	99.60%	99.59%	99.51%

The differences of the two cipher images for the four tests are given in Table 1. From the table, it can be concluded that the proposed method is very sensitive to the key; a small change of the key will generate a different decryption result and one cannot get the correct plain image.

(2) *Key Sensitivity in Decryption.* In the encryption scheme, small changes to key can lead to completely incorrect image. For the image of gray Lena shown in Figure 5(a), the decryption result with right key is shown in Figure 6(a) and the incorrect decrypted image is shown in Figure 6(b) when the

Table 2: The comparison of NPCR and UACI between proposed method and literature [14].

(m, n)	NPCR		UACI	
	Our method	Literature [14]	Our method	Literature [14]
(1, 2)	0.0016	0.0002	0.0004	0.00004
(2, 2)	0.1260	0.0110	0.0440	0.0027
(2, 3)	0.4697	0.0173	0.1628	0.0046
(3, 2)	0.8840	0.4388	0.3006	0.1195
(3, 3)	0.9866	0.5662	0.3326	0.1554
(4, 4)	0.9959	0.9899	0.3358	0.3109
(6, 4)	0.9961	0.9961	0.3351	0.3346

Table 3: The comparison of correlation coefficients between two adjacent pixels.

	Gray Lena image	Encrypted image with our method	Encrypted image in literature [14]	Random image
Horizontal	0.965	0.002952	0.002453	0.001562
Vertical	0.941	−0.001829	0.004864	0.005962
Diagonal	0.915	0.001236	0.007525	0.004006

value of x_0 has tiny change (10^{-14}). That is, tiny deviation of decryption key can lead to completely meaningless image.

3.2.3. Differential Attack. One of the security requirements of an effective image encryption scheme is its ability to resist differential attacks. To measure the influence of one-pixel change on the cipher image, two common quantitative measures are adopted.

NPCR (number of pixels change rate);

$$\mathrm{NPCR} = \frac{\sum_{ij} D(i,j)}{M \times N} \times 100\% \tag{30}$$

UACI (unified average changing intensity):

$$\mathrm{UACI} = \frac{1}{M \times N} \sum_{ij} \frac{\left|C_1(i,j) - C_2(i,j)\right|}{255} \times 100\%, \tag{31}$$

where C_1 and C_2 are the pixel value matrices of two different cipher images, respectively; D is the change of the corresponding pixel value, which is defined as

$$D(i,j) = \begin{cases} 0 & C_1(i,j) = C_2(i,j) \\ 1 & C_1(i,j) \neq C_2(i,j). \end{cases} \tag{32}$$

Next, two plain images are considered: one is the original image shown in Figure 5(a); the other is a changed image that adds 1 to the pixel value in the lower right corner of original image. When we encrypt the two plain images with the same encryption key, we can obtain two different cipher images C_1 and C_2. Several comparisons of NPCR and UACI between our method and literature [14] with different values of m and n are given in Table 2. Compared with the results of literature [14], we can achieve a much more better performance NPCR > 0.996 and UACI > 0.334 with $m = n = 4$, which can be obtained with $m = 6$ in literature [14].

3.2.4. Statistical Analysis. To test the correlation between two adjacent pixels, the following procedures are carried out. The correction coefficients r_{xy} of two horizontally, vertically, and diagonally adjacent pixels in the plain image and the cipher image are calculated according to the following formulas:

$$r_{xy} = \frac{E\left((x - E(x))\left(y - E(y)\right)\right)}{\sqrt{D(x)}\sqrt{D(y)}},$$
$$E(x) = \frac{1}{S}\sum_{i=1}^{S} x_i, \tag{33}$$
$$D(x) = \frac{1}{S}\sum_{i=1}^{S}\left[x_i - E(x)\right]^2,$$

where x and y are pixel values of two adjacent pixels in the image, $E(x)$ is the mean value of x, and $D(x)$ is the variance of x, $S = M \times N/2$.

Here, we use the 256×256 gray Lena image, encrypted image with our method, encrypted image in literature [14], and random image for simulation. The results are given in Table 3.

Meanwhile, we randomly select 2000 pairs of two horizontally adjacent pixels from the Lena image. The correlation distribution of the pixels in the plain image and the cipher image is illustrated in Figure 7. Both the correlation coefficients and the figures justify that neighboring pixels of the plain image can be decorrelated by the proposed cryptosystem effectively. Therefore, the proposed algorithm has high security against statistical attacks.

4. Conclusions

In this paper, for the first time, an OPCL coupling scheme is utilized to achieve the MPS between two different fractional-order dynamical systems in the presence of mismatch. Based on the stability theory of fractional-order system, the MPS

(a) (b)

Figure 6: The decrypted results for Lena image: (a) decrypted image with correct key; (b) decrypted image with wrong key.

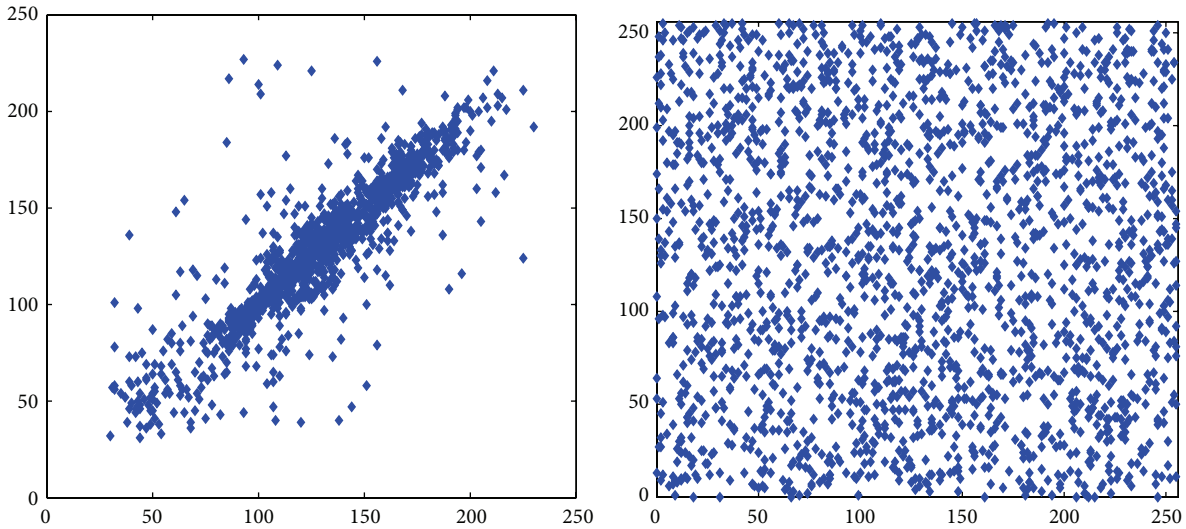

(a) (b)

Figure 7: Correlation analysis of two horizontally adjacent pixels in (a) the plain Lena image and (b) the cipher image obtained by the proposed scheme.

of two incommensurate or commensurate fractional-order systems can be achieved. Both numerical simulations and computer graphics show that the developed coupling scheme works well. Apparently, the proposed method possesses generality and is still appropriate for the case of MPS between two fractional-order systems without parameter mismatch. Meanwhile, because the complete synchronization, antisynchronization, and projective synchronization are all included in modified projective synchronization, our results contain and extend most of the existing works.

In image encryption application, we adopt the data from the MPS to encrypt the image. Experimental results and security analysis show that the algorithm can be easily implemented and its encryption effect is satisfactory. Moreover, the algorithm possesses high security in terms of the resistance to exhaustive attack, statistical attack, and differential attack. This scheme is particularly suitable for Internet image encryption and transmission applications.

Conflict of Interests

The authors declare that there is no conflict of interests regarding the publication of this paper.

Acknowledgments

This research was supported by the National Natural Science Foundation of China (Grant nos. 60872040 and 61104074), the Fundamental Research Funds for the Central Universities (Grant nos. N100604007, N110417004, N110417005, and N110617001), and the Ph.D. Start-up Foundation of Liaoning Province, China (Grant nos. 20111001 and 20100471462).

References

[1] I. Grigorenko and E. Grigorenko, "Chaotic dynamics of the fractional Lorenz system," *Physical Review Letters*, vol. 91, Article ID 034101, 2003.

[2] W. Deng and C. Li, "Chaos synchronization of the fractional Lü system," *Physica A*, vol. 353, pp. 61–72, 2005.

[3] C. Li and G. Chen, "Chaos and hyperchaos in the fractional-order Rössler equations," *Physica A*, vol. 341, pp. 55–61, 2004.

[4] J. Lu, "Chaotic dynamics and synchronization of fractional-order Arneodo's systems," *Chaos, Solitons & Fractals*, vol. 26, no. 4, pp. 1125–1133, 2005.

[5] R. Zhang and S. Yang, "Adaptive synchronization of fractional-order chaotic systems via a single driving variable," *Nonlinear Dynamics*, vol. 66, no. 4, pp. 831–837, 2011.

[6] J. G. Lu, "Nonlinear observer design to synchronize fractional-order chaotic systems via a scalar transmitted signal," *Physica A*, vol. 359, pp. 107–118, 2006.

[7] D. Chen, Y. Liu, X. Ma, and R. Zhang, "Control of a class of fractional-order chaotic systems via sliding mode," *Nonlinear Dynamics*, vol. 67, no. 1, pp. 893–901, 2012.

[8] S. Li and Z. Ge, "Generalized synchronization of chaotic systems with different orders by fuzzy logic constant controller," *Expert Systems with Applications*, vol. 38, no. 3, pp. 2302–2310, 2011.

[9] E. Jackson and I. Grosu, "An open-plus-closed-loop (OPCL) control of complex dynamic systems," *Physica D*, vol. 85, no. 1-2, pp. 1–9, 1995.

[10] I. Grosu, E. Padmanaban, P. K. Roy, and S. K. Dana, "Designing coupling for synchronization and amplification of chaos," *Physical Review Letters*, vol. 100, Article ID 234102, 2008.

[11] K. S. Sudheer and M. Sabir, "Modified function projective synchronization of hyperchaotic systems through open-plus-closed-loop coupling," *Physics Letters A*, vol. 374, no. 19-20, pp. 2017–2023, 2010.

[12] X. Wang, R. Liu, and N. Zhang, "Function projective synchronization of fractional-order hyperchaotic system based on open-plus-closed-looping," *Communications in Theoretical Physics*, vol. 55, no. 4, pp. 617–621, 2011.

[13] J. Wang, Z. Li, and Q. Ma, "Inverse synchronization of coupled fractional-order systems through open-plus-closed-loop control," *Pramana*, vol. 76, no. 3, pp. 385–396, 2011.

[14] S. G. Lian, J. S. Sun, and Z. Q. Wang, "A block cipher based on a suitable use of the chaotic standard map," *Chaos, Solitons & Fractals*, vol. 26, no. 1, pp. 117–129, 2005.

[15] M. Caputo, "Linear models of dissipation whose Q is almost frequency independent-II," *Geophysical Journal of the Royal Astronomical Society*, vol. 13, no. 5, pp. 529–539, 1967.

[16] M. S. Tavazoei and M. Haeri, "Chaotic attractors in incommensurate fractional order systems," *Physica D*, vol. 237, no. 20, pp. 2628–2637, 2008.

[17] W. Deng, C. Li, and J. Lü, "Stability analysis of linear fractional differential system with multiple time delays," *Nonlinear Dynamics*, vol. 48, no. 4, pp. 409–416, 2007.

[18] D. Matignon, "Stability results for fractional differential equations with applications to control processing," *Computational Engineering in Systems Applications*, vol. 2, pp. 963–968, 1996.

[19] K. Diethelm, N. Ford, and A. Freed, "A predictor-corrector approach for the numerical solution of fractional differential equations," *Nonlinear Dynamics*, vol. 29, no. 1–4, pp. 3–22, 2002.

Hindawi Publishing Corporation
Mathematical Problems in Engineering
Volume 2014, Article ID 252393, 18 pages
http://dx.doi.org/10.1155/2014/252393

Research Article

Finite Series Representation of the Inverse Mittag-Leffler Function

John W. Hanneken and B. N. Narahari Achar

Department of Physics, University of Memphis, Memphis, TN 38152, USA

Correspondence should be addressed to John W. Hanneken; jhannekn@memphis.edu

Received 11 December 2013; Accepted 5 February 2014; Published 25 March 2014

Academic Editor: J. A. Tenreiro Machado

The inverse Mittag-Leffler function $E_{\alpha,\beta}^{-1}(z)$ is valuable in determining the value of the argument of a Mittag-Leffler function given the value of the function and it is not an easy problem. A finite series representation of the inverse Mittag-Leffler function has been found for a range of the parameters α and β; specifically, $0 < \alpha < 1/2$ for $\beta = 1$ and for $\beta = 2$. This finite series representation of the inverse Mittag-Leffler function greatly expedites its evaluation and has been illustrated with a number of examples. This represents a significant advancement in the understanding of Mittag-Leffler functions.

1. Introduction

The Mittag-Leffler function $E_{\alpha,\beta}(z)$ is defined by the power series [1]

$$E_{\alpha,\beta}(z) = \sum_{k=0}^{\infty} \frac{z^k}{\Gamma(\alpha k + \beta)} \quad z \in \mathbb{C}. \tag{1}$$

While the argument z and the parameters α and β can in general be complex provided $\operatorname{Re} \alpha > 0$, in this work z, α, and β will be restricted to those values most commonly found in physical problems; namely, the argument z will be restricted to real numbers and α and β will be restricted to positive real numbers. The Mittag-Leffler function is a generalization of the exponential function and arises frequently in the solutions of differential and/or integral equations of fractional (noninteger) order in much the same way as the exponential function appears in solutions of differential equations of integer order. Thus, Mittag-Leffler functions play a fundamental role in the theory of fractional differential equations. Consequently, books devoted to the subject of fractional differential equations (i.e., Podlubny [2], Kilbas et al. [3], and Diethelm [4]) all contain sections on the Mittag-Leffler functions. In addition to their inherent mathematical interest, Mittag-Leffler functions are also important in theoretical and applied physics and all the sciences (i.e., Hilfer [5], Mainardi [6], and Magin [7]). The works of Mainardi and Gorenflo [8], Magin [9], Berberan-Santos [10], Gupta and Debnath [11], and Haubold et al. [12] are a few of the numerous articles also worth noting.

The inverse Mittag-Leffler function $E_{\alpha,\beta}^{-1}(z)$ is defined as the solution of (2) [13]

$$E_{\alpha,\beta}^{-1}\left[E_{\alpha,\beta}(z)\right] = z. \tag{2}$$

Despite the inherent importance of Mittag-Leffler functions in fractional differential equations, with the wealth of analytical information about $E_{\alpha,\beta}(z)$, the inverse $E_{\alpha,\beta}^{-1}(z)$ has been largely unexplored. The one exception is the excellent work of Hilfer and Seybold [13] who have determined its principal branch numerically.

The power series representation of any Mittag-Leffler function can be inverted yielding an infinite series for the inverse. However, these infinite series are slow to converge and terminating the series always introduces error which is hard to evaluate. This present work identifies regions in the domain of α and β where the inverse of the Mittag-Leffler function can be written as a finite series. This represents the first time the inverse Mittag-Leffler function has been written as a finite series as opposed to an infinite series which greatly

expedites its evaluation. Before deriving these expressions for the inverse Mittag-Leffler function, a brief review of the theory of power series and their inverses is in order.

2. Theory

Consider the convergent series which expresses the function $w = f(z)$ in terms of powers of $(z - z_o)$ with the corresponding coefficients a_k given by

$$w = f(z) = \sum_{k=0}^{\infty} a_k (z - z_o)^k = a_o + a_1 (z - z_o) + a_2 (z - z_o)^2 + \cdots . \tag{3}$$

The inversion of the function $f(z)$ requires only the sole assumption that $a_1 \neq 0$. That is, there exists one and only one function which represents the inverse of the $f(z)$, $z - z_o = f^{-1}(w)$, which is expressible by a convergent power series of the form [14]

$$z - z_o = f^{-1}(w) = \sum_{k=1}^{\infty} b_k (w - a_o)^k = b_1 (w - a_o) + b_2 (w - a_o)^2 + \cdots . \tag{4}$$

The process of finding the series expansion for $f^{-1}(w)$ is called reversion of the series. The coefficients b_k can be determined in terms of the coefficients a_k by substituting (3) into (4) and equating coefficients of like powers of $(z - z_o)^k$ on both sides of the equation yielding

$$b_1 = \frac{1}{a_1}, \qquad b_3 = \frac{1}{a_1^5}\left(2a_2^2 - a_1 a_3\right),$$
$$b_2 = -\frac{a_2}{a_1^3}, \qquad b_4 = \frac{1}{a_1^7}\left(5a_1 a_2 a_3 - a_1^2 a_4 - 5a_2^3\right). \tag{5}$$

The coefficients $b_1, b_2, b_3, \ldots, b_7$ can be found in the literature [15–17]. An explicit expression for the coefficients b_k can be derived using the Lagrange inversion theorem. If $f(z)$ is analytic at $z = z_o$ and $f'(z_o) \neq 0$, then the inverse of $f(z)$ exists and is analytic about $f(z_o)$. Furthermore, if $f(z) = w$, the Lagrange inversion theorem gives the Taylor series expansion of the inverse function $f^{-1}(w)$ as [15]

$$f^{-1}(w) = z - z_o = \sum_{k=1}^{\infty} \frac{(w - a_o)^k}{k!} \frac{d^{k-1}}{dz^{k-1}} \left\{ \frac{(z - z_o)^k}{[f(z) - a_o]^k} \right\}_{z=z_o} . \tag{6}$$

The coefficients b_k are determined by comparing (6) and (4) yielding

$$b_k = \frac{1}{k!} \frac{d^{k-1}}{dz^{k-1}} \left\{ \frac{(z - z_o)^k}{[f(z) - a_o]^k} \right\}_{z=z_o} . \tag{7}$$

Substituting $f(z) - a_o$ from (3) yields

$$b_k = \frac{1}{k!} \frac{d^{k-1}}{dz^{k-1}} \left\{ \left[a_1 + a_2 (z - z_o) + a_3 (z - z_o)^2 + \cdots \right]^{-k} \right\}_{z=z_o} . \tag{8}$$

Factoring out a_1^k in (8) and defining $x = z - z_o$ yields

$$b_k = \frac{1}{a_1^k k!} \frac{d^{k-1}}{dz^{k-1}} \times \left\{ \left[1 + \left(\frac{a_2}{a_1}\right) x + \left(\frac{a_3}{a_1}\right) x^2 + \left(\frac{a_4}{a_1}\right) x^3 + \cdots \right]^{-k} \right\}_{x=0} . \tag{9}$$

Using the multinomial expansion and performing the required differentiation yields the desired result [18]

$$b_k = \frac{1}{k a_1^k} \times \sum_{s,t,u,\ldots} (-1)^{s+t+u+\cdots} \frac{(k)(k+1)\cdots(k-1+s+t+u\cdots)}{s!t!u!\cdots} \times \left(\frac{a_2}{a_1}\right)^s \left(\frac{a_3}{a_1}\right)^t \left(\frac{a_3}{a_1}\right)^u \cdots , \tag{10}$$

where $s + 2t + 3u + \cdots = k - 1$ and the numbers $s, t, u, \ldots$ are nonnegative integers and the summation extends over all partitions of $k - 1$. For example, b_5 contains 5 terms since the Diophantine equation $s + 2t + 3u + 4v = 4$ has 5 integer solutions or partitions. The number of partitions for $k = 11$ is 42; for $k = 51$ there are 204226 partitions and for $k = 101$ the number of partitions is 190569292. Consequently, the explicit tabulation of the full expression for the coefficients b_k rapidly becomes a rather tedious task. Nevertheless, the coefficients $b_1, b_2, b_3, \ldots, b_{14}$ are given in Table 1. An equivalent expression for the general term b_k in the reversion of series is given in a different form by McMahon [19].

By an appropriate change of variables it is always possible to write the power series in a form which results in simplified expressions for the coefficients in the reversed power series. Equation (3) can be rewritten as

$$\frac{w - a_o}{a_1} = (z - z_o)\left[1 + \frac{a_2}{a_1}(z - z_o) + \frac{a_3}{a_1}(z - z_o)^2 + \cdots \right]. \tag{11}$$

Defining the new variables $W = (w - a_o)/a_1$, $A_1 = -a_2/a_1$, $A_2 = -a_3/a_1$, and so forth, (11) becomes

$$W = (z - z_o)\left[1 - \sum_{k=1}^{\infty} A_k (z - z_o)^k \right] \tag{12}$$

and the reversed series is given by

$$(z - z_o) = W\left[1 - \sum_{k=1}^{\infty} B_k W^k \right]. \tag{13}$$

Table 1: Coefficients of the inverse function for a power series.

k	Coefficient b_k
1	$\frac{1}{a_1}$
2	$-\frac{a_2}{a_1^3}$
3	$\frac{1}{a_1^5}\left(2a_2^2 - a_1a_3\right)$
4	$\frac{1}{a_1^7}\left(-5a_2^3 + 5a_1a_2a_3 - a_1^2a_4\right)$
5	$\frac{1}{a_1^9}\left(14a_2^4 - 21a_1a_2^2a_3 + 3a_1^2a_3^2 + 6a_1^2a_2a_4 - a_1^3a_5\right)$
6	$\frac{1}{a_1^{11}}\left(-42a_2^5 + 84a_1a_2^3a_3 - 28a_1^2a_2a_3^2 - 28a_1^2a_2^2a_4 + 7a_1^3a_3a_4 + 7a_1^3a_2a_5 - a_1^4a_6\right)$
7	$\frac{1}{a_1^{13}}(132a_2^6 - 330a_1a_2^4a_3 + 180a_1^2a_2^2a_3^2 - 12a_1^3a_3^3 + 120a_1^2a_2^3a_4 - 72a_1^3a_2a_3a_4 + 4a_1^4a_4^2 - 36a_1^3a_2^2a_5 + 8a_1^4a_3a_5 + 8a_1^4a_2a_6 - a_1^5a_7)$
8	$\frac{1}{a_1^{15}}(-429a_2^7 + 1287a_1a_2^5a_3 - 990a_1^2a_2^3a_3^2 + 165a_1^3a_2a_3^3 - 495a_1^2a_2^4a_4 + 495a_1^3a_2^2a_3a_4 - 45a_1^4a_3^2a_4 - 45a_1^4a_2a_4^2 + 165a_1^3a_2^3a_5$ $-90a_1^4a_2a_3a_5 + 9a_1^5a_4a_5 - 45a_1^4a_2^2a_6 + 9a_1^5a_3a_6 + 9a_1^5a_2a_7 - a_1^6a_8)$
9	$\frac{1}{a_1^{17}}(1430a_2^8 - 5005a_1a_2^6a_3 + 5005a_1^2a_2^4a_3^2 - 1430a_1^3a_2^2a_3^3 + 55a_1^4a_3^4 + 2002a_1^2a_2^5a_4 - 2860a_1^3a_2^3a_3a_4 + 660a_1^4a_2a_3^2a_4 + 330a_1^4a_2^2a_4^2$ $-55a_1^5a_3a_4^2 - 715a_1^3a_2^4a_5 + 660a_1^4a_2^2a_3a_5 - 55a_1^5a_3^2a_5 - 110a_1^5a_2a_4a_5 + 5a_1^6a_5^2 + 220a_1^4a_2^3a_6 - 110a_1^5a_2a_3a_6 + 10a_1^6a_4a_6$ $-55a_1^5a_2^2a_7 + 10a_1^6a_3a_7 + 10a_1^6a_2a_8 - a_1^7a_9)$
10	$\frac{1}{a_1^{19}}(-4862a_2^9 + 19448a_1a_2^7a_3 - 24024a_1^2a_2^5a_3^2 + 10010a_1^3a_2^3a_3^3 - 1001a_1^4a_2a_3^4 - 8008a_1^2a_2^6a_4 + 15015a_1^3a_2^4a_3a_4 - 6006a_1^4a_2^2a_3^2a_4$ $+286a_1^5a_3^3a_4 - 2002a_1^4a_2^3a_4^2 + 858a_1^5a_2a_3a_4^2 - 22a_1^6a_4^3 + 3003a_1^3a_2^5a_5 - 4004a_1^4a_2^3a_3a_5 + 858a_1^5a_2a_3^2a_5 + 858a_1^5a_2^2a_4a_5$ $-132a_1^6a_3a_4a_5 - 66a_1^6a_2a_5^2 - 1001a_1^4a_2^4a_6 + 858a_1^5a_2^2a_3a_6 - 66a_1^6a_3^2a_6 - 132a_1^6a_2a_4a_6 + 11a_1^7a_5a_6 + 286a_1^5a_2^3a_7$ $-132a_1^6a_2a_3a_7 + 11a_1^7a_4a_7 - 66a_1^6a_2^2a_8 + 11a_1^7a_3a_8 + 11a_1^7a_2a_9 - a_1^8a_{10})$
11	$\frac{1}{a_1^{21}}(16796a_2^{10} - 75582a_1a_2^8a_3 + 111384a_1^2a_2^6a_3^2 - 61880a_1^3a_2^4a_3^3 + 10920a_1^4a_2^2a_3^4 - 273a_1^5a_3^5 + 31824a_1^2a_2^7a_4 - 74256a_1^3a_2^5a_3a_4$ $+43680a_1^4a_2^3a_3^2a_4 - 5460a_1^5a_2a_3^3a_4 + 10920a_1^4a_2^4a_4^2 + -8190a_1^5a_2^2a_3a_4^2 + 546a_1^6a_3^2a_4^2 + 364a_1^6a_2a_4^3 - 12376a_1^3a_2^6a_5$ $+21840a_1^4a_2^4a_3a_5 + -8190a_1^5a_2^2a_3^2a_5 + 364a_1^6a_3^3a_5 - 5460a_1^5a_2^3a_4a_5 + 2184a_1^6a_2a_3a_4a_5 - 78a_1^7a_4^2a_5 + 546a_1^6a_2^2a_5^2$ $-78a_1^7a_3a_5^2 + 4368a_1^4a_2^5a_6 - 5460a_1^5a_2^3a_3a_6 + 1092a_1^6a_2a_3^2a_6 + 1092a_1^6a_2^2a_4a_6 - 156a_1^7a_3a_4a_6 - 156a_1^7a_2a_5a_6 + 6a_1^8a_6^2$ $-1365a_1^5a_2^4a_7 + 1092a_1^6a_2^2a_3a_7 + -78a_1^7a_3^2a_7 - 156a_1^7a_2a_4a_7 + 12a_1^8a_5a_7 + 364a_1^6a_2^3a_8 - 156a_1^7a_2a_3a_8 + 12a_1^8a_4a_8$ $+ - 78a_1^7a_2^2a_9 + 12a_1^8a_3a_9 + 12a_1^8a_2a_{10} - a_1^9a_{11})$
12	$\frac{1}{a_1^{23}}(-58786a_2^{11} + 293930a_1a_2^9a_3 - 503880a_1^2a_2^7a_3^2 + 352716a_1^3a_2^5a_3^3 - 92820a_1^4a_2^3a_3^4 + 6188a_1^5a_2a_3^5 + -125970a_1^2a_2^8a_4$ $+352716a_1^3a_2^6a_3a_4 - 278460a_1^4a_2^4a_3^2a_4 + 61880a_1^5a_2^2a_3^3a_4 - 1820a_1^6a_3^4a_4 + -55692a_1^4a_2^5a_4^2 + 61880a_1^5a_2^3a_3a_4^2$ $-10920a_1^6a_2a_3^2a_4^2 - 3640a_1^6a_2^2a_4^3 + 455a_1^7a_3a_4^3 + 50388a_1^3a_2^7a_5 - 111384a_1^4a_2^5a_3a_5 + 61880a_1^5a_2^3a_3^2a_5 - 7280a_1^6a_2a_3^3a_5$ $+30940a_1^5a_2^4a_4a_5 + -21840a_1^6a_2^2a_3a_4a_5 + 1365a_1^7a_3^2a_4a_5 + 1365a_1^7a_2a_4^2a_5 - 3640a_1^6a_2^3a_5^2 + 1365a_1^7a_2a_3a_5^2 + -91a_1^8a_4a_5^2$ $-18564a_1^4a_2^6a_6 + 30940a_1^5a_2^4a_3a_6 - 10920a_1^6a_2^2a_3^2a_6 + 455a_1^7a_3^3a_6 + -7280a_1^6a_2^3a_4a_6 + 2730a_1^7a_2a_3a_4a_6 - 91a_1^8a_4^2a_6$ $+1365a_1^7a_2^2a_5a_6 - 182a_1^8a_3a_5a_6 + -91a_1^8a_2a_6^2 + 6188a_1^5a_2^5a_7 - 7280a_1^6a_2^3a_3a_7 + 1365a_1^7a_2a_3^2a_7 + 1365a_1^7a_2^2a_4a_7$ $+ - 182a_1^8a_3a_4a_7 - 182a_1^8a_2a_5a_7 + 13a_1^9a_6a_7 - 1820a_1^6a_2^4a_8 + 1365a_1^7a_2^2a_3a_8 - 91a_1^8a_3^2a_8 + -182a_1^8a_2a_4a_8 + 13a_1^9a_5a_8$ $+455a_1^7a_2^3a_9 - 182a_1^8a_2a_3a_9 + 13a_1^9a_4a_9 - 91a_1^8a_2^2a_{10} + 13a_1^9a_3a_{10} + 13a_1^9a_2a_{11} - a_1^{10}a_{12})$

Table 1: Continued.

k	Coefficient b_k
13	$\frac{1}{a_1^{25}}(208012a_2^{12} - 1144066a_1a_2^{10}a_3 + 2238390a_1^2a_2^8a_3^2 - 1899240a_1^3a_2^6a_3^3 + 678300a_1^4a_2^4a_3^4 + -81396a_1^5a_2^2a_3^5 + 1428a_1^6a_3^6$ $+497420a_1^2a_2^9a_4 - 1627920a_1^3a_2^7a_3a_4 + 1627920a_1^4a_2^5a_3^2a_4 + -542640a_1^5a_2^3a_3^3a_4 + 42840a_1^6a_2a_3^4a_4 + 271320a_1^4a_2^6a_4^2$ $-406980a_1^5a_2^4a_3a_4^2 + 128520a_1^6a_2^2a_3^2a_4^2 - 4760a_1^7a_3^3a_4^2 + 28560a_1^6a_2^3a_4^3 - 9520a_1^7a_2a_3a_4^3 + 140a_1^8a_4^4 + -203490a_1^3a_2^8a_5$ $+542640a_1^4a_2^6a_3a_5 - 406980a_1^5a_2^4a_3^2a_5 + 85680a_1^6a_2^2a_3^3a_5 - 2380a_1^7a_3^4a_5 + -162792a_1^5a_2^5a_4a_5 + 171360a_1^6a_2^3a_3a_4a_5$ $-28560a_1^7a_2a_3^2a_4a_5 - 14280a_1^7a_2^2a_4^2a_5 + 1680a_1^8a_3a_4^2a_5 + 21420a_1^6a_2^4a_5^2 - 14280a_1^7a_2^2a_3a_5^2 + 840a_1^8a_3^2a_5^2 + 1680a_1^8a_2a_4a_5^2$ $-35a_1^9a_5^3 + 77520a_1^4a_2^7a_6 - 162792a_1^5a_2^5a_3a_6 + 85680a_1^6a_2^3a_3^2a_6 - 9520a_1^7a_2a_3^3a_6 + 42840a_1^6a_2^4a_4a_6 + -28560a_1^7a_2^2a_3a_4a_6$ $+1680a_1^8a_3^2a_4a_6 + 1680a_1^8a_2a_4^2a_6 - 9520a_1^7a_2^3a_5a_6 + 3360a_1^8a_2a_3a_5a_6 + -210a_1^9a_4a_5a_6 + 840a_1^8a_2^2a_6^2 - 105a_1^9a_3a_6^2$ $-27132a_1^5a_2^6a_7 + 42840a_1^6a_2^4a_3a_7 - 14280a_1^7a_2^2a_3^2a_7 + 560a_1^8a_3^3a_7 - 9520a_1^7a_2^3a_4a_7 + 3360a_1^8a_2a_3a_4a_7 - 105a_1^9a_4^2a_7$ $+1680a_1^8a_2^2a_5a_7 - 210a_1^9a_3a_5a_7 + -210a_1^9a_2a_6a_7 + 7a_1^{10}a_7^2 + 8568a_1^6a_2^5a_8 - 9520a_1^7a_2^3a_3a_8 + 1680a_1^8a_2a_3^2a_8 + 1680a_1^8a_2^2a_4a_8$ $+ - 210a_1^9a_3a_4a_8 - 210a_1^9a_2a_5a_8 + 14a_1^{10}a_6a_8 - 2380a_1^7a_2^4a_9 + 1680a_1^8a_2^2a_3a_9 - 105a_1^9a_3^2a_9 + -210a_1^9a_2a_4a_9 + 14a_1^{10}a_5a_9$ $+560a_1^8a_2^3a_{10} - 210a_1^9a_2a_3a_{10} + 14a_1^{10}a_4a_{10} - 105a_1^9a_2^2a_{11} + 14a_1^{10}a_3a_{11} + 14a_1^{10}a_2a_{12} - a_1^{11}a_{13})$
14	$\frac{1}{a_1^{27}}(-742900a_2^{13} + 4457400a_1a_2^{11}a_3 - 9806280a_1^2a_2^9a_3^2 + 9806280a_1^3a_2^7a_3^3 - 4476780a_1^4a_2^5a_3^4 + 813960a_1^5a_2^3a_3^5 - 38760a_1^6a_2a_3^6$ $-1961256a_1^2a_2^{10}a_4 + 7354710a_1^3a_2^8a_3a_4 - 8953560a_1^4a_2^6a_3^2a_4 + 4069800a_1^5a_2^4a_3^3a_4 - 581400a_1^6a_2^2a_3^4a_4 + 11628a_1^7a_3^5a_4$ $-1279080a_1^4a_2^7a_4^2 + 2441880a_1^5a_2^5a_3a_4^2 - 1162800a_1^6a_2^3a_3^2a_4^2 + 116280a_1^7a_2a_3^3a_4^2 - 193800a_1^6a_2^4a_4^3 + 116280a_1^7a_2^2a_3a_4^3$ $+ - 6120a_1^8a_3^2a_4^3 - 3060a_1^8a_2a_4^4 + 817190a_1^3a_2^9a_5 - 2558160a_1^4a_2^7a_3a_5 + 2441880a_1^5a_2^5a_3^2a_5 + -775200a_1^6a_2^3a_3^3a_5$ $+58140a_1^7a_2a_3^4a_5 + 813960a_1^5a_2^6a_4a_5 - 1162800a_1^6a_2^4a_3a_4a_5 + 348840a_1^7a_2^2a_3^2a_4a_5 - 12240a_1^8a_3^3a_4a_5 + 116280a_1^7a_2^3a_4^2a_5$ $-36720a_1^8a_2a_3a_4^2a_5 + 680a_1^9a_4^3a_5 - 116280a_1^6a_2^5a_5^2 + 116280a_1^7a_2^3a_3a_5^2 - 18360a_1^8a_2a_3^2a_5^2 - 18360a_1^8a_2^2a_4a_5^2 + 2040a_1^9a_3a_4a_5^2$ $+680a_1^9a_2a_5^3 - 319770a_1^4a_2^8a_6 + 813960a_1^5a_2^6a_3a_6 - 581400a_1^6a_2^4a_3^2a_6 + 116280a_1^7a_2^2a_3^3a_6 - 3060a_1^8a_3^4a_6 - 232560a_1^6a_2^5a_4a_6$ $+232560a_1^7a_2^3a_3a_4a_6 + -36720a_1^8a_2a_3^2a_4a_6 - 18360a_1^8a_2^2a_4^2a_6 + 2040a_1^9a_3a_4^2a_6 + 58140a_1^7a_2^4a_5a_6 - 36720a_1^8a_2^2a_3a_5a_6$ $+2040a_1^9a_3^2a_5a_6 + 4080a_1^9a_2a_4a_5a_6 - 120a_1^{10}a_5^2a_6 - 6120a_1^8a_2^3a_6^2 + 2040a_1^9a_2a_3a_6^2 - 120a_1^{10}a_4a_6^2 + 116280a_1^5a_2^7a_7$ $-232560a_1^6a_2^5a_3a_7 + 116280a_1^7a_2^3a_3^2a_7 - 12240a_1^8a_2a_3^3a_7 + 58140a_1^7a_2^4a_4a_7 + -36720a_1^8a_2^2a_3a_4a_7 + 2040a_1^9a_3^2a_4a_7$ $+2040a_1^9a_2a_4^2a_7 - 12240a_1^8a_2^3a_5a_7 + 4080a_1^9a_2a_3a_5a_7 + -240a_1^{10}a_4a_5a_7 + 2040a_1^9a_2^2a_6a_7 - 240a_1^{10}a_3a_6a_7 - 120a_1^{10}a_2a_7^2$ $-38760a_1^6a_2^6a_8 + 58140a_1^7a_2^4a_3a_8 - 18360a_1^8a_2^2a_3^2a_8 + 680a_1^9a_3^3a_8 - 12240a_1^8a_2^3a_4a_8 + 4080a_1^9a_2a_3a_4a_8 + -120a_1^{10}a_4^2a_8$ $+2040a_1^9a_2^2a_5a_8 - 240a_1^{10}a_3a_5a_8 - 240a_1^{10}a_2a_6a_8 + 15a_1^{11}a_7a_8 + 11628a_1^7a_2^5a_9 + -12240a_1^8a_2^3a_3a_9 + 2040a_1^9a_2a_3^2a_9$ $+2040a_1^9a_2^2a_4a_9 - 240a_1^{10}a_3a_4a_9 - 240a_1^{10}a_2a_5a_9 + 15a_1^{11}a_6a_9 - 3060a_1^8a_2^4a_{10} + 2040a_1^9a_2^2a_3a_{10} - 120a_1^{10}a_3^2a_{10}$ $-240a_1^{10}a_2a_4a_{10} + 15a_1^{11}a_5a_{10} + 680a_1^9a_2^3a_{11} - 240a_1^{10}a_2a_3a_{11} + 15a_1^{11}a_4a_{11} - 120a_1^{10}a_2^2a_{12} + 15a_1^{11}a_3a_{12} + 15a_1^{11}a_2a_{13} - a_1^{12}a_{14})$

The resulting coefficients B_k for $k = 1, 2, 3$, and 4 are given by

$$\begin{aligned} -B_1 &= A_1, \\ -B_3 &= A_3 + 5A_1A_2 + 5A_1^3, \\ -B_2 &= A_2 + 2A_1^2, \\ -B_4 &= A_4 + 6A_1A_3 + 3A_2^2 + 21A_1^2A_2 + 14A_1^4. \end{aligned} \tag{14}$$

These can be shown to be equivalent to (5) by setting $-B_k = b_{k+1}a_1^{k+1}$ and $A_k = -a_{k+1}/a_1$. The coefficients B_k for $k = 1, 2, \ldots, 7$ can be found tabulated in [20], for $k = 1, 2, \ldots, 9$ in [21] and for $k = 1, 2, \ldots, 12$ they are tabulated in [22] with a different choice of the sign of B_k. Müller [23] has reported an alternative expression for B_k and some symmetry relations for the coefficients.

3. Application to Mittag-Leffler Functions

Many Mittag-Leffler functions can be represented in terms of elementary functions. For example,

$$E_{1,1}(-z) = \sum_{k=0}^{\infty} \frac{(-z)^k}{\Gamma(k+1)} = \operatorname{Exp}(-z)$$

$$E_{1/2,3}(-z) = \sum_{k=0}^{\infty} \frac{(-z)^k}{\Gamma(k/2+3)} = \frac{\operatorname{Exp}\left(z^2\right)\operatorname{erfc}(z) - 1}{z^4} - \frac{1}{z^2} + \frac{4}{3z\sqrt{\pi}} + \frac{2}{z^3\sqrt{\pi}}. \tag{15}$$

Applying (10) from the above theory to these functions whose values can be determined as accurately as possible using their alternative representations yields

$$-z = E_{1,1}^{-1}(w) = (w-1) - \frac{1}{2}(w-1)^2 + \frac{1}{3}(w-1)^3 - \frac{1}{4}(w-1)^4 + \cdots = \sum_{k=1}^{\infty} \frac{(-1)^{k+1}(w-1)^k}{k}, \tag{16}$$

$$-z = E_{1/2,3}^{-1}(w) = \frac{15\sqrt{\pi}}{8}\left(w - \frac{1}{2}\right) - \frac{1125\pi^{3/2}}{1024}\left(w - \frac{1}{2}\right)^2 + \frac{3375\pi^{3/2}(175\pi - 256)}{458752}\left(w - \frac{1}{2}\right)^3 + \cdots. \tag{17}$$

A few observations are in order. Equations (16) and (17) are typical of the inverse of most infinite series; that is, they are also infinite series and do not converge rapidly. This can be easily illustrated by the following examples. For $w = \operatorname{Exp}(-1)$, (16) should yield $-z = -1$ (equivalently $z = 1$). However, (16) requires 20 terms before the value of z is as large as 0.99999 (5 nines), 44 terms for 10 nines, 68 terms for 15 nines, and 92 terms for 20 nines. Whereas for $w = \operatorname{Exp}(-10)$, where (16) should yield $z = 10$, 156995 terms are required before the value of z is as large as 9.9999 (5 nines), 391895 terms for 10 nines, 635259 for 15 nines, and 881815 terms for 20 nines. Similarly, for $w = \operatorname{Exp}(-15)$ where (16) should yield $z = 15$, 16730862 terms are required before the value of z is as large as 14.999 (3 nines), 51041531 terms for 8 nines, 87009540 terms for 13 nines, and 123532970 terms for 18 nines. For $w = \operatorname{Exp}(-z)$, as z becomes large (or equivalently $w \to 0$), the number of terms in (16) required to yield a value accurate to a given number of significant digits becomes astronomically large.

A similar behavior is exhibited in (17). For $w = 0.30821552131\ldots$, (17) should yield $z = 1$. To obtain a value of z as large as 0.99999 (5 nines), 12 terms are required, 24 terms for 10 nines, 36 terms for 15 nines, and 48 terms for 20 nines. For $w = 0.0662592710\ldots$, (17) should yield $z = 10$, but 81 terms are required to obtain a value of z as large as 9.9999 (5 nines), 162 for 10 nines, 243 terms for 15 nines, and 324 terms for 20 nines. For $w = 0.007423646216\ldots$, (17) should

Table 2: Coefficients b_k for the inverse Mittag-Leffler function $-z = E_{1/7,1}^{-1}(w)$.

k	b_k
1	+0.93543756289254634824
2	+0.90975389394768139194
3	+0.90540301580659885103
4	+0.90454074680764978103
5	+0.90437439055401830557
6	+0.90434827833630659461
7	+0.90434699795298307168
8	+0.90434836056866111562
9	+0.90434917779666970118
10	+0.90434948952806441367
11	+0.90434957941529405394
12	+0.90434959664285150118
13	+0.90434959619870743701
14	+0.90434959373645610938
15	+0.90434959223258048967
16	+0.90434959159682667227
17	+0.90434959139076386922
18	+0.90434959134523887081
19	+0.90434959134495719874
20	+0.90434959135163221718
21	+0.90434959135628153678
22	+0.90434959135847703425
23	+0.90434959135928171696
24	+0.90434959135949807367
25	+0.90434959135952104631
26	+0.90434959135950171101
27	+0.90434959135948382131
28	+0.90434959135947403392
29	+0.90434959135946990785
30	+0.90434959135946855244
31	+0.90434959135946826616
32	+0.90434959135946829135
33	+0.90434959135946836127
34	+0.90434959135946840959
35	+0.90434959135946843362
36	+0.90434959135946844315
37	+0.90434959135946844604
38	+0.90434959135946844650
39	+0.90434959135946844632
40	+0.90434959135946844609
41	+0.90434959135946844595
42	+0.90434959135946844588
43	+0.90434959135946844585
44	+0.90434959135946844585
45	+0.90434959135946844584
46	+0.90434959135946844585

Table 3: Number of terms required in the finite representation of $E^{-1}_{\alpha,\beta}(z)$ for 20-significant-digit accuracy.

α	$\beta = 1$	$\beta = 2$
1/100	11	9
1/10	32	25
1/9	35	27
1/8	40	28
1/7	46	33
1/6	52	38
1/5	64	46
1/4	92	63
1/3	156	91
1/2	562	262
4/7	1051	429
3/5	1469	548

Table 4: Index of Mittag-Leffler inverse examples.

α	$\beta = 1$	$\beta = 2$
1/3	Equation (22) and Table 5	Equation (29) and Table 12
1/4	Equation (23) and Table 6	Equation (30) and Table 13
1/5	Equation (24) and Table 7	Equation (31) and Table 14
1/6	Equation (25) and Table 8	Equation (32) and Table 15
1/7	Equation (19) and Table 2	Equation (33) and Table 16
1/8	Equation (26) and Table 9	Equation (34) and Table 17
1/9	Equation (27) and Table 10	Equation (35) and Table 18
1/10	Equation (28) and Table 11	Equation (36) and Table 19

yield $z = 100$, but 770 terms are required to obtain a value of z as large as 99.999 (5 nines) and 1540 terms for 10 nines. There is, however, one big difference between (16) and (17). Equation (16) is one of the few inverses of a Mittag-Leffler function, where the coefficients b_k in the inverse given in (10) and itemized in Table 1 for $b_1 - b_{14}$ simplify to a tractable expression; in this case $b_k = (-1)^{k+1}/k$. The mathematical manipulations required to obtain the coefficients b_k in (17) using (10) become algebraically intensive as k becomes large. Whereas b_{14} given in Table 1 contains 101 terms, b_{1000} contains more than 2.4×10^{31} terms. Consequently, although the infinite series given in (17) correctly represents the inverse Mittag-Leffler function, it is impractical to use for anything other than small z where only a reasonable number of terms are needed for the required accuracy. This is the case for most of the inverse Mittag-Leffler functions.

Consider the inverse of the Mittag-Leffler function $E_{1/7,1}(-z)$. The coefficients b_k calculated from (10) are given in Table 2 (truncated to 20 significant digits).

It is obvious in looking at the coefficients b_k in Table 2 that they are approaching a constant as k becomes large. In this case, the constant is $1/\Gamma(6/7)$. Subsequently, the first 20 significant digits for all coefficients after b_{46} are identical

Table 5: Coefficients b_k for the inverse Mittag-Leffler function $-z = E^{-1}_{1/3,1}(w)$.

k	b_k
1	+0.89297951156924921122
2	+0.78878610417460496420
3	+0.75763354875769329328
4	+0.74579778773344787841
5	+0.74098130749558031810
6	+0.73904720310555344414
7	+0.73834522959265981505
8	+0.73816142472165138055
9	+0.73817790739448622896
10	+0.73825511074871374070
11	+0.73833571434942144250
12	+0.73839997927465491398
13	+0.73844449496113714586
14	+0.73847210628873099793
15	+0.73848730878287129409
16	+0.73849432235279002530
17	+0.73849644605470171587
18	+0.73849598893480155549
19	+0.73849442620461442205
20	+0.73849261331276901456
21	+0.73849098486630158241
22	+0.73848971269933349619
23	+0.73848881978568953731
24	+0.73848825605202219473
25	+0.73848794494184281702
26	+0.73848780930951379358
27	+0.73848778373908570968
28	+0.73848781862086802257
29	+0.73848787970874775507
30	+0.73848794558318757255
31	+0.73848800448141685314
32	+0.73848805128840606965
33	+0.73848808504905157547
34	+0.73848810710188503719
35	+0.73848811979412736597
36	+0.73848812567490815232
37	+0.73848812704699497915
38	+0.73848812576600764535
39	+0.73848812319593135382
40	+0.73848812025242302623
41	+0.73848811748639447885
42	+0.73848811517762375779
43	+0.73848811342117360995
44	+0.73848811219849196547
45	+0.73848811143091641775
46	+0.73848811101668555873
47	+0.73848811085420482928
48	+0.73848811085483076012

Table 5: Continued.

k	b_k
49	+0.73848811094828991640
50	+0.73848811108336786221
51	+0.73848811122590646140
52	+0.73848811135556505150
53	+0.73848811146230003348
54	+0.73848811154312398420
55	+0.73848811159941978280
56	+0.73848811163489404655
57	+0.73848811165413834046
58	+0.73848811166170643685
59	+0.73848811166159371995
60	+0.73848811165700633342
61	+0.73848811165032209352
62	+0.73848811164316504107
63	+0.73848811163653598310
64	+0.73848811163095974872
65	+0.73848811162662488952
66	+0.73848811162350289072
67	+0.73848811162144189450
68	+0.73848811162023502242
69	+0.73848811161966626697
70	+0.73848811161953822181
71	+0.73848811161968617262
72	+0.73848811161998269778
73	+0.73848811162033624249
74	+0.73848811162068634439
75	+0.73848811162099743490
76	+0.73848811162125249050
77	+0.73848811162144729066
78	+0.73848811162158565606
79	+0.73848811162167577734
80	+0.73848811162172758004
81	+0.73848811162175098150
82	+0.73848811162175485904
83	+0.73848811162174654725
84	+0.73848811162173170072
85	+0.73848811162171438724
86	+0.73848811162169730770
87	+0.73848811162168206810
88	+0.73848811162166945421
89	+0.73848811162165967945
90	+0.73848811162165259141
91	+0.73848811162164783248
92	+0.73848811162164495684
93	+0.73848811162164350958
94	+0.73848811162164307502
95	+0.73848811162164330226
96	+0.73848811162164391339
97	+0.73848811162164470224

Table 5: Continued.

k	b_k
98	+0.73848811162164552587
99	+0.73848811162164629360
100	+0.73848811162164695521
101	+0.73848811162164748994
102	+0.73848811162164789692
103	+0.73848811162164818753
104	+0.73848811162164837957
105	+0.73848811162164849309
106	+0.73848811162164854766
107	+0.73848811162164856073
108	+0.73848811162164854687
109	+0.73848811162164851751
110	+0.73848811162164848112
111	+0.73848811162164844359
112	+0.73848811162164840865
113	+0.73848811162164837840
114	+0.73848811162164835374
115	+0.73848811162164833471
116	+0.73848811162164832086
117	+0.73848811162164831146
118	+0.73848811162164830565
119	+0.73848811162164830260
120	+0.73848811162164830154
121	+0.73848811162164830182
122	+0.73848811162164830293
123	+0.73848811162164830447
124	+0.73848811162164830614
125	+0.73848811162164830777
126	+0.73848811162164830923
127	+0.73848811162164831046
128	+0.73848811162164831145
129	+0.73848811162164831220
130	+0.73848811162164831273
131	+0.73848811162164831309
132	+0.73848811162164831331
133	+0.73848811162164831342
134	+0.73848811162164831345
135	+0.73848811162164831343
136	+0.73848811162164831338
137	+0.73848811162164831331
138	+0.73848811162164831323
139	+0.73848811162164831316
140	+0.73848811162164831310
141	+0.73848811162164831304
142	+0.73848811162164831300
143	+0.73848811162164831297
144	+0.73848811162164831294
145	+0.73848811162164831292
146	+0.73848811162164831291

Table 5: Continued.

k	b_k
147	+0.73848811162164831291
148	+0.73848811162164831291
149	+0.73848811162164831291
150	+0.73848811162164831291
151	+0.73848811162164831291
152	+0.73848811162164831292
153	+0.73848811162164831292
154	+0.73848811162164831292
155	+0.73848811162164831292
156	+0.73848811162164831293

differing only after the first 20 digits. Thus, applying (4) with $z_o = 0$, $a_o = 1$, the inverse for $E_{1/7,1}(-z)$ can be written as

$$-z = E_{1/7,1}^{-1}(w) = -\sum_{k=1}^{46} b_k (1-w)^k - \sum_{k=47}^{\infty} \frac{(1-w)^k}{\Gamma(6/7)}. \quad (18)$$

Equation (18) assumes that all coefficients b_k for $k > 46$ can be approximated by $1/\Gamma(6/7)$. The approximation is valid provided that an answer accurate to no more than 20 significant digits is sufficient. The last term in (18) is a geometric series which can be replaced by its corresponding sum yielding

$$-z = E_{1/7,1}^{-1}(w) = -\sum_{k=1}^{46} b_k (1-w)^k - \frac{1}{\Gamma(6/7)} \frac{(1-w)^{47}}{w}. \quad (19)$$

Equation (19) represents a finite series for the inverse Mittag-Leffler function for $w \leq 1$ or equivalently $-z \leq 0$ accurate to 20 significant digits. The series has been tested numerically and in all cases tested gives the correct answer to at least 20 significant digits $0 \geq -z < -\infty$ or equivalently $0 < w \leq 1$. This finite series representation of the inverse Mittag-Leffler function has at least 3 advantages over the infinite series representation: (1) the finite series greatly expedites the evaluation of the inverse, (2) it is not limited to small $|-z|$, and (3) there is no ambiguity concerning the number of terms needed in the series to obtain a required accuracy in the final answer.

Note that if the required accuracy is only 10 significant digits, the first 10 digits of the coefficients b_k after b_{17} are identical differing only after the first 10 digits. In this case, the equation for the inverse can be written as

$$-z = E_{1/7,1}^{-1}(w) = -\sum_{k=1}^{17} b_k (1-w)^k - \frac{1}{\Gamma(6/7)} \frac{(1-w)^{18}}{w}. \quad (20)$$

The fact that the coefficients b_k approached a constant as k becomes large allowed the infinite series to be written as a finite series. For what other Mittag-Leffler functions do the coefficients in the inverse approach a constant?

Table 6: Coefficients b_k for the inverse Mittag-Leffler function $-z = E_{1/4,1}^{-1}(w)$.

k	b_k
1	0.90640247705547707798
2	0.84026894007589891391
3	0.82351018992990700207
4	0.81828957550795105766
5	0.81660707076917509278
6	0.81610221036029616113
7	0.81598545033147361884
8	0.81598379842062516042
9	0.81600622129819404882
10	0.81602620538545447950
11	0.81603889114688882765
12	0.81604558885224673170
13	0.81604856137343865455
14	0.81604957197906280172
15	0.81604970482268525625
16	0.81604953186530296411
17	0.81604931188945210690
18	0.81604913762546883873
19	0.81604902563306262589
20	0.81604896432490207114
21	0.81604893634591082941
22	0.81604892711529213868
23	0.81604892680747229621
24	0.81604892974411138067
25	0.81604893311589531898
26	0.81604893581695267902
27	0.81604893761527447364
28	0.81604893864655309011
29	0.81604893914547956993
30	0.81604893932600511441
31	0.81604893934331182207
32	0.81604893929407644732
33	0.81604893923044766688
34	0.81604893917568606393
35	0.81604893913673190214
36	0.81604893911270302848
37	0.81604893909990779088
38	0.81604893909439699044
39	0.81604893909300259361
40	0.81604893909356459299
41	0.81604893909479532456
42	0.81604893909603395768
43	0.81604893909701259830
44	0.81604893909767829618
45	0.81604893909807584283
46	0.81604893909827997471
47	0.81604893909836178143
48	0.81604893909837594019

Table 6: Continued.

k	b_k
49	0.81604893909835900689
50	0.81604893909833251654
51	0.81604893909830737526
52	0.81604893909828785893
53	0.81604893909827462118
54	0.81604893909826667548
55	0.81604893909826254932
56	0.81604893909826086189
57	0.81604893909826054632
58	0.81604893909826087970
59	0.81604893909826142714
60	0.81604893909826196124
61	0.81604893909826238717
62	0.81604893909826268505
63	0.81604893909826287085
64	0.81604893909826297283
65	0.81604893909826301912
66	0.81604893909826303243
67	0.81604893909826302882
68	0.81604893909826301846
69	0.81604893909826300704
70	0.81604893909826299725
71	0.81604893909826298997
72	0.81604893909826298513
73	0.81604893909826298224
74	0.81604893909826298074
75	0.81604893909826298012
76	0.81604893909826298002
77	0.81604893909826298015
78	0.81604893909826298038
79	0.81604893909826298060
80	0.81604893909826298078
81	0.81604893909826298092
82	0.81604893909826298100
83	0.81604893909826298105
84	0.81604893909826298108
85	0.81604893909826298109
86	0.81604893909826298109
87	0.81604893909826298109
88	0.81604893909826298109
89	0.81604893909826298108
90	0.81604893909826298108
91	0.81604893909826298108
92	0.81604893909826298107

4. Inverse Mittag-Leffler Functions for Which b_k Approach a Constant

Evaluation of great many inverse Mittag-Leffler functions reveals several important points. (1) It has been shown that the Mittag-Leffer function with these α and β parameters,

Table 7: Coefficients b_k for the inverse Mittag-Leffler function $-z = E^{-1}_{1/5,1}(w)$.

k	b_k
1	+0.91816874239976061064
2	+0.87239815820597071525
3	+0.86241404655813210186
4	+0.85979515758722241525
5	+0.85910249498870304439
6	+0.85894043515591457893
7	+0.85891680448152655590
8	+0.85892230156211349359
9	+0.85892962600662844119
10	+0.85893406838573395241
11	+0.85893613453863527233
12	+0.85893690887578873062
13	+0.85893711768226131089
14	+0.85893712714123260150
15	+0.85893708951453251359
16	+0.85893705517782142799
17	+0.85893703407253609369
18	+0.85893702365426492211
19	+0.85893701950167094637
20	+0.85893701834496455469
21	+0.85893701834146563837
22	+0.85893701863535859269
23	+0.85893701890846377513
24	+0.85893701908567480745
25	+0.85893701917914447317
26	+0.85893701921959129502
27	+0.85893701923250482423
28	+0.85893701923367892385
29	+0.85893701923119867846
30	+0.85893701922846356042
31	+0.85893701922650554665
32	+0.85893701922537418952
33	+0.85893701922482812463
34	+0.85893701922461848499
35	+0.85893701922457079400
36	+0.85893701922458522240
37	+0.85893701922461381792
38	+0.85893701922463819190
39	+0.85893701922465413251
40	+0.85893701922466286636
41	+0.85893701922466687324
42	+0.85893701922466827905
43	+0.85893701922466848269
44	+0.85893701922466825732
45	+0.85893701922466796298
46	+0.85893701922466773028
47	+0.85893701922466758222
48	+0.85893701922466750209

Table 7: Continued.

k	b_k
49	+0.85893701922466746565
50	+0.85893701922466745311
51	+0.85893701922466745162
52	+0.85893701922466745405
53	+0.85893701922466745708
54	+0.85893701922466745948
55	+0.85893701922466746103
56	+0.85893701922466746188
57	+0.85893701922466746229
58	+0.85893701922466746243
59	+0.85893701922466746246
60	+0.85893701922466746244
61	+0.85893701922466746241
62	+0.85893701922466746238
63	+0.85893701922466746236
64	+0.85893701922466746235

namely, $0 < \alpha < 1$ and $\beta > \alpha$, is a completely monotonic decreasing function [24, 25], and thus the inverse is guaranteed to be single valued. (2) The coefficients b_k in the inverse approach a constant only when the parameter β is either 1 or 2. (3) The coefficients b_k approach a constant only when the parameter $\alpha < 1$. (4) The coefficients b_k approach a constant given by

$$\lim_{k\to\infty} b_k = \frac{1}{\Gamma(\beta-\alpha)}. \tag{21}$$

Consequently, as $\alpha \to 0$, the coefficient $b_k \to 1$ for both $\beta = 1$ and 2. However, for $\beta = 1$ the coefficient b_k is always less than 1 while for $\beta = 2$, b_k is always greater than 1 as $\alpha \to 0$. (5) The smaller the value of α, the fewer the numerical terms required in the inverse series to obtain a given significant digit accuracy. This is illustrated in Table 3 which gives the number of terms required in the finite representation of the inverse Mittag-Leffler function for 20-significant-digit accuracy for various values of α with $\beta = 1$ and $\beta = 2$.

Extending this logic to its natural conclusion implies that at $\alpha = 0$ no terms will be required in the series. To see that this is correct, note that using (1) both $w = E_{0,1}(-z)$ and $w = E_{0,2}(-z)$ reduce to $w = 1/(1+z)$ when $\alpha = 0$. Inverting and solving for $-z$ yield $-z = -(1-w)/w$. This is consistent with (19) which reduces to this same result when the upper limit on the summation is $k = 0$ (no terms in the summation) and the factor $1/\Gamma(6/7)$ is replaced by the more general equation (21) which gives unity for $\alpha = 0$ and $\beta = 1$ or $\beta = 2$.

Conversely, as α approaches 1, an increasingly larger number of numerical terms are required in the inverse series to obtain a given significant digit accuracy as Table 3 illustrates. (6) Consequently, as α increases above 1/2, the inverse Mittag-Leffler function described by a finite series requires more and more terms becoming less practical. For example, for $\alpha = 0.74$ and $\beta = 1$, for b_k to converge to just 5 significant digits requires 2215 terms while, for $\alpha = 0.825$ and $\beta = 2$, requiring 1828 terms for the same convergence.

Table 8: Coefficients b_k for the inverse Mittag-Leffler function $-z = E^{-1}_{1/6,1}(w)$.

k	b_k
1	+0.92771933363003920070
2	+0.89414577241424278746
3	+0.88773763213642664587
4	+0.88628977973846244289
5	+0.88596635420228565868
6	+0.88590523526021224793
7	+0.88589982030554044972
8	+0.88590275825406298752
9	+0.88590511036557706322
10	+0.88590621213903655148
11	+0.88590660928393383455
12	+0.88590671636180511607
13	+0.88590672946995710075
14	+0.88590672153714995480
15	+0.88590671360108075777
16	+0.88590670912379822800
17	+0.88590670718459732010
18	+0.88590670653013358196
19	+0.88590670638937664049
20	+0.88590670640476657586
21	+0.88590670644420859302
22	+0.88590670647244801433
23	+0.88590670648712373933
24	+0.88590670649321013736
25	+0.88590670649512780068
26	+0.88590670649542543061
27	+0.88590670649526508181
28	+0.88590670649506835081
29	+0.88590670649493875951
30	+0.88590670649487287445
31	+0.88590670649484578753
32	+0.88590670649483743413
33	+0.88590670649483637544
34	+0.88590670649483735333
35	+0.88590670649483843570
36	+0.88590670649483914752
37	+0.88590670649483951597
38	+0.88590670649483967198
39	+0.88590670649483972248
40	+0.88590670649483973021
41	+0.88590670649483972509
42	+0.88590670649483971872
43	+0.88590670649483971430
44	+0.88590670649483971188
45	+0.88590670649483971080
46	+0.88590670649483971040
47	+0.88590670649483971032
48	+0.88590670649483971034

Table 8: Continued.

k	b_k
49	+0.88590670649483971037
50	+0.88590670649483971040
51	+0.88590670649483971042
52	+0.88590670649483971043

Table 9: Coefficients b_k for the inverse Mittag-Leffler function $-z = E^{-1}_{1/8,1}(w)$.

k	b_k
1	+0.94174269984970148808
2	+0.92145833616345434435
3	+0.91837205036733785079
4	+0.91782768940815950206
5	+0.91773538138444524775
6	+0.91772307499596115692
7	+0.91772281742094063440
8	+0.91772345536444575339
9	+0.91772376557618704885
10	+0.91772386504763452141
11	+0.91772388849585357984
12	+0.91772389156330350231
13	+0.91772389092194344445
14	+0.91772389025312412600
15	+0.91772388994408363001
16	+0.91772388984022900150
17	+0.91772388981468002747
18	+0.91772388981165650624
19	+0.91772388981289452457
20	+0.91772388981401655984
21	+0.91772388981455209678
22	+0.91772388981474237399
23	+0.91772388981479260777
24	+0.91772388981479946414
25	+0.91772388981479716385
26	+0.91772388981479476203
27	+0.91772388981479352017
28	+0.91772388981479304158
29	+0.91772388981479290058
30	+0.91772388981479287486
31	+0.91772388981479287784
32	+0.91772388981479288351
33	+0.91772388981479288690
34	+0.91772388981479288835
35	+0.91772388981479288884
36	+0.91772388981479288896
37	+0.91772388981479288897
38	+0.91772388981479288896
39	+0.91772388981479288895
40	+0.91772388981479288894

Table 10: Coefficients b_k for the inverse Mittag-Leffler function $-z = E^{-1}_{1/9,1}(w)$.

k	b_k
1	0.94696534880216399450
2	0.93053890407728875727
3	0.92827170167793346183
4	0.92791158668373485876
5	0.92785715845937955393
6	0.92785088338236675169
7	0.92785088003507065240
8	0.92785119095520099570
9	0.92785131874466606751
10	0.92785135396452045173
11	0.92785136086263488623
12	0.92785136142419633245
13	0.92785136114025016525
14	0.92785136095166820529
15	0.92785136088086115418
16	0.92785136086138201458
17	0.92785136085777479380
18	0.92785136085772523465
19	0.92785136085805437723
20	0.92785136085823967523
21	0.92785136085830846162
22	0.92785136085832754930
23	0.92785136085833100710
24	0.92785136085833091281
25	0.92785136085833047865
26	0.92785136085833023736
27	0.92785136085833014532
28	0.92785136085833011870
29	0.92785136085833011354
30	0.92785136085833011358
31	0.92785136085833011420
32	0.92785136085833011458
33	0.92785136085833011473
34	0.92785136085833011478
35	0.92785136085833011479

(7) For the same α, the number of terms in the inverse for a desired accuracy is less for $\beta = 2$ than for $\beta = 1$. (8) According to (21), when $\alpha = 1$ and $\beta = 1$, the coefficients b_k in the inverse for the Mittag-Leffler function $E_{1,1}(-z)$ approach the constant zero as $k \to \infty$ as seen in (16) while for $\alpha = 1$ and $\beta = 2$ the coefficients b_k in the inverse for the Mittag-Leffler function $E_{1,2}(-z)$ approach 1 as $k \to \infty$. (9) As noted above, according to (21), for $\beta = 2$ the coefficients b_k as $k \to \infty$ approach 1 as $\alpha \to 0$ and as $\alpha \to 1$ and b_k is greater than 1 for $0 < \alpha < 1$. This implies that there exists a relative maximum value of b_k as $k \to \infty$ in the range $0 < \alpha < 1$. This maximum occurs at $\alpha = 0.5383678550\ldots$ and corresponds to $b_k = 1.129173885\ldots$ as $k \to \infty$. Illustrating the above observations are numerous examples in the next section.

Table 11: Coefficients b_k for the inverse Mittag-Leffler function $-z = E^{-1}_{1/10,1}(w)$.

k	b_k
1	+0.95135076986687318362
2	+0.93777687277778653379
3	+0.93606310059788083658
4	+0.93581557876046714164
5	+0.93578185282959558380
6	+0.93577844037062189666
7	+0.93577848991569929215
8	+0.93577864855859718780
9	+0.93577870513836571828
10	+0.93577871876872861069
11	+0.93577872101504047108
12	+0.93577872110471635717
13	+0.93577872099247192203
14	+0.93577872093543535964
15	+0.93577872091738487402
16	+0.93577872091324677459
17	+0.93577872091268732351
18	+0.93577872091275010310
19	+0.93577872091282731969
20	+0.93577872091286047983
21	+0.93577872091287052264
22	+0.93577872091287272009
23	+0.93577872091287295145
24	+0.93577872091287287167
25	+0.93577872091287280852
26	+0.93577872091287278263
27	+0.93577872091287277485
28	+0.93577872091287277316
29	+0.93577872091287277300
30	+0.93577872091287277308
31	+0.93577872091287277314
32	+0.93577872091287277317

5. Results for Specific α and β

In this section, specific examples of various inverse Mittag-Leffler functions calculated using (10) will be given. Since the number of terms in the finite series for the inverse increases dramatically for $\alpha \geq 1/2$, then all examples will be for $\alpha < 1/2$. All equations for the inverses are written assuming a desired 20-significant-digit accuracy. This is far greater accuracy than most requirements might call for; however, the equations can then be easily modified to any degree of accuracy less than 20 as outlined in the discussion of (20). Each Mittag-Leffler inverse $-z = E^{-1}_{\alpha,\beta}(w)$ example includes the equation of the form given in (19) valid for $0 \geq -z < -\infty$ (equivalently $0 < w \leq 1$) representing the finite series representation of the inverse and a table with the corresponding coefficients b_k truncated to 20 significant digits. The specific values of α and β in each example are itemized in Table 4 which includes references to the

Table 12: Coefficients b_k for the inverse Mittag-Leffler function $-z = E^{-1}_{1/3,2}(w)$.

k	b_k
1	1.1906393487589989482
2	1.1218291259372159490
3	1.1091651079345480360
4	1.1070518842541741977
5	1.1071094825114241570
6	1.1074303857224016589
7	1.1076404430424683811
8	1.1077314700191564271
9	1.1077553955944287187
10	1.1077524578488089226
11	1.1077434947715842855
12	1.1077363499227504156
13	1.1077324896384468086
14	1.1077310965875528477
15	1.1077310087501244588
16	1.1077313864890338427
17	1.1077317908641062832
18	1.1077320654748424695
19	1.1077322009818539445
20	1.1077322408861236149
21	1.1077322323951713722
22	1.1077322084738571023
23	1.1077321862732534401
24	1.1077321716839450156
25	1.1077321645662504099
26	1.1077321625611127907
27	1.1077321631931161511
28	1.1077321646957392674
29	1.1077321661093029166
30	1.1077321670760136784
31	1.1077321675814921360
32	1.1077321677525601222
33	1.1077321677362930981
34	1.1077321676460497809
35	1.1077321675494545998
36	1.1077321674764692276
37	1.1077321674332138537
38	1.1077321674142290519
39	1.1077321674107002345
40	1.1077321674147729438
41	1.1077321674210887571
42	1.1077321674267605861
43	1.1077321674307081625
44	1.1077321674329036944
45	1.1077321674337785530
46	1.1077321674338524401
47	1.1077321674335523501
48	1.1077321674331583587

Table 12: Continued.

k	b_k
49	1.1077321674328171346
50	1.1077321674325809580
51	1.1077321674324479205
52	1.1077321674323926738
53	1.1077321674323855472
54	1.1077321674324019711
55	1.1077321674324254123
56	1.1077321674324467750
57	1.1077321674324623978
58	1.1077321674324719027
59	1.1077321674324764817
60	1.1077321674324777720
61	1.1077321674324772490
62	1.1077321674324759894
63	1.1077321674324746516
64	1.1077321674324735591
65	1.1077321674324728113
66	1.1077321674324723822
67	1.1077321674324721933
68	1.1077321674324721578
69	1.1077321674324722031
70	1.1077321674324722781
71	1.1077321674324723525
72	1.1077321674324724118
73	1.1077321674324724522
74	1.1077321674324724754
75	1.1077321674324724857
76	1.1077321674324724876
77	1.1077321674324724851
78	1.1077321674324724809
79	1.1077321674324724766
80	1.1077321674324724731
81	1.1077321674324724707
82	1.1077321674324724692
83	1.1077321674324724685
84	1.1077321674324724683
85	1.1077321674324724684
86	1.1077321674324724686
87	1.1077321674324724688
88	1.1077321674324724691
89	1.1077321674324724692
90	1.1077321674324724693
91	1.1077321674324724694

corresponding equations and table numbers for each example inverse.

For $\alpha = 1/3$ and $\beta = 1$, the equation for the inverse is given by

$$-z = E_{1/3,1}^{-1}(w) = -\sum_{k=1}^{156} b_k (1-w)^k - \frac{1}{\Gamma(2/3)} \frac{(1-w)^{157}}{w}, \tag{22}$$

Table 13: Coefficients b_k for the inverse Mittag-Leffler function $-z = E_{1/4,2}^{-1}(w)$.

k	b_k
1	1.1330030963193463474
2	1.0941001823904933774
3	1.0884969259036715641
4	1.0878558386282093564
5	1.0879299260072536857
6	1.0880196901607404297
7	1.0880580603477134188
8	1.0880679256317365431
9	1.0880681582727259222
10	1.0880666922539625425
11	1.0880656824079111948
12	1.0880652661105853859
13	1.0880651718209129462
14	1.0880651893915501135
15	1.0880652225919339689
16	1.0880652438081294238
17	1.0880652525894990987
18	1.0880652545116835036
19	1.0880652539426656281
20	1.0880652530160160191
21	1.0880652524013356965
22	1.0880652521279001619
23	1.0880652520573054501
24	1.0880652520688854981
25	1.0880652520973313877
26	1.0880652521186658457
27	1.0880652521294678814
28	1.0880652521330822285
29	1.0880652521332880539
30	1.0880652521324663677
31	1.0880652521316757550
32	1.0880652521311980579
33	1.0880652521309915951
34	1.0880652521309409874
35	1.0880652521309543925
36	1.0880652521309814562
37	1.0880652521310025596
38	1.0880652521310142006
39	1.0880652521310188181
40	1.0880652521310196801
41	1.0880652521310191068
42	1.0880652521310183025
43	1.0880652521310177100
44	1.0880652521310173883
45	1.0880652521310172608
46	1.0880652521310172369
47	1.0880652521310172534
48	1.0880652521310172768

Table 13: Continued.

k	b_k
49	1.0880652521310172946
50	1.0880652521310173047
51	1.0880652521310173090
52	1.0880652521310173101
53	1.0880652521310173098
54	1.0880652521310173091
55	1.0880652521310173086
56	1.0880652521310173082
57	1.0880652521310173081
58	1.0880652521310173080
59	1.0880652521310173080
60	1.0880652521310173080
61	1.0880652521310173080
62	1.0880652521310173080
63	1.0880652521310173081

where $1/\Gamma(2/3) = 0.73848811162164831293\ldots$ and the coefficients b_k are given in Table 5.

For $\alpha = 1/4$ and $\beta = 1$, the equation for the inverse is given by

$$-z = E_{1/4,1}^{-1}(w) = -\sum_{k=1}^{92} b_k(1-w)^k - \frac{1}{\Gamma(3/4)}\frac{(1-w)^{93}}{w}, \tag{23}$$

where $1/\Gamma(3/4) = 0.81604893909826298107\ldots$ and the coefficients b_k are given in Table 6.

For $\alpha = 1/5$ and $\beta = 1$, the equation for the inverse is given by

$$-z = E_{1/5,1}^{-1}(w) = -\sum_{k=1}^{64} b_k(1-w)^k - \frac{1}{\Gamma(4/5)}\frac{(1-w)^{65}}{w}, \tag{24}$$

where $1/\Gamma(4/5) = 0.85893701922466746235\ldots$ and the coefficients b_k are given in Table 7.

For $\alpha = 1/6$ and $\beta = 1$, the equation for the inverse is given by

$$-z = E_{1/6,1}^{-1}(w) = -\sum_{k=1}^{52} b_k(1-w)^k - \frac{1}{\Gamma(5/6)}\frac{(1-w)^{53}}{w}, \tag{25}$$

where $1/\Gamma(5/6) = 0.88590670649483971043\ldots$ and the coefficients b_k are given in Table 8.

For $\alpha = 1/8$ and $\beta = 1$, the equation for the inverse is given by

$$-z = E_{1/8,1}^{-1}(w) = -\sum_{k=1}^{40} b_k(1-w)^k - \frac{1}{\Gamma(7/8)}\frac{(1-w)^{41}}{w}, \tag{26}$$

where $1/\Gamma(7/8) = 0.91772388981479288894\ldots$ and the coefficients b_k are given in Table 9.

Table 14: Coefficients b_k for the inverse Mittag-Leffler function $-z = E_{1/5,2}^{-1}(w)$.

k	b_k
1	1.1018024908797127327
2	1.0767885838427981399
3	1.0738409976565079202
4	1.0735918587371880661
5	1.0736317220842957450
6	1.0736613247947013790
7	1.0736705276938335590
8	1.0736719763838959650
9	1.0736717194169915685
10	1.0736714224350730386
11	1.0736712961819915731
12	1.0736712656573585536
13	1.0736712658337183805
14	1.0736712703837243345
15	1.0736712730893571885
16	1.0736712740367576320
17	1.0736712741927198324
18	1.0736712741349301121
19	1.0736712740710214284
20	1.0736712740390593289
21	1.0736712740290815387
22	1.0736712740281108537
23	1.0736712740292769055
24	1.0736712740302628755
25	1.0736712740307308734
26	1.0736712740308721433
27	1.0736712740308820173
28	1.0736712740308614201
29	1.0736712740308445464
30	1.0736712740308363495
31	1.0736712740308337294
32	1.0736712740308334598
33	1.0736712740308337982
34	1.0736712740308341087
35	1.0736712740308342730
36	1.0736712740308343326
37	1.0736712740308343434
38	1.0736712740308343390
39	1.0736712740308343332
40	1.0736712740308343296
41	1.0736712740308343281
42	1.0736712740308343277
43	1.0736712740308343277
44	1.0736712740308343278
45	1.0736712740308343278
46	1.0736712740308343279

Table 15: Coefficients b_k for the inverse Mittag-Leffler function $-z = E^{-1}_{1/6,2}(w)$.

k	b_k
1	1.0823392225683790674
2	1.0649027775627960975
3	1.0631672235921470234
4	1.0630530019556810014
5	1.0630738792005841325
6	1.0630852477868224812
7	1.0630879790229538911
8	1.0630882395356188174
9	1.0630881350924325915
10	1.0630880687069684272
11	1.0630880487821691319
12	1.0630880460752193502
13	1.0630880468406782122
14	1.0630880475089981383
15	1.0630880477592756779
16	1.0630880478102509927
17	1.0630880478069487489
18	1.0630880477988781918
19	1.0630880477949003960
20	1.0630880477937454972
21	1.0630880477936234680
22	1.0630880477937097855
23	1.0630880477937763019
24	1.0630880477938030729
25	1.0630880477938094515
26	1.0630880477938094111
27	1.0630880477938084584
28	1.0630880477938078846
29	1.0630880477938076743
30	1.0630880477938076305
31	1.0630880477938076352
32	1.0630880477938076449
33	1.0630880477938076504
34	1.0630880477938076523
35	1.0630880477938076527
36	1.0630880477938076527
37	1.0630880477938076526
38	1.0630880477938076525

For $\alpha = 1/9$ and $\beta = 1$, the equation for the inverse is given by

$$-z = E^{-1}_{1/9,1}(w) = -\sum_{k=1}^{35} b_k (1-w)^k - \frac{1}{\Gamma(8/9)} \frac{(1-w)^{36}}{w}, \tag{27}$$

where $1/\Gamma(8/9) = 0.92785136085833011479\ldots$ and the coefficients b_k are given in Table 10.

Table 16: Coefficients b_k for the inverse Mittag-Leffler function $-z = E^{-1}_{1/7,2}(w)$.

k	b_k
1	1.0690715004486243979
2	1.0562222079392582146
3	1.0551161172778792415
4	1.0550572191430135037
5	1.0550686438367760540
6	1.0550735765579806638
7	1.0550745305844060375
8	1.0550745824286880798
9	1.0550745442484434695
10	1.0550745270114378657
11	1.0550745231398621545
12	1.0550745229039529066
13	1.0550745231150647888
14	1.0550745232236878646
15	1.0550745232523526379
16	1.0550745232552728533
17	1.0550745232539308640
18	1.0550745232530327777
19	1.0550745232527427584
20	1.0550745232526945061
21	1.0550745232527008669
22	1.0550745232527090401
23	1.0550745232527124342
24	1.0550745232527132611
25	1.0550745232527133099
26	1.0550745232527132427
27	1.0550745232527132021
28	1.0550745232527131884
29	1.0550745232527131859
30	1.0550745232527131861
31	1.0550745232527131865
32	1.0550745232527131867
33	1.0550745232527131868

For $\alpha = 1/10$ and $\beta = 1$, the equation for the inverse is given by

$$-z = E^{-1}_{1/10,1}(w) = -\sum_{k=1}^{32} b_k (1-w)^k - \frac{1}{\Gamma(9/10)} \frac{(1-w)^{33}}{w}, \tag{28}$$

where $1/\Gamma(9/10) = 0.93577872091287277317\ldots$ and the coefficients b_k are given in Table 11.

For $\alpha = 1/3$ and $\beta = 2$, the equation for the inverse is given by

$$-z = E^{-1}_{1/3,2}(w) = -\sum_{k=1}^{91} b_k (1-w)^k - \frac{1}{\Gamma(5/3)} \frac{(1-w)^{92}}{w}, \tag{29}$$

where $1/\Gamma(5/3) = 1.1077321674324724694\ldots$ and the coefficients b_k are given in Table 12.

Table 17: Coefficients b_k for the inverse Mittag-Leffler function $-z = E^{-1}_{1/8,2}(w)$.

k	b_k
1	1.0594605373309141740
2	1.0495986360361847141
3	1.0488511439374145246
4	1.0488179924913977120
5	1.0488245771415334177
6	1.0488269350920946859
7	1.0488273133611761220
8	1.0488273231954621562
9	1.0488273085970012075
10	1.0488273034622550713
11	1.0488273025690472404
12	1.0488273025660372711
13	1.0488273026212509980
14	1.0488273026418176097
15	1.0488273026458036695
16	1.0488273026458799051
17	1.0488273026456156560
18	1.0488273026455029277
19	1.0488273026454771037
20	1.0488273026454752946
21	1.0488273026454766352
22	1.0488273026454773654
23	1.0488273026454775715
24	1.0488273026454775998
25	1.0488273026454775944
26	1.0488273026454775895
27	1.0488273026454775877
28	1.0488273026454775873

Table 18: Coefficients b_k for the inverse Mittag-Leffler function $-z = E^{-1}_{1/9,2}(w)$.

k	b_k
1	1.0521837208912933272
2	1.0443758743852848005
3	1.0438473880668843474
4	1.0438274217379570018
5	1.0438314036520292794
6	1.0438326220325679883
7	1.0438327879063812056
8	1.0438327888679432382
9	1.0438327828921939645
10	1.0438327811719258151
11	1.0438327809347620508
12	1.0438327809451382984
13	1.0438327809605757500
14	1.0438327809650783542
15	1.0438327809657296823
16	1.0438327809656925712
17	1.0438327809656403057
18	1.0438327809656237760
19	1.0438327809656210337
20	1.0438327809656210870
21	1.0438327809656212900
22	1.0438327809656213646
23	1.0438327809656213797
24	1.0438327809656213804
25	1.0438327809656213796
26	1.0438327809656213792
27	1.0438327809656213791

For $\alpha = 1/4$ and $\beta = 2$, the equation for the inverse is given by

$$-z = E^{-1}_{1/4,2}(w) = -\sum_{k=1}^{63} b_k (1-w)^k - \frac{1}{\Gamma(7/4)} \frac{(1-w)^{64}}{w}, \tag{30}$$

where $1/\Gamma(7/4) = 1.0880652521310173081\ldots$ and the coefficients b_k are given in Table 13.

For $\alpha = 1/5$ and $\beta = 2$, the equation for the inverse is given by

$$-z = E^{-1}_{1/5,2}(w) = -\sum_{k=1}^{46} b_k (1-w)^k - \frac{1}{\Gamma(9/5)} \frac{(1-w)^{47}}{w}, \tag{31}$$

where $1/\Gamma(9/5) = 1.0736712740308343279\ldots$ and the coefficients b_k are given in Table 14.

For $\alpha = 1/6$ and $\beta = 2$, the equation for the inverse is given by

$$-z = E^{-1}_{1/6,2}(w) = -\sum_{k=1}^{38} b_k (1-w)^k - \frac{1}{\Gamma(11/6)} \frac{(1-w)^{39}}{w}, \tag{32}$$

where $1/\Gamma(11/6) = 1.0630880477938076525\ldots$ and the coefficients b_k are given in Table 15.

For $\alpha = 1/7$ and $\beta = 2$, the equation for the inverse is given by

$$-z = E^{-1}_{1/7,2}(w) = -\sum_{k=1}^{33} b_k (1-w)^k - \frac{1}{\Gamma(13/7)} \frac{(1-w)^{34}}{w}, \tag{33}$$

where $1/\Gamma(13/7) = 1.0550745232527131868\ldots$ and the coefficients b_k are given in Table 16.

For $\alpha = 1/8$ and $\beta = 2$, the equation for the inverse is given by

$$-z = E^{-1}_{1/8,2}(w) = -\sum_{k=1}^{28} b_k (1-w)^k - \frac{1}{\Gamma(15/8)} \frac{(1-w)^{29}}{w}, \tag{34}$$

where $1/\Gamma(15/8) = 1.0488273026454775873\ldots$ and the coefficients b_k are given in Table 17.

Table 19: Coefficients b_k for the inverse Mittag-Leffler function $-z = E^{-1}_{1/10,2}(w)$.

k	b_k
1	1.0464858468535605019
2	1.0401508480560282303
3	1.0397635665515442126
4	1.0397508768185132109
5	1.0397533885835924940
6	1.0397540594403559415
7	1.0397541383662199550
8	1.0397541376605313080
9	1.0397541350429188308
10	1.0397541344064541458
11	1.0397541343357544813
12	1.0397541343417232130
13	1.0397541343464255068
14	1.0397541343475460327
15	1.0397541343476671587
16	1.0397541343476507388
17	1.0397541343476394778
18	1.0397541343476366678
19	1.0397541343476363331
20	1.0397541343476363726
21	1.0397541343476364046
22	1.0397541343476364135
23	1.0397541343476364148
24	1.0397541343476364147
25	1.0397541343476364146

For $\alpha = 1/9$ and $\beta = 2$, the equation for the inverse is given by

$$-z = E^{-1}_{1/9,2}(w) = -\sum_{k=1}^{27} b_k (1-w)^k - \frac{1}{\Gamma(17/9)} \frac{(1-w)^{28}}{w}, \tag{35}$$

where $1/\Gamma(17/9) = 1.0438327809656213791\ldots$ and the coefficients b_k are given in Table 18.

For $\alpha = 1/10$ and $\beta = 2$, the equation for the inverse is given by

$$-z = E^{-1}_{1/10,2}(w) = -\sum_{k=1}^{25} b_k (1-w)^k - \frac{1}{\Gamma(19/10)} \frac{(1-w)^{26}}{w}, \tag{36}$$

where $1/\Gamma(19/10) = 1.0397541343476364146\ldots$ and the coefficients b_k are given in Table 19.

6. Summary

A finite series representation of the inverse Mittag-Leffler function has been found for a range of the parameters α and β; specifically $0 < \alpha < 1/2$ for $\beta = 1$ and for $\beta = 2$. Various properties of the coefficients b_k in the finite series have been examined. In addition, a formula for b_k as $k \to \infty$ is established and the limiting cases were investigated. These properties are illustrated in 16 examples of inverse Mittag-Leffler functions. Determining the value of the argument of a Mittag-Leffler function given the value of the function is not an easy problem and the finite series representation of the inverse Mittag-Leffler function greatly expedites their evaluation and represents a significant advancement.

Conflict of Interests

The authors declare that there is no conflict of interests regarding the publication of this paper.

References

[1] A. Erdélyi, Ed., *Higher Transcendental Functions*, vol. 3, McGraw-Hill, New York, NY, USA, 1955.

[2] I. Podlubny, *Fractional Differential Equations*, vol. 198 of *Mathematics in Science and Engineering*, Academic Press, San Diego, Calif, USA, 1999.

[3] A. A. Kilbas, H. M. Srivastava, and J. J. Trujillo, *Theory and Applications of Fractional Differential Equations*, vol. 204 of *North-Holland Mathematics Studies*, Elsevier Science B.V., Amsterdam, The Netherlands, 2006.

[4] K. Diethelm, *The Analysis of Fractional Differential Equations*, vol. 2004 of *Lecture Notes in Mathematics*, Springer, New York, NY, USA, 2010.

[5] R. Hilfer, *Applications of Fractional Calculus in Physics*, World Scientific, Singapore, 2000.

[6] F. Mainardi, *Fractional Calculus and Waves in Linear Viscoelasticity*, Imperial College Press, London, UK, 2010.

[7] R. L. Magin, *Fractional Calculus in Bioengineering*, Begell House Publishers, Redding, Conn, USA, 2006.

[8] F. Mainardi and R. Gorenflo, "On Mittag-Leffler-type functions in fractional evolution processes," *Journal of Computational and Applied Mathematics*, vol. 118, no. 1-2, pp. 283–299, 2000.

[9] R. L. Magin, "Fractional calculus in bioengineering," *Critical Reviews in Biomedical Engineering*, vol. 32, no. 1, pp. 1–104, 2004.

[10] M. N. Berberan-Santos, "Properties of the Mittag-Leffler relaxation function," *Journal of Mathematical Chemistry*, vol. 38, no. 4, pp. 629–635, 2005.

[11] I. S. Gupta and L. Debnath, "Some properties of the Mittag-Leffler functions," *Integral Transforms and Special Functions*, vol. 18, no. 5-6, pp. 329–336, 2007.

[12] H. J. Haubold, A. M. Mathai, and R. K. Saxena, "Mittag-Leffler functions and their applications," *Journal of Applied Mathematics*, vol. 2011, Article ID 298628, 51 pages, 2011.

[13] R. Hilfer and H. J. Seybold, "Computation of the generalized Mittag-Leffler function and its inverse in the complex plane," *Integral Transforms and Special Functions*, vol. 17, no. 9, pp. 637–652, 2006.

[14] K. Knopp, *Theory and Application of Infinite Series*, Dover, New York, NY, USA, 1990.

[15] M. Abramowitz and I. A. Stegun, *Handbook of Mathematical Functions with Formulas, Graphs, and Mathematical Tables*, Dover, New York, NY, USA, 1965.

[16] H. B. Dwight, *Tables of Integrals and Other mathematical Data*, The Macmillan Company, New York, NY, USA, 4th edition, 1961.

[17] W. H. Beyer, *CRC Standard Mathematical Tables*, CRC Press, Boca Raton, Fla, USA, 27th edition, 1984.

[18] P. Morse and H. Feshbach, *Methods of Theoretical Physics*, vol. 1, McGraw-Hill Book, New York, NY, USA, 1953.

[19] J. McMahon, "On the general term in the reversion of series," *Bulletin of the American Mathematical Society*, vol. 3, no. 7, pp. 170–172, 1894.

[20] E. P. Adams and R. L. Hippisley, *Smithsonian Mathematical Formulae and Tables of Elliptical Functions*, Smithsonian miscellaneous Collections 74(1), Publication 2672, Smithsonian Institution, Washington, DC, USA, 1939.

[21] J. Riordan, *Combinatorial Identities*, John Wiley & Sons, New York, NY, USA, 1968.

[22] C. E. Van Orstrand, "Reversion of power series," *Philosophical Magazine*, vol. 19, series 6, pp. 366–376, 1910.

[23] J. W. Müller, "Some observations on the reversion of series," Rapport BIPM-85/1, Bureau International des Poids et Mesures, Sèvres, France, 1985.

[24] K. S. Miller and S. G. Samko, "A note on the complete monotonicity of the generalized Mittag-Leffler function," *Real Analysis Exchange*, vol. 23, no. 2, pp. 753–755, 1997.

[25] K. S. Miller and S. G. Samko, "Completely monotonic functions," *Integral Transforms and Special Functions*, vol. 12, no. 4, pp. 389–402, 2001.

Hindawi Publishing Corporation
Mathematical Problems in Engineering
Volume 2014, Article ID 645059, 9 pages
http://dx.doi.org/10.1155/2014/645059

Research Article

Image Watermarking in the Linear Canonical Transform Domain

Bing-Zhao Li and Yu-Pu Shi

School of Mathematics and Statistics of Beijing Institute of Technology, Beijing 100081, China

Correspondence should be addressed to Bing-Zhao Li; li_bingzhao@bit.edu.cn

Received 26 December 2013; Revised 19 February 2014; Accepted 19 February 2014; Published 24 March 2014

Academic Editor: Juan J. Trujillo

The linear canonical transform, which can be looked at the generalization of the fractional Fourier transform and the Fourier transform, has received much interest and proved to be one of the most powerful tools in fractional signal processing community. A novel watermarking method associated with the linear canonical transform is proposed in this paper. Firstly, the watermark embedding and detecting techniques are proposed and discussed based on the discrete linear canonical transform. Then the Lena image has been used to test this watermarking technique. The simulation results demonstrate that the proposed schemes are robust to several signal processing methods, including addition of Gaussian noise and resizing. Furthermore, the sensitivity of the single and double parameters of the linear canonical transform is also discussed, and the results show that the watermark cannot be detected when the parameters of the linear canonical transform used in the detection are not all the same as the parameters used in the embedding progress.

1. Introduction

Over the past several decades, digital watermarking become more and more important in the application of copyright protection for digital media as image, video, and audio [1–3]. A digital watermark is a code which embeds copyright information including sequence number, a picture, and text into the multimedia for copyright protection. The watermark must be easily detected by the copyright owner, the creator of the work, and the authorized consumer while is hardly read by the people who want to counterfeit the copyright of the data without authorization. Digital watermarking is an emerging technology in signal processing and communications which is under active development. The methods used to embed the watermark influence both the robustness and the detection algorithm. One of the hottest directions of the watermarking method is the watermarking in the transform domain, for example, in the discrete Fourier transform (DFT) domain [4–6] and in the discrete cosine transform (DCT) domain [7, 8], and the watermark proposed in [7] is two Gaussian sequences and it is embedded in the magnitude of the DCT transformation coefficients. A wealth of information and references can be found on the site of Watermarking World [9].

Recently, with the development of the fractional signal and processing technologies, the research results of the fractional Fourier transform (FRFT) and fractional Fourier operators have shown that the fractional domain signal processing can be looked at as one of the hottest research topics for nonstationary signals processing [10–15]. Several digital watermarking methods are proposed in the FRFT Domain [16–19] base on these novel results of the FRFT. A nonsensical watermark embedded in the FRFT domain was proposed in [16], and it has a more security because of the free parameter of the FRFT. Bultheel [18] describes the implementation of a watermark embedding technique in the FRFT domain in detail and also discusses the embedding several watermarks at the same time for images. The practical detecting threshold proposed in [18] is one of the most important contributions of the paper. All of these results, which come from the digital watermarking technology in the FRFT domain, have shown that the watermarking method in these transform domains can be more secure and hard to be detected compared to the traditional method in the classical DFT and DCT domain.

The linear canonical transform (LCT) [20], which can be looked at as the further generalization of the fractional

Fourier transform, is introduced in the 1970s with three free parameters and has been proven to be one of the most powerful tools for nonstationary signal processing. The well-known signal processing operations, such as the Fourier transform (FT), the FRFT, the Fresnel transform, and the scaling operations, are all special cases of the LCT [20]. The digital computation methods of the LCT have been proposed in [21–24], and the sampling theories associated with the LCT have been studied in [25–29], and the eigenfunction [30], the convolution and product function [31, 32], and the uncertainty principle [33] have also been investigated in detail. Therefore, understanding the LCT may help to gain more insight into its special cases and to carry the knowledge gained from one subject to others [20].

However, for the best of our knowledge, there are no papers published about the watermarking in the LCT domain. So it is interesting and worthwhile to investigate the watermarking method and technique associated with the LCT. Focusing on this problem, a novel watermarking technique based on the discrete LCT proposed in [23] is proposed in this paper. The experiment results show that the embedded watermarks are both perceptually invisible and robust to various image processing techniques. The remaining of this paper can be divided into the following sections. The LCT is described in Section 2. Section 3 develops watermark embedding in LCT domain. Numerical examples and the discussion of the simulation results are given in Section 4, and Section 5 is the conclusion.

2. The Linear Canonical Transform

2.1. The Continuous LCT. The continuous LCT of a signal $f(x)$ with parameter matrix $A = \left(\begin{smallmatrix} a & b \\ c & d \end{smallmatrix}\right)$ can be defined as [20]

$$f_A(y) = C_A(f)(y) = \int_{-\infty}^{+\infty} f(x) C_A(x,y)\, dx,$$
$$C_A(x,y) = \sqrt{\frac{1}{b}} e^{-j\pi/4} \exp\left\{ j\pi \left[\left(\frac{a}{b}\right) x^2 - \left(\frac{2}{b}\right) xy + \left(\frac{d}{b}\right) y^2 \right] \right\}, \tag{1}$$

where C_A is the LCT operator and a, b, c, d are real parameters. Furthermore the constraint $ad - bc = 1$ must be satisfied to make the transform unitary. Actually the LCT has three free parameters; if we let $a = \gamma/\beta$, $b = 1/\beta$, $c = -\beta + \alpha\gamma/\beta$, $d = \alpha/\beta$, the LCT of $f(x)$ can be rewritten as [23]

$$f_A(y) = C_A(f)(y) = \int_{-\infty}^{+\infty} f(x) C_A(x,y)\, dx,$$
$$C_A(x,y) = \sqrt{\beta} e^{-j\pi/4} \exp\left[j\pi \left(\gamma x^2 - 2\beta xy + \alpha y^2 \right) \right], \tag{2}$$

where parameter matrix

$$A = \begin{pmatrix} a & b \\ c & d \end{pmatrix} = \begin{pmatrix} \dfrac{\gamma}{\beta} & \dfrac{1}{\beta} \\ -\beta + \dfrac{\alpha\gamma}{\beta} & \dfrac{\alpha}{\beta} \end{pmatrix}. \tag{3}$$

Two of interesting and important properties of LCT are reversibility and index additivity. Index additivity means that, if two LCTs with matrices A_1, A_2 operate in a successive manner, then the equivalent transform is an LCT with the matrix $A = A_1 A_2$. Because of the index additivity, the inverse of the LCT with matrix A is an LCT with the matrix A^{-1}.

With the development of the fractional signal processing method, the properties and applications of the LCT have been investigated in detail; for more information associated with the continuous LCT, one can refer to [14, 15, 20].

2.2. The Discrete LCT. Besides the continuous LCT, we often encounter the computation of the discrete LCT because we must process discrete data by computer. There are lots of discrete and the fast LCT methods proposed in the literature [21, 23, 24]. If we set $\delta_x = \delta_y = (N|\beta|)^{-1/2}$, $x = n\delta_x$, $y = m\delta_y$, and $m, n = 0, 1, \ldots, N-1$, the N point discrete LCT (DLCT) of $f(n)$ can be defined as [23]

$$f_A(m) = \sum_{n=0}^{N-1} f(n) C_A(m,n), \tag{4}$$

where

$$C_A(m,n) = \frac{\sqrt{\beta} e^{-(j\pi/4)}}{\sqrt{N|\beta|}} \exp\left[j\pi \frac{1}{N|\beta|} \left(\alpha m^2 - 2\beta mn + \gamma n^2 \right) \right]. \tag{5}$$

This kind of DLCT method is available for image processing, because it is interval-independent and unitary. Moreover, it also has the property of index additivity.

Following this method, the two-dimensional DLCT of a size $H \times N$ image $I(h,n)$ can be rewritten as

$$I_A(k,l) = \sum_{n=0}^{N-1} C_A(l,n) \sum_{h=0}^{H-1} I(h,n) C_A(k,m) \tag{6}$$

with $k = 0, 1, \ldots, H-1$, $l = 0, 1, \ldots, N-1$, and $C_A(k,m)$, $C_A(l,n)$ being the same as (4). It is shown in [23] that this kind of DLCT is analogous to the DFT and approximates the continuous LCT in the same sense that the DFT approximates the continuous Fourier transform. We will use this method to compute the 2D LCT of an image in the following sections.

3. Watermark Embedding and Detecting

It is well known that the watermarking process contains the watermark embedding and detecting steps; we propose a new kind of watermarking scheme following the idea of [18] in this section.

3.1. Watermark Embedding. The watermark itself is a sequence of M complex numbers [18], denoted by $s_i = c_i + jd_i$, $i = 1, 2, \ldots, M$, and the real and imaginary parts of s_i are obtained from a normal distribution with mean zero

and variance $\sigma^2/2$. In order to embed this watermark into an image I of size $H \times N$, we first computed the DLCT of this image I to derive the transform coefficients $\{S_i : i = 1 \times N\}$ and then reordered the transform coefficients in nonincreasing sequence as follows:

$$S_i = C_i + jD_i : |S_i| \leq |S_{i+1}|, \quad i = 1, 2 \ldots H \times N. \tag{7}$$

Similar with the method in [16], we chose the middle reordered transform coefficients to embed the watermarks; in other words, we embed the watermark into the coefficients $S_i, i = L+1, L+2, \ldots, L+M$. This is because if we embedded the watermarks in the lowest coefficients, they would be sensitive to noise removing or compressing operations, while if we embedded the watermarks in the highest coefficients, they would significantly affect the imperceptibility of the watermarks. So, the watermarks were embedded as follows:

$$S_i^w = S_i + c_i |C_i| + jd_i |D_i|, \quad i = L+1, \ldots, L+M, \tag{8}$$

where S_i^w is the watermarked image of I and (c_i, d_i) is the watermarks sequence.

3.2. Watermark Detecting. When the watermark is embedded in the image, then the image is transferred to the watermark detection process to see whether it contains watermark. The detection of the watermark can be described like this: given the watermarked image I^a, maybe under some attacks such as low pass and median filtering, addition of Gaussian noise, and resizing, we compute the DLCT of I^a and obtain the transform coefficients S^a and then compute the detection value [16]:

$$d = \sum_{i=L+1}^{L+M} (c_i - jd_i) S_i^{(a)}. \tag{9}$$

The threshold can be achieved according to the statistical performance of the proposed algorithm. The expected value of d is

$$E[d] = \frac{\sigma^2}{2} \sum_{i=L+1}^{L+M} (|C_i| + |D_i|). \tag{10}$$

In [16], Djurovic et al. propose a useful and simple threshold as $E[d]/2$; when the value of d is larger than the threshold, it is decided that a watermark has been detected. Otherwise, there is no watermark. However, it is shown in [18] that this kind of threshold suffers from the false conclusion; therefore we use an adaptive threshold proposed in [18], because it is more practical when we deal with the image after some attacks. Therefore, the threshold can be computed by the following steps.

(i) First, we compute the value of d of all the random watermarks (maybe 1000 watermarks).

(ii) Then, we compute the average (say μ) and the standard deviation (say σ) of these d.

(iii) At last, we can achieve the threshold $\tau = \mu + p\sigma$ where p is a suitable number.

4. Simulation Examples

4.1. Watermark Embedding and Detecting. The Lena (512×512) was chosen as the test image in the simulations. According to some experiments, the value of p in threshold $\tau = \mu + p\sigma$ was chosen to be 5. The 2D DLCT parameters are $\alpha_1 = \alpha_2 = 0.2, \beta_1 = \beta_2 = 0.6, \gamma_1 = \gamma_2 = 0.1$ and can be described as $(\alpha_1, \beta_1, \gamma_1, \alpha_2, \beta_2, \gamma_2) = (0.2, 0.6, 0.1, 0.2, 0.6, 0.1)$. Therefore, the 2D DLCT parameter matrixes can be rewritten as

$$A_1 = A_2 = \begin{pmatrix} \frac{\gamma}{\beta} & \frac{1}{\beta} \\ -\beta + \frac{\alpha\gamma}{\beta} & \frac{\alpha}{\beta} \end{pmatrix} = \begin{pmatrix} \frac{1}{6} & \frac{5}{3} \\ -\frac{17}{30} & \frac{1}{3} \end{pmatrix}, \tag{11}$$

and the 2D DLCT is performed based on (6). The simulations performed using Matlab version 7.5.0 in Windows 8 system and the processer of the system is Intel(R) Core(TM) i5-3337U; the CPU and the RAM of the system are 1.80 GHz and 4.00 GB, respectively. We chose $L = 96000$, $M = 12000$, $\sigma^2 = 60$ in the simulation. In order to test the performance of the proposed method, we use the PSNR and the elapsed time of the process to measure the performance of the watermarking technology [18].

The original and watermarked images are shown in Figures 1(a) and 1(b), respectively. It is shown that the watermarked picture Figure 1(b) is almost the same as the original Figure 1(a). The detection of the correct watermark from the watermarked image over the other 1000 different watermarks, which are also Gaussian white noise with variance $\sigma_G^2 = \sigma^2/2 = 30$. The detection result is plotted in Figure 2. In this case, the PSNR and the elapsed time are 39.27 dB and 16.147 seconds, respectively.

In Figure 2, we can easily find that the detection value of the correct watermark is significantly larger than the threshold and other false watermarks. So, the watermark can be detected by the comparison.

4.2. The Robustness. In this subsection, we investigate the robustness of the algorithm after the following attacks: adding noise, upper cropping, central cropping, and central cropping after adding noise. These experiments have been performed as the following.

Firstly, Figures 3 and 4 plot the robustness of the watermarking under the Gaussian noise. Figure 3(a) is the noisy image of the watermarked image in Figure 1(b) by adding mean zero and variance 200 Gaussian noise, while the variance of Figure 4(a) is 600. Figures 3(b) and 4(b) are detection results of these two situations, the PSNR are 19.76 dB and 15.08 dB, the elapsed times are 9.75 and 26.82 seconds, respectively. This result shows that the method is robust against noise, because the watermark can be still detected.

Secondly, we cropped the watermarked image Figure 1(b) from the size 512×512 to 412×212 and 212×212, and obtain Figures 5(a) and 6(a), respectively. The detection results are shown in Figures 5(b) and 6(b), respectively. It is shown in Figures 5 and 6 that the watermark can also be detected. In this situation, the PSNR are 1.51 dB and 0.82 dB, the elapsed time are 28.70 and 29.65 seconds, respectively.

(a) (b)

Figure 1: (a) The original image of "Lena", (b) the watermarked image of "Lena".

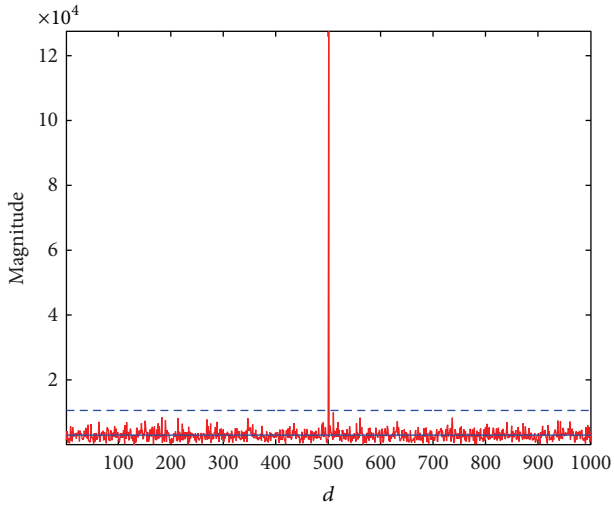

Figure 2: The detection result from the watermarked Figure 1(b).

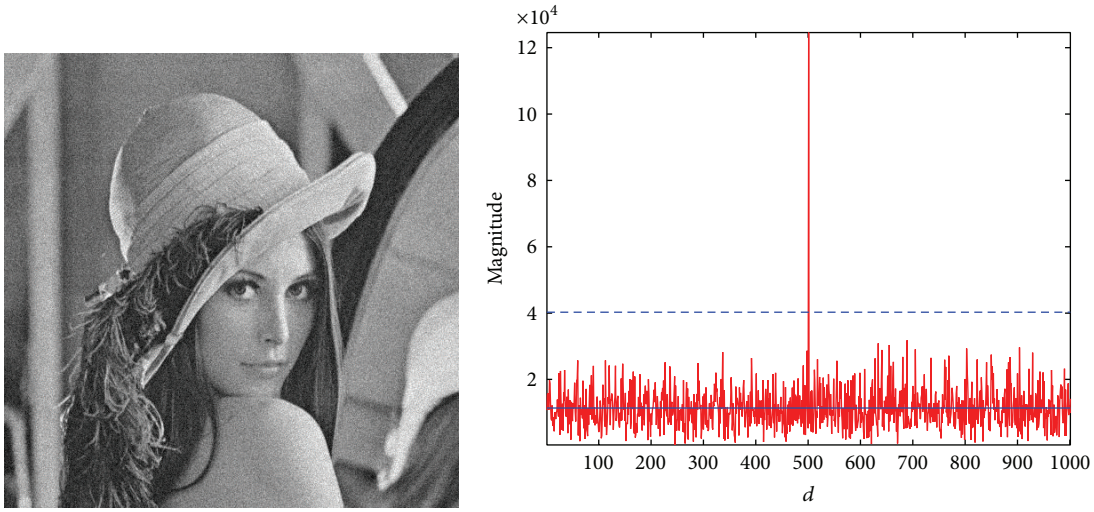

(a) (b)

Figure 3: (a) The noisy "Lena," var = 200. (b) The detection of the noisy "Lena."

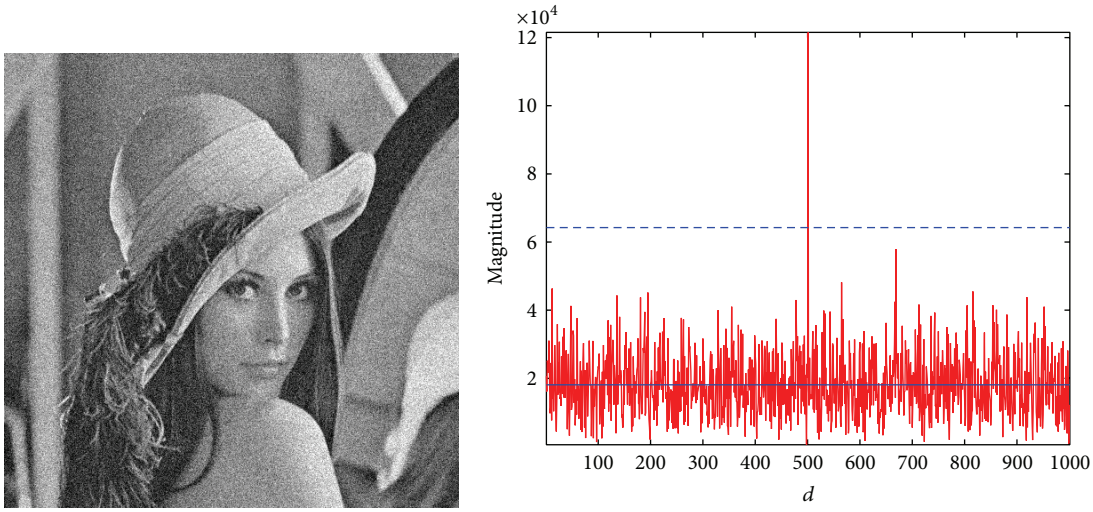

(a) (b)

Figure 4: (a) The noisy "Lena," var = 600. (b) The detection of the noisy "Lena."

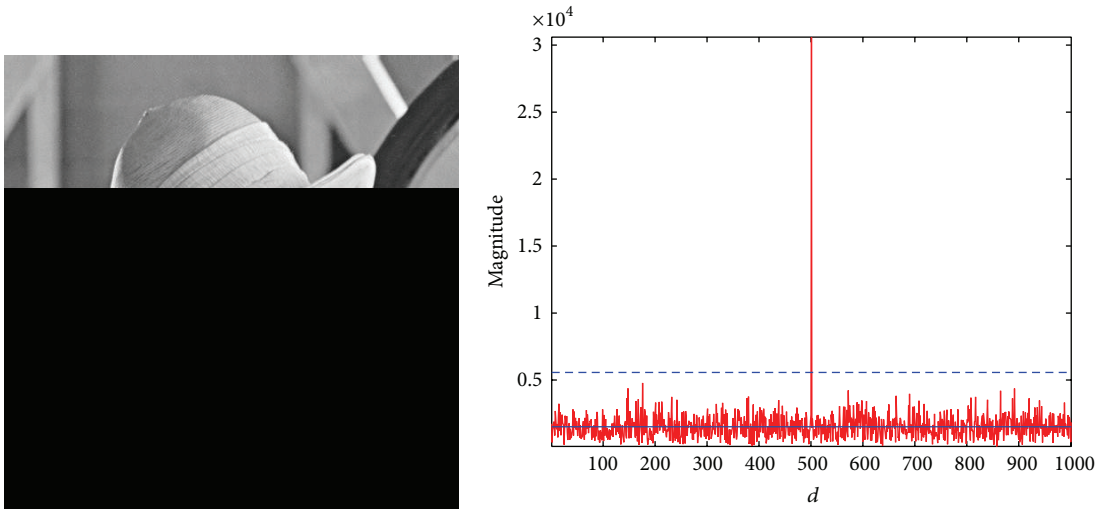

(a) (b)

Figure 5: (a) The upper cropped image of Figure 1(b). (b) The detection of upcropped image.

Thirdly, we perform the upper cropping of the noisy image in Figures 3(a) and 4(a) in the same way as in Figure 5(a) and obtain Figures 7(a) and 8(a). The detection results are plotted in Figures 7(b) and 8(b), respectively. It is shown in Figure 7 that the watermark can also be detected for the upper cropped noisy watermarked image of variance 200. We can still detect the watermark for the upper cropped noisy image of variance 600 as shown in Figure 8. In this situation, the PSNR are 1.50 dB and 1.48 dB, and the elapsed times are 28.70 and 29.288 seconds, respectively.

Lastly, we central crop the noisy image in Figures 3(a) and 4(a) in the same way as in Figure 6(a) and obtain Figures 9(a) and 10(a). The detection results are plotted in Figure 9(b) and Figure 10(b), respectively. It is shown in Figure 9 that the watermark can also be detected for the central cropped noisy watermarked image of variance 200. We can still detect the watermark for the central cropped noisy image of variance 600 as shown in Figure 10. In this situation, the PSNR are 0.8 dB and 0.78 dB, and the elapsed times are 29.45 and 29.03 seconds, respectively.

From these simulations, it can be concluded that the proposed method is robust under the common image attacks, such as the noise, crops, and the crops of the noisy image. It should be also noticed from Figures 8 and 10 that the proposed method still works under the attack of cropping if the variance of the adding noise is about 600.

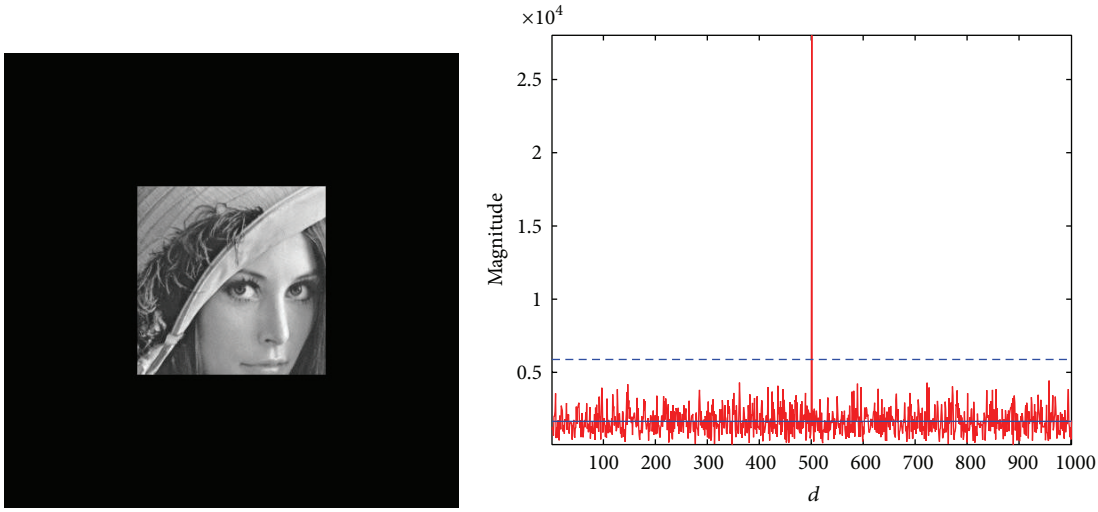

(a) (b)

Figure 6: (a) The central cropped image of Figure 1(b). (b) The detection of central cropped image.

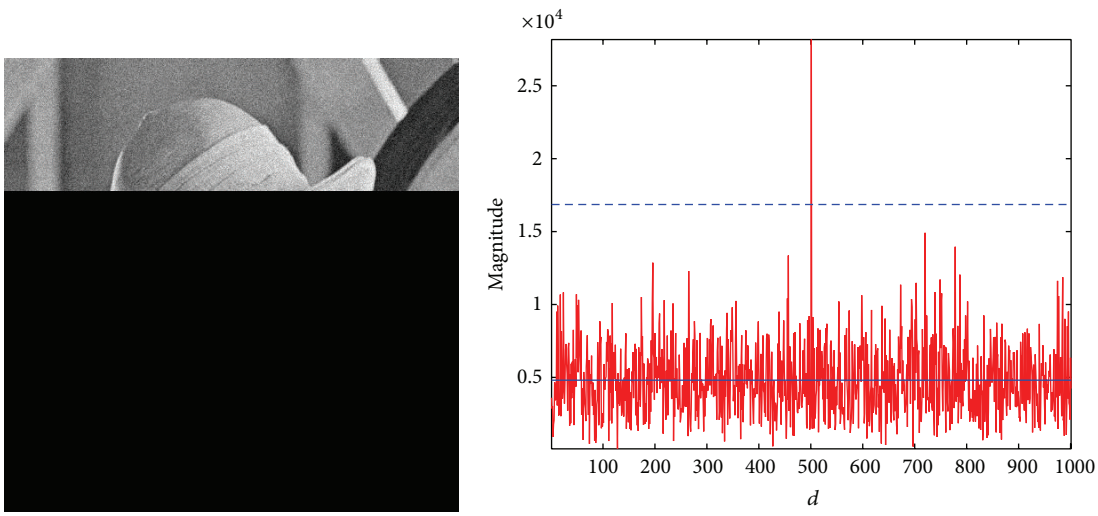

(a) (b)

Figure 7: (a) The upper cropped noisy "Lena" of Figure 3(a). (b) The detection of the upcropped noisy "Lena."

4.3. The Parameters' Sensitivity. As compared to the traditional watermarking method, for example, the DFT and DCT domain method [5–8], the advantage of the proposed method is that it has three more free parameters, and this can enhance the security and robustness of the watermarking images. It is well known that the parameters of the LCT are two more than the parameters of the FRFT, and for the 2D-LCT there are six parameters. So, when we need to detect the watermarks, we not only need the watermarked keys but also need the six parameters which is three times the number of the FRFT's parameter. Therefore, it is more difficult for the unauthorized person to detect the watermark and destroy it.

In order to show the advantage of the LCT based watermarking method proposed in this paper, the sensitivity of the parameter $(\alpha_1, \beta_1, \gamma_1, \alpha_2, \beta_2, \gamma_2)$ is discussed in this subsection. We use the watermarked image in Figure 1(b) as tested image, we set $(\alpha_2, \beta_2, \gamma_2) = (0.2, 0.6, 0.1)$, and do not know the value of α_1, β_1, and γ_1 in simulations; the value of d is sensitive with the α_1, β_1, and γ_1 as plotted in Figure 11.

It is shown in Figure 11 that the value of d is significantly larger when the value of α_1, β_1, and γ_1 are more correct than the false values of the parameters. For example, when the unauthorized people know $(\beta_1, \gamma_1, \alpha_2, \beta_2, \gamma_2) = (0.6, 0.1, 0.2, 0.6, 0.1)$, the correct place of the watermark, and the correct watermark but not sure about the value of α_1, the watermark still cannot be detected because only the d value of correct α_1 can reach the peak according to Figure 11(a). We can also see that the sensitivity of α_1 and β_1 is good, while

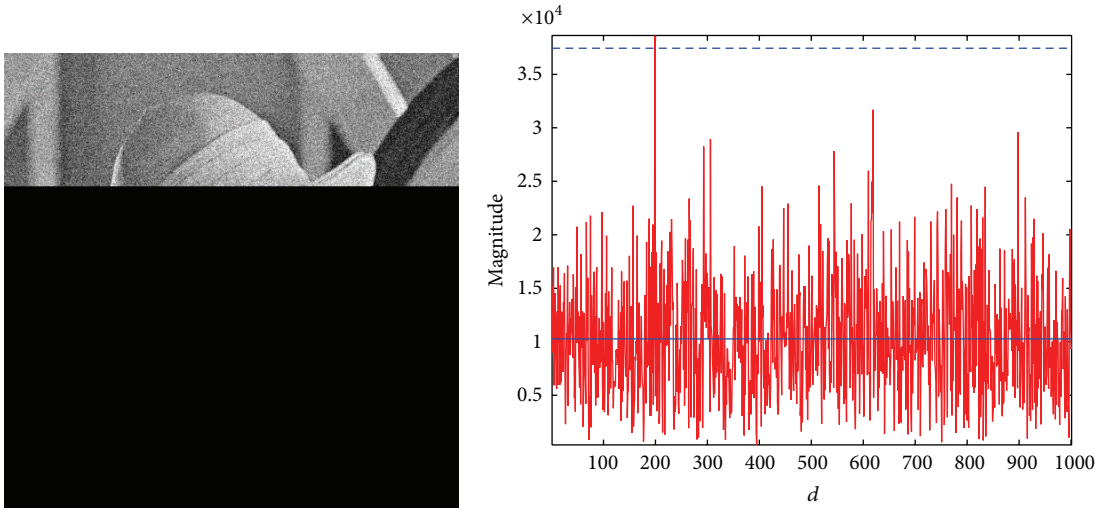

(a) (b)

Figure 8: (a) The upcropped noisy "Lena" of Figure 4(a). (b) The detection of the upcropped noisy "Lena."

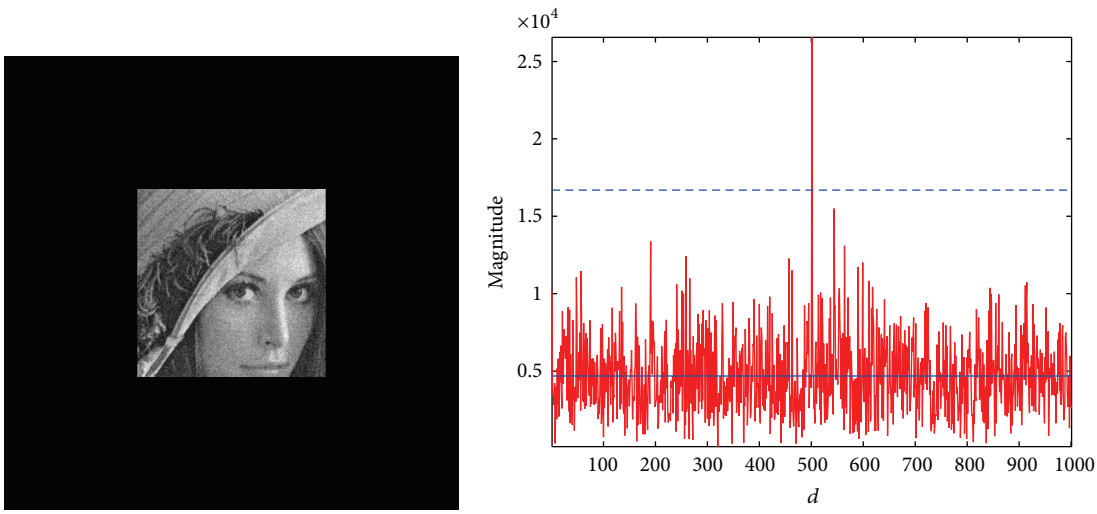

(a) (b)

Figure 9: (a) The central cropped noisy "Lena" of Figure 3(a). (b) The detection of the central cropped noisy "Lena."

the sensitivity of γ_1 is not so gratifying especially when γ_1 is between 0.25 and 0.5 in Figure 11(c).

5. Conclusion

A novel watermarking technique based on the discrete LCT is proposed in this paper. In this kind of method, the watermarks are embedded in the middle coefficients in the transform domain, and the detecting threshold is determined adaptively. The simulations for the robustness of the proposed method under the common image processing are performed, and the simulation results fit the theories well. The proposed watermarking is more secure than the watermarking based on FRFT or DCT domain because it has more free parameters. We also discussed the parameter's sensitivity of the proposed method in the paper and showed that this kind of watermarking method is sensitive to the parameters of the LCT.

Conflict of Interests

The authors declare that there is no conflict of interests regarding the publication of this paper.

Acknowledgments

This work was supported by the National Natural Science Foundation of China (no. 61072097 and no. 61171195) and

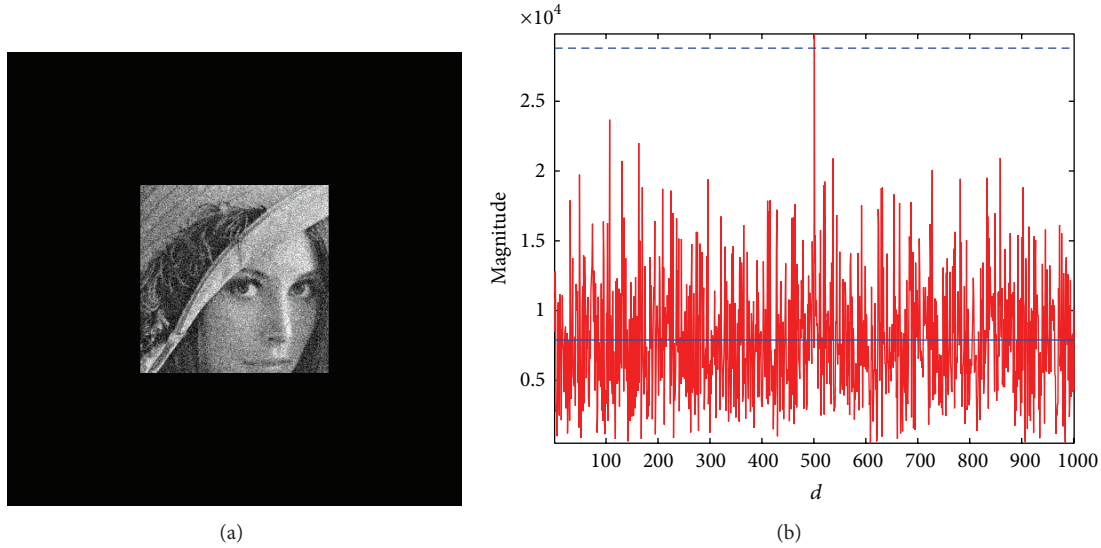

Figure 10: (a) The central cropped noisy "Lena" of Figure 4(a). (b) The detection of the central cropped noisy "Lena."

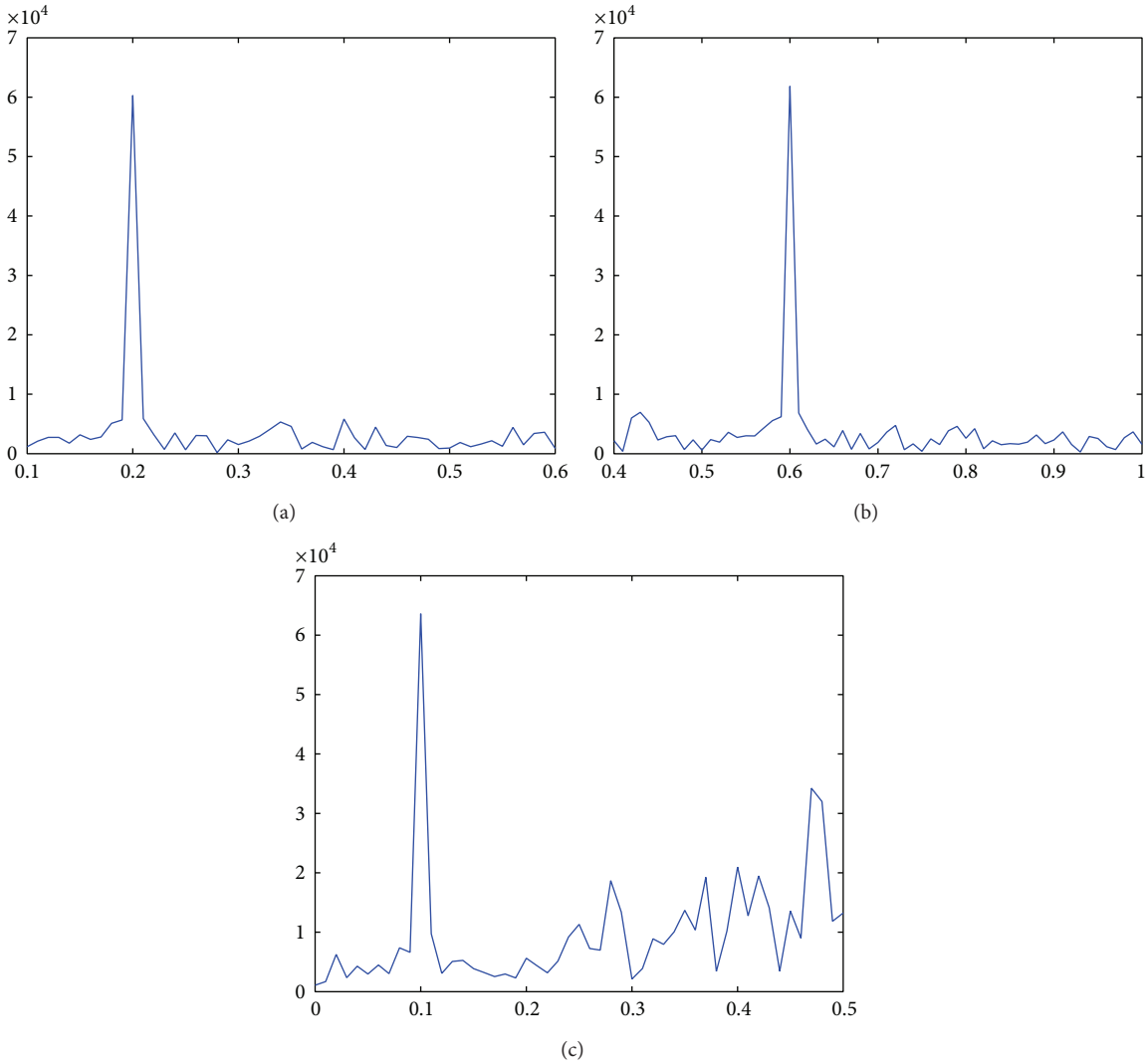

Figure 11: The sensitivity of parameters. (a) The sensitivity of α_1, (b) the sensitivity of β_1, and (c) the sensitivity of γ_1.

is also supported by Program for New Century Excellent Talents in University (no. NCET-12-0042).

References

[1] I. J. Cox, J. Kilian, T. Leighton, and T. Shamoon, "Secure spread spectrum watermarking for images, audio and video," in *Proceedings of the IEEE International Conference on Image Processing (ICIP '96)*, vol. 3, pp. 243–246, Lausanne, Switzerland, September 1996.

[2] K. Eckhard, J. Rindfrey, and J. Zhao, "Copyright protection for multimedia data," in *Proceedings of the International Conference on Digital Media and Electronic Publishing*, vol. 32, 1994.

[3] I. J. Cox, J. Kilian, F. T. Leighton, and T. Shamoon, "Secure spread spectrum watermarking for multimedia," *IEEE Transactions on Image Processing*, vol. 6, no. 12, pp. 1673–1687, 1997.

[4] J. J. K. O'Ruanaidh, W. J. Dowling, and F. M. Boland, "Phase watermarking of digital images," in *Proceedings of the IEEE International Conference on Image Processing (ICIP '96)*, vol. 3, pp. 239–242, Lausanne, Switzerland, September 1996.

[5] V. Solachidis and I. Pitas, "Circularly symmetric watermark embedding in 2-D DFT domain," *IEEE Transactions on Image Processing*, vol. 10, no. 11, pp. 1741–1753, 2001.

[6] S. Liu, B. M. Hennelly, and J. T. Sheridan, "Digital image watermarking spread-space technique based on double random phase encoding," *Optical Communications*, vol. 300, pp. 162–177, 2013.

[7] M. Barni, F. Bartolini, V. Cappellini, and A. Piva, "A DCT-domain system for robust image watermarking," *Signal Processing*, vol. 66, no. 3, pp. 357–372, 1998.

[8] A. Piva, M. Barni, F. Bartolini, and V. Cappellini, "DCT-based watermark recovering without resorting to the uncorrupted original image," in *Proceedings of the International Conference on Image Processing*, vol. 1, pp. 520–523, October 1997.

[9] M. Kutter, "Watermarking world," http://www.watermarking-world.org/.

[10] C. Candan, M. A. Kutay, and H. M. Ozaktas, "The discrete fractional Fourier transform," *IEEE Transactions on Signal Processing*, vol. 48, no. 5, pp. 1329–1337, 2000.

[11] H. M. Ozaktas, N. Erkaya, and M. A. Kutay, "Effect of fractional Fourier transformation on time-frequency distributions belonging to the Cohen class," *IEEE Signal Processing Letters*, vol. 3, no. 2, pp. 40–41, 1996.

[12] H. Ozaktas and D. Mendlovic, "Fractional Fourier transforms and their optical implementation. II," *Journal of the Optical Society of America A*, vol. 10, no. 12, pp. 2522–2531, 1993.

[13] S.-C. Pei, C.-C. Tseng, M.-H. Yeh, and J.-J. Shyu, "Discrete fractional hartley and fourier transforms," *IEEE Transactions on Circuits and Systems II: Analog and Digital Signal Processing*, vol. 45, no. 6, pp. 665–675, 1998.

[14] H. M. Ozaktas, M. A. Kutay, and Z. Zalevsky, *The Fractional Fourier Transform With Applications in Optics and Signal Processing*, Wiley, New York, NY, USA, 2000.

[15] R. Tao, B. Deng, and Y. Wang, *Fractional Fourier Transform and Its Applications*, University Press, Beijing, China, 2009.

[16] I. Djurovic, S. Stankovic, and I. Pitas, "Digital watermarking in the fractional Fourier transformation domain," *Journal of Network and Computer Applications*, vol. 24, no. 2, pp. 167–173, 2001.

[17] M. A. Savelonas and S. Chountasis, "Noise-resistant watermarking in the fractional Fourier domain utilizing moment-based image representation," *Signal Processing*, vol. 90, no. 8, pp. 2521–2528, 2010.

[18] A. Bultheel, "Digital watermarking of images in the fractional Fourier domain," TW Report TW497, 2007.

[19] N. K. Nishchal, "Hierarchical encrypted image watermarking using fractional Fourier domain random phase encoding," *Optical Engineering*, vol. 50, no. 9, Article ID 097003, 2011.

[20] T.-Z. Xu and B.-Z. Li, *Linear Canonical Transform and Its Applications*, Science Press, Beijing, China, 2013.

[21] S.-C. Pei and J.-J. Ding, "Closed-form discrete fractional and affine Fourier transforms," *IEEE Transactions on Signal Processing*, vol. 48, no. 5, pp. 1338–1353, 2000.

[22] A. Koç, H. M. Ozaktas, C. Candan, and M. A. Kutay, "Digital computation of linear canonical transforms," *IEEE Transactions on Signal Processing*, vol. 56, no. 6, pp. 2383–2394, 2008.

[23] F. S. Oktem and H. M. Ozaktas, "Exact relation between continuous and discrete linear canonical transforms," *IEEE Signal Processing Letters*, vol. 16, no. 8, pp. 727–730, 2009.

[24] J. J. Healy and J. T. Sheridan, "Sampling and discretization of the linear canonical transform," *Signal Processing*, vol. 89, no. 4, pp. 641–648, 2009.

[25] B.-Z. Li, R. Tao, and Y. Wang, "New sampling formulae related to linear canonical transform," *Signal Processing*, vol. 87, no. 5, pp. 983–990, 2007.

[26] A. Stern, "Sampling of linear canonical transformed signals," *Signal Processing*, vol. 86, no. 7, pp. 1421–1425, 2006.

[27] R. Tao, B.-Z. Li, Y. Wang, and G. K. Aggrey, "On sampling of band-limited signals associated with the linear canonical transform," *IEEE Transactions on Signal Processing*, vol. 56, no. 11, pp. 5454–5464, 2008.

[28] B.-Z. Li and T.-Z. Xu, "Spectral analysis of sampled signals in the linear canonical transform domain," *Mathematical Problems in Engineering*, vol. 2012, Article ID 536464, 19 pages, 2012.

[29] B.-Z. Li and T.-Z. Xu, "Sampling in the linear canonical transform domain," *Mathematical Problems in Engineering*, vol. 2012, Article ID 504580, 13 pages, 2012.

[30] S.-C. Pei and J.-J. Ding, "Eigenfunctions of linear canonical transform," *IEEE Transactions on Signal Processing*, vol. 50, no. 1, pp. 11–26, 2002.

[31] D. Wei, Q. Ran, Y. Li, J. Ma, and L. Tan, "A convolution and product theorem for the linear canonical transform," *IEEE Signal Processing Letters*, vol. 16, no. 10, pp. 853–856, 2009.

[32] B. Deng, R. Tao, and Y. Wang, "Convolution theorems for the linear canonical transform and their applications," *Science in China. Series F. Information Sciences*, vol. 49, no. 5, pp. 592–603, 2006.

[33] J. Zhao, R. Tao, Y.-L. Li, and Y. Wang, "Uncertainty principles for linear canonical transform," *IEEE Transactions on Signal Processing*, vol. 57, no. 7, pp. 2856–2858, 2009.

Hindawi Publishing Corporation
Mathematical Problems in Engineering
Volume 2014, Article ID 705364, 7 pages
http://dx.doi.org/10.1155/2014/705364

Research Article

Fundamental Solutions to Time-Fractional Advection Diffusion Equation in a Case of Two Space Variables

Y. Z. Povstenko

Institute of Mathematics and Computer Science, Jan Długosz University in Częstochowa, Waszyngtona 4/8, 42-200 Częstochowa, Poland

Correspondence should be addressed to Y. Z. Povstenko; j.povstenko@ajd.czest.pl

Received 28 December 2013; Accepted 6 February 2014; Published 11 March 2014

Academic Editor: J. A. Tenreiro Machado

The fundamental solutions to time-fractional advection diffusion equation in a plane and a half-plane are obtained using the Laplace integral transform with respect to time t and the Fourier transforms with respect to the space coordinates x and y. The Cauchy, source, and Dirichlet problems are investigated. The solutions are expressed in terms of integrals of Bessel functions combined with Mittag-Leffler functions. Numerical results are illustrated graphically.

1. Introduction

The classical advection diffusion equation

$$\frac{\partial c}{\partial t} = a\Delta c - \mathbf{v}\cdot\nabla c, \tag{1}$$

where a is the diffusivity coefficient, $\mathbf{v}$ is the velocity vector, has several physical interpretations in terms of Brownian motion, diffusion or heat transport with external force or with additional velocity field, diffusion of charge in the electrical field on comb structure, transport processes in porous media, groundwater hydrology, and so forth [1–7].

In the case of one spatial coordinate x, (1) has the following form:

$$\frac{\partial c}{\partial t} = a\,\frac{\partial^2 c}{\partial x^2} - v\,\frac{\partial c}{\partial x}. \tag{2}$$

Investigation of different physical phenomena in media with complex internal structure has led to considering differential equations with derivatives of fractional order. The space-fractional [8–19], time-fractional [20–31], and space-time-fractional [32–39] generalizations of the advection diffusion equation were studied by many authors. In the majority of the abovementioned papers, the fractional generalizations of one-dimensional equation (2) were considered. In the papers dealing with space-fractional or space-time-fractional equations, one term with space derivative was substituted by the corresponding term with the fractional derivative [8, 9, 11–19, 33, 39] or both terms with space derivatives had fractional order [32, 35–38]. Several numerical schemes were proposed: the implicit difference method based on the shifted Grünwald-Letnikov approximation [14, 37], the explicit difference scheme [37], transformation of fractional differential equation into a system of ordinary differential equations and using the method of lines [15], the random walk algorithms [16, 17], the spectral regularization method [28], the Crank-Nicholson difference scheme [29], Adomian's decomposition [26], a spatial and temporal discretization [30, 39], the fractional variational iteration method [31], and the homotopy perturbation method [27, 38].

In [24, 25], the analytical solution to one-dimensional time-fractional advection diffusion equation was obtained in terms of integrals of the H-function.

In this paper, we study the fundamental solutions to time-fractional advection diffusion equation

$$\frac{\partial^\alpha c}{\partial t^\alpha} = a\,\Delta c - \mathbf{v}\cdot\nabla c \tag{3}$$

in a plane and a half-plane. The Laplace transform with respect to time and the Fourier transform with respect to the space coordinates are used. The Cauchy and the source problems in a plane and the Dirichlet problem for a half-plane are solved. The analytical solutions are expressed in terms of

integrals of the Mittag-Leffler functions. Numerical results are illustrated graphically.

In (3) we use the Caputo fractional derivative [40–42]:

$$\frac{\mathrm{d}^{\alpha}c(t)}{\mathrm{d}t^{\alpha}} = \begin{cases} \dfrac{1}{\Gamma(n-\alpha)}\displaystyle\int_0^t (t-\tau)^{n-\alpha-1}\frac{\mathrm{d}^n c(\tau)}{\mathrm{d}\tau^n}\mathrm{d}\tau, \\ \qquad n-1<\alpha<n, \\ \dfrac{\mathrm{d}^n c(t)}{\mathrm{d}t^n}, \qquad \alpha = n, \end{cases} \tag{4}$$

where $\Gamma(\alpha)$ is the gamma function. For its Laplace transform rule, the Caputo fractional derivative requires the knowledge of the initial values of the function $c(t)$ and its integer derivatives of order $k = 1, 2, \ldots, n-1$:

$$\mathscr{L}\left\{\frac{\mathrm{d}^{\alpha}c(t)}{\mathrm{d}t^{\alpha}}\right\} = s^{\alpha}\mathscr{L}\{c(t)\} - \sum_{k=0}^{n-1} c^{(k)}(0^+)\, s^{\alpha-1-k}, \qquad n-1<\alpha<n, \tag{5}$$

where s is the transform variable.

2. The Fundamental Solution to the Cauchy Problem

Consider the time-fractional advection diffusion equation

$$\frac{\partial^{\alpha}c}{\partial t^{\alpha}} = a\left(\frac{\partial^2 c}{\partial x^2} + \frac{\partial^2 c}{\partial y^2}\right) - v\,\frac{\partial c}{\partial x} - v\,\frac{\partial c}{\partial y}, \qquad -\infty<x<\infty,\ -\infty<y<\infty, \qquad 0<t<\infty,\ 0<\alpha\le 1, \tag{6}$$

under initial condition

$$t = 0: \quad c = p_0\delta(x)\,\delta(y). \tag{7}$$

In (7) we have introduced the constant multiplier p_0 to obtain the nondimensional quantity $\bar{c}$ (see (23)) displayed in Figures.

The zero conditions at infinity are also imposed:

$$\lim_{x\to\pm\infty} c(x,y,t) = 0, \qquad \lim_{y\to\pm\infty} c(x,y,t) = 0. \tag{8}$$

Introducing the new sought function

$$c(x,y,t) = \exp\left[\frac{v(x+y)}{2a}\right] u(x,y,t) \tag{9}$$

and taking into account that for the Dirac delta function, $f(x)\delta(x) = f(0)\delta(x)$, the initial-value problem (6)–(8) is reduced to the following ones:

$$\frac{\partial^{\alpha}u}{\partial t^{\alpha}} = a\left(\frac{\partial^2 u}{\partial x^2} + \frac{\partial^2 u}{\partial y^2}\right) - \frac{v^2}{2a}\,u, \tag{10}$$

$$t = 0: \quad u = p_0\delta(x)\,\delta(y), \tag{11}$$

$$\lim_{x\to\pm\infty} u(x,y,t) = 0, \qquad \lim_{y\to\pm\infty} u(x,y,t) = 0. \tag{12}$$

Next, we use the Laplace transform with respect to time t (designated by the asterisk) and the double exponential Fourier transform with respect to the space coordinates x and y (marked by the tilde). In the transform domain, we get

$$\tilde{\tilde{u}}^* = \frac{p_0}{2\pi}\,\frac{s^{\alpha-1}}{s^{\alpha} + a(\xi^2+\eta^2) + v^2/2a}. \tag{13}$$

Here, s is the Laplace transform variable and ξ and η are the Fourier transform variables.

Inversion of the integral transforms gives

$$u(x,y,t) = \frac{p_0}{4\pi^2}\int_{-\infty}^{\infty}\int_{-\infty}^{\infty} E_{\alpha}\left\{-\left[a\left(\xi^2+\eta^2\right) + \frac{v^2}{2a}\right]t^{\alpha}\right\} \times \cos(x\xi)\cos(y\eta)\,\mathrm{d}\xi\,\mathrm{d}\eta, \tag{14}$$

where the formula [40–42]

$$\mathscr{L}^{-1}\left\{\frac{s^{\alpha-1}}{s^{\alpha}+b}\right\} = E_{\alpha}\left(-bt^{\alpha}\right) \tag{15}$$

has been used with $E_{\alpha}(z)$ being the Mittag-Leffler function in one parameter α:

$$E_{\alpha}(z) = \sum_{k=0}^{\infty}\frac{z^k}{\Gamma(\alpha k+1)}, \quad \alpha>0,\ z\in C. \tag{16}$$

Solution (14) is not convenient for numerical calculations. To obtain the solution amenable to numerical treatment, we introduce the polar coordinates in the (ξ,η)-plane:

$$\xi = \rho\cos\theta, \qquad \eta = \rho\sin\theta. \tag{17}$$

Hence,

$$u(x,y,t) = \frac{p_0}{4\pi^2}\int_0^{\infty}\int_0^{2\pi} E_{\alpha}\left[-\left(a\rho^2 + \frac{v^2}{2a}\right)t^{\alpha}\right] \times \cos(x\rho\cos\theta)\cos(y\rho\sin\theta)\,\rho\,\mathrm{d}\rho\,\mathrm{d}\theta. \tag{18}$$

Due to periodic properties of the integrand

$$\int_0^{2\pi}\cos(x\rho\cos\theta)\cos(y\rho\sin\theta)\,\mathrm{d}\theta = 4\int_0^{\pi/2}\cos(x\rho\cos\theta)\cos(y\rho\sin\theta)\,\mathrm{d}\theta. \tag{19}$$

Changing variable $w = \sin\theta$ and taking into account the following integral [43]:

$$\int_0^1 \frac{\cos\left(p\,\sqrt{1-x^2}\right)}{\sqrt{1-x^2}}\cos(qx)\,\mathrm{d}x = \frac{\pi}{2}J_0\left(\sqrt{p^2+q^2}\right), \tag{20}$$

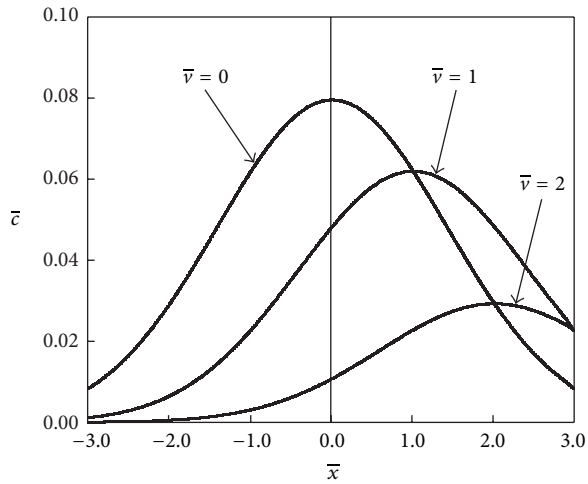

Figure 1: Dependence of the fundamental solution to the Cauchy problem on distance (the classical advection diffusion equation, $\alpha = 1$).

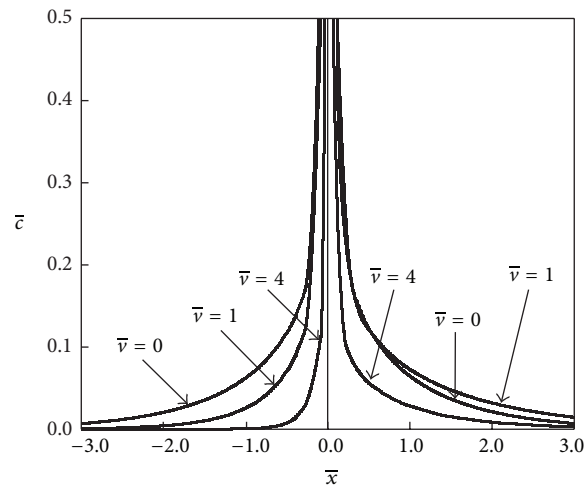

Figure 2: Dependence of the fundamental solution to the Cauchy problem on distance (the time-fractional advection diffusion equation, $\alpha = 0.5$).

where $J_n(z)$ is the Bessel function of the order n, we arrive at

$$u(x,y,t) = \frac{p_0}{2\pi}\int_0^\infty E_\alpha\left[-\left(a\rho^2 + \frac{v^2}{2a}\right)t^\alpha\right] \times J_0\left(\sqrt{x^2+y^2}\rho\right)\rho\,\mathrm{d}\rho \tag{21}$$

and, returning to the quantity $c(x,y,t)$ according to (9), we get

$$c(x,y,t) = \frac{p_0}{2\pi}\exp\left[\frac{v(x+y)}{2a}\right] \times \int_0^\infty E_\alpha\left[-\left(a\rho^2 + \frac{v^2}{2a}\right)t^\alpha\right] \times J_0\left(\sqrt{x^2+y^2}\rho\right)\rho\,\mathrm{d}\rho. \tag{22}$$

The particular case of solution (22) corresponding to the time-fractional diffusion equation ($v = 0$) was considered in [44, 45].

The results of numerical computations for $y = 0$ are presented in Figure 1 for $\alpha = 1$ and in Figure 2 for $\alpha = 0.5$.

The following nondimensional quantities:

$$\bar{c} = \frac{at^\alpha}{p_0}c, \qquad \bar{v} = \frac{t^{\alpha/2}}{\sqrt{a}}v \tag{23}$$

and the nondimensional coordinates (the similarity variables)

$$\bar{x} = \frac{x}{\sqrt{a}t^{\alpha/2}}, \qquad \bar{y} = \frac{y}{\sqrt{a}t^{\alpha/2}} \tag{24}$$

have been introduced.

To calculate the Mittag-Leffler function $E_\alpha(-x)$ in solution (22), we applied the algorithm suggested in [46].

3. The Fundamental Solution to the Source Problem

Consider the time-fractional advection diffusion equation with the source term

$$\begin{gathered}\frac{\partial^\alpha c}{\partial t^\alpha} = a\left(\frac{\partial^2 c}{\partial x^2} + \frac{\partial^2 c}{\partial y^2}\right) - v\frac{\partial c}{\partial x} - v\frac{\partial c}{\partial y} \\ + q_0\delta(x)\delta(y)\delta(t), \\ -\infty < x < \infty, \\ -\infty < y < \infty, \\ 0 < t < \infty,\ 0 < \alpha \le 1,\end{gathered} \tag{25}$$

under zero initial condition,

$$t = 0: \quad c = 0 \tag{26}$$

and conditions (8) at infinity.

The integral transform technique leads to

$$\tilde{\tilde{u}}^* = \frac{q_0}{2\pi}\frac{1}{s^\alpha + a(\xi^2+\eta^2) + v^2/2a}, \tag{27}$$

$$c(x,y,t) = \frac{q_0 t^{\alpha-1}}{2\pi}\exp\left[\frac{v(x+y)}{2a}\right] \times \int_0^\infty E_{\alpha,\alpha}\left[-\left(a\rho^2 + \frac{v^2}{2a}\right)t^\alpha\right] \times J_0\left(\sqrt{x^2+y^2}\rho\right)\rho\,\mathrm{d}\rho. \tag{28}$$

Here, $E_{\alpha,\beta}(z)$ is the generalized Mittag-Leffler function in two parameters α and β:

$$E_{\alpha,\beta}(z) = \sum_{k=0}^\infty \frac{z^k}{\Gamma(\alpha k + \beta)}, \quad \alpha > 0,\ \beta > 0,\ z \in C, \tag{29}$$

and the formula [40–42]

$$\mathscr{L}^{-1}\left\{\frac{s^{\alpha-\beta}}{s^{\alpha}+b}\right\}=t^{\beta-1}E_{\alpha,\beta}\left(-bt^{\alpha}\right) \tag{30}$$

for the inverse Laplace transform has been used.

The particular case of solution (28) corresponding to the time-fractional diffusion equation with $v=0$ was considered in [45, 47]. Solutions (22) and (28) coincide for $\alpha=1$.

The results of numerical computations for $y=0$ are presented in Figure 3 for $\alpha=0.5$ with

$$\bar{c}=\frac{at}{q_0}c. \tag{31}$$

4. The Fundamental Solution to the Dirichlet Problem

In this case the time-fractional advection diffusion equation,

$$\begin{gathered}\frac{\partial^{\alpha}c}{\partial t^{\alpha}}=a\left(\frac{\partial^2 c}{\partial x^2}+\frac{\partial^2 c}{\partial y^2}\right)-v\frac{\partial c}{\partial x}-v\frac{\partial c}{\partial y},\\ 0<x<\infty,\ -\infty<y<\infty,\\ 0<t<\infty,\ 0<\alpha\le 1,\end{gathered} \tag{32}$$

is considered under zero initial condition

$$t=0:\quad c=0 \tag{33}$$

and the Dirichlet boundary condition

$$x=0:\quad c=g_0\delta(y)\delta(t). \tag{34}$$

The zero conditions at infinity are imposed as follows:

$$\lim_{x\to\infty}c(x,y,t)=0,\qquad \lim_{y\to\pm\infty}c(x,y,t)=0. \tag{35}$$

As above, the new sought function u is introduced (see (9)), and, for (10) in the half-plane $x>0$, the Laplace transform with respect to time t, the exponential Fourier transform with respect to the spatial coordinate y, and the sin-Fourier transform with respect to the spatial coordinate x are used. In the transform domain, we get

$$\tilde{\bar{u}}^{*}=\frac{ag_0\xi}{\sqrt{2\pi}}\frac{1}{s^{\alpha}+a\left(\xi^2+\eta^2\right)+v^2/2a} \tag{36}$$

and, after inversion of the integral transforms,

$$\begin{aligned}u(x,y,t)&\\ =\frac{ag_0t^{\alpha-1}}{\pi^2}&\int_{-\infty}^{\infty}\int_0^{\infty}E_{\alpha,\alpha}\left\{-\left[a\left(\xi^2+\eta^2\right)+\frac{v^2}{2a}\right]t^{\alpha}\right\}\\ &\times\sin(x\xi)\cos(y\eta)\,\xi\,\mathrm{d}\xi\,\mathrm{d}\eta.\end{aligned} \tag{37}$$

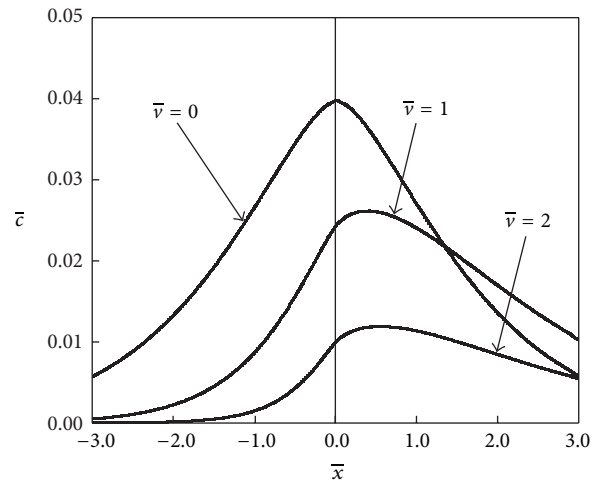

Figure 3: Dependence of the fundamental solution to the source problem on distance (the time-fractional advection diffusion equation, $\alpha=0.5$).

Introducing the polar coordinates in the (ξ,η)-plane gives

$$\begin{aligned}u(x,y,t)&\\ =\frac{ag_0t^{\alpha-1}}{\pi^2}&\int_0^{\infty}\int_0^{\pi}E_{\alpha}\left[-\left(a\rho^2+\frac{v^2}{2a}\right)t^{\alpha}\right]\\ &\times\sin(x\rho\cos\theta)\\ &\times\cos(y\rho\sin\theta)\,\rho^2\cos\theta\,\mathrm{d}\rho\,\mathrm{d}\theta.\end{aligned} \tag{38}$$

Changing variables $w=\sin\theta$ and taking into account the following integral [43]:

$$\begin{aligned}&\int_0^1\sin\left(p\sqrt{1-x^2}\right)\cos(qx)\,\mathrm{d}x\\ &\quad=\frac{\pi}{2}\frac{p}{\sqrt{p^2+q^2}}J_1\left(\sqrt{p^2+q^2}\right),\end{aligned} \tag{39}$$

we obtain

$$\begin{aligned}u(x,y,t)=\frac{ag_0t^{\alpha-1}x}{\pi\sqrt{x^2+y^2}}&\int_0^{\infty}E_{\alpha,\alpha}\left[-\left(a\rho^2+\frac{v^2}{2a}\right)t^{\alpha}\right]\\ &\times J_1\left(\sqrt{x^2+y^2}\rho\right)\rho^2\mathrm{d}\rho,\end{aligned} \tag{40}$$

$$\begin{aligned}c(x,y,t)=\frac{ag_0t^{\alpha-1}x}{\pi\sqrt{x^2+y^2}}&\exp\left[\frac{v(x+y)}{2a}\right]\\ &\times\int_0^{\infty}E_{\alpha,\alpha}\left[-\left(a\rho^2+\frac{v^2}{2a}\right)t^{\alpha}\right]\\ &\times J_1\left(\sqrt{x^2+y^2}\rho\right)\rho^2\mathrm{d}\rho.\end{aligned} \tag{41}$$

The particular case of solution (41) corresponding to the time-fractional diffusion equation ($v=0$) was considered in [48].

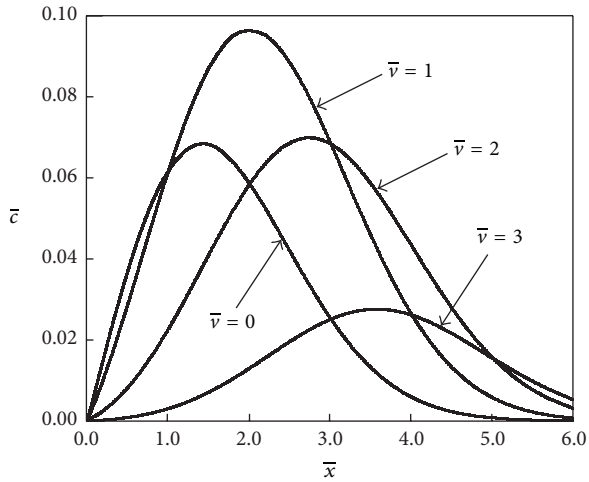

Figure 4: Dependence of the fundamental solution to the Dirichlet problem on distance (the classical advection diffusion equation, $\alpha = 1$).

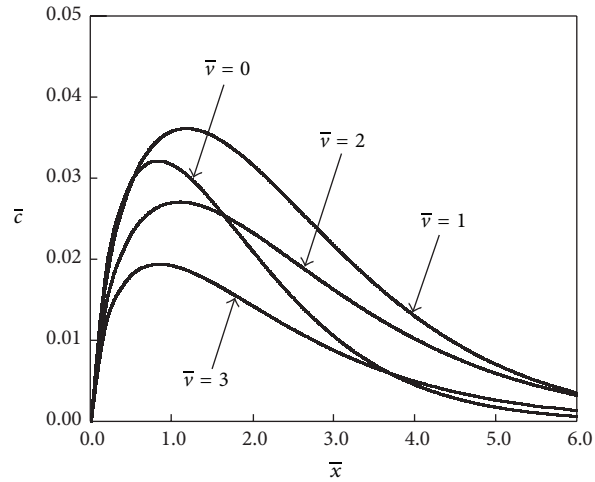

Figure 5: Dependence of the fundamental solution to the Dirichlet problem on distance (the time-fractional advection diffusion equation, $\alpha = 0.5$).

The results of numerical computations according to solution (41) for $y = 0$ are presented in Figure 4 for $\alpha = 1$ and in Figure 5 for $\alpha = 0.5$ with

$$\bar{c} = \frac{\sqrt{a}t^{1+\alpha/2}}{g_0}\, c. \tag{42}$$

Other nondimensional quantities are the same as in (23) and (24).

5. Conclusions

We have considered the time-fractional advection diffusion equation in a plane and in a half-plane. The fundamental solutions to the Cauchy problem and to the source problem in a plane have been obtained as well as to the Dirichlet problem in a half-plane. It should be emphasized that the fundamental solution to the Cauchy problem in the case $0 < \alpha < 1$ has the logarithmic singularity at the origin:

$$c(x, y, t) \sim -\frac{p_0}{2\pi\Gamma(1-\alpha)\, a t^{\alpha}} \exp\left[\frac{v(x+y)}{2a}\right] \times \ln\left(\sqrt{1+\frac{v^2 t^{\alpha}}{2a}}\, \frac{\sqrt{x^2+y^2}}{\sqrt{a}t^{\alpha/2}}\right). \tag{43}$$

This result is similar to the case of the time-fractional diffusion equation when $v = 0$ (see [44, 49]). Such a singularity disappears only for the classical advection diffusion equation ($\alpha = 1$). Due to singularity of the solution at the origin, in the case of $0 < \alpha < 1$, drift caused by the quantity v is less noticeable than in the case of $\alpha = 1$ (compare Figures 1 and 2).

Conflict of Interests

The author declares that there is no conflict of interests regarding the publication of this paper.

References

[1] W. Feller, *An Introduction to Probability Theory and Its Applications*, John Wiley & Sons, New York, NY, USA, 2nd edition, 1971.

[2] A. E. Scheidegger, *The Physics of Flow through Porous Media*, University of Toronto Press, Toronto, Canada, 3rd edition, 1974.

[3] N. G. van Kampen, *Stochastic Processes in Physics and Chemistry*, North-Holland, Amsterdam, The Netherlands, 1981.

[4] H. Risken, *The Fokker-Planck Equation*, Springer, Berlin, Germany, 1989.

[5] M. Kaviany, *Principles of Heat Transfer in Porous Media*, Springer, New York, NY, USA, 2nd edition, 1995.

[6] V. E. Arkhincheev, "Anomalous diffusion and charge relaxation on comb model: exact solutions," *Physica A*, vol. 280, no. 3, pp. 304–314, 2000.

[7] D. A. Nield and A. Bejan, *Convection in Porous Media*, Springer, New York, NY, USA, 3rd edition, 2006.

[8] A. S. Chaves, "A fractional diffusion equation to describe Lévy flights," *Physics Letters A*, vol. 239, no. 1-2, pp. 13–16, 1998.

[9] S. Jespersen, R. Metzler, and H. C. Fogedby, "Lévy flights in external force fields: Langevin and fractional Fokker-Planck equations and their solutions," *Physical Review E*, vol. 59, no. 3, pp. 2736–2745, 1999.

[10] V. V. Yanovsky, A. V. Chechkin, D. Schertzer, and A. V. Tur, "Lévy anomalous diffusion and fractional Fokker-Planck equation," *Physica A*, vol. 282, no. 1-2, pp. 13–34, 2000.

[11] D. A. Benson, S. W. Wheatcraft, and M. M. Meerschaert, "Application of a fractional advection-dispersion equation," *Water Resources Research*, vol. 36, no. 6, pp. 1403–1412, 2000.

[12] D. A. Benson, S. W. Wheatcraft, and M. M. Meerschaert, "The fractional-order governing equation of Lévy motion," *Water Resources Research*, vol. 36, no. 6, pp. 1413–1423, 2000.

[13] J. H. Cushman and T. R. Ginn, "Fractional advection-dispersion equation: a classical mass balance with convolution-Fickian flux," *Water Resources Research*, vol. 36, no. 12, pp. 3763–3766, 2000.

[14] M. M. Meerschaert and C. Tadjeran, "Finite difference approximations for fractional advection-dispersion flow equations," *Journal of Computational and Applied Mathematics*, vol. 172, no. 1, pp. 65–77, 2004.

[15] F. Liu, V. Anh, and I. Turner, "Numerical solution of the space fractional Fokker-Planck equation," *Journal of Computational and Applied Mathematics*, vol. 166, no. 1, pp. 209–219, 2004.

[16] Y. Zhang, D. A. Benson, M. M. Meerschaert, and H.-P. Scheffler, "On using random walks to solve the space-fractional advection-dispersion equations," *Journal of Statistical Physics*, vol. 123, no. 1, pp. 89–110, 2006.

[17] Q. Liu, F. Liu, I. Turner, and V. Anh, "Approximation of the Lévy-Feller advection-dispersion process by random walk and finite difference method," *Journal of Computational Physics*, vol. 222, no. 1, pp. 57–70, 2007.

[18] Y. Zhang, D. A. Benson, M. M. Meerschaert, and E. M. LaBolle, "Space-fractional advection-dispersion equations with variable parameters: diverse formulas, numerical solutions, and application to the Macrodispersion Experiment site data," *Water Resources Research*, vol. 43, no. 5, Article ID W05439, 2007.

[19] R. Schumer, M. M. Meerschaert, and B. Baeumer, "Fractional advection-dispersion equations for modeling transport at the Earth surface," *Journal of Geophysical Research*, vol. 114, no. 4, Article ID F00A07, 2009.

[20] G. Jumarie, "A Fokker-Planck equation of fractional order with respect to time," *Journal of Mathematical Physics*, vol. 33, no. 10, pp. 3536–3542, 1992.

[21] R. Metzler, E. Barkai, and J. Klafter, "Anomalous diffusion and relaxation close to thermal equilibrium: a fractional Fokker-Planck equation approach," *Physical Review Letters*, vol. 82, no. 18, pp. 3563–3567, 1999.

[22] E. Barkai, R. Metzler, and J. Klafter, "From continuous time random walks to the fractional Fokker-Planck equation," *Physical Review E*, vol. 61, no. 1, pp. 132–138, 2000.

[23] E. Barkai, "Fractional Fokker-Planck equation, solution, and application," *Physical Review E*, vol. 63, no. 4, Article ID 046118, 17 pages, 2001.

[24] F. Liu, V. Anh, I. Turner, and P. Zhuang, "Time fractional advection-dispersion equation," *Journal of Applied Mathematics and Computing*, vol. 13, no. 1-2, pp. 233–245, 2003.

[25] F. Huang and F. Liu, "The time fractional diffusion equation and the advection-dispersion equation," *ANZIAM Journal*, vol. 46, no. 3, pp. 317–330, 2005.

[26] S. Momani, "An algorithm for solving the fractional convection-diffusion equation with nonlinear source term," *Communications in Nonlinear Science and Numerical Simulation*, vol. 12, no. 7, pp. 1283–1290, 2007.

[27] S. Momani and A. Yıldırım, "Analytical approximate solutions of the fractional convection-diffusion equation with nonlinear source term by He's homotopy perturbation method," *International Journal of Computer Mathematics*, vol. 87, no. 5, pp. 1057–1065, 2010.

[28] G. H. Zheng and T. Wei, "Spectral regularization method for a Cauchy problem of the time fractional advection-dispersion equation," *Journal of Computational and Applied Mathematics*, vol. 233, no. 10, pp. 2631–2640, 2010.

[29] I. Karatay and S. R. Bayramoglu, "An efficient scheme for time fractional advection dispersion equations," *Applied Mathematics Sciences*, vol. 6, no. 98, pp. 4869–4878, 2012.

[30] H. Huang and X. Cao, "Numerical method for two dimensional fractional reaction subdiffusion equation," *European Physical Journal*, vol. 222, no. 8, pp. 1961–1973, 2013.

[31] M. Merdan, "Analytical approximate solutions of fractional convection-diffusion equation with modified Riemann-Liouville derivative by means of fractional variational iteration method," *Iranian Journal of Science & Technology*, no. 1, pp. 83–92, 2013.

[32] G. M. Zaslavsky, M. Edelman, and B. A. Niyazov, "Self-similarity, renormalization, and phase space nonuniformity of Hamiltonian chaotic dynamics," *Chaos*, vol. 7, no. 1, pp. 159–181, 1997.

[33] A. I. Saichev and G. M. Zaslavsky, "Fractional kinetic equations: solutions and applications," *Chaos*, vol. 7, no. 4, pp. 753–764, 1997.

[34] K. M. Kolwankar and A. D. Gangal, "Local fractional Fokker-Planck equation," *Physical Review Letters*, vol. 80, no. 2, pp. 214–217, 1998.

[35] D. Kusnezov, A. Bulgac, and G. D. Dang, "Quantum Lévy processes and fractional kinetics," *Physical Review Letters*, vol. 82, no. 6, pp. 1136–1139, 1999.

[36] G. M. Zaslavsky, *Hamiltonian Chaos and Fractional Dynamics*, Oxford University Press, New York, NY, USA, 2005.

[37] F. Liu, P. Zhuang, V. Anh, I. Turner, and K. Burrage, "Stability and convergence of the difference methods for the space-time fractional advection-diffusion equation," *Applied Mathematics and Computation*, vol. 191, no. 1, pp. 12–20, 2007.

[38] A. Yıldırım and H. Koçak, "Homotopy perturbation method for solving the space-time fractional advection-dispersion equation," *Advances in Water Resources*, vol. 32, no. 12, pp. 1711–1716, 2009.

[39] E. A. Abdel-Rehim, "Explicit approximation solutions and proof of convergence of space-time fractional advection dispersion equations," *Applied Mathematics*, vol. 4, no. 10, pp. 1427–1440, 2013.

[40] R. Gorenflo and F. Mainardi, "Fractional calculus: integral and differential equations of fractional order," in *Fractals and Fractional Calculus in Continuum Mechanics*, pp. 223–276, Springer, Wien, Austria, 1997.

[41] I. Podlubny, *Fractional Differential Equations*, Academic Press, New York, NY, USA, 1999.

[42] A. A. Kilbas, H. M. Srivastava, and J. J. Trujillo, *Theory and Applications of Fractional Differential Equations*, Elsevier, Amsterdam, The Netherlands, 2006.

[43] A. P. Prudnikov, Y. A. Brychkov, and O. I. Marichev, *Integrals and Series. Elementary Functions*, Nauka, Moscow, Russia, 1981 (Russian).

[44] Y. Z. Povstenko, "Fractional heat conduction equation and associated thermal stress," *Journal of Thermal Stresses*, vol. 28, no. 1, pp. 83–102, 2005.

[45] Y. Z. Povstenko, "Two-dimensional axisymmetric stresses exerted by instantaneous pulses and sources of diffusion in an infinite space in a case of time-fractional diffusion equation," *International Journal of Solids and Structures*, vol. 44, no. 7-8, pp. 2324–2348, 2007.

[46] R. Gorenflo, J. Loutchko, and Y. Luchko, "Computation of the Mittag-Leffler function and its derivatives," *Fractional Calculus and Applied Analysis*, vol. 5, no. 4, pp. 491–518, 2002.

[47] Y. Z. Povstenko, "Stresses exerted by a source of diffusion in a case of a non-parabolic diffusion equation," *International Journal of Engineering Science*, vol. 43, no. 11-12, pp. 977–991, 2005.

[48] Y. Povstenko, "Signaling problem for time-fractional diffusion-wave equation in a half-plane," *Fractional Calculus and Applied Analysis*, vol. 11, no. 3, pp. 329–352, 2008.

[49] W. R. Schneider, "Fractional diffusion," in *Dynamics and Stochastic Processes*, vol. 355 of *Lecture Notes in Physics*, pp. 276–286, Springer, Berlin, Germany, 1990.

Hindawi Publishing Corporation
Mathematical Problems in Engineering
Volume 2013, Article ID 847076, 11 pages
http://dx.doi.org/10.1155/2013/847076

Research Article

Raman Spectra of Nanodiamonds: New Treatment Procedure Directed for Improved Raman Signal Marker Detection

Raoul R. Nigmatullin,[1] Dumitru Baleanu,[2,3,4] Diana Povarova,[1] Numan Salah,[5] Sami S. Habib,[5] and Adnan Memic[5]

[1] *Theoretical Physics Department, Institute of Physics, Kazan (Volga region) Federal University, Kremlevskaya street 18, Kazan 420008, Russia*
[2] *Chemical and Materials Engineering Department, Faculty of Engineering, King Abdulaziz University, P.O. Box 80204, Jeddah 21589, Saudi Arabia*
[3] *Department of Mathematics and Computer Sciences, Faculty of Arts and Sciences, Cankaya University, 06530 Ankara, Turkey*
[4] *Institute of Space Sciences, Magurele, 077125 Bucharest, Romania*
[5] *Center of Nanotechnology, King Abdulaziz University, P.O. Box 80216, Jeddah 21589, Saudi Arabia*

Correspondence should be addressed to Adnan Memic; amemic@kau.edu.sa

Received 11 October 2013; Accepted 12 November 2013

Academic Editor: J. A. Tenreiro Machado

Detonation nanodiamonds (NDs) have shown to be promising agents in several industries, ranging from electronic to biomedical applications. These NDs are characterized by small particle size ranging from 3 to 6 nm, while having a reactive surface and a stable inert core. Nanodiamonds can exhibit novel intrinsic properties such as fluorescence, high refractive index, and unique Raman signal making them very attractive imaging agents. In this work, we used several nanodiamond preparations for Raman spectroscopic studies. We exposed these nanodiamonds to increasing temperature treatments at constant heating rates (425–575°C) aiding graphite release. We wanted to correlate changes in the nanodiamond surface and properties with Raman signal which could be used as a *detection marker*. These observations would hold potential utility in biomedical imaging applications. First, the procedure of optimal linear smoothing was applied successfully to eliminate the high-frequency fluctuations and to extract the smoothed Raman spectra. After that we applied the secondary Fourier transform as the fitting function based on some significant set of frequencies. The remnant noise was described in terms of the beta-distribution function. We expect this data treatment to provide better results in biomolecule tracking using nanodiamond base Raman labeling.

1. Introduction

Diamond is an important material for both scientific and industrial applications due to its extreme physical, chemical, and biological properties [1]. It is the hardest material known to science and has widespread applications such as cutting and drilling tools, thermal dissipation for electronics, infrared window in harsh environments, filter for surface acoustic wave device, field emission display device, electrochemical sensors in harsh/corrosive environments, biomedical imaging, and so on [2–6]. Diamond exhibits low toxicity and excellent biocompatibility and therefore has great potential as a novel material with potential biomedical applications [6]. There is increasing interest for using nanodiamond as biosensors and fabricating fluorescent nanoscale diamond particles for optical labeling and drug or gene delivery [4–6].

Currently, there are several methods developed for diamond synthesis in general [7–15]. The most common are methods based on high-pressure high-temperature approaches (HPHT) [7] and chemical vapour deposition methods (CVD) [8, 9]. Other methods include explosive formation (forming detonation nanodiamonds) [10, 11], sonication of graphite solutions (ultrasound cavitation) [1, 12], laser ablation [12], high-energy ball milling of HPHT diamond microcrystals [13], autoclave synthesis from supercritical

fluids [14], chlorination of carbides [15], ion irradiation of graphite [16], electron irradiation of carbon "onions" [17] which were also established.

Diamond's outstanding physical and chemical properties when combined with nanostructure form may lead to hybrid nanodevices with excellent and unique functions and performance [1, 10, 14]. These nanostructures diamonds are often referred as nanodiamonds (NDs) with the expectation of being the next-generation electronic material for specialized nanoelectromechanical systems (NEMS), nanoelectronic devices, and field emission applications [18]. Furthermore, nanodiamonds also have a potential application in biology such as carriers for drugs, genes, or proteins; novel imaging techniques; coatings for implantable materials; biosensors and biomedical nanorobots [19].

Diamond nanoparticles were produced for the first time by detonation method in 1960 [20], but they became popular only by the end of the 1980s [21]. In 1990, a number of important research results led to wider interest in these nanoparticles. For example, colloidal suspended nanodiamonds with particle size in the range of 4-5 nm became available [22]. Researchers proposed using fluorescent nanodiamonds as a non-toxic alternative to quantum dots for biomedical imaging [5, 6]. Nanodiamonds were also developed for fabricating magnetic sensors [23]. The nanodiamonds have a good surface chemical reactivity [24–26]; therefore it is possible to tailor the properties of nanodiamonds for use in different applications such as composites [27–31] or attaching drugs and biomolecules when dealing with biological applications [32–34]. In addition, nanodiamonds were found to be less toxic than other carbon nanoparticles such as carbon nanotubes [35–38] and, as a result, are currently being considered for applications in biomedical imaging, drug delivery, and other areas of medicine [19, 38].

Fluorescent nanodiamonds are emerging as a new type of nanomaterial that have great promise for biological applications [37, 39]. The nanodiamonds that contain a high concentration of nitrogen-vacancy (N-V) defect centers as fluorophores exhibit several remarkable features such as emission of bright photoluminescence in the extended red region, no photobleaching and photoblinking, and easiness of surface functionalization for specific or nonspecific binding with nucleic acids and proteins [40, 41]. The capability of emitting light at 700 nm, where cell autofluorescence signal is low, [19], makes nanodiamonds suitable for cellular imaging application. These excellent photophysical properties, together with the good biocompatibility of the material [5], can enable 3D tracking of a single 35 nm nanodiamond particle in a live mammalian cell using confocal microscopy [42].

However, ensuring purity of synthesized nanodiamonds is paramount to their application to the field of biomedical imaging in general and Raman tracking in specific. Often other contaminants such as graphite or similar carbon based by-products can be found during the synthesis procedure [7–15]. These impurities can induce fluctuations in the intrinsic Raman signal and therefore they can have negative effects when using the Raman signal as a detection marker. Furthermore, biological molecules can be adsorbed on the nanodiamond surface providing them a traceable label. Specifically, synthesized nanodiamonds can be characterized by their sharp band using Raman spectroscopy. This band is the characteristic peak of the sp^3 structural diamond [10], mostly observed at around 1430 cm^{-1}. However, synthesized nanodiamonds contain considerable amount of graphite, which can be detected by Raman spectrum. The presence of a broad band at around 1590 cm^{-1} is the in-plane vibrations of graphite (G band) [18, 43, 44]. Therefore, Raman spectrum is considered to be a powerful tool to potential tracking of nanodiamonds. The graphite phase can be removed with treatment at relatively lower temperatures in comparison to that of diamonds [44]. This can be seen clearly in the intensity reduction of the corresponding G band compared with that of diamonds. However, the obtained bands/signals have some noise/fluctuations, which might require further theoretical analysis to observe the actual trends/variations allowing for accurate and improved signal tracking.

In this work, we have prepared three nanodiamond samples, heated at 425°C, 475°C, and 575°C, respectively. Next, we obtained Raman spectroscopy spectra for all three heated samples in addition to the untreated "as obtained" nanodiamonds. Our goal was initiating the release of graphite impurities with these temperature treatments, changing the nanodiamond surface/interface properties. We then observed the changes in the Raman spectra based on this treatment. Since even minute amounts of graphite can generate a significant background noise [43, 44], novel signal treatment methods are required in order to improve the ability of using the Raman signal as a bioprobe or molecular detection marker. To tackle these challenges we applied the procedure of the optimal linear smoothing (POLS) [45] for the measured Raman spectra of nanodiamonds. Raman spectra for all heat treated and "as obtained" nanodiamonds were used for analysis and comparison in this study. We applied the procedure of POLS in order to eliminate the high-frequency fluctuations and extract the desired trend (smoothed Raman spectrum), aiding in assessing potential application of the Raman tracking signal produced by the nanodiamonds as a detection marker.

2. Experimental Details

Detonation nanodiamond particles of size around 6 nm and purity of more than 98% were obtained from Nanostructured & Amorphous Materials Inc., USA (http://www.nanoamor.com/). These samples were used for further treatments. These nanodiamonds were oxidized at three different temperatures. Specifically we carried out heating at 425°C, 475°C, and 575°C for equal amounts of time, which is 60 min. The heating rate is 10°C/min. After heating the sample at the desired temperature it was slowly cooled down to room temperature. Raman spectra were measured and collected using a DXR Raman Microscope, Thermo Scientific, using a 532 nm laser as the excitation source at 8 mW power.

3. Results and Discussion

3.1. Application of the Procedure of Optimal Linear Smoothing (POLS). For the measured Raman spectra of nanodiamonds we applied initially the procedure of the optimal linear smoothing (POLS) suggested in [45] in order to eliminate the high-frequency fluctuations and extract the desired trend (smoothed Raman spectrum). We omit the details of this procedure because the POLS have been described earlier in papers [45–48]. In order to decrease the influence of these fluctuations we applied this procedure to the curves that are obtained from the initial ones by numerical integration relatively to its mean value. The usefulness of this procedure was demonstrated earlier in recent paper [47]. In the result of application of the POLS we obtain the smoothed trends that can be analyzed in terms of the secondary Fourier transform (SFT) described below.

The results of the application of the POLS are depicted in Figures 1(a), 1(b), 1(c), and 1(d). Each figure shows the desired trend (smoothed Raman spectrum at the fixed annealing temperature). Usually the optimal value of the smoothing window is located in the interval $[\Delta/10, \Delta/1000]$, where Δ defines the relative length of the initial interval $\Delta = x_N - x_0$. For simplicity we use as the independent x variable the normalized value of the wavelength λ; that is, $x = \lambda/100$. In order to have more reliable result for calculation of the value of the optimal smoothing window, we used as an independent criterion the behavior of the generalized Pearson correlation function (GPCF). The GPCF (based on the statistics of the fractional moments [49]) was introduced previously in paper [50] and it is determined as

$$\mathrm{GPCF}_p = \frac{\mathrm{GMV}_p(1,2)}{\sqrt{\mathrm{GMV}_p(1,1)\cdot \mathrm{GMV}_p(2,2)}}, \tag{1}$$

where the generalized mean value function (GMV-function), in turn, is defined as

$$\mathrm{GMV}_p(k,l) = \left(\frac{1}{N}\sum_{j=1}^{N}\left|\mathrm{nrm}_j(k)\cdot \mathrm{nrm}_j(l)\right|^{\mathrm{mom}_p}\right)^{1/\mathrm{mom}_p},$$
$$\mathrm{mom}_p = \exp\left(Ln_p\right), \qquad Ln_p = mn + \left(\frac{p}{P}\right)\cdot(mx - mn), \qquad p = 0, 1, \ldots, P. \tag{2}$$

Here the values k and l numerate a couple of compared sequences. At $\mathrm{mom}_p = 1$ expression (2) coincides with the conventional definition of the Pearson correlation coefficient. The normalized sequences located in the interval $0 < \mathrm{nrm}(y) < 1$ are determined below by expression (3). The value mom_p determines the current moment from the interval $[0, P]$. The value P determines the final value of the function Ln_p located in the interval $[mn, mx]$. The values mn and mx define correspondingly to the limits of the moments in the uniform logarithmic scale. In many practical cases, these values are chosen as $mn = -15$ and $mx = 15$ and P is chosen as integer value from the interval [50–100]. This empirical choice is related to the fact that the transition region of the random sequences considered expressed in the form of the GMV-functions are concentrated in the interval $\mathrm{Ln}_p \in [-5, 5]$ and the extended interval $[-15, 15]$ is taken for showing the limiting values of this function in the space of moments. The initial sequences are chosen in that way: the minimum of the GMV-function coincides with zero value while the maximal value of this function coincides with $\max(\mathrm{nrm}_j(y))$. In (2) the random sequences are supposed to be normalized to the unit value in accordance with expression

$$\text{(A)} \quad \mathrm{nrm}_j(y) = \frac{y_j^{(+)}}{\max\left(y_j^{(+)}\right)} - \frac{y_j^{(-)}}{\min\left(y_j^{(-)}\right)},$$
$$y_j^{(\pm)} = \frac{1}{2}\left(y_j \pm \left|y_j\right|\right),$$
$$\text{(B)} \quad \mathrm{nrm}_j(y) = \frac{\Delta y_j}{\max\left(\Delta y_j\right)}, \qquad \Delta y_j = y_j - \min\left(y_j\right),$$
$$j = 1, 2, \ldots, N, \quad 0 < \mathrm{nrm}(y) < 1. \tag{3}$$

Here the set y_j defines the initial random sequence that can contain the trend or can be compared with another sequence without trend. The symbol $|\cdots|$ and index j determine the absolute value and number of the measured points, correspondingly. The second case (B) in (3) corresponds to the case when the initial sequence is completely *positive*. If the limits mn and mx in (2) have opposite signs and accept sufficiently large values then the GPCF function has two plateaus equaled one at small numbers of mn (i.e., $\mathrm{GPCF}_{mn} = 1$) and another limiting value GPCF_{mx} depends on the degree of correlation between the random sequences compared. This right-hand limit (defined as L) is located between two values:

$$M \equiv \min\left(\mathrm{GPCF}_p\right) \le L \equiv \mathrm{GPCF}_{mx} \le 1. \tag{4}$$

The appearance of two plateaus implies that all information about possible correlations is *complete* and further increasing of the limiting numbers (mx, mn) figuring in (7) is not necessary. The numerous test calculations show that the high degree of correlations between two random sequences compared is observed when GPCF_{mx} coincides with the unit value, while the lowest correlations are observed when GPCF_{mx} is equaled to its minimal value (M). This simple observation having general character for all random sequences allows us to introduce new correlation parameter, (CC) complete correlation-factor, which is determined as

$$\mathrm{CC} = \left(\frac{L}{M}\right)\cdot\left(\frac{L-M}{1-M}\right). \tag{5}$$

We would like to stress here that this factor is determined on the *total* set of the fractional moments located between exp (mn) and exp (mx) values (see definition (2)). As it has been remarked above, in practical calculations for many cases it is sufficient to put $mn = -15$ and $mx = +15$, correspondingly. The upper row in (10) is referred to the CCL

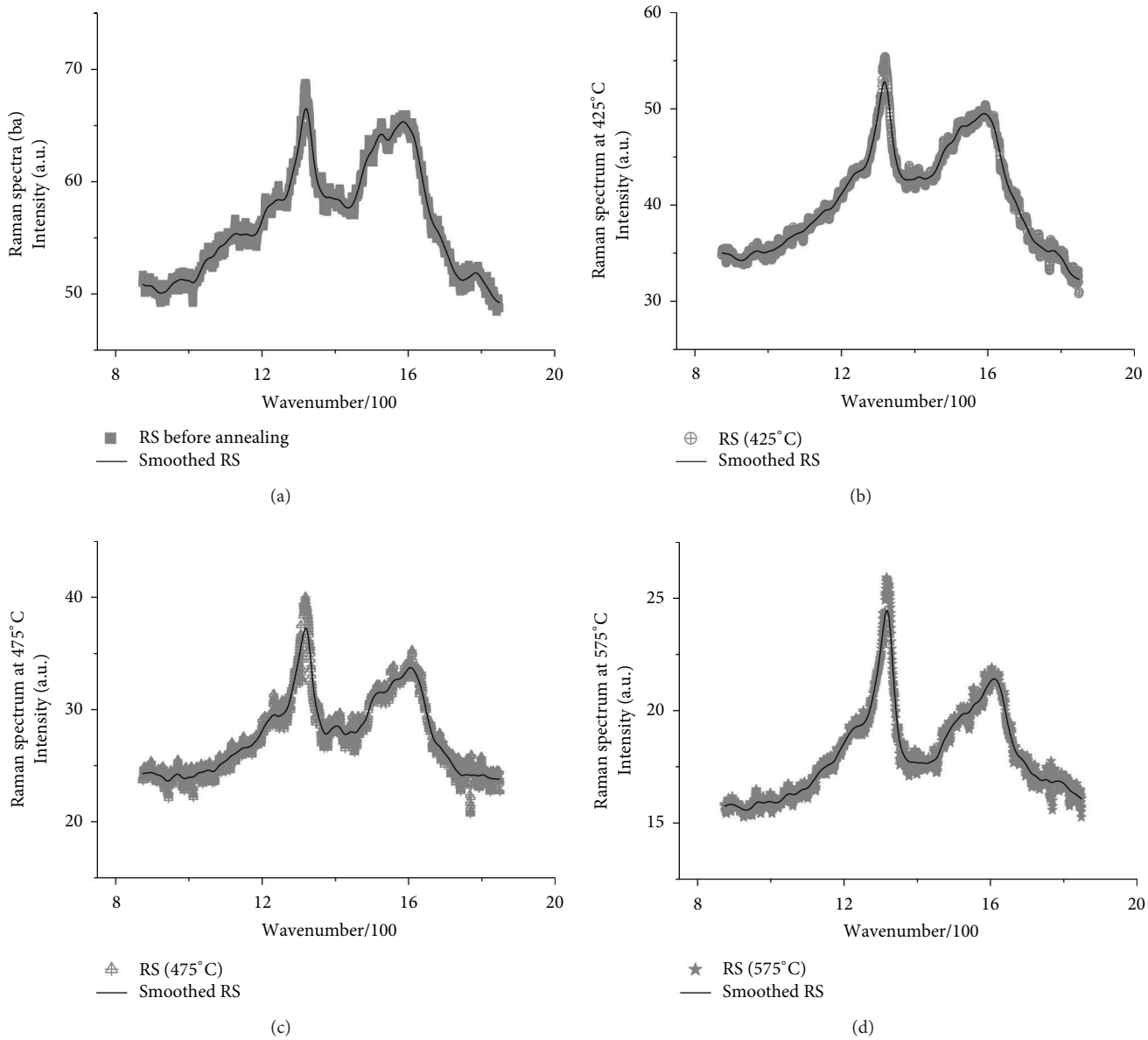

Figure 1: (a) The initial Raman spectrum (before annealing (ba) marked by grey squares) and its optimal trend (black solid line) obtained by application of the POLS. The optimal value of the smoothing window is shown in Figures 2(a) and 2(b). (b) The initial Raman spectrum (grey crossed points) measured at 425°C and its optimal trend (black solid line) obtained by application of the POLS. The optimal value of the smoothing window is shown in Figures 2(a) and 2(b). (c). The initial Raman spectrum (grey crossed triangles) measured at 475°C and its optimal trend (black solid line) obtained by application of the POLS. The optimal value of the smoothing window is shown in Figures 2(a) and 2(b). (d) The initial Raman spectrum (grey stars) measured at 575°C and its optimal trend (black solid line) obtained by application of the POLS. The optimal value of the smoothing window is shown in Figures 2(a) and 2(b).

(with respect to the limiting value L) while the low row determines the factor associated with the minimal value M. In practical calculations, both factors are useful for analysis but the CCL-factor is less sensitive to the strong correlations (or small perturbations of the initial sequence) in comparison with the CCM-factor. In addition, we want to stress also the following fact. This statistical parameter does not depend on the amplitudes of the random sequences compared. The pair random sequences compared should be normalized to the interval: $0 \leq |y_j| \leq 1$. It reflects the *internal* structure of correlations of the compared random sequences based presumably on the similarity of the probability distribution functions that are not known in many cases. In order to see how the high-frequency fluctuations are separated from the low-frequency fluctuations (which is conventionally defined as a trend) we put as initial function initial Raman spectrum (RS(d)) where d determines the initial RS before annealing (ba, $d = 0$) and after annealing measured at three temperatures (425°C,

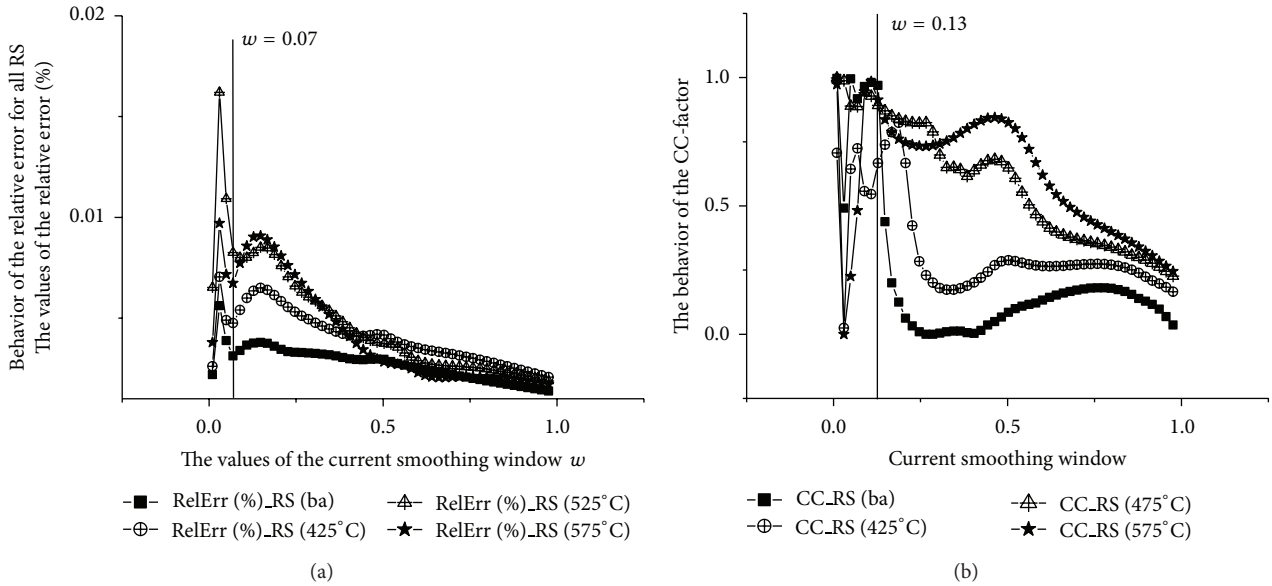

Figure 2: (a) The behavior of the relative error for all Raman spectra with respect to the current smoothing window. The value of the first minimum is equaled approximately 0.07. (b) The behavior of the complete correlation factor (expression (7)) is shown for all Raman spectra data. The value of the smoothing window $w = 0.13$ shows approximately the boundary dividing the high-frequency fluctuations from the low-frequency fluctuations (trend). From these two plots we chose the mean value of the smoothing window $w = 0.1$ which is identified as the optimal one.

$d = 1$), (525°C, $d = 2$), and (575°C, $d = 3$), correspondingly. As a second sequence we use the smoothed spectra obtained at the fixed value of the current smoothing window w_k from the interval $[w_{\min} = \Delta/1000, w_{\max} = \Delta/10]$. It is calculated as

$$y_j(d, w_k) = \mathrm{Gsm}(x, y, w_k) \equiv \frac{\sum_{j=1}^{N} K\left(\left(x_i - x_j\right)/w_k\right) y_j(d)}{\sum_{j=1}^{N} K\left(\left(x_i - x_j\right)/w_k\right)}, \quad K(x) = \exp\left(-\frac{x^2}{2}\right), \tag{6}$$

$$\mathrm{GPCF}_p\left(\mathrm{nrm}(d), y\mathrm{nrm}(d, w_k)\right) \longrightarrow \mathrm{CCM}_k = \frac{(L_k - M_k)}{1 - M_k}. \tag{7}$$

These expressions combined together allow calculating the complete correlation factor CCM_k as a function of the current smoothing window w_k. This value $w_{\mathrm{bound}} \approx w_{\mathrm{opt}}$ separates the correlations evoked by high-frequency fluctuations from low-frequency ones. This observation helps to find some additional arguments that justify the selection of the optimal trend in accordance with expressions (7). This additional criterion is important especially in cases when the first local minimum in the relative error function in expression (8) is not clearly expressed:

$$\tilde{y}_{w'} = \mathrm{Gsm}\left(x, \tilde{y}_w, w'\right), \quad w' < w,$$

$$\min(\mathrm{Re\ lErr}) = \left[\frac{\mathrm{stdev}\left(\left|y_{w'} - y_w\right|\right)}{\mathrm{mean}\left(\left|y_w\right|\right)}\right] \cdot 100\%,$$

$$\mathrm{stdev}(y) = \left(\frac{1}{N}\sum_{j=1}^{N}\left(\Delta y_j\right)^2\right)^{1/2}, \quad \Delta y_j = y_j - \mathrm{mean}(y), \quad \mathrm{mean}(y) = \frac{1}{N}\sum_{j=1}^{N} y_j. \tag{8}$$

That is why this optimal trend can be defined as the *pseudo-fitting* function which divides the high-frequency fluctuations from a trend. The behavior of the functions (8) and (7) is shown in Figures 2(a) and 2(b), correspondingly.

3.2. Application of the Secondary Fourier Transform as the Fitting Function. One can use the secondary Fourier transform as the *fitting* function based on some significant set of "frequencies." In accordance with conventional definition we determine this transformation of the second order as

$$\mathrm{SmRS}\left(x_j; d\right) \cong F\left(x_j\right) = A_0^{(d)} + \sum_{k=1}^{K}\left[\mathrm{Ac}_k^{(d)} \cos\left(2\pi k \frac{x_j}{L_d}\right), + \mathrm{As}_k^{(d)} \sin\left(2\pi k \frac{x_j}{L_d}\right)\right], \quad \omega_k = 2\pi k\left(\frac{1}{L_d}\right). \tag{9}$$

We suppose that the characteristic inverse length L_d ($d = 0, 1, 2, 3$ is the type of the RS defined above) coincides with the maximal length of the interval $\Delta = x_N - x_0 = L$ (x defines the normalized wave-number/100) and is measured in the same units as wavelength λ. If the value L is supposed to be known then the unknown decomposition coefficients Ac_k and As_k can be found by the linear-least square method (LLSM) and the limiting value K can be found from the condition of minimization of the value of the relative error:

$$1\% < \mathrm{Re\ lErr} = \left[\frac{\mathrm{stdev}\left(\left|\mathrm{SmRS}\left(x_j, d\right) - F\left(x_j, K\right)\right|\right)}{\mathrm{mean}\left(\left|\mathrm{SmRS}\left(x_j, d\right)\right|\right)}\right] \cdot 100\% < 10\%, \tag{10}$$

which should be located in the reasonable interval (1–10%) of the calculated errors. It is interesting to note that this new interpretation of the discrete Fourier transform as the fitting function of the initial signal does not coincide with conventional presentation of the Fourier transform as presentation of the function in the frequency space. The coefficients Ac_k and As_k found in the result of the application LLSM do not coincide with decomposition coefficients found in the result of application of the conventional program based on the fast Fourier transformation (FFT) and its modifications. Initially, we suppose simply that the period is found from the condition $\Delta = x_N - x_0 = L$. But further investigations show that this supposition can be *corrected* in order to decrease the value of the fitting error. This observation is illustrated by the plot depicted in Figure 3. After selection of the optimal value of L one can fit function (9) to the smoothed Raman spectra for nanodiamonds obtained in Section 3.1. In order to compare them with each other we chose the limiting value of modes K (number of components figuring in (9)) equaled 40. The results of the fitting of the smoothed Raman spectra corresponding to different annealing temperatures are shown in Figure 4. The additional fitting parameters are shown in Table 1. We want to stress here that in the absence of the microscopic model the application of the secondary Fourier transform allow us to reduce the 2025 measured points for each spectrum to 40 fitting parameters $19(\mathrm{Ac}_k) + 19(\mathrm{As}_k)$ amplitudes figuring in decomposition (9) plus free fitting constant $A_0^{(d)}$ and L_d for 4 types of Raman spectra. This reduced presentation with the help of the secondary Fourier transform is very convenient when the actual microscopic model describing the vibrations in nanodiamond dusts is *absent* but the barest necessity of description these RS exits. So, in brief, with the help of secondary Fourier transform we can reduce the Raman spectra to its amplitude-"frequency" response (AFR). Schematically, it can be written as

$$\mathrm{Spectrum}\,(\lambda, N) \longrightarrow \mathrm{AFR}\left(\mathrm{Ac}_k,\ \mathrm{As}_k,\ K\right), \quad K \ll N. \tag{11}$$

So, analysis of the Raman spectra can be based on the additional analysis of the amplitude-"frequency" responses (AFR) (we should notice again that in our case a "frequency" coincides with the value $\omega_k = 2\pi k/L$). This set of "frequencies" giving the acceptable accuracy should be located in the interval $[\omega_{\min} = 2\pi/L, \omega_{\max} = 2\pi K/L]$. So, we show that the secondary application of the Fourier transform (used as a fitting function of the initial signal) gives new possibilities for the interpretation of the smoothed RS data in terms of the reduced set of the calculated amplitudes Ac_k and As_k. Figure 4 demonstrates the fitting of the smoothed Raman spectra in the frame of this secondary Fourier analysis. The variations of the decomposition parameters $(\mathrm{Ac}_k, \mathrm{As}_k)$ together with its modulus for all Raman spectra are shown in Figures 5(a), 5(b), and 5(c). Other additional parameters are collected in Table 1.

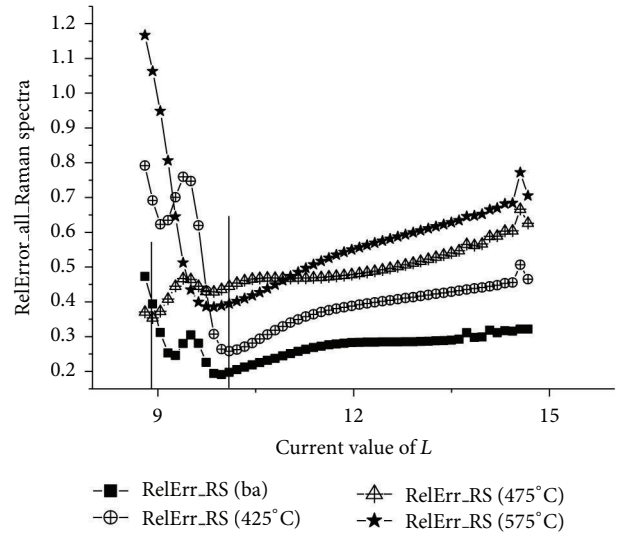

Figure 3: This plot clearly demonstrates that the relative fitting error can be essentially decreased (on the half-order of magnitude at least) if the optimal L in decomposition (9) can be found. The initial points located on the left-hand side correspond to the initial selection of L from the condition $x_N - x_0 = L$. The minimal (optimal) values of L are collected in Table 1. The bold vertical lines show the limits of the optimal values of L. All these plots are obtained for the limiting value of $K = 40$ in (9), which is chosen as the optimal for the fitting purposes.

3.3. "Reading" of the Remnant Noise in Terms of the Beta-Distribution Function. Usually, analysis of experimental data is finished after selection of the proper fitting function corresponding to some model and the "remnants" defined as the difference between the spectra analyzed and its fitting function is usually not analyzed. However, recent achievements associated with detection of the universal distribution function for the strongly correlated sequences allow realizing the fit of the remnants (noise) to the fitting function corresponding to beta-distribution [51]:

$$\mathrm{Jb}\,(x) = A(x - x_0)^{\alpha}(x_N - x)^{\beta} + B \tag{12}$$

and express quantitatively the remnant noise in terms of 4 fitting parameters (A, B, α, and β) only. This possibility gives a unique chance to compare the remnant functions with each other *quantitatively*. In order to obtain the bell-like curve

Table 1: The additional parameters of the secondary Fourier fitting.

Number of Raman spectrum	The value of L_{opt} from decomposition (9)	The value of A_0 (d) from decomposition (9)	The value of the fitting error (%)	Pearson correlation coefficient (PCC)
RS (ba), $d = 0$	9,97637	56,4327	0,19051	0,99976
RS (425C) $d = 1$	10,0937	40,5278	0,25801	0,9998
RS (475C) $d = 2$	8,92004	28,021	0,35399	0,9996
RS (575C) $d = 3$	9,859	18,0758	0,38478	0,99938

It is interesting to note that the values in columns 3 and 4 have the monotone behavior and so this peculiarity can be used for calibration purposes.

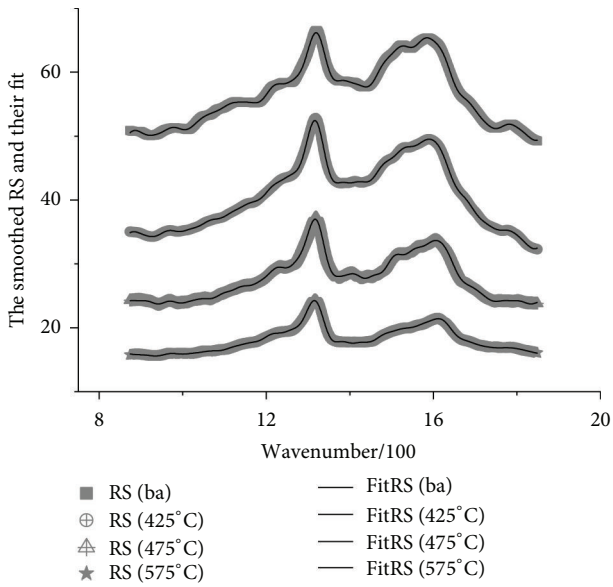

Figure 4: Here we show the results of the fitting of the secondary Fourier transform to the smoothed Raman spectra. The value of a free constant (from (9)) and other parameters (L_{opt}) are collected in Table 1.

from the remnant function it is necessary to do the following steps.

(S1) Calculate the difference

$$\mathrm{Rmf}(x,d) = \mathrm{Spectrum}(x,d) - \mathrm{Fit}(x,d), \tag{13}$$

where Rmf (x) defines the remnant function, Spectrum(x) defines the smoothed spectrum, and Fit(x) is associated with the corresponding fitting function. Index d as before defines the type of the Raman spectra.

(S2) Then, it is necessary to sort the amplitudes of the Rmf(x) in descending order ($y_1 > y_2 > \cdots > y_N$), subtract its mean value, and numerically integrate the rest:

$$\begin{gathered} Dy_j = y_j - \mathrm{mean}(y), \\ Jy_j = Jy_{j-1} + 0.5 \cdot \left(x_j - x_{j-1}\right) \cdot \left(Dy_j + Dy_{j-1}\right), \\ Jy_0 = 0, \quad j = 1, 2, \ldots, N. \end{gathered} \tag{14}$$

In the results of these manipulations we obtain the bell-like curve that can be fitted to expression (13) with the help of Eigen-coordinates (ECs) method [52]. Figure 6 demonstrates these two steps transforming the desired remnant function corresponding to the Raman spectrum ($d = 0$). In Figure 7 we show the final fit of all bell-like curves to the fitting function (12). We want to stress here that the ECs method [52] allows fitting the sufficient number of the measured points (2025) and reducing all fit to the conventional LLSM. The fitting parameters are collected in Table 2. Analysis of these curves shows clearly that the distribution of their heights with respect to increasing of the annealing temperature is not monotonic. The highest curve belongs to the annealing spectrum with 475°C. Then the curves belonging to RS before annealing and 425°C follow to monotone behavior and the lowest curve belongs to the annealing temperature 475°C.

4. Conclusions

The use of nanodiamonds as potential labels, probes, or tracers based on Raman specific detection is of great biological importance. In our study, we used three heat treated samples and compared them to the "as obtained" nanodiamond Raman signal. We showed that inducing the graphite heat release changes the nanodiamond surface interface that affected the Raman spectrum. It is clear from our data that these Raman signals were in need of data treatment due to their high-frequency fluctuations that could prove problematic in noisy cellular environments. Based on the four Raman spectra we are able to extract signal trends in the Raman signal resulting from the heat induced changes and finding the optimal for Raman signal fitting. Therefore, this can aid noise removal that is beneficial for future Raman based signal tracking based on nanodiamond particles in biological environments. In general, we were able to improve access to Raman spectroscopic mapping and signal tracking. We realized this procedure by application of the additional Fourier analysis using the finite Fourier decomposition as an additional fitting function (see expression (9)). This simple procedure helps decrease the number of the fitting parameters and gives a possibility to compare the spectra with each other. We demonstrate also how to read a remnant noise after elimination of the smoothed spectra. It helps also compare the noise in terms of the fitting parameters describing beta-function. Definitely, these new innovation elements can be applied in different nanotechnologies at analysis of small amount of materials, when the influence of

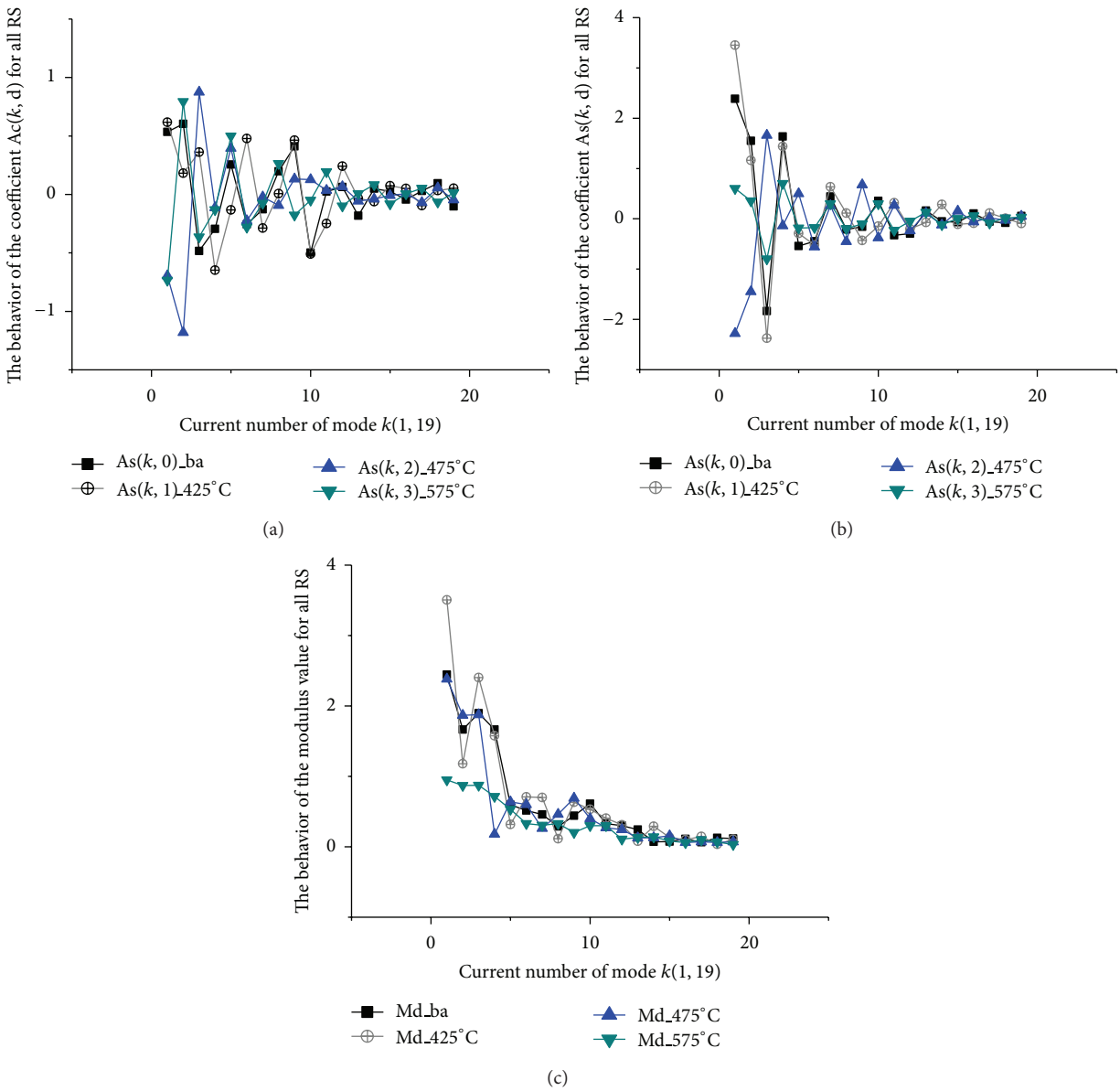

Figure 5: (a) Here we show the variations of the constant $\mathrm{Ac}(k, d)$ figuring in decomposition (9) for all 4 Raman spectra analyzed. (b) The variations of the constant $\mathrm{As}(k, d)$ from decomposition (9) for all 4 Raman spectra analyzed. (c) Here we demonstrate the variations of the modulus $(\mathrm{Ac}(k, d)^2 + \mathrm{As}(k, d)^2)^{1/2}$ for all 4 Raman spectra analyzed.

Table 2: The fitting parameters of all beta-distribution functions.

Number of Raman spectrum	A, B	α	β	$x_{\max}$ $y_{\max}$	RelErr (%)
RS (ba), $d = 0$	0,18165 −0.01731	0,76645	0,79319	13,5731 2.13296	0,40539
RS (425C), $d = 1$	0,22442 −0.05682	0,64713	0,7052	13,4381 1.8564	0,85344
RS (475C), $d = 2$	0,27183 −0.03377	0,70987	0,70286	13,7273 2.52004	0,61121
RS (575C), $d = 3$	0,12765 −0.01564	0,67151	0,72011	13,5682 1.14542	0,93181

In contrast with Table 1 the values in columns 5 and 6 have the nonmonotone behavior.

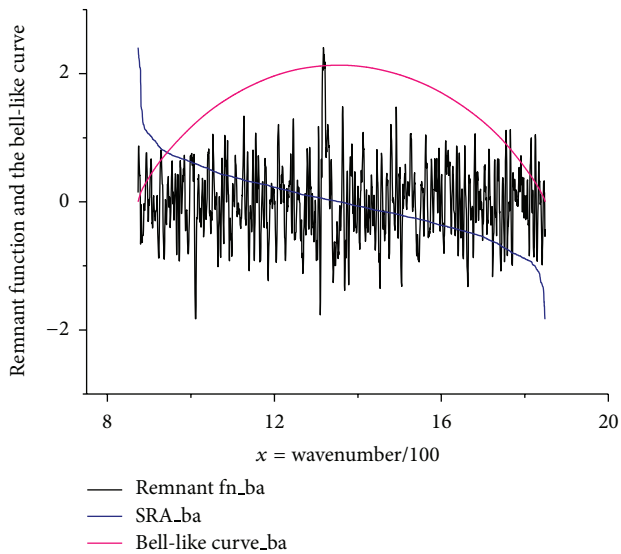

Figure 6: This plot demonstrates two steps (described in the text) that allow transforming the initial remnant function (marked by black line) for the RS ($d = 0$) to the sequence of the ranged amplitudes (SRA) and finally to the bell-like curve (marked by red solid line).

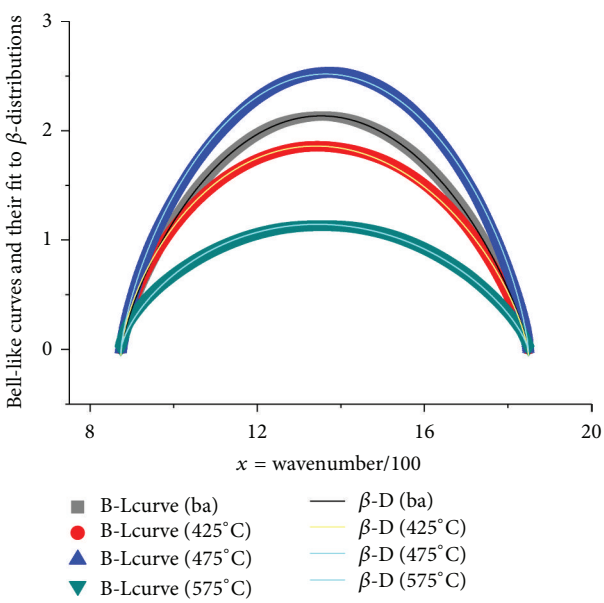

Figure 7: This plot shows the calculated bell-like curves and their fit to the beta-distribution function (12). The fitting parameters are collected in Table 2. One can notice that the behavior of these curves with respect to the values of the annealing temperatures is not monotone. The highest curve belongs to the annealing spectrum with 475°C. Then the curves belonging to RS before annealing and 425°C have monotone behavior and the lowest curve belongs to the annealing temperature 575°C.

noise fluctuations cannot be eliminated easily because of their quantum character. This current research (applied in the first time to nanodiamonds Raman spectra) undoubtedly merits a further research.

Acknowledgments

Raoul R. Nigmatullin and Diana Povarova express their thankfulness to the authorities of Kazan Federal University for financial support of this research. This study was funded by the Deanship of Scientific Research (DSR), King Abdulaziz University, Jeddah, Saudi Arabia, under Grant no. 903-003-D1434. The authors thank the DSR for the technical and financial support.

References

[1] X. Jiang, J. Zhao, C. Zhuang, B. Wen, and X. Jiang, "Mechanical and electronic properties of ultrathin nanodiamonds under uniaxial compressions," *Diamond and Related Materials*, vol. 19, no. 1, pp. 21–25, 2010.

[2] M. Werner and R. Locher, "Growth and application of undoped and doped diamond films," *Reports on Progress in Physics*, vol. 61, no. 12, pp. 1665–1710, 1998.

[3] E. Osawa, "Recent progress and perspectives in single-digit nanodiamond," *Diamond and Related Materials*, vol. 16, no. 12, pp. 2018–2022, 2007.

[4] É. M. Galimov, A. M. Kudin, V. N. Skorobogatskiĭ et al., "Experimental corroboration of the synthesis of diamond in the cavitation process," *Doklady Physics*, vol. 49, no. 3, pp. 150–153, 2004.

[5] Y. R. Chang, H.-Y. Lee, K. Chen et al., "Mass production and dynamic imaging of fluorescent nanodiamonds," *Nature Nanotechnology*, vol. 3, no. 5, pp. 284–288, 2008.

[6] V. N. Mochalin and Y. Gogotsi, "Wet chemistry route to hydrophobic blue fluorescent nanodiamond," *Journal of the American Chemical Society*, vol. 131, no. 13, pp. 4594–4595, 2009.

[7] Y. Zhang, C. Zang, H. Ma et al., "HPHT synthesis of large single crystal diamond doped with high nitrogen concentration," *Diamond and Related Materials*, vol. 17, no. 2, pp. 209–211, 2008.

[8] D. M. Gnien, "Nanocrystalline diamondfilms1," *Annual Review of Materials Science*, vol. 29, pp. 211–259, 1999.

[9] A. K. Dua, V. C. George, M. Friedrich, and D. R. T. Zahn, "Effect of deposition parameters on different stages of diamond deposition in HFCVD technique," *Diamond and Related Materials*, vol. 13, no. 1, pp. 74–84, 2004.

[10] Q. Zou, Y. G. Li, L. H. Zou, and M. Z. Wang, "Characterization of structures and surface states of the nanodiamond synthesized by detonation," *Materials Characterization*, vol. 60, no. 11, pp. 1257–1262, 2009.

[11] T. Jiang and K. Xu, "FTIR study of ultradispersed diamond powder synthesized by explosive detonation," *Carbon*, vol. 33, no. 12, pp. 1663–1671, 1995.

[12] G.-W. Yang, J.-B. Wang, and Q.-X. Liu, "Preparation of nanocrystalline diamonds using pulsed laser induced reactive quenching," *Journal of Physics Condensed Matter*, vol. 10, no. 35, pp. 7923–7927, 1998.

[13] J.-P. Boudou, P. A. Curmi, F. Jelezko et al., "High yield fabrication of fluorescent nanodiamonds," *Nanotechnology*, vol. 20, no. 23, Article ID 235602, 2009.

[14] Y. G. Gogotsi, "Structure of carbon produced by hydrothermal treatment of β-SiC powder," *Journal of Materials Chemistry*, vol. 6, no. 4, pp. 595–604, 1996.

[15] S. Welz, Y. Gogotsi, and M. J. McNallan, "Nucleation, growth, and graphitization of diamond nanocrystals during chlorination of carbides," *Journal of Applied Physics*, vol. 93, no. 7, pp. 4207–4214, 2003.

[16] T. L. Daulton, M. A. Kirk, R. S. Lewis, and L. E. Rehn, "Production of nanodiamonds by high-energy ion irradiation of graphite at room temperature," *Nuclear Instruments and Methods in Physics Research B*, vol. 175–177, pp. 12–20, 2001.

[17] F. Banhart and P. M. Ajayan, "Carbon onions as nanoscopic pressure cells for diamond formation," *Nature*, vol. 382, no. 6590, pp. 433–435, 1996.

[18] X. C. LeQuan, W. P. Kang, J. L. Davidson, M. Guo, and B. K. Choi, "Micro-Raman, SEM, XPS, and electron field emission characterizations of nitrogen-induced shallow defects on nanodiamond films fabricated with different growth parameters," *Diamond and Related Materials*, vol. 18, no. 2-3, pp. 191–195, 2009.

[19] A. M. Schrand, H. Huang, C. Carlson et al., "Are diamond nanoparticles cytotoxic?" *Journal of Physical Chemistry B*, vol. 111, no. 1, pp. 2–7, 2007.

[20] V. V. Danilenko, "On the history of the discovery of nanodiamond synthesis," *Physics of the Solid State*, vol. 46, no. 4, pp. 595–599, 2004.

[21] N. R. Greiner, D. S. Phillips, J. D. Johnson, and F. Volk, "Diamonds in detonation soot," *Nature*, vol. 333, no. 6172, pp. 440–442, 1988.

[22] M. Ozawa, M. Inaguma, M. Takahashi, F. Kataoka, A. Krüger, and E. Osawa, "Preparation and behavior of brownish, clear nanodiamond colloids," *Advanced Materials*, vol. 19, no. 9, pp. 1201–1206, 2007.

[23] J. R. Maze, P. L. Stanwix, J. S. Hodges et al., "Nanoscale magnetic sensing with an individual electronic spin in diamond," *Nature*, vol. 455, no. 7213, pp. 644–647, 2008.

[24] A. Krueger, "Diamond nanoparticles: jewels for chemistry and physics," *Advanced Materials*, vol. 20, no. 12, pp. 2445–2449, 2008.

[25] W.-W. Zheng, Y.-H. Hsieh, Y.-C. Chiu, S.-J. Cai, C.-L. Cheng, and C. Chen, "Organic functionalization of ultradispersed nanodiamond: synthesis and applications," *Journal of Materials Chemistry*, vol. 19, no. 44, pp. 8432–8441, 2009.

[26] B. V. Spitsyn, J. L. Davidson, M. N. Gradoboev et al., "Inroad to modification of detonation nanodiamond," *Diamond and Related Materials*, vol. 15, no. 2-3, pp. 296–299, 2006.

[27] K. D. Behler, A. Stravato, V. Mochalin, G. Korneva, G. Yushin, and Y. Gogotsi, "Nanodiamond-polymer composite fibers and coatings," *ACS Nano*, vol. 3, no. 2, pp. 363–369, 2009.

[28] Q. Zhang, V. N. Mochalin, I. Neitzel et al., "Fluorescent PLLA-nanodiamond composites for bone tissue engineering," *Biomaterials*, vol. 32, no. 1, pp. 87–94, 2011.

[29] D. H. Wang, L.-S. Tan, H. Huang, L. Dai, and E. Osawa, "In-situ nanocomposite synthesis: arylcarbonylation and grafting of primary diamond nanoparticles with a poly(ether-ketone) in polyphosphoric acid," *Macromolecules*, vol. 42, no. 1, pp. 114–124, 2009.

[30] J. Cheng, J. He, C. Li, and Y. Yang, "Facile approach to functionalize nanodiamond particles with V-shaped polymer brushes," *Chemistry of Materials*, vol. 20, no. 13, pp. 4224–4230, 2008.

[31] V. N. Mochalin, I. Neitzel, B. J. M. Etzold, A. Peterson, G. Palmese, and Y. Gogotsi, "Covalent incorporation of aminated nanodiamond into an epoxy polymer network," *ACS Nano*, vol. 5, no. 9, pp. 7494–7502, 2011.

[32] R. A. Shimkunas, E. Robinson, R. Lam et al., "Nanodiamond-insulin complexes as pH-dependent protein delivery vehicles," *Biomaterials*, vol. 30, no. 29, pp. 5720–5728, 2009.

[33] K. V. Purtov, A. I. Petunin, A. E. Burov, A. P. Puzyr, and V. S. Bondar, "Nanodiamonds as carriers for address delivery of biologically active substances," *Nanoscale Research Letters*, vol. 5, no. 3, pp. 631–636, 2010.

[34] A. Alhaddad, M.-P. Adam, J. Botsoa et al., "Nanodiamond as a vector for siRNA delivery to Ewing sarcoma cells," *Small*, vol. 7, no. 21, pp. 3087–3095, 2011.

[35] A. Schrand, J. Johnson, L. Dai et al., "Cytotoxicity and genotoxicity of carbon nanomaterials," in *Safety of Nanoparticles*, T. J. Webster, Ed., pp. 159–187, Springer, New York, NY, USA, 2009.

[36] A. M. Schrand, S. A. C. Hens, and O. A. Shenderova, "Nanodiamond particles: properties and perspectives for bioapplications," *Critical Reviews in Solid State and Materials Sciences*, vol. 34, no. 1-2, pp. 18–74, 2009.

[37] C.-C. Fu, H.-Y. Lee, K. Chen et al., "Characterization and application of single fluorescent nanodiamonds as cellular biomarkers," *Proceedings of the National Academy of Sciences of the United States of America*, vol. 104, no. 3, pp. 727–732, 2007.

[38] S.-J. Yu, M.-W. Kang, H.-C. Chang, K.-M. Chen, and Y.-C. Yu, "Bright fluorescent nanodiamonds: no photobleaching and low cytotoxicity," *Journal of the American Chemical Society*, vol. 127, no. 50, pp. 17604–17605, 2005.

[39] L.-C. L. Huang and H.-C. Chang, "Adsorption and immobilization of cytochrome c on nanodiamonds," *Langmuir*, vol. 20, no. 14, pp. 5879–5884, 2004.

[40] X. Kong, L. C. L. Huang, S.-C. V. Liau, C.-C. Han, and H.-C. Chang, "Polylysine-coated diamond nanocrystals for MALDI-TOF mass analysis of DNA oligonucleotides," *Analytical Chemistry*, vol. 77, no. 13, pp. 4273–4277, 2005.

[41] J. R. Mansfield, K. W. Gossage, C. C. Hoyt, and R. M. Levenson, "Autofluorescence removal, multiplexing, and automated analysis methods for in-vivo fluorescence imaging," *Journal of Biomedical Optics*, vol. 10, no. 4, Article ID 041207, 2005.

[42] Z. Y. Lien, T. C. Hsu, K. K. Liu, W. S. Liao, K. C. Hwang, and J. I. Chao, "Cancer cell labeling and tracking using fluorescent and magnetic nanodiamond," *Biomaterials*, vol. 33, no. 26, pp. 6172–6185, 2012.

[43] S. Michaelson and A. Hoffman, "Hydrogen bonding, content and thermal stability in nano-diamond films," *Diamond and Related Materials*, vol. 15, no. 4–8, pp. 486–497, 2006.

[44] Y. Tzeng and Y. K. Liu, "Diamond CVD by microwave plasmas in argon-diluted methane without or with 2% hydrogen additive," *Diamond and Related Materials*, vol. 14, no. 3–7, pp. 261–265, 2005.

[45] C.-M. Băleanu, R. R. Nigmatullin, S. S. Cetin et al., "New method and treatment technique applied to interband transition in $GaAs_{1-x}P_x$ ternary alloys," *Central European Journal of Physics*, vol. 9, no. 3, pp. 729–739, 2011.

[46] M. L. Ciurea, S. Lazanu, I. Stavarache et al., "Stress-induced traps in multilayered structures," *Journal of Applied Physics*, vol. 109, no. 1, Article ID 013717, 2011.

[47] R. R. Nigmatullin, C. Ionescu, and D. Baleanu, "NIMRAD: novel technique for respiratory data treatment," *Signal, Image and Video Processing*, pp. 1–16, 2012.

[48] R. R. Nigmatullin, C.-M. Ionescu, S. Osokin et al., "Non-invasive methods applied for complex signals," *Romanian Reports in Physics*, vol. 64, no. 4, pp. 1032–1045, 2012.

[49] R. R. Nigmatullin, "The statistics of the fractional moments: is there any chance to "read quantitatively" any randomness?" *Signal Processing*, vol. 86, no. 10, pp. 2529–2547, 2006.

[50] R. R. Nigmatullin, A. A. Arbuzov, S. O. Nelson, and S. Trabelsi, "Dielectric relaxation in complex systems: quality sensing and dielectric properties of honeydew melons from 10 MHz to 1.8 GHz," *Journal of Instrumentation*, vol. 1, no. 1, pp. 1–20, 2006.

[51] R. R. Nigmatullin, "Universal distribution function for the strongly-correlated fluctuations: general way for description of different random sequences," *Communications in Nonlinear Science and Numerical Simulation*, vol. 15, no. 3, pp. 637–647, 2010.

[52] R. R. Nigmatullin, "Recognition of nonextensive statistical distributions by the eigencoordinates method," *Physica A*, vol. 285, no. 3, pp. 547–565, 2000.

Hindawi Publishing Corporation
Mathematical Problems in Engineering
Volume 2013, Article ID 560932, 6 pages
http://dx.doi.org/10.1155/2013/560932

Research Article

Local Fractional Discrete Wavelet Transform for Solving Signals on Cantor Sets

Yang Zhao,[1,2] Dumitru Baleanu,[3,4,5] Carlo Cattani,[6] De-Fu Cheng,[1] and Xiao-Jun Yang[7]

[1] *College of Instrumentation & Electrical Engineering, Jilin University, Changchun 130061, China*
[2] *Electronic and Information Technology Department, Jiangmen Polytechnic, Jiangmen 529090, China*
[3] *Department of Chemical and Materials Engineering, Faculty of Engineering, King Abdulaziz University, P.O. Box 80204, Jeddah 21589, Saudi Arabia*
[4] *Department of Mathematics and Computer Sciences, Faculty of Arts and Sciences, Cankaya University, 06530 Ankara, Turkey*
[5] *Institute of Space Sciences, Magurele, 077125 Bucharest, Romania*
[6] *Department of Mathematics, University of Salerno, Via Ponte don Melillo, Fisciano, 84084 Salerno, Italy*
[7] *Department of Mathematics and Mechanics, China University of Mining and Technology, Xuzhou Campus, Xuzhou, Jiangsu 221008, China*

Correspondence should be addressed to De-Fu Cheng; chengdefu@jlu.edu.cn

Received 15 September 2013; Accepted 22 October 2013

Academic Editor: J. A. Tenreiro Machado

The discrete wavelet transform via local fractional operators is structured and applied to process the signals on Cantor sets. An illustrative example of the local fractional discrete wavelet transform is given.

1. Introduction

In recent years, the classical wavelet theory [1–7] has played an important role in many scientific fields such as signal processing [8], electrical systems [9], image processing [10], and differential equations [11]. The continuous wavelet transform is applied to handle the analyzing nonstationary signals, which have some characteristics of instantaneous peaks or discontinuities, where the mother wavelet met scaling and translation operations [3]. Two major categories of wavelet transforms are continuous and discrete [5]. When the mother wavelet functions are orthonormal, the discrete wavelet transform [12] gives multiresolution algorithm decomposing signals into scales with different time and frequency resolution, which leads to finite number of wavelet comparisons of signals, and improves the computational speeds because of the functions that are stretched or compressed and placed at many positions along the signals [13].

Based on the fractional Fourier transform [14–17], the fractional wavelet transform, which was a good tool for processing transient signals and compressing images, was structured in [18, 19]. The fractional wavelet transform has some applications in various branches of science and engineering [20–23]. For example, the simultaneous spectral analysis of a binary mixture system was presented in [20] by using the fractional wavelet transform. Application of the fractional wavelet transform to the simultaneous determination of ampicillin sodium and sulbactam sodium in a binary mixture was considered in [21]. The fractional wavelet transform for the quantitative spectral resolution of the composite signals of the active compounds in a two-component mixture was suggested in [22]. The optical image encryption based on fractional wavelet transform was given in [23]. By discretizing continuous fractional wavelet transform, the discrete fractional wavelet transform was reported and its application to multiple encryptions was considered in [24].

The wavelet method and its fractional counterpart have many applications in various branches of science and engineering. However, they are invalid for solving the signals

defined on Cantor sets. The local fractional calculus theory [25–34] was applied to handle the functions defined on Cantor sets, which are local fractional continuous. A natural question is to generalize signals concepts on the Cantor set, which are the nondifferentiable functions defined on Cantor sets [24, 26] and the Cantor function [35]. The mathematical theory of the local fractional wavelet transform of the local fractional continuous signal was structured in [25, 36] based on the basic idea.

One of the open problems in this area is how to improve the computational speeds of the local fractional wavelet theory as in the classical one. The aim of this paper is to structure the discrete version of the local fractional wavelet transform based on the generalized inner production space. The paper has been organized as follows. In Section 2, we introduce some basic notations and theorems of the generalized inner product space. In Section 3, we propose the local fractional discrete wavelet transform. In Section 4, one example is presented. Finally, Section 5 is conclusions.

2. Preliminaries

In this section, we give some basic notations and theorems of the generalized inner product space.

Let [25]

$$L_{2,\alpha}[R]=\left\{f(x)\in C_\alpha[R]:\left(\frac{1}{\Gamma(1+\alpha)}\int_{-\infty}^{\infty}\left|f(x)\right|^p(dx)^\alpha\right)^{1/p}<\infty, 1\le p<\infty\right\}. \tag{1}$$

Here, the local fractional integral operator $f(x)$ in the interval $[a,b]$ was defined in [25–30] as

$$\begin{aligned}{}_aI_b^{(\alpha)}f(x)&=\frac{1}{\Gamma(1+\alpha)}\int_a^b f(t)(dt)^\alpha\\&=\frac{1}{\Gamma(1+\alpha)}\lim_{\Delta t\to 0}\sum_{j=0}^{j=N-1}f\left(t_j\right)\left(\Delta t_j\right)^\alpha,\end{aligned} \tag{2}$$

where a partition of the interval $[a,b]$ is denoted as $\Delta t_j = t_{j+1}-t_j$, $\Delta t=\max\{\Delta t_0,\Delta t_1,\Delta t_j,\ldots\}$ and $j=0,\ldots,N-1$, $t_0=a$, $t_N=b$. Local fractional operators were applied to model some nondifferentiable problems [25–32].

From (1) the generalized inner product space of $L_{2,\alpha}[R]$ is defined as follows [25]:

$$\langle f,g\rangle_\alpha=\frac{1}{\Gamma(1+\alpha)}\int_{-\infty}^{\infty}f(x)\overline{g(x)}(dx)^\alpha. \tag{3}$$

The two useful theorems are presented as follows.

Theorem 1 (see [25]). *Let X be an inner product space. If $\{e_n^\alpha\}$ is an orthonormal system in X, then one has that*

$$\|f\|_\alpha^2=\sum_{i=1}^{\infty}\left|\langle f,e_i^\alpha\rangle_\alpha\right|^2, \tag{4}$$

$$f=\sum_{i=1}^{\infty}\langle f,e_i^\alpha\rangle_\alpha e_i^\alpha \tag{5}$$

are equivalent, where $\|f\|_\alpha^2$ is a norm of the function f and $\{e_n^\alpha\}$ has the following properties:

$$\begin{gathered}\|e_n^\alpha\|_\alpha=1,\\ \left\langle e_i^\alpha,e_j^\alpha\right\rangle=\begin{cases}0, & i\ne j,\\ 1, & i=j.\end{cases}\end{gathered} \tag{6}$$

Proof. See [25]. □

Theorem 2 (see [25]). *Let X be an inner product space and $\{e_n^\alpha\}$ be an orthonormal system in X. If $x^\alpha\in\operatorname{span}\{e_1^\alpha,\ldots,e_n^\alpha\}$, then for all $x^\alpha\in X$ one has*

$$x^\alpha=\sum_{i=1}^{n}\langle x^\alpha,e_i^\alpha\rangle_\alpha e_i^\alpha, \tag{7}$$

where $\operatorname{span}\{x_1^\alpha,\ldots,x_n^\alpha\}$ is the linear subspace of X of the linear span of the local fractional vectors [25], namely,

$$\operatorname{span}\{x_1^\alpha,\ldots,x_n^\alpha\}=\left\{x^\alpha=\sum_{i=1}^{n}a_ix_i^\alpha:a_i\in E\right\}. \tag{8}$$

Proof. See [25]. □

3. Local Fractional Discrete Wavelet Transform for Signals on Cantor Sets

3.1. Local Fractional Continuous Wavelet Transformation for Signals on Cantor Sets. The local fractional continuous wavelet transform of the local fractional continuous signal $f(t)$ was presented in [25, 26, 36] as

$$W_{\varphi,\alpha}f(a,b)=\frac{a^{-(\alpha/2)}}{\Gamma(1+\alpha)}\int_{-\infty}^{\infty}f(t)\overline{\varphi_{a,b,\alpha}(t)}(dt)^\alpha,\quad 0<\alpha\le 1, \tag{9}$$

where the local fractional daughter's wavelets were suggested in [25, 26, 36] by

$$\varphi_{a,b,\alpha}(t)=\frac{1}{a^{\alpha/2}}\varphi\left(\frac{t-b}{a}\right), \tag{10}$$

where a is the dyadic dilation, b is the dyadic position, and $a^{-(\alpha/2)}$ is the normalization Cantor factor. The inverse

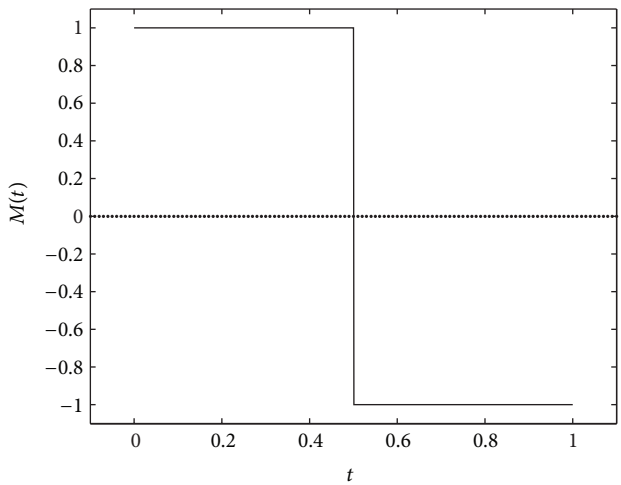

FIGURE 1: The graph of the local fractional mother wavelet.

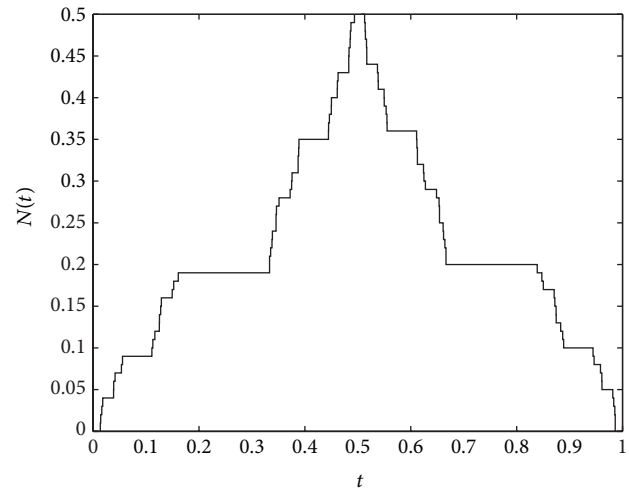

FIGURE 2: The graph of the local fractional integral of local fractional mother wavelet.

formula of local fractional wavelet transform was given in [25, 36] by

$$f(x) = \frac{C_{\varphi,\alpha}}{\Gamma^2(1+\alpha)} \times \int_{-\infty}^{\infty}\int_{-\infty}^{\infty} a^{-2\alpha} W_{\varphi,\alpha} f(a,b)\, \varphi_{a,b,\alpha}(t)(da)^{\alpha}(db)^{\alpha}, \quad 0 < \alpha \le 1, \tag{11}$$

where the parameter is [25, 36]

$$C_{\varphi,\alpha} = \frac{1}{\Gamma(1+\alpha)} \int_{-\infty}^{\infty} \frac{|f(x)|^2}{|x|^{\alpha}} (dx)^{\alpha}, \quad 0 < \alpha \le 1. \tag{12}$$

We notice that the classical continuous wavelet transform is the local fractional one in case of fractal dimension $\alpha = 1$.

3.2. Local Fractional Discrete Wavelet Transform for Signals on Cantor Sets. Let us structure the local fractional daughter wavelet in the form

$$\varphi_{a,b,\alpha}(t) = \frac{1}{a^{\alpha/2}} \varphi\left(\frac{t-b}{a}\right), \tag{13}$$

where $\varphi \in L_{2,\alpha}[R]$.

When $a = 2^{-j}$ and $b = k2^{-j}$, we get

$$\varphi_{a,b,\alpha}(t) = \varphi_{j,k,\alpha}(t) = \varphi_{2^{-j},k2^{-j},\alpha}(t) = 2^{j\alpha/2} \varphi\left(2^j t - k\right) \tag{14}$$

for integers $j, k \in Z$.

Let $\varphi_{j,k,\alpha}(t) = 2^{j\alpha/2}\varphi(2^j t - k)$ be orthogonal set of local fractional wavelets. Then we can obtain

$$\left\langle \varphi_{j,k,\alpha}, \varphi_{m,n,\alpha} \right\rangle_{\alpha} = \delta_{j,m}^{\alpha} \delta_{k,n}^{\alpha}, \quad j,k,m,n \in Z, \tag{15}$$

where $\delta_{j,m}^{\alpha}$ and $\delta_{k,n}^{\alpha}$ are local fractional Kronecker delta [27].

Making use of (7), for $j, k, m \in Z$ we have

$$f(x) = \sum_{j=-\infty}^{\infty} \sum_{m=-\infty}^{\infty} a_{j,k,\alpha} e_{j,k}^{\alpha}, \tag{16}$$

where its coefficients are

$$a_{j,k} = \left\langle f(x), e_{j,k}^{\alpha} \right\rangle_{\alpha} = W_{\varphi,\alpha} f\left(2^{-j}, k2^{-j}\right). \tag{17}$$

Here, $a_{j,k}$ is called as the local fractional discrete wavelet transform of the signal $f(x)$.

4. An Illustrative Example

Local fractional mother wavelet is defined in [26] as

$$\varphi_{H(\alpha)}(t) = M(t) = \begin{cases} 1, & 0 \le t < \frac{1}{2} \\ -1, & \frac{1}{2} \le t < 1 \\ 0, & \text{else} \end{cases} \tag{18}$$

and local fractional integral of local fractional mother wavelet reads as

$$\phi_{H(\alpha)}(t) = N(t) = \begin{cases} \dfrac{t^{\alpha}}{\Gamma(1+\alpha)}, & 0 \le t < \frac{1}{2} \\ \dfrac{(1-t)^{\alpha}}{\Gamma(1+\alpha)}, & \frac{1}{2} \le t < 1 \\ 0, & \text{else.} \end{cases} \tag{19}$$

Figure 1 shows the graph of the local fractional mother wavelet and Figure 2 shows the graph of the local fractional integral of local fractional mother wavelet.

When fractal dimension $\alpha = 1$, we have

$$\varphi_{H(1)}(t) = M(t) \tag{20}$$

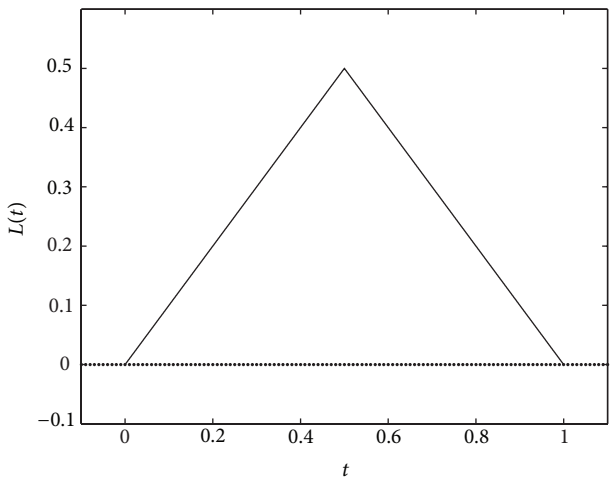

Figure 3: The graph of the integral of the mother wavelet.

so that

$$\phi_{H(1)}(t) = L(t) = \begin{cases} t, & 0 \le t < \frac{1}{2} \\ 1-t, & \frac{1}{2} \le t < 1 \\ 0, & \text{else.} \end{cases} \tag{21}$$

Figure 3 shows the graph of the integral of mother wavelet $\varphi_{H(1)}(t)$.

For integers $j, k \in \mathrm{Z}$, we have [26]

$$\varphi_{H(\alpha)}^{j,k}(t) = 2^{j\alpha/2}\varphi_{H(\alpha)}\left(2^j t - k\right), \tag{22}$$

where

$$\varphi_{H(\alpha)}(t) = \begin{cases} 1, & 0 \le t < \frac{1}{2}, \\ -1, & \frac{1}{2} \le t < 1, \\ 0, & \text{else.} \end{cases} \tag{23}$$

Hence, we have

$$\begin{aligned} &\left\langle \varphi_{H(\alpha)}^{j,k}, \varphi_{H(\alpha)}^{m,n} \right\rangle_\alpha \\ &\quad = \frac{1}{\Gamma(1+\alpha)} \int_{-\infty}^{\infty} \varphi_{H(\alpha)}^{j,k}(t)\, \varphi_{H(\alpha)}^{m,n}(t)\,(dt)^\alpha \\ &\quad = \frac{1}{\Gamma(1+\alpha)} \\ &\qquad \times \int_{-\infty}^{\infty} 2^{j\alpha/2}\varphi_{H(\alpha)}\left(2^j t - k\right) 2^{m\alpha/2}\varphi_{H(\alpha)} \\ &\qquad\qquad \times \left(2^m t - n\right)(dt)^\alpha \\ &\quad = 2^{(j+m)\alpha/2}\frac{1}{\Gamma(1+\alpha)} \\ &\qquad \times \int_{-\infty}^{\infty} \varphi_{H(\alpha)}\left(2^j t - k\right)\varphi_{H(\alpha)}\left(2^m t - n\right)(dt)^\alpha \\ &\quad = 2^{(m-j)\alpha/2}\frac{1}{\Gamma(1+\alpha)} \\ &\qquad \times \int_{-\infty}^{\infty} \varphi_{H(\alpha)}(s)\,\varphi_{H(\alpha)}\left(2^{m-j}(s+k) - n\right)(ds)^\alpha, \end{aligned} \tag{24}$$

where $s = 2^j t - k$.

In view of (24), we obtain [15]

$$\begin{aligned} \frac{1}{\Gamma(1+\alpha)} \int_{-\infty}^{\infty} \left[\varphi_{H(\alpha)}^{j,k}(t)\right]^2 (dt)^\alpha &= 1, \\ \frac{1}{\Gamma(1+\alpha)} \int_{-\infty}^{\infty} \varphi_{H(\alpha)}^{j,k}(t)\,(dt)^\alpha &= 0, \end{aligned} \tag{25}$$

where $j = m$ and $k = n$, $j, k \in \mathrm{Z}$.

When $j = m$, $j, k, m \in \mathrm{Z}$, from (24) we obtain

$$\begin{aligned} &\left\langle \varphi_{H(\alpha)}^{j,k}, \varphi_{H(\alpha)}^{j,n} \right\rangle_\alpha \\ &\quad = \frac{1}{\Gamma(1+\alpha)} \int_{-\infty}^{\infty} \varphi_{H(\alpha)}^{j,k}(t)\,\varphi_{H(\alpha)}^{m,n}(t)\,(dt)^\alpha \\ &\quad = 2^{(j+m)\alpha/2}\frac{1}{\Gamma(1+\alpha)} \\ &\qquad \times \int_{-\infty}^{\infty} \varphi_{H(\alpha)}\left(2^j t - k\right)\varphi_{H(\alpha)}\left(2^m t - n\right)(dt)^\alpha \\ &\quad = 2^{(m-j)\alpha/2}\frac{1}{\Gamma(1+\alpha)} \\ &\qquad \times \int_{-\infty}^{\infty} \varphi_{H(\alpha)}(s)\,\varphi_{H(\alpha)}\left(2^{m-j}(s+k) - n\right)(ds)^\alpha \\ &\quad = \frac{1}{\Gamma(1+\alpha)} \\ &\qquad \times \int_{-\infty}^{\infty} \varphi_{H(\alpha)}(s)\,\varphi_{H(\alpha)}(s+k-n)\,(ds)^\alpha \\ &\quad = \delta_{0,k-n}^{\alpha} \\ &\quad = \delta_{k,n}^{\alpha}, \end{aligned} \tag{26}$$

where $s = 2^j t - k$.

When $g = m - j > 0$, $j, k, m, n \in \mathrm{Z}$, from (24) we have

$$\begin{aligned} &\left\langle \varphi_{H(\alpha)}^{j,k}, \varphi_{H(\alpha)}^{m,n} \right\rangle_\alpha \\ &\quad = \frac{1}{\Gamma(1+\alpha)} \int_{-\infty}^{\infty} \varphi_{H(\alpha)}^{j,k}(t)\,\varphi_{H(\alpha)}^{m,n}(t)\,(dt)^\alpha \\ &\quad = 2^{g\alpha/2}\frac{1}{\Gamma(1+\alpha)} \\ &\qquad \times \int_{-\infty}^{\infty} \varphi_{H(\alpha)}(s)\,\varphi_{H(\alpha)}\left(2^g(s+k) - n\right)(ds)^\alpha \\ &\quad = 2^{g\alpha/2}\frac{1}{\Gamma(1+\alpha)} \\ &\qquad \times \int_{-\infty}^{\infty} \varphi_{H(\alpha)}(s)\,\varphi_{H(\alpha)}\left(2^g s + \eta\right)(ds)^\alpha, \end{aligned} \tag{27}$$

where $s = 2^j t - k$ and $\eta = 2^g k - n$. Consider

$$\begin{aligned}
&\left\langle \varphi_{H(\alpha)}^{j,k}, \varphi_{H(\alpha)}^{m,n} \right\rangle_\alpha \\
&\quad = 2^{g\alpha/2} \frac{1}{\Gamma(1+\alpha)} \\
&\qquad \times \int_{-\infty}^{\infty} \varphi_{H(\alpha)}(s)\, \varphi_{H(\alpha)}(2^g s + \eta)\, (ds)^\alpha \\
&\quad = 2^{g\alpha/2} \frac{1}{\Gamma(1+\alpha)} \\
&\qquad \times \int_{-\infty}^{\infty} \varphi_{H(\alpha)}(s)\, \varphi_{H(\alpha)}(2^g s + \eta)\, (ds)^\alpha \\
&\quad = 2^{g\alpha/2} \left[\frac{1}{\Gamma(1+\alpha)} \int_0^{1/2} \varphi_{H(\alpha)}(2^g s + \eta)\, (ds)^\alpha \right. \\
&\qquad \left. - \frac{1}{\Gamma(1+\alpha)} \int_{1/2}^{1} \varphi_{H(\alpha)}(2^g s + \eta)\, (ds)^\alpha \right] \\
&\quad = 2^{-g\alpha/2} \left[\frac{1}{\Gamma(1+\alpha)} \int_{\eta}^{2^{g-1}+\eta} \varphi_{H(\alpha)}(q)\, (dq)^\alpha \right. \\
&\qquad \left. - \frac{1}{\Gamma(1+\alpha)} \int_{2^{g-1}+\eta}^{2^g+\eta} \varphi_{H(\alpha)}(q)\, (dq)^\alpha \right],
\end{aligned} \tag{28}$$

where

$$\begin{gathered}
q = 2^g s + \eta, \\
\frac{1}{\Gamma(1+\alpha)} \int_{\eta}^{2^{g-1}+\eta} \varphi_{H(\alpha)}(q)\, (dq)^\alpha = 0, \\
\frac{1}{\Gamma(1+\alpha)} \int_{2^{g-1}+\eta}^{2^g+\eta} \varphi_{H(\alpha)}(q)\, (dq)^\alpha = 0,
\end{gathered} \tag{29}$$

with $\eta > 1$, $2^{g-1} + \eta > 1$, and $2^g + \eta > 1$.

Hence, taking $e_{j,k}^\alpha = \varphi_{H(\alpha)}^{j,k}$ gives

$$f(x) = \sum_{j=-\infty}^{\infty} \sum_{m=-\infty}^{\infty} a_{j,k,\alpha} \varphi_{H(\alpha)}^{j,k}(x), \tag{30}$$

where

$$\begin{aligned}
a_{j,k} &= \left\langle f(x), \varphi_{H(\alpha)}^{j,k}(x) \right\rangle_\alpha \\
&= W_{\varphi,\alpha} f\left(2^{-j}, k2^{-j}\right) \\
&= 2^{j\alpha/2} \frac{1}{\Gamma(1+\alpha)} \int_{-\infty}^{\infty} f(x)\, \overline{\varphi}_{H(\alpha)}^{j,k}(x)\, (dx)^\alpha.
\end{aligned} \tag{31}$$

Appling (4), we have

$$f^2(x) = \sum_{i=1}^{\infty} \left| a_{j,k} \right|^2 \tag{32}$$

with

$$a_{j,k} = 2^{j\alpha/2} \frac{1}{\Gamma(1+\alpha)} \int_{-\infty}^{\infty} f(x)\, \overline{\varphi}_{H(\alpha)}^{j,k}(x)\, (dx)^\alpha. \tag{33}$$

Hence, from (32) we find that the energy is conserved.

5. Conclusions

In this work the local fractional discrete wavelet transform based on the local fractional calculus theory was proposed. By using the basic theorems of generalized inner product space, the local fractional discrete wavelet transform and its reconstruction formula were discussed. We find that the energy of the signal on Cantor sets is conserved. An illustrative example for the local fractional wavelet transform of the signal on Cantor sets was given. It is shown that the classical discrete wavelet transform is the local fractional one in case of fractal dimension $\alpha = 1$.

Conflict of Interests

The authors declare that they have no conflict of interests regarding this paper.

Acknowledgment

The authors would like to thank the referees for their useful comments and remarks. s

References

[1] I. Daubechies, *Ten Lectures on Wavelets*, vol. 61 of *CBMS-NSF Regional Conference Series in Applied Mathematics*, Society for Industrial and Applied Mathematics (SIAM), Philadelphia, Pa, USA, 1992.

[2] D. Baleanu, *Advances in Wavelet Theory and Their Applications in Engineering, Physics and Technology*, InTech, Rijeka, Croatia, 2012.

[3] I. Daubechies, "The wavelet transform, time-frequency localization and signal analysis," *IEEE Transactions on Information Theory*, vol. 36, no. 5, pp. 961–1005, 1990.

[4] A. Grossmann and J. Morlet, "Decomposition of Hardy functions into square integrable wavelets of constant shape," *SIAM Journal on Mathematical Analysis*, vol. 15, no. 4, pp. 723–736, 1984.

[5] C. E. Heil and D. F. Walnut, "Continuous and discrete wavelet transforms," *SIAM Review*, vol. 31, no. 4, pp. 628–666, 1989.

[6] C. Cattani, "Shannon wavelets theory," *Mathematical Problems in Engineering*, vol. 2008, Article ID 164808, 24 pages, 2008.

[7] X.-G. Xia and Z. Zhang, "On sampling theorem, wavelets, and wavelet transforms," *IEEE Transactions on Signal Processing*, vol. 41, no. 12, pp. 3524–3535, 1993.

[8] O. Rioul and M. Vetterli, "Wavelets and signal processing," *IEEE Signal Processing Magazine*, vol. 8, no. 4, pp. 14–38, 1991.

[9] S.-J. Huang, T.-M. Yang, and J.-T. Huang, "FPGA realization of wavelet transform for detection of electric power system disturbances," *IEEE Transactions on Power Delivery*, vol. 17, no. 2, pp. 388–394, 2002.

[10] A. M. Wink and J. B. T. M. Roerdink, "Denoising functional MR images: a comparison of wavelet denoising and Gaussian smoothing," *IEEE Transactions on Medical Imaging*, vol. 23, no. 3, pp. 374–387, 2004.

[11] C. Cattani, "Harmonic wavelets towards the solution of nonlinear PDE," *Computers & Mathematics with Applications*, vol. 50, no. 8-9, pp. 1191–1210, 2005.

[12] M. J. Shensa, "The discrete wavelet transform: wedding the atrous and Mallat algorithms," *IEEE Transactions on Signal Processing*, vol. 40, no. 10, pp. 2464–2482, 1992.

[13] M. Bahoura and H. Ezzaidi, "FPGA-implementation of discrete wavelet transform with application to signal denoising," *Circuits, Systems, and Signal Processing*, vol. 31, no. 3, pp. 987–1015, 2012.

[14] D. Mendlovic and H. M. Ozaktas, "Fractional Fourier transforms and their optical implementation. I," *Journal of the Optical Society of America A*, vol. 10, no. 9, pp. 1875–1881, 1993.

[15] L. B. Almeida, "Fractional fourier transform and time-frequency representations," *IEEE Transactions on Signal Processing*, vol. 42, no. 11, pp. 3084–3091, 1994.

[16] J. Tenreiro MacHado, F. B. Duarte, and G. Monteiro Duarte, "Analysis of financial data series using fractional Fourier transform and multidimensional scaling," *Nonlinear Dynamics*, vol. 65, no. 3, pp. 235–245, 2011.

[17] D. Baleanu, K. Diethelm, E. Scalas, and J. J. Trujillo, *Fractional Calculus Models and Numerical Methods*, vol. 3 of *Series on Complexity, Nonlinearity and Chaos*, World Scientific, Hackensack, NJ, USA, 2012.

[18] D. Mendlovic, Z. Zalevsky, D. Mas, J. García, and C. Ferreira, "Fractional wavelet transform," *Applied Optics*, vol. 36, no. 20, pp. 4801–4806, 1997.

[19] M. Unser and T. Blu, "Fractional splines and wavelets," *SIAM Review*, vol. 42, no. 1, pp. 43–67, 2000.

[20] E. Dinç, E. Büker, and D. Baleanu, "Fractional and continuous wavelet transforms for the simultaneous spectral analysis of a binary mixture system," *Communications in Nonlinear Science and Numerical Simulation*, vol. 16, no. 12, pp. 4602–4609, 2011.

[21] E. Dinç and D. Baleanu, "A new fractional wavelet approach for the simultaneous determination of ampicillin sodium and sulbactam sodium in a binary mixture," *Spectrochimica Acta A*, vol. 63, no. 3, pp. 631–638, 2006.

[22] E. Dinç and D. Baleanu, "Fractional wavelet transform for the quantitative spectral resolution of the composite signals of the active compounds in a two-component mixture," *Computers & Mathematics with Applications*, vol. 59, no. 5, pp. 1701–1708, 2010.

[23] L. Chen and D. Zhao, "Optical image encryption based on fractional wavelet transform," *Optics Communications*, vol. 254, no. 4–6, pp. 361–367, 2005.

[24] G. Bhatnagar, Q. M. J. Wu, and B. Raman, "Discrete fractional wavelet transform and its application to multiple encryption," *Information Sciences*, vol. 223, pp. 297–316, 2013.

[25] X. J. Yang, *Local Fractional Functional Analysis and Its Applications*, Asian Academic Publisher , Hong Kong, 2011.

[26] X. J. Yang, D. Baleanu, H. M. Srivastava, and J. A. Tenreiro Machado, "On local fractional continuous wavelet transform," *Abstract and Applied Analysis*, vol. 2013, Article ID 725416, 5 pages, 2013.

[27] X. J. Yang, *Advanced Local Fractional Calculus and Its Applications*, World Science , New York, NY, USA, 2012.

[28] C. F. Liu, S. S. Kong, and S. J. Yuan, "Reconstructive schemes for variational iteration method within Yang-Laplace transform with application to fractal heat conduction problem," *Thermal Science*, vol. 17, no. 3, pp. 715–721, 2013.

[29] A. M. Yang, Y. Z. Zhang, and Y. Long, "The Yang-Fourier transforms to heat-conduction in a semi-infinite fractal bar," *Thermal Science*, vol. 17, no. 3, pp. 707–713, 2013.

[30] X. J. Yang, D. Baleanu, and J. A. T. Machado, "Mathematical aspects of Heisenberg uncertainty principle within local fractional Fourier analysis," *Boundary Value Problems*, no. 1, pp. 131–146, 2013.

[31] X.-J. Yang, H. M. Srivastava, J.-H. He, and D. Baleanu, "Cantor-type cylindrical-coordinate method for differential equations with local fractional derivatives," *Physics Letters A*, vol. 377, no. 28–30, pp. 1696–1700, 2013.

[32] X.-J. Yang, D. Baleanu, and J. A. Tenreiro Machado, "Systems of Navier-Stokes equations on Cantor sets," *Mathematical Problems in Engineering*, vol. 2013, Article ID 769724, 8 pages, 2013.

[33] A. Carpinteri, B. Chiaia, and P. Cornetti, "The elastic problem for fractal media: basic theory and finite element formulation," *Computers and Structures*, vol. 82, no. 6, pp. 499–508, 2004.

[34] A. K. Golmankhaneh, V. Fazlollahi, and D. Baleanu, "Newtonian mechanics on fractals subset of real-line," *Romania Reports in Physics*, vol. 65, pp. 84–93, 2013.

[35] O. Dovgoshey, O. Martio, V. Ryazanov, and M. Vuorinen, "The Cantor function," *Expositiones Mathematicae*, vol. 24, no. 1, pp. 1–37, 2006.

[36] X. J. Yang, "Local fractional calculus and its applications," in *Proceedings of the 5th IFAC Workshop Fractional Differentiation and Its Applications (FDA '12)*, pp. 1–8, Nanjing, China, 2012.